Imperial College London
Department of Earth Science and Engineering

Use of X-ray Computed Microtomography to Measure the Leaching Behaviour of Metal Sulphide Ores

Qingyang Lin

February 2015

Submitted in part fulfilment of the requirements for the degree of
Doctor of Philosophy in Earth Science and Engineering of Imperial College London
and the Diploma of Imperial College London

Abstract

Heap leaching is an important hydrometallurgical method to extract valuable metals from ores, especially low grade ores. The main disadvantages of heap leaching are the long processing time and low extraction efficiencies. Currently, a major barrier in fully understanding the leaching process is the study of the mass transport and surface chemistry at individual ore particle and mineral grain scale. This thesis describes a combined experimental and modelling approach to visualise, quantify and predict the leach behaviour based on X-ray Computed Microtomography (XMT, or micro-CT).

An automatic image processing package was developed to process the 3D volume data. Individual ore particles as well as individual mineral grains can be tracked using a centroid tracking algorithm and a novel fast tracking algorithm respectively. The systematic and random errors and uncertainties in the image volume measurements were quantified. It was found that both the systematic and random errors are a strong function of the grain size relative to the voxel size. The random error can be reduced by combining the results from either multiple scans of the same object or scans of multiple similar objects while the systematic error can be eliminated by using volume standards.

The leach performance for a leaching column was quantified at different scales and it was found that the leach behaviour and its variability were difficult to quantify at large scales (column and individual ore particle scale), but can be quantified at mineral grain scale by using a novel statistical analysis method. The tracked grains were divided into different size-distance categories to analyse the average leach performance and the variation for each category. Both grain size and distance dependencies were observed. The size dependency is more dominant at the early stage of leaching whereas the distance dependency can significantly influence the ultimate recovery. A method for using the data to estimate the variability in the in-situ surface kinetics was also developed.

A model for simulating the grain dissolution and the resultant kinetics based directly on XMT based 3D volume is introduced. The simulations were able to accurately predict both the overall leaching trends, as well as the leaching behaviour of mineral grains in classes based on their size and distance to the particle surface.

Declaration of Originality

I hereby declare that this work is original research undertaken by me and that no part of this thesis has been submitted for consideration towards another degree at this or any other institution. Any work in this thesis which is not my own work has been properly referenced.

Qingyang Lin
February 2015

Copyright Declaration

The copyright of this thesis rests with the author and is made available under a Creative Commons Attribution Non-Commercial No Derivatives licence. Researchers are free to copy, distribute or transmit the thesis on the condition that they attribute it, that they do not use it for commercial purposes and that they do not alter, transform or build upon it. For any reuse or redistribution, researchers must make clear to others the licence terms of this work.

Acknowledgements

I would like to thank my supervisor Dr Stephen Neethling for accepting as his PhD student. He is always willing to share his knowledge, experience and idea and give me any support during these years. I would also like to thank Prof Peter Lee for his supervision as my co-supervisor. He has shared lots of his research experience and given me great support during my PhD. Particular thanks for his organisation for letting me use the lab facilities and X-ray facilities at The University of Manchester and Research Complex at Harwell.

I am also grateful to all the current and past members of the Rio Tinto Centre at Imperial College who have made my PhD time at Imperial College enjoyable and productive. Particular thanks to Dr Dan Barker for sharing his computational knowledge helping me to start programming, developing models for the leaching simulation and carrying out Neutron experiment in the Swiss Light Source; Dr Saman Ilankoon for his help in the lab since I started, really nice experience doing Positron Emission Tomography experiment at The University of Birmingham and going for conference in Chile together. Another particular thank to our technician, Mr Graham Nash, for his great technical support during my entire PhD period.

I would like to express my gratitude to Rio Tinto for sponsoring this project under the auspices of their Centre for Advanced Minerals Recovery.

Last but not least, I would like to thank my family and friends for all their love and support.

Contents

Abstract i

Declaration of Originality ii

Copyright Declaration iii

Acknowledgements iv

Contents v

List of Figures x

List of Tables xv

1. Introduction 1

1.1. Motivation 1

1.2. Thesis Outline 3

2. Literature Review 5

2.1. Introduction 5

2.1.1. Current Status of Hydrometallurgy 6

2.1.2. Various Leaching Methods 7

2.1.2.1. Heap Leaching 8

2.1.2.2. Dump Leaching 9

2.1.2.3. Vat Leaching 9

2.1.2.4. Agitation Leaching 9

2.1.2.5. Pressure Oxidation Leaching 10

2.1.2.6. In-situ Leaching 10

2.1.2.7. Summary of Leaching Methods 10

2.2. Fundamentals of Heap Leaching . . . 10
2.2.1. Operational Procedure of Heap Leaching . . . 10
2.2.1.1. Ore Preparation . . . 11
2.2.1.2. Heap Construction . . . 13
2.2.1.3. Leaching Solution Application . . . 14
2.2.1.4. Pregnant Leaching Solution Collection . . . 14
2.2.1.5. Solvent Extraction . . . 14
2.2.1.6. Electro-winning . . . 14
2.2.2. Factors Affecting Heap Leaching . . . 15
2.3. Leaching Chemistry of Copper Minerals . . . 18
2.3.1. Fundamentals of Leaching Chemistry . . . 18
2.3.1.1. Leaching Agent . . . 19
2.3.1.2. Leaching of Oxide and Sulphide Minerals . . . 21
2.3.2. Copper Minerals in Heap Leaching . . . 23
2.3.3. Secondary Copper Mineral Leaching . . . 24
2.3.3.1. Copper Oxides Leaching . . . 24
2.3.3.2. Copper Sulphides Leaching . . . 25
2.3.3.3. Bacterial Actions . . . 26
2.3.4. Primary Copper Mineral Leaching: Chalcopyrite . . . 27
2.3.4.1. Introduction to Chalcopyrite . . . 27
2.3.4.2. Chemistry of Chalcopyrite Leaching . . . 27
2.3.4.3. Factors Affecting Chalcopyrite Leaching . . . 30
2.4. Ore Particle Effects in Heap Leaching . . . 33
2.4.1. Scales in Heap Leaching . . . 34
2.4.2. Leaching Behaviour at Individual Ore Particle Scale . . . 35
2.4.2.1. Ore Particle Size . . . 35
2.4.2.2. Grain Distribution and Accessibility to Leaching Solution 36
2.4.2.3. Porosity . . . 38
2.4.2.4. Gangue Minerals . . . 39
2.4.3. Ore Particle Level Modelling . . . 39
2.5. XMT application in heap leaching . . . 40
2.6. X-ray Computed Microtomography (XMT) . . . 42
2.6.1. Essentials of XMT . . . 42
2.6.2. Types of XMT . . . 46
2.6.3. Artefacts and Partial Volume Effects in Geological Applications . 48
2.6.3.1. Beam Hardening . . . 49

2.6.3.2. Ring Artefacts . . . 51
2.6.3.3. Partial Volume Effects . . . 51
2.7. General Image Processing . . . 53
2.7.1. Data Conversion . . . 53
2.7.2. Intensity Normalisation . . . 53
2.7.3. Image Filtering . . . 54
2.7.4. Thresholding . . . 54
2.8. Summary . . . 56

3. Experimental Methodology for Column Leaching **59**
3.1. Introduction . . . 59
3.2. Ore Samples . . . 59
3.3. Copper Content from Sample Decomposition . . . 60
3.4. Design of Experiment . . . 61
3.4.1. Controlling Parameters . . . 61
3.4.2. Leaching Solution . . . 61
3.4.3. Experimental Rigs . . . 62
3.4.4. Multi-channel Peristaltic Pump for Flow Rate Control . . . 63
3.5. Feed Composition for the Leaching Experiment . . . 64
3.5.1. pH and Acid Concentration . . . 65
3.5.2. Calibration of Iron Concentration from Raw Chemical Reagents . . . 67
3.5.3. Inductively Coupled Plasma Optical Emission Spectrometry . . . 68
3.6. Summary . . . 70

4. 4D Automatic Quantification of Ore Particles **71**
4.1. Introduction . . . 71
4.2. X-ray Computed Microtomography (XMT) . . . 73
4.2.1. X-ray CT Systems . . . 73
4.2.2. Centre of Rotation Determination and Image Reconstruction . . . 74
4.3. Image Processing . . . 76
4.3.1. Image Pre-processing . . . 76
4.3.2. Thresholding, Segmentation and Labelling of Ore Particles . . . 77
4.3.3. Particle Tracking and Registration of Ore Particles . . . 80
4.3.4. Thresholding of Metal Sulphide Grains . . . 82
4.3.5. Connectivity Analysis and Labelling of Mineral Grains . . . 85
4.3.6. Preliminary Quantification of Ore Particles . . . 85

4.4. Mineral Grain Tracking . . . 86
4.4.1. Mineral Grain Tracking Methodology . . . 87
4.4.2. Preliminary Quantification of An Ore Particle Based on Mineral Grain Tracking . . . 89
4.5. Quantifying and Minimising Systematic and Random Errors in Volume Measurements . . . 91
4.5.1. Sensitivity of Measured Volume to Threshold Changes . . . 95
4.5.2. Estimation of Grain Volume Uncertainty . . . 97
4.6. Obtaining Consistent Results in The Face of Systematic Errors by Changing Threshold Values . . . 100
4.7. Comparing Different Thresholding Methods and Their Consistency . . . 104
4.8. Summary . . . 108

5. Leaching Analysis Based on XMT **110**
5.1. Introduction . . . 110
5.2. Relationship between Image Measurement and Chemistry Measurement . . . 111
5.3. Leach Performance Analysis at Larger Scales . . . 114
5.3.1. Column Scale Analysis . . . 114
5.3.2. Individual Ore Particle Scale . . . 115
5.4. Statistical Analysis at the Grain Scale . . . 120
5.4.1. Leaching Performance Analysis for Different Categories . . . 122
5.4.2. Error Analysis of Leaching at the Grain Scale . . . 129
5.4.3. Effects of leaching parameters at sub particle level . . . 131
5.5. Summary . . . 133

6. Modelling of Apparent Leach Kinetics **136**
6.1. Introduction . . . 136
6.2. 3D Image Processing . . . 137
6.3. Mathematical Model . . . 137
6.3.1. Reagent Motion . . . 138
6.3.2. Mineral Grain Dissolution . . . 141
6.4. Ore Particle Case Study . . . 142
6.4.1. Diffusion Limited and Reaction Limited Case . . . 142
6.4.2. Reaction Kinetics Distribution . . . 146
6.4.3. Simulation Results with Gamma Distributed Kinetics . . . 149
6.5. Summary . . . 151

7. Conclusions and Future Directions **153**
7.1. Future Work 155

Bibliography **157**

Appendices **167**

Appendix A. Expectational procedure and related information **168**
A.1. Procedure for sample decomposition 168
A.2. Procedure for acid titration 169
A.3. Procedure for validating iron content from raw chemicals 169
A.4. Standard potentials (mV) of some reference electrodes 170
A.5. Interference table for Cu and Fe measurement using ICP-OES 171

Appendix B. Derivations **172**
B.1. Derivation of measurement error within each categories 172

Appendix C. Codes and Scripts **173**

Appendix D. Publications **175**

List of Figures

2.1. Global copper production and copper unit value. 6
2.2. The declining copper ore grade in the United States. 7
2.3. Different leaching methods with different particle sizes and ore grades. . . 8
2.4. Main processes of heap leaching. 12
2.5. Different processing routines treating ores for heap leaching and conventional pyrometallurgy method. 13
2.6. Schematic diagram of leaching process. 19
2.7. Recovery rate with increasing time. 19
2.8. A simplified Pourbaix diagrams of iron. 22
2.9. Pourbaix diagram for Cu-O-S-H2O system at 25 °C. 25
2.10. Pourbaix diagram for the $CuFeS_2$-H_2O system at 25 °C. 28
2.11. The relationship between the initial concentration ratio of ferric to ferrous ions and the initial redox potential E (mV vs. SHE) in 0.1M sulphuric acid. 29
2.12. Illustration of different sub-processes scales in heap leaching. 34
2.13. Ferric diffusion through rim leach in large particles. 36
2.14. Schematic diagram showing the principle of the shrinking core model. . . 39
2.15. Schematic illustration of X-ray CT acquisition and reconstruction processes. 43
2.16. Linear attenuation coefficient as function of incident X-ray energy of four different minerals. 44
2.17. Illustration of two primary experimental approaches to XMT data collection. 47
2.18. Scans through 6-in diameter column of saprolite encased in PVC pipe, showing scanning artefacts and results of various strategies for remedying them showing different artefacts. 48
2.19. The phenomenon of beam hardening. 50
2.20. An example showing partial volume effect. 52
2.21. Illustration of a simple image segmentation procedure. 55
2.22. Segmentation of solid phases. 57

3.1. Schematic diagram of the experimental rig for column leaching experiment. 63
3.2. Experimental rig for column leaching experiment. 63
3.3. Temperature controlled heater and multi-channel peristaltic pump for column experiment. 64
3.4. Glass leaching column. 65
3.5. Glass leaching column with ore samples. 66
3.6. Plot of linearity relationship in ICP-OES calibration standards measurements. 69

4.1. Illustration of XMT system. 73
4.2. Photo of Nikon Metris Custom Bay. 74
4.3. Examples of two slices reconstructed with different centre of rotation. . . 75
4.4. Example slice of a scanned leaching column from a reconstruction image. 76
4.5. The histogram of a typical scanning volume with estimated thresholding values for ore and metal sulphide grains. 77
4.6. An example slice from a volume data showing the results of thresholding, separation and labelling. 79
4.7. The principle of distance map and marker control based watershed algorithm to separate connected objects. 81
4.8. Principle of watershed algorithm. 81
4.9. Principle of merging local maxima for maker control watershed separation. 82
4.10. An example of ore particle tracking and relabelling of a volume in two different scans. 82
4.11. Registration example of an ore particles after 136 days leaching. 83
4.12. The comparison of different methods to threshold metal sulphide grains using Max Entropy and 3D watershed. 84
4.13. An example slice of distance map of ore particles and inside metal sulphide grains for an example ore particles. 86
4.14. Plot of total volume of metal sulphide grain at a specific distance against distance for different leaching days for an example ore particles. 86
4.15. Percentage leaching after 136 leaching days based on distance map for an example ore particles. 87
4.16. A slice through a 3D tomogram of an ore particle showing the different stages in identifying the same grains in different images. 89
4.17. Unassigned rims not covered by the mask. 90
4.18. Example of reference label transformation. 91

4.19. 3D visualisation of grain tracking for an example ore particle. 92
4.20. Isosurface images for an example grain after identification. 93
4.21. An example quantification of an ore particles with four scanning points combining individual grain leaching efficiency with particle size and distance to nearest surface. 93
4.22. a) A 2D slice through a 3D tomography volume of example data showing mineral grains within an ore particle. b) A region of interest demonstrating diffuse boundaries. 94
4.23. The relationship between the change in mineral grain volume and the variation in the threshold value. 96
4.24. The plot of the relative change in grain volume as a function of the volume for two different threshold changes. 97
4.25. Plot of prefactor k as threshold value changes. 98
4.26. Standard deviation in the relative error in the grain volume as a function of the grain volume. 99
4.27. Number of repeats required to reduce the random component of the uncertainty (relative standard deviation) in the volume to a given level as function of the object volume. 100
4.28. The discrepancy in volume between reference scan and repeated scan. . . 102
4.29. Amount of grains at specific size range with volume percentage in Scan 1 (reference). 103
4.30. Mean relative error in metal sulphide grain volume as a function of the grain volume. 104
4.31. Histogram plot of the example ore particle with indication of threshold calculation using Max Entropy and Moments algorithms. 106
4.32. Comparison between Max Entropy and Moments algorithms to threshold mineral grains within an ore particle. 106
4.33. The plot of percentage difference for grains having minimum distance to nearest surface of 70 pixels when between Day 0 and Day 1. 108

5.1. Mineral recovery based on image quantification from XMT images. . . . 112
5.2. Copper recovery based on chemistry measurements from ICP-OES. . . . 113
5.3. Relationship of recovery between image measurement and chemistry measurement from ICP-OES. 114
5.4. The initial conditions of scanned volumes and their overall leach recovery. 116

5.5. Plot of the average recovery for the entire column, the average recovery for the three scanned volumes (top, middle and bottom) within the column and the recovery for the individual ore particles. 117
5.6. The leach recovery for all the tracked ore particles against their initial ore particle sizes. 118
5.7. The leach recovery for all the tracked ore particles against their initial mineral grain content. 118
5.8. The leach recovery for all the tracked ore particles against the distance between the centroid of the ore particle and the centre of the column (pixels). 119
5.9. Distance plot for an example ore particle along 168 days leaching period. 120
5.10. The average leach recovery for all the tracked ore particles against the distance between grains and nearest surfaces after 168 leaching days. . . 121
5.11. The change in recovery of 25 example grains with initial volumes of between 500 and 1000 voxels over the 168 days of leaching. 122
5.12. Dividing tracked grains into different categories according to size and distance to surface. 123
5.13. Plots of average metal sulphide recovery in each size-distance category in three difference time points using colour map indicating percentage recovery. 124
5.14. The recovery for all the size-distance categories with average initial grain size larger than 100 voxels after Day 11 and Day 168. 125
5.15. The recovery for categories with different average initial grain size at different distance against leaching time. 127
5.16. The recovery for different categories at different distance against average initial mineral grain size. 128
5.17. The plot of standard deviation of the error error in volume. 130
5.18. Plot of overall uncertainty (expressed as a relative standard deviation) and measurement uncertainty (underlying uncertainty is the difference) for the example ore particle at Day 11 and Day 168. 132
5.19. Comparison of the average leach recovery at different distance to surface values among three columns with different flow rates at Day 168. 134

6.1. Example slice showing phase segmentation. 138
6.2. The steady-state reagent concentration within the ore. 140
6.3. Reagent concentration for an ore particle at four different time steps with $\delta = 0.01$ (diffusion limited). 143

6.4. 3D visualisation of the simulation of mineral grains within an ore particle. 144
6.5. Reagent concentration for an ore particle at four different time steps with $\delta = 1000$ (diffusion limited). 145
6.6. Comparison between: a) reaction limited case; and b) diffusion limited case showing recovery against distance. 146
6.7. Cumulative distribution function of the rate constants for different size and distance categories, with the average distribution function for all the plotted data. 148
6.8. Probability density function of individual reaction kinetics over average reaction kinetics with fitted gamma distribution. 149
6.9. Recovery against distance for an example ore particle based on simulation ($\delta = 1$). 150
6.10. Comparison between experiment from XMT measurement and simulation using both single leach kinetics and Gamma distributed kinetics. 151
6.11. Plot of average recovery based on XMT measurement against simulation results for different size-distance categories with fitted lines. 152

List of Tables

2.1. Advantages and disadvantages of heap leaching comparing with conventional pyrometallurgy methods. 9
2.2. Comparison of different leaching methods of copper. 11
2.3. Factors and parameters affecting heap leaching. 18
2.4. Typical leaching agents with their applications. 23
2.5. Methods of leaching sulphides. 23
2.6. Common copper minerals in heap leaching. 24
2.7. Effect of temperature during chalcopyrite leaching with ferric ion. 32
2.8. Mineral grain distribution based on accessibility to leaching solution. . . 37
2.9. Some limitations of the shrinking core model. 40

3.1. Measured copper content from ICP-OES. 60
3.2. Design of column leaching experiment. 61
3.3. Recorded pH, Eh, initial Cu and Fe concentrations for feed solutions. . . 62
3.4. Calibration of multi-channel peristaltic pump. 65
3.5. Results of sulphuric acid titration using sodium hydroxide solution and methyl orange as indicator. 67
3.6. Iron concentration based on VWR catalogue. 67
3.7. ICP-OES results for iron concentration in analytical reagents. 68
3.8. Amount of 1000 ppm Cu/Fe solution for ICP-OES calibration standards. 69

4.1. Main steps and difficulties in order to carrying efficient and consistent 4D image quantification. 72
4.2. Scanning time points for the column leaching experiment. 74
4.3. The main scanning settings for column leaching. 75

A.1. Volts (mV) related to standard hydrogen electrode. 170

C.1. Codes for 3D image processing, quantification and modelling. 174

Chapter 1

Introduction

1.1. Motivation

The global metal demand has been increasing rapidly in recent years, but this has been accompanied by a decline in high grade ore resources. The traditional method to treat high grade ores is flotation followed by smelting. However, this method is not economically efficient when treating low grade ores due to the increasing costs when the grade of ores decreases. Therefore, having an alternative technique to extract valuable metals from low grade ores in an economic way is becoming even more important. Heap leaching is an important hydrometallurgical technology which extracts valuable metals, such as gold, silver, copper, from ores (especially from low grade ores). Although the cost of heap leaching is much lower than conventional pyrometallurgy methods, the main disadvantages are the long processing time and relatively low extraction efficiencies, especially when treating primary sulphides like chalcopyrite.

The efficiency of a heap leaching system is controlled by different parameters including physicochemical parameters, microbiological parameters, mineral properties and processing conditions (Brandl, 2008). Each of these parameters can alter the leach behaviour and finally affect the leaching kinetics and dissolution rate. Despite extensive study it remains challenging to fully parametrise and quantify the leaching process, and the process optimisation is therefore limited due to the large size and complexity of the real system. Normally, the leaching related research can be divided into different scales, including:

- Heap and other large scale systems to understand macroscopic behaviour such as fluid dynamics and liquid hold up, and the overall leach performance (van Hille et al., 2010; Ilankoon and Neethling, 2013; Mostaghimi et al., 2014).

- Small scale column leaching to understand overall leach behaviour at different leaching conditions such as different temperatures, different ore types, different leaching reagents, etc... (Dixon and Petersen, 2003).

- Individual ore particle scale to understand the mineralogy of ores and its change during leaching which currently is mainly achieved by looking at polished thin sections (Ghorbani et al., 2011a; Kodali et al., 2011).

- Mineral grain scale to understand the surface chemistry and the leaching kinetics by doing stirred tank leaching using micron level milled ore samples (Córdoba et al., 2008a; Klauber, 2008; Watling, 2006).

Currently, there is a lack of information about the mass transport and surface reaction within individual ore particles during leaching. This information is a key requirement in understanding and finally simulating and predicting the leaching process. While some of this information can be obtained by comparing thin sections through leached and unleached materials, this is destructive and requires assumptions to be made about how representative the chosen particles are. As a non-destructive method for imaging the internal structure of ore particles, X-ray Computed Microtomography (XMT, or micro-CT) has gained popularity for the non-destructive qualitative and quantitative investigation of the internal structure of objects. It has been widely applied across material science (Puncreobutr et al., 2012; Stock, 1999), engineering (Aydoan et al., 2006; Ghorbani et al., 2011a; Ketcham and Carlson, 2001) and biological sciences (Yue et al., 2011) to provide quantitative data about the structure and morphology of 3D objects and features within them (crystals, pores, fractures etc.).

XMT has already been quite widely applied in heap leaching applications due to its non-destructive manner. However, most of this work has either been relatively qualitative in nature, for instance focussing on the distribution of grains, cracks, pores etc. within the particle or, in quantitative terms, have tracked the mineral volume reduction either overall or as a function of position within the column or particle (Burlion et al., 2006; Ghorbani et al., 2011b; Ketcham and Carlson, 2001; Kodali et al., 2011; Lin and Miller, 2005).

In this thesis, the main objective is to measure, quantify and finally model leach performance at ore particle scale and mineral grain scale. This can be achieved by completing the following sub aims and objectives:

- Develop image processing algorithms to process image data automatically.

- Track the extent of leaching within the ore particles, as well as at mineral grain level.
- Understand image measurement errors and uncertainties in leach behaviour measurements.
- Quantify and analyse leach behaviour at individual ore particle scale and mineral grain level to study the effect of morphological parameters such as the size and shape of the ore particles and the distribution of the mineral grains within them.
- Use the initial XMT image and extracted leach behaviour to simulate long term leach process.

1.2. Thesis Outline

Chapter 2 is a review of literature relevant to this work. The importance of doing heap leaching research is explained, followed by the description of the principle of this technique. The basic chemistry of leaching copper minerals including chalcopyrite (which is the main copper containing mineral in the ore samples in this study) is reviewed. The main aspects affecting the leaching efficiency are also reviewed. The relevant research at different research scales is summarised and the lack of information from individual ore particle scale due to the limited technique is highlighted. As a 3D non-destructive technique, the principles and essentials of the XMT system and 3D volume images are also explained. The general image processing technique steps in image processing and quantification are reviewed with examples. The existing barrirs using XMT in leaching related studies are reviewed and discussed.

Chapter 3 describes the experimental methodology for a series of small scale column leaching experiments. The detailed design of the experiments, including the experimental setup, controlling parameters such as temperature, ore types, flow rate ranges, leaching agents, are explained. The details of feed solution and relevant chemistry measurement are also introduced.

Chapter 4 describes the XMT system used for the experiment. The theory of XMT image reconstruction from a series of 2D projections to a 3D volume image is demonstrated with examples. A series of image processing algorithms to process the reconstructed image data, including filtering algorithm to reduce the noise level, thresholding algorithms to segment and extract different phases (air phase, rock phase and mineral grain phase), centroid tracking to track ore particles in series of scans, and the fast track-

ing algorithm developed to track thousands of mineral grains within each ore particles are introduced. Error and uncertainty analysis is carried out to quantify the systematic and random errors in the image processing and the relevant analysis, particularly in the volume measurements. Based on the error analysis, a method which can minimise the measurement error is demonstrated. Different thresholding algorithms are compared quantitatively based on the grain tracking algorithm.

In Chapter 5, the leach performance is quantified and analysed by applying the imaging technique developed in Chapter 4. The results from the image analysis and chemistry measurements are compared due to the limitation of XMT in distinguishing different mineral phases. An example leaching column is used to demonstrate the multi-scale analysis to quantify the leach performance at different research scales. The relevant errors and uncertainties are also taken into consideration. Statistical analysis of leach performance at the mineral grain level is carried out to understand the leach performance and its variability. By applying the statistical analysis, leaching parameters can also be analysed to undertand how each parameter can affect the leach behaviour.

Chapter 6 introduces a numerical model that uses that XMT data as input. It is then used to predict both the overall and grain scale leach behaviour, which is compared to the experimentally obtained results.

The thesis finishes with Chapter 7 which provides a summary of the contributions of the work presented in context and discusses the shortcomings and directions to be taken in the future.

Chapter 2

Literature Review

2.1. Introduction

The main objective of this study is to use advanced techniques to quantify and have a better understanding of leach performance in heap leaching application, which is a hydrometallurgical technique used to extract metals from low grade ores. Although studying mass transfer and surface chemistry are crucial in heap leaching research, the majority of the existing studies have focused on either heap and other large scale to understand overall leach behaviour, or mineral grain scale using milled powder to understand surface chemistry. There is a gap in studying leach performance inside individual ore particles, which is limited by the conventional research techniques.

In the first part of this chapter, the overall status of hydrometallurgy is reviewed, focusing on the copper industry. The various operational stages of heap leaching including the fundamental chemistry based on tank leaching study in copper leaching are reviewed and discussed. As the most important and most difficult leach material, chalcopyrite leaching is reviewed specifically. Moreover, the study of individual ore particles including the ore particle level modelling is also reviewed.

Due to the lack of information in understanding mass transfer and surface chemistry within individual ore particles, X-ray Computed Microtomography (XMT) is introduced as a more advanced alternative technique to visualise and quantify the leach performance. The current leaching related research based on XMT and imaging is reviewed and the existing barraier of applying imaging techniques to understand leach performance is addressed. This is followed by the review of the fundamentals of XMT and relevant artefacts within scanning. The general procedure of image processing is also described.

2.1.1. Current Status of Hydrometallurgy

Global demand for metals has been increasing rapidly in recent years. For instance, the world copper production reached approximately 17 millions of tonnes in 2010, which was approximately eight times more than the production in 1960 (Figure 2.1) (Schlesinger et al., 2011; U.S. Geological Survey, 2014). However, the increase of demand has been accompanied by a decline in the high grade ore resources. For example in the United States, the average grade of copper ore has declined from 2.5% in 1930 to approximately 0.5% in 2000 (Figure 2.2) (Wills and Napier-Munn, 2006; McKinney L. et al., 2007). Therefore, extracting valuable metals from ores, especially low grade ores, in a more efficient and economic way becomes crucial in the mineral processing industry.

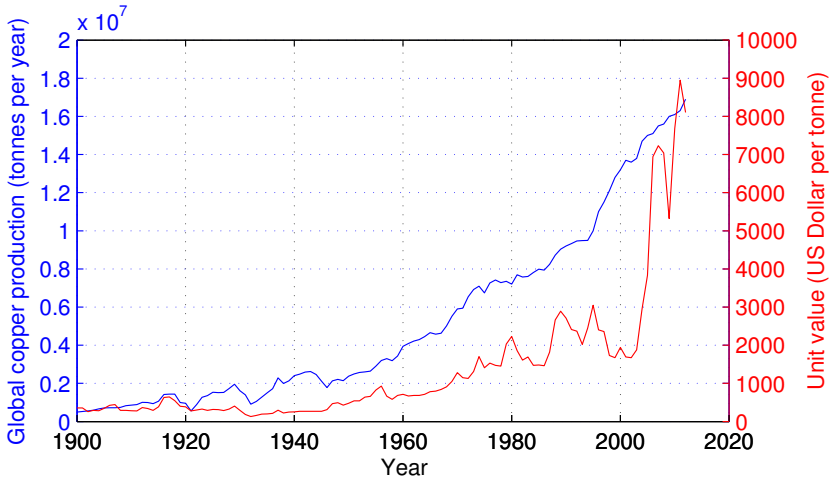


Figure 2.1.: Global copper production and copper unit value. Data source: U.S. Geological Survey (2014).

Extractive metallurgy can be defined as extracting valuable metals from ores using physical and chemical techniques. The three main methods are hydrometallurgy, pyrometallurgy and electrometallurgy (Habashi, 1999). Currently, the main technique to extract metals from ores is the pyrometallurgy route, which is flotation followed by smelting. In the copper industry up to 2010, approximately 70% to 80% of primary copper production converting copper minerals into pure copper was achieved by the conventional pyrometallurgy method (Schlesinger et al., 2011). However, the conventional pyrometallurgy technique is only cost effective for ores with relatively higher grade, but is not appropriate and efficient for low grade ores due to the increasing capital and operation costs as the grade of ores decreases. In recent years, hydrometallurgy, or leaching, which extracts metals from ores using aqueous solutions to dissolve target minerals within the ores, is becoming more and more attractive and is widely applied in mining and mineral

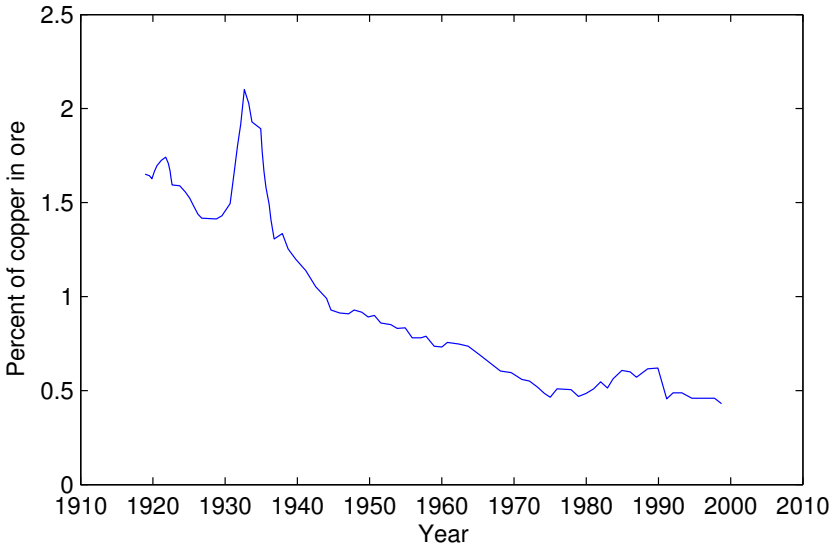


Figure 2.2.: The declining copper ore grade in the United States (McKinney L. et al., 2007).

processing industries. In 2010, approximately 4.5 million tons of copper per year were produced by leaching and most of the production was achieved by heap leaching, which covered approximately 20% to 30% of the global copper production (Davenport et al., 2002; Schlesinger et al., 2011). In the United States, approximately 30% of the gold and copper production are achieved by heap leaching (Ghorbani et al., 2011a). Due to its lower capital and operating costs as compared to conventional pyrometallurgy techniques, there are an increasing number of heap leaching equipped copper and gold mines throughout the world (Acevedo, 2002). In 2010, nine of the twenty largest copper mines treated a portion of ores, usually the lower grade ones, using heap leaching (Ghorbani et al., 2011a; Pradhan et al., 2008).

2.1.2. Various Leaching Methods

There are six main types of leaching methods (Schlesinger et al., 2011):

- In-situ leaching
- Dump leaching
- Heap leaching
- Vat leaching
- Agitation leaching

- Pressure oxidation leaching

Heap leaching, dump leaching and vat leaching all belong to percolation leaching using unsaturated solution flowing through the ore mass. Percolation leaching usually involves two fluid phases which are the leaching agent and the air, while flooded leaching maintain the condition that the ore mass is saturated with the solution (Bartlett, 1998). Different leaching methods normally have different suitable particle sizes. Mular et al. (2002) summarised the ore grade and particle size which are suitable for different leaching methods, shown in Figure 2.3.

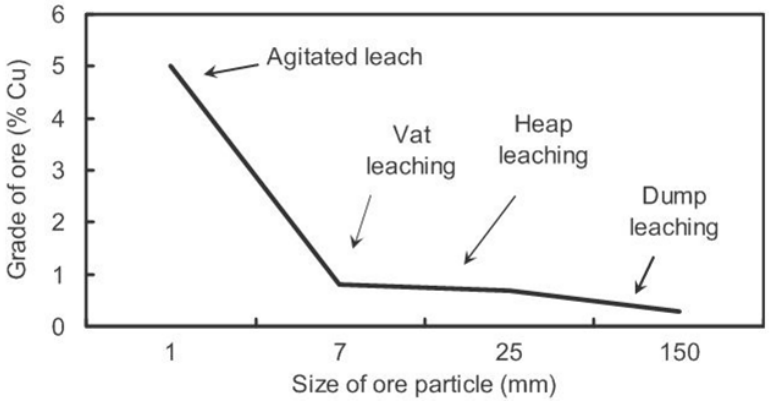


Figure 2.3.: Different leaching methods with different particle sizes and ore grades (Mular et al., 2002).

2.1.2.1. Heap Leaching

Heap leaching is a hydrometallurgical method to extract metals from run-of-mine (ROM) ores. The typical ore particle size in a heap leaching system is around 12-25 mm with copper content around 0.5%. The detailed principle and operational procedure of heap leaching is described in Section 2.2.

Heap leaching has several advantages over other conventional pyrometallurgy techniques. One of the primary advantages is the relatively low capital and operating costs, as well as lower energy consumption (Bartlett, 1998; Ghorbani et al., 2011a; Habashi, 1999). This makes heap leaching one of the few methods for extracting with low grade ores economically (Bartlett, 1998).

However, there are still many limitations for heap leaching application, including lower recoveries, relatively high operation cost due to the acid consumption, complex and difficult system control, and long extraction time (Bartlett, 1998; Ghorbani et al., 2011a; Habashi, 1999; Pradhan et al., 2008). The advantages and disadvantages of heap leaching

as compared to conventional pyrometallurgy methods are listed Table 2.1. The biggest disadvantages of heap leaching, though, are the long processing time and relatively low extraction efficiencies, especially for primary sulphides.

Table 2.1.: Advantages and disadvantages of heap leaching comparing with conventional pyrometallurgy methods (Schlesinger et al., 2011).

Advantages	Disadvantages
Low capital and operating costs	Lower recoveries
Absence of milling step, may require crushing and agglomeration	Long leach cycles and hold-up
Simplicity of atmospheric leach processes	Lengthy pilot test programme
Can be used to treat low-grade ores, wastes and small deposits	Large footprint
Absence of liquid-solid separation step - counter current operation	Environmental release of PLS
Metal tenor may be built up by recycling solution over heaps	Difficult control
Simplicity in equipment and operation	
Shorter start-up times	
Less intensive environmental regulatory concerns	

2.1.2.2. Dump Leaching

Dump leaching is a similar process to heap leaching, but it is usually applied to treat ROM ores with copper content lower than 0.5% and the particle size is up to 500 mm (Schlesinger et al., 2011). Unlike heap leaching, ores are taken directly from a mine without having crushing or agglomeration processes. Dump leaching is a preferable method to treat the waste from mines with very low copper content and the leaching cost is relatively low. However, the whole leaching process may take much longer than heap leaching (Bartlett, 1998; Schlesinger et al., 2011).

2.1.2.3. Vat Leaching

Vat leaching happens in large reaction vessels, known as vats, and it is usually used to extract minerals from relatively high copper content (around 1%) ore with fast kinetics and short leaching time (Schlesinger et al., 2011). In heap or dump leaching, leaching solution is applied from the top of a heap or dump whereas in vat leaching, the leaching solution is pumped from the bottom of ore mass and collected on the top to keep fine particles in suspension and to avoid the vat being plugged.

2.1.2.4. Agitation Leaching

Agitation leaching is carried out in stirred tanks and is suitable for relative high grade ores with copper content approximately from 0.8% to 5% (Schlesinger et al., 2011).

Most of these kinds of minerals are oxide and carbonate minerals. As the particles are crushed and milled, they are fine and thus have fast kinetics.

2.1.2.5. Pressure Oxidation Leaching

Pressure oxidation leaching method is a relatively new method used routinely for a number of different minerals such as chalcopyrite, under high pressures and temperatures (Schlesinger et al., 2011). This method can also be used to extract the remaining copper from the concentrate product with low copper content after the froth flotation process.

2.1.2.6. In-situ Leaching

Unlike heap or dump leaching, in-situ leaching means the leaching process happens before the rocks are mined out. In-situ leaching is not as common as other leaching methods because this method has the potential environmental problem that the leaching solution could contaminate groundwater (Schlesinger et al., 2011).

2.1.2.7. Summary of Leaching Methods

Leaching plays an important role in global metal production. Each leaching method has its own characteristics and applications, although the primary principle is similar. The main characteristics of different leaching methods in copper production are summarised in Table 2.2.

2.2. Fundamentals of Heap Leaching

2.2.1. Operational Procedure of Heap Leaching

Heap leaching involves stacking prepared ores into a heap on a leach pad (impermeable layer), irrigating the ores using a leaching agent (chemical solution) to dissolve minerals containing metal for a certain period and collecting leachate from the bottom of the heap for further extraction including solvent extraction and electro-winning (shown in Figure 2.4) (Ghorbani et al., 2011a; Kappes, 2005; Schlesinger et al., 2011). The general operational procedure of heap leaching is:

- Ore preparation
- Heap construction
- Leaching solution application (leaching)

Table 2.2.: Comparison of different leaching methods of copper (Schlesinger et al., 2011).

Parameter	Dump	Heap	Vat	Agitation		Pressure
Target minerals	ROM, oxides, secondary sulphide	Oxides, secondary sulphide, tailings, usually milled, agglomerated, and acid cured, bacteria-assisted	Oxides, secondary sulphide, secondary leach of tailings, agglomerated and acid cured.	Oxides and tailings	Sulphides	Primary and secondary sulphides, refractory flotation concentrates
Cu grade (%)	0.1-0.4	0.2-2.3	>0.8	0.8-5.0	>6	Up to 25
Particle size (mm)	Up to 1000	12-50	0.5-2	0.1-0.2	0.1-0.2	0.01-0.75
Leaching time	Years	Months to years	Weeks	Days	Days	Hours
Cu in PLS (g/L)	0.5-3	1.5-8	6-40	2-30	12-45	25-80
Cu recovery (%)	35-75	Up to 90	>90	85-100	95-98	>96

- Pregnant leach solution (PLS) collection
- Solvent extraction
- Electro-winning

2.2.1.1. Ore Preparation

Ore preparation can vary depending on several factors including ore type, quantity, ore grade, operational conditions and project economics (Ilankoon and Neethling, 2012). Crushed, or crushed and agglomerated, ores are the typical materials stacked in heap leaching piles (Bouffard and West-Sells, 2009). The particle size of ores used in heap leaching can vary from coarse materials (few centimetres) to very fine materials (few millimetres or even smaller). This is common when ROM ores are used directly in heap leaching. In these cases, the leach recovery can be affected due to the profile heterogeneity of the heap. Ore preparation normally includes ore blending for grade control, crushing and agglomeration (Bartlett, 1998). Figure 2.5 shows the principle difference in ore preparation between heap leaching and conventional pyrometallurgy methods. For the conventional pyrometallurgy method, the ore feed needs to be crushed or milled into

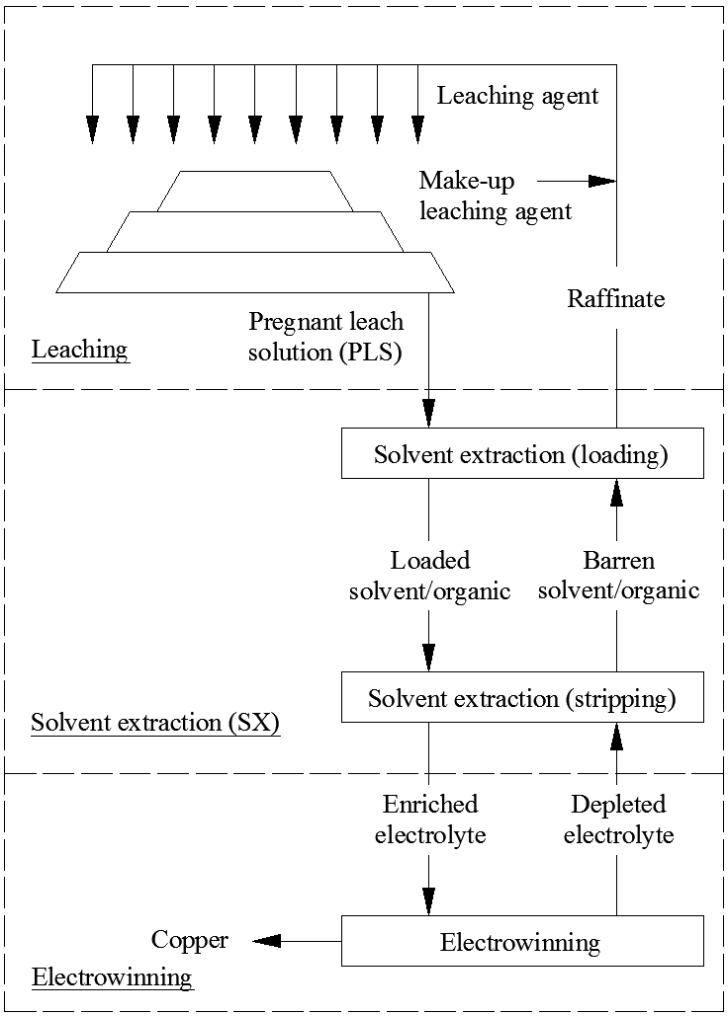


Figure 2.4.: Main processes of heap leaching.

particles with sizes smaller than valuable mineral grains before being separated from each other using a physical method like flotation (Hsih et al., 1995). When considering a hydrometallurgical method (e.g. heap leaching), partial exposure of mineral grains providing accessibility for the leaching solution is sufficient (Hsih et al., 1995). A suitable condition for leaching can be achieved and enhanced in ore preparation stage by applying crushing and grinding operations to increase liberation. High pressure grinding rolls (Baum and Ausburn, 2011) and microwave assisted technologies (Al-Harahsheh and Kingman, 2004; Al-Harahsheh et al., 2005) are two existing solutions to achieve better ore liberation.

According to Figure 2.3, the common size range for ore particles in a heap leaching system is around 12-25 mm which can be achieved by two stage crushing (Bartlett, 1998). Crushing will also produce fine particles which can be problematic as they can

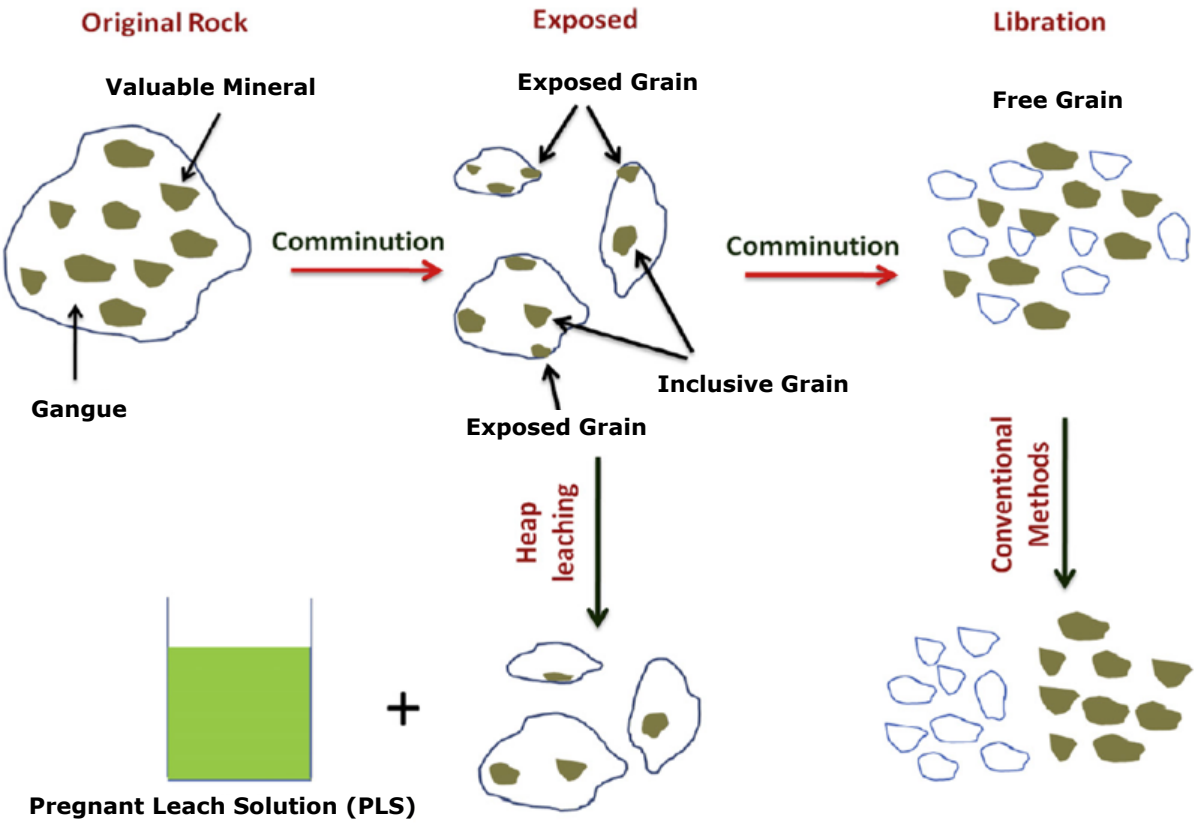


Figure 2.5.: Different processing routines treating ores for heap leaching and conventional pyrometallurgy method (Ghorbani et al., 2011a; Hsih et al., 1995).

lower the heap permeability and can prevent uniform liquid flow through the heap which finally reduces recovery (Bartlett, 1998). This problem can be alleviated by applying agglomeration which makes fines stick onto the larger ore particles to generate a relatively narrow size distribution.

2.2.1.2. Heap Construction

The first stage of heap construction is the leach pad construction. A leach pad can prevent leaching solution going into the ground water, causing metal production reduction and potential environmental issues due to the heavy metals within the solution (Bartlett, 1998). The prepared ores are then dumped from haul trucks, stacked with a front end loader and mechanically stacked using conveyor belts on the leach pad (Bartlett, 1998; Ilankoon and Neethling, 2012). A completed heap can have a large surface area from a fraction of a square kilometre to a few square kilometres and height up to 100 metres (Ilankoon and Neethling, 2012). The height of the heap and the construction method used can influence the permeability due to crushing and compaction of the particles and

agglomeration potentially resulting in maldistribution of the liquid.

2.2.1.3. Leaching Solution Application

During heap leaching, the leaching solution is applied on top of the heap via an irrigation system. In the copper industry, H_2SO_4 is normally used as the leaching solution and the whole process occurs under normal atmospheric conditions (Schlesinger et al., 2011). The irrigation system is normally made from plastic to minimise the cost and prevent corrosion due to the acidic condition (Bartlett, 1998; Ilankoon and Neethling, 2012). In many heap leaching applications, oxygen plays an important role in the reactions (Bouffard and West-Sells, 2009). Therefore, the flow control of the leaching solution becomes crucial as it needs to be ensured that the system is not saturated and the leaching solution only occupies part of the void space and leaves space for the air. In some systems, air is blown in from the bottom of the heap using a blower.

2.2.1.4. Pregnant Leaching Solution Collection

After leaching reactions, the solution containing metals is known as the pregnant leaching solution (PLS). PLS is collected at the bottom of the heap, connecting to a PLS pond via a drainage system (Bartlett, 1998; Ghorbani et al., 2011a).

2.2.1.5. Solvent Extraction

The collected PLS is then sent to be contacted with a Cu-specific liquid organic extraction solvent. In this process, Cu^{2+} is transferred from the PLS to the organic solution. The aqueous solution is then separated from the organic solution by gravity. This Cu-loaded organic solution is sent to contact with an electrolyte containing strong H_2SO_4 and Cu is transferred again, from organic solution into the electrolyte. At the same time, the raffinate solution (PLS after losing most Cu^{2+}) is sent back to the leaching process for recycling, and the stripped organic solution (organic solution after losing most Cu) is sent back to the beginning to strip Cu from the PLS.

2.2.1.6. Electro-winning

There are three main processes in electro-winning. The first step is to immerse metal cathodes (which are usually stainless steel blanks) and anodes (which are usually Pb-alloy sheets) into the electrolyte mainly containing $CuSO_4$ and H_2SO_4 (Schlesinger et al., 2011). A direct current is applied from an external source to let the current flow between cathodes and anodes through the electrolyte to activate the process. Due to the

reduction reaction, Cu^{2+} is reduced to Cu and electroplates on the cathodes, and O_2 and H_2SO_4 are produced at the anodes. The Cu-depleted electrolyte is then sent back for solvent extraction.

2.2.2. Factors Affecting Heap Leaching

The total metal extraction in heap leaching process is usually affected by several key factors, involving environmental, biological physical and chemical factors (Pradhan et al., 2008). Brandl (2008) summarised the key parameters that need to be considered (Table 2.3). The optimum leaching condition is determined by balancing both positive and negative effects. A correct and suitable condition for a leaching system involves a suitable ore particle size, access of oxygen and humidity to the mineral surfaces, reduced acid consumption, the presence of sulphides susceptible to bacterial oxidation, and the possible elimination of precipitated basic ferric salts like Jarosite that might block the percolation channels (Pradhan et al., 2008). The main factors and parameters that need to be considered are:

- Mineralogy

  The performance of a heap leaching process is highly depend on the nature and characteristics of the mineral types (Muñoz et al., 1995). Copper oxide and secondary sulphide minerals are much easier to leach than primary sulphide minerals. Porosity of the ores is also an important factor; higher porosity allows the solution to access more of the ore body (Pradhan et al., 2008). Containing sufficient amount of nutrients is another key aspects as micro-organisms, which is a key factor in heap leaching, need nutrients for their growth (Muñoz et al., 1995).

- Ore Particle size

  Ore particle size is one of the dominant aspects affecting the recovery and the leaching kinetics. The recovery generally increases with decreased particle size of ores. However, more grinding or crushing can lead to higher cost and energy consumption and more fine particles which can cause low permeability problems (Habashi, 1999). The economics of heap leaching should be determined by the trade-off between slow and incomplete leaching from ores and the cost of grinding or crushing finer (Ghorbani et al., 2011a). One of cost effective methods is to achieve more efficient crushing and grinding. For example, comparing with the use of a conventional cone crusher, the use of high pressure grinding rolls (HPGR) can

improve the leaching process by achieving better leach behaviour, but lower costs (Ghorbani et al., 2011a).

- Permeability

  Permeability is a crucial aspect affecting the recovery rate in the heap leaching system. The permeability of a heap needs to be even and the heap should not be too compacted. If the permeability is uneven, the leaching solution can also be distributed unevenly which leads to the situation that parts of the heap may have less leaching solution passing through (Ghorbani et al., 2011a). If the heap is too compacted, the direct influence is an increase in the leaching period as leaching solution cannot percolate rapidly enough through the heap. Both of these potential problems can be caused by fine materials, which can be overcome by agglomeration of fine particles to improve the overall permeability (Ghorbani et al., 2011a).

- Concentration of leaching agent

  Higher concentration of leaching agent can increase the recovery rate in leaching, but it can also lead to an increase of leaching agent consumption because more undesirable minerals can be dissolved.

- Aeration

  Aeration supplies both O_2 and CO_2 to the leaching system to feed bacteria as most of them are aerobic and chemolithotrophic in nature and CO_2 is supplied as a source of carbon to produce biomass (Pradhan et al., 2008). Aeration of heaps can increase the leaching rate and reduce the leaching period. O_2 and CO_2 usually come from the supply of air, which can be injected into heaps using low pressure high volume fans or blowers, and distributed via distribution pipework from the base of heaps in a gravel layer (Pradhan et al., 2008).

  The oxygen concentration from the bottom to the top of the heap decreases when the height of the heap increases. The existence of the gradient with depth is due to the bacteria catalysing sulphide oxidation that consumes oxygen (Pradhan et al., 2008). As a result, the nearly saturated oxygen in the bottom when it is forced to be blown into a heap becomes depleted when it reaches to the top.

  Normally, oxygen consumption is an important factor in copper sulphide leaching because it reflects the degree of bacteria activity (Pradhan et al., 2008). If the heap is in an oxygen depletion condition, increasing aeration may enhance the leaching

rate. However, if oxygen is sufficient in the heap, increasing aeration may not make any contribution, but increase operation cost.

- Irrigation

  Continuous and discontinuous irrigation methods are the two main irrigation methods. In discontinuous irrigation, which is accepted as a preferable irrigation method, leaching solution is sprayed onto the heap surface over set intervals with interspersed drainage periods during which no liquid addition occurs (Pradhan et al., 2008). Pradhan et al. (2008) state that discontinuous irrigation is more effective in leaching coarse ores, since alternate draining and drying of the capillaries is quicker than ionic diffusion through static capillaries full of fluid and it can also increase the diffusion of O_2 and CO_2 to the ore surface for bacteria activity. As an significant factor in heap leaching, the frequency of irrigation needs to be considered carefully. It is reported that in industry, the frequency is determined by the rate of evaporation and the concentration of the metal in the exiting liquid phase (Pradhan et al., 2008).

- Temperature

  Micro-organisms can be classified into three categories based on the temperature range they can survive in, namely thermophiles (within optimum temperature between 30 °C and 40 °C), moderate thermophiles (between 45 °C and 55 °C) and extreme thermophiles (above 65 °C) (Petersen and Dixon, 2002; Pradhan et al., 2008). Microbes become inactive when temperature is below the optimum temperature and are destroyed when temperature is above the extreme temperature. Biooxidation of sulphide minerals is an exothermic process which produces a significant amount of heat in heaps and the temperature inside a heap can reach up to around 50 °C to 60 °C (Pradhan et al., 2008). The higher temperature can enhance the leaching process as the recovery rate of the leaching process increases with increased temperature, but undesirable minerals are also easier to be dissolved at higher temperature which leads to higher leaching agent consumption.

  It is also difficult to achieve temperature control within heaps which are heated due to the growth of micro-organisms and the oxidation reactions of sulphide minerals. According to the temperature range for different kinds of micro-organisms, when temperature reaches higher than 40 °C, thermophiles lose their activity and are replaced by moderate thermophiles, which can also be replaced when temperature reaches more than 65 °C. The activity of micro-organisms can also be affected by

the seasonal temperature change. Based on a study of heat generation in chalcopyrite concentrates, temperature control can be partially influenced by aeration and irrigation and the height of the heap (Ghorbani et al., 2011a). The height is an important factor affecting the temperature within the heap. The temperature normally increases with the height (Pradhan et al., 2008; Ritchie, 1997). It has been reported that shorter heaps seem to be able to achieve a more preferable temperature profile than taller heaps (Petersen and Dixon, 2002).

- Passivation

  In heap leaching process, the formation of passivation layers is a key problem that can inhibit the whole process. Once the passivation layer is formed on the mineral surfaces, it reduces the effectiveness of reagent and mineral surface interaction and thus inhibits leaching reactions (Pradhan et al., 2008). The passivation problem is more significant when leaching primary sulphide minerals like chalcopyrite and this will be discussed in later sections.

Table 2.3.: Factors and parameters affecting heap leaching (Brandl, 2008).

Factors	Parameters
Physicochemical parameters	Temperature, pH, redox potential, water potential, oxygen content and availability, carbon dioxide content, mass transfer nutrient availability, ferric ion concentration, light, pressure surface tension, presence of inhibitors.
Microbiological parameters	Microbial diversity, population density, microbial activities, spatial distribution of micro-organisms, metal tolerance, adaptation abilities of micro-organisms.
Properties of the minerals	Mineral type, mineral composition, mineral dissemination, grain size, surface area, porosity, hydrophobicity, galvanic interactions, formation of secondary minerals, porosity, gangue mineral.
Processing	Leaching mode (in situ, heap, dump, or tank leaching), pulp density, stirring rate (in case of tank leaching operations), heap geometry (in case of heap leaching), permeability.

2.3. Leaching Chemistry of Copper Minerals

2.3.1. Fundamentals of Leaching Chemistry

The leaching process is a selective dissolution process of metals from ores, Figure 2.6 is a schematic diagram showing the principle of leaching process. The leaching agent

dissolves the minerals within the ore particles with/without the existence of the oxidant. Pregnant leaching solution is collected at the outlet that can be used for further solvent extraction and electro-winning.

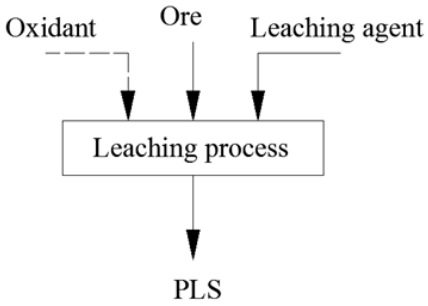


Figure 2.6.: Schematic diagram of leaching process.

For a typical leaching process, the leaching rate can be expressed by using the percentage recovery of the metal (e.g. copper) as a function of time (Figure 2.7). Normally, the leaching rate, which can be reflected by the slope in the diagram, is high at the beginning of the process and gradually decreases with time (Barriga Mateos et al., 1987; Córdoba et al., 2009; Hackl et al., 1995). The leaching rate naturally decreases as available material decreases but passivation and locked grains (grains that have no accessibility to leaching agent) also decrease the leaching rate through time before materials are depleted.

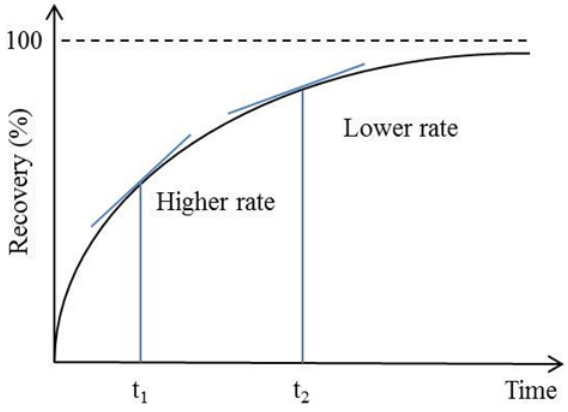


Figure 2.7.: Recovery rate with increasing time.

2.3.1.1. Leaching Agent

The leaching agent is one of the key aspects affecting the leaching process. The key factors determining the appropriate leaching agent are: solubility, cost, materials of construction, selectivity and regeneration (Habashi, 1999). Most leaching agents fall into

three categories: acid, base and aqueous salt solutions. The leaching agent can be used either alone or in combination with oxidising agents or reducing agents.

1. Acid

   Sulphuric acid (H_2SO_4) is the most commonly used leaching agent in industry due to its relatively lower cost compared with bases and its wide application to many minerals (Habashi, 1999). Acids can be sub-divided into three categories, namely oxidising (Nitric: HNO_3), non-oxidising (Hydrochloric: HCl, Sulphuric: H_2SO_4) and reducing (Sulphurous: H_2SO_3). The selection of acid as leaching agent also depends on the leaching conditions.

2. Base

   The most common bases are sodium hydroxide (NaOH) and ammonium hydroxide (NH_4OH). Usually, acids are the preferred choice, but bases could be more appropriate choices in two conditions: negligible corrosion problems under high pH and more selective in basic condition (Habashi, 1999). The term "more selective" means that although acids are suitable for most minerals, they could be less competitive than bases when gangue minerals react with acid. This can make the whole leaching process less cost effectiveness due to large acid consumption. Examples of those kind of gangue minerals which can react with acids are: limestone, dolomite, iron oxide, etc... (Habashi, 1999).

3. Aqueous salt solution

   Ferric salts (Fe^{3+}) are one of the main leaching agents within the aqueous salt solution category. Ferric salt solutions are oxidising agents and they are mainly used for leaching sulphide minerals with reaction:

$$MS + 2\,Fe^{3+} \longrightarrow M^{2+} + 2\,Fe^{2+} + S \tag{2.1}$$

   Another advantage for selecting ferric salts is that they are inexpensive and are easy to regenerate. Take ferric sulphate as an example, it can be industrially prepared by aqueous oxidation of pyrite (Habashi, 1999):

$$2\,FeS_2 + \frac{15}{2}O_2 + H_2O \longrightarrow Fe_2(SO_4)_3 + H_2SO_4 \tag{2.2}$$

   The ferric ion will become ferrous ion after reaction and the regeneration can also be achieved by:

$$2\,Fe^{2+} + 2\,H^{+} + \frac{1}{2}O_2 \longrightarrow 2\,Fe^{3+} + H_2O \tag{2.3}$$

4. Combination

   A typical example for using combined leaching agents is the combination of ferric salt and acid. In this case, one factor that needs to be considered is the form of ferric hydroxide, which is illustrated by Pourbaix diagrams (Eh−pH diagram) shown in Figure 2.8. Ferric hydroxide, $Fe(OH)_3$, can be formed in highly oxidising conditions at low pH level due to a series of hydrolysis reactions, which are (Habashi, 1999):

$$Fe^{3+} + H_2O \longrightarrow FeOH^{2+} + H^{+} \tag{2.4}$$

$$FeOH_2{}^{+} + H_2O \longrightarrow Fe(OH)_2{}^{+} + H^{+} \tag{2.5}$$

$$Fe(OH)_2{}^{+} + H_2O \longrightarrow Fe(OH)_3 + H^{+} \tag{2.6}$$

   To avoid the precipitation of ferric hydroxide, the pH of the solution should be controlled at a level below 3 if the leaching temperature is around room temperature and below around 1.5 at high temperature (Habashi, 1999). Acidic conditions are therefore required to prevent this precipitation and this is the key reason for using the combination of acid with ferric salt. It needs to be noted that ferric ions can be naturally produced in heaps through the oxidation of pyrite.

Other than the leaching agents listed above, there are other kinds of agent with relatively narrow application. Due to the cheap price and non-corrosive property, water can be regarded as a suitable leaching agent but only for few kinds of minerals like sulphates, chlorides and borates. Other examples like chlorine water and hypochlorite can be used in leaching gold ores (Habashi, 1999).

The most common aqueous leaching agents are summarised in Table 2.4. Combining with Table 2.2, it can be seen that leaching method is always used to leach oxide and sulphide minerals although it can also treat other kinds of materials, such as metals, selenides and tellurides, borates, silicates, etc. (Habashi, 1999).

2.3.1.2. Leaching of Oxide and Sulphide Minerals

Leaching of oxide and hydroxide minerals mainly involve leaching bauxite, laterites, copper, manganese and uranium ores using mainly H_2SO_4 (Habashi, 1999). Compared with sulphide leaching, leaching these kinds of minerals has relatively higher leaching kinetic rate.

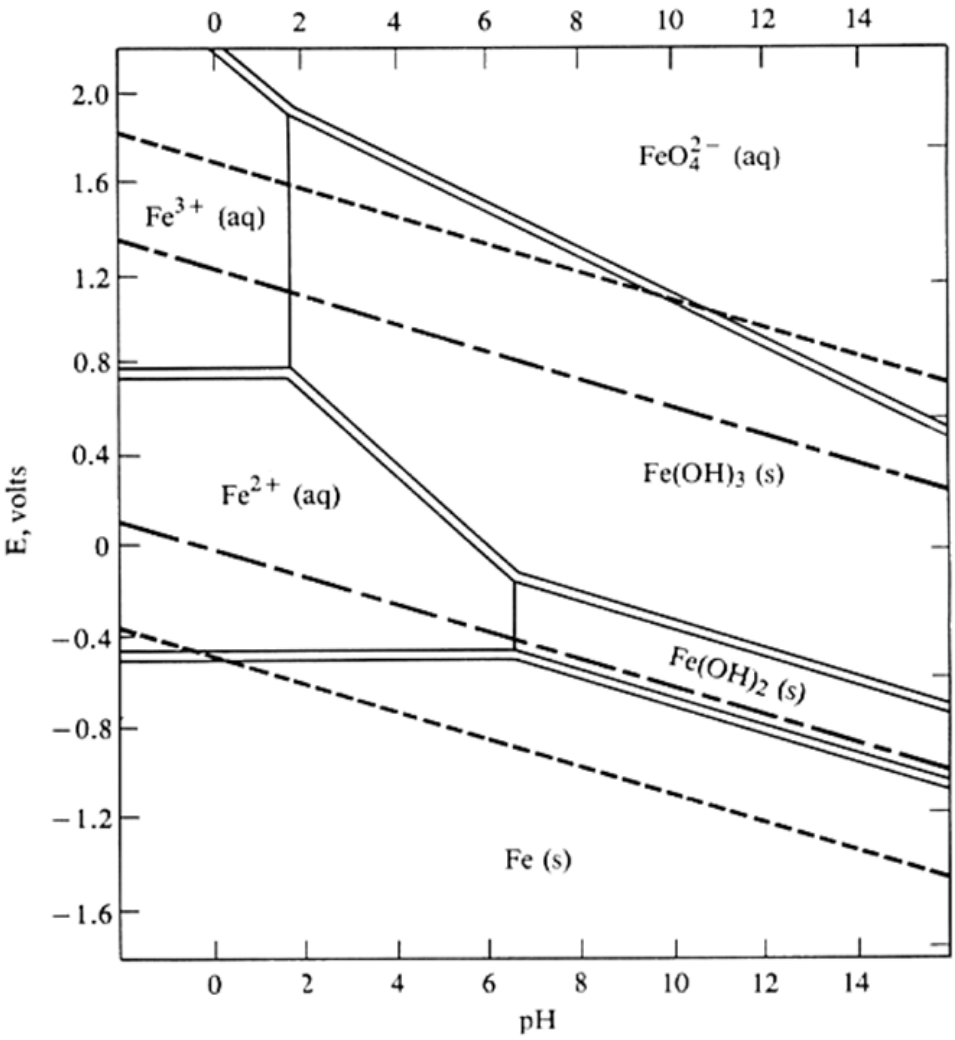


Figure 2.8.: A simplified Pourbaix diagrams of iron (Wulfsberg, 1992).

According to Habashi (1999), sulphide minerals can be dissolved under either reducing conditions or oxidising conditions:

- Under reducing conditions: sulphide minerals which are dissolved in acids forming H_2S or dissolved in bases forming sulphide ion.
- Under oxidising conditions: elemental sulphur occurs in acids and it further oxidises to sulphate in neutral or basic medium.

Few sulphide minerals can be leached in absence of oxidising agents unless they are acid-soluble (e.g. NiS, CoS, FeS), alkali-soluble (e.g. PbS, ZnS) or complex-forming (e.g. As_2S_3, SnS, SnS_2, HgS) (Habashi, 1999). Few industrial processes use this technology. Leaching with oxidising agents is much more popular in industry and most commonly

Table 2.4.: Typical leaching agents with their applications (Habashi, 1999).

Category	Reagent examples	Application
Water	H_2O	Sulphates, chlorides, borates
Bases	NaOH	Bauxite
	NH_4OH (+air)	Nickel sulphide concentrates
Acids	H_2SO_4 (Dilute)	Copper oxide ores, zinc oxide
	H_2SO_4 (Dilute) + oxidant	Uranium ores, sulphides
	HCl	Chemical beneficiation of limonite
	HNO_3	Uranium concentrates
Aqueous salt solution	$FeCl_3$, $Fe_2(SO_4)_3$	Copper sulphide concentrates
	Na_2CO_3	Tungsten ores
	Na_2CO_3 + oxidant	Uranium ores
Chlorine	Cl_2	Gold ores

used oxidising agents involves: oxygen, ferric ion, nitric acid, concentrated H_2SO_4, chlorine water and sodium hypochlorite (Habashi, 1999). The general principle of leaching sulphide minerals is summarised in Table 2.5.

Table 2.5.: Methods of leaching sulphides (Habashi, 1999).

Oxidiser	Medium	Reaction	Example
N/A	Acid	$MS + 2\,H^+ \longrightarrow M^{2+}H_2S$	NiS, CoS, FeS
	Base	$MS + 4\,OH^- \longrightarrow {MO_2}^{2-} + S^{2-} + 2\,H_2O$	PbS, ZnS
	Alkali sulphide	$MS + S^{2-} \longrightarrow {MS_2}^{2-}$	As_2S_3, SnS, SnS_2, HgS
O_2	Water	$MS + 2\,O_2 \longrightarrow M^{2+}{SO_4}^{2-}$	ZnS, MoS_2
	Ammonia	$MS + nNH_3 + 2\,O_2 \longrightarrow [M(NH_3)n]^{2+} + {SO_4}^{2-}$	NiS
	Base	$MS + 4\,OH^- + 2\,O_2 \longrightarrow {MO_2}^{2-} + {SO_4}^{2-} + 2\,H_2O$	MoS_2
	Acid	$MS + 2\,H^+ + 0.5\,O_2 \longrightarrow M^{2+} + S + H_2O$	ZnS, $CuFeS_2$, Cu_2S, FeAsS
Ferric	Acid	$MS + 2\,Fe^{3+} \longrightarrow M^{2+} + 2\,Fe^{2+} + S$	Cu_2S, CuS, $CuFeS_2$, PbS

In sulphide leaching, the system usually make use of bioleaching technologies in which micro-organisms leach minerals (e.g. copper minerals) either directly or through the production of ferric ions.

2.3.2. Copper Minerals in Heap Leaching

Copper minerals can be divided into two main categories, namely secondary and primary sulphide minerals. Table 2.6 shows the most common copper minerals that occur in heap leaching. Currently, it is difficult to find large copper deposits with average copper content greater than 1% and most current copper deposits have copper contents of approximate 0.5% or less (Figure 2.2).

Table 2.6.: Common copper minerals in heap leaching (Schlesinger et al., 2011).

Type	Minerals	Mineral formula	Theoretical Cu%
Secondary minerals			
Carbonates	Azurite	$(CuCO_3)_2 \cdot Cu(OH)_2$	55.3
	Malachite	$(CuCO_3)_2 \cdot Cu(OH)_2$	57.5
Hydroxy-silicates	Chrysocolla	$CuO \cdot SiO_2 \cdot 2\,H_2O$	36.2
Native copper	Metal	Cu^0	100
Oxides	Cuprite	Cu_2O	88.8
	Tenorite	CuO	79.9
Sulphates	Antlerite	$CuSO_4 \cdot 2\,Cu(OH)_2$	53.7
	Brochantite	$CuSO_4 \cdot 3\,Cu(OH)_2$	56.2
Supergene sulphide	Chalcocite	Cu_2S	79.9
	Covellite	CuS	66.5
	Digenite	$Cu_1 \cdot 8\,S$	78.1
Primary minerals			
(Hypogene sulphides)	Chalcopyrite	$CuFeS_2$	34.6
	Bornite	Cu_5FeS_4	63.3
	Pyrite*	FeS_2	N/A

* Pyrite does not contain copper but it always exists with copper minerals.

Sulphuric acid is the most common leaching agent or medium used in heap leaching. Most copper minerals are able to be leached under atmospheric conditions, either with or without oxidising agents. Oxide minerals can be leached readily in acidic condition without adding oxidising agents while secondary sulphide minerals, like bornite, covellite and chalcocite, can be leached under biological oxidising conditions (Schlesinger et al., 2011). Primary sulphide minerals like chalcopyrite cannot be easily leached in heap leaching, but it can be leached using pressure oxidation leaching under high pressure and temperature, and oxidising conditions. Research into the heap leaching of chalcopyrite is an active topic as chalcopyrite is the most abundant copper mineral in most sulphide deposits (Córdoba et al., 2008a, 2009; Ghorbani et al., 2011a; Pradhan et al., 2008; Watling, 2006). This topic is discussed in Section 2.3.4.

2.3.3. Secondary Copper Mineral Leaching

2.3.3.1. Copper Oxides Leaching

Figure 2.9 is the Pourbaix diagram for the Cu-O-S-H_2O system, which is useful to identify the status of Cu at specific pH and Eh values. Copper can be dissolved as Cu^{2+} in acidic condition with pH lower than 6. Examples of reactions of leaching of copper oxide minerals are:

$$CuO + H_2SO_4 \longrightarrow Cu^{2+} + {SO_4}^{2-} + H_2O \tag{2.7}$$

$$Cu_2O + H_2SO_4 \longrightarrow Cu^{2+} + {SO_4}^{2-} + Cu + H_2O \tag{2.8}$$

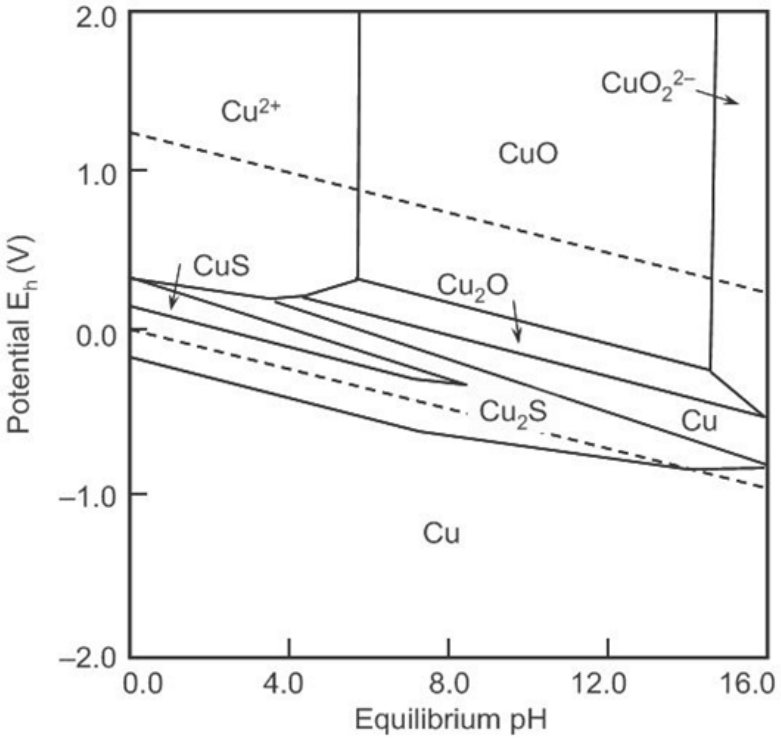


Figure 2.9.: Pourbaix diagram for Cu-O-S-H_2O system at 25 °C (House, 1987; Schlesinger et al., 2011).

2.3.3.2. Copper Sulphides Leaching

Copper sulphide minerals normally need oxidising agents, such as Fe^{3+} or O_2, under acidic conditions to break the mineral lattice and release Cu^{2+} into the solution (Schlesinger et al., 2011). Taking chalcocite leaching as an example, if the oxidising agent is O_2 (normally dissolved O_2 from the air). The reaction is:

$$Cu_2S + \frac{1}{2}O_2 + H_2SO_4 \longrightarrow CuS + CuSO_4 + H_2O \tag{2.9}$$

It needs to be noted that the CuS in the reaction is a product rather than covellite. Under acidic conditions, if ferric ion acts as both leaching and oxidising agent, the reaction becomes:

$$Cu_2S + Fe_2(SO_4)_3 \longrightarrow Cu^{2+} + {SO_4}^{2-} + CuS + 2\,FeSO_4 \tag{2.10}$$

During the reaction, Fe^{3+} is reduced to Fe^{2+} but it can be re-oxidised to Fe^{3+} due

to the occurrence of O_2 dissolved in the solution:

$$4\,FeSO_4 + O_2 + 2\,H_2SO_4 \longrightarrow 2\,Fe_2(SO_4)_3 + 2\,H_2O \tag{2.11}$$

If there is enough oxygen, an overall reaction can be obtained by adding the previous two reactions together:

$$Cu_2S + \frac{1}{2}O_2 + H_2SO_4 \longrightarrow Cu^{2+} + {SO_4}^{2-} + CuS + H_2O \tag{2.12}$$

It can be seen that if there is enough oxygen, ferric and ferrous ion act in a catalytic manner. Similar catalytic reactions occur in the leaching of other minerals, such as covellite:

$$CuS + Fe_2(SO_4)_3 \longrightarrow Cu^{2+} + {SO_4}^{2-} + 2\,FeSO_4 + S \tag{2.13}$$

$$4\,FeSO_4 + O_2 + 2\,H_2SO_4 \longrightarrow 2\,Fe_2(SO_4)_3 + 2\,H_2O \tag{2.14}$$

$$CuS + \frac{1}{2}O_2 + H_2SO_4 \longrightarrow Cu^{2+} + {SO_4}^{2-} + H_2O + S \tag{2.15}$$

Elemental sulphur may occur in leaching of most secondary sulphide minerals. As a reaction product, elemental sulphur can be converted to sulphuric acid under some conditions, especially some bioleaching conditions (Schlesinger et al., 2011):

$$2\,S + 3\,O_2 + 2\,H_2O \longrightarrow 2\,H_2SO_4 \tag{2.16}$$

2.3.3.3. Bacterial Actions

The most significant role of micro-organisms in heap leaching is to catalyse the process by regenerating ferric ion and protons from ferrous ion and sulphur oxidation. Fe^{3+} can enhance the leaching process due to its strong oxidising ability. As mentioned in Table 2.6, pyrite, which always occurs with sulphide minerals, is a source of Fe^{2+}, Fe^{3+}, and H_2SO_4. Pyrite is reduced by sulphur-oxidising bacteria and Fe^{3+} is reduced to Fe^{2+}. The produced Fe^{2+} is then re-oxidised to Fe^{3+} by oxygen, catalysed by ferrous-oxidising bacteria (Schlesinger et al., 2011). Using leaching chalcocite as an example:

$$2\,FeS_2 + 7\,O_2 + 2\,H_2O \longrightarrow 2\,Fe^{2+} + 2\,{SO_4}^{2-} + 2\,H_2SO_4 \tag{2.17}$$

$$4\,Fe^{2+} + 4\,{SO_4}^{2-} + O_2 + 2\,H_2SO_4 \longrightarrow 4\,Fe^{3+} + 6\,{SO_4}^{2-} + 2\,H_2O \tag{2.18}$$

$$Cu_2S + Fe_2(SO_4)_3 \longrightarrow Cu^{2+} + {SO_4}^{2-} + CuS + 2\,FeSO_4 \tag{2.19}$$

$$CuS + Fe_2(SO_4)_3 \longrightarrow Cu^{2+} + {SO_4}^{2-} + 2\,FeSO_4 + S \tag{2.20}$$

$$2\,S + 3\,O_2 + 2\,H_2O \longrightarrow 2\,H_2SO_4 \tag{2.21}$$

In heap leaching of sulphide minerals using ferric ion under acidic conditions there are three major processes: acid ferric leaching of sulphide minerals (Equation (2.19) and Equation (2.20)), the microbial oxidation of ferrous ion to ferric ion (Equation (2.18)) and the microbial oxidation of sulphur (Equation (2.21)) (Ghorbani et al., 2011a).

2.3.4. Primary Copper Mineral Leaching: Chalcopyrite

2.3.4.1. Introduction to Chalcopyrite

Chalcopyrite ($CuFeS_2$), which contains 34.5 wt% copper, is the most abundant copper mineral in the world, accounting for approximately 70% of the global copper reserves (Koleini et al., 2011). Heap leaching of oxide and secondary sulphide copper minerals has been developed for many years and it has been widely applied in the mineral processing industry. However, it is still difficult to treat refractory primary sulphide copper minerals like chalcopyrite using leaching at a commercial scale (Watling, 2006). Due to the surface transformations which render products very stable under oxidising conditions (Córdoba et al., 2008a), chalcopyrite becomes recalcitrant under most hydrometallurgical conditions (Córdoba et al., 2008a; Pradhan et al., 2008). However, the increase in copper consumption and depletion of high grade copper ore deposits has encouraged the development of treatments for chalcopyrite using hydrometallurgical methodologies (Córdoba et al., 2008a,b; Watling, 2006).

2.3.4.2. Chemistry of Chalcopyrite Leaching

The leaching of chalcopyrite can be achieved using an acidic medium (e.g. sulphuric acid) containing a reasonable concentration of ferric ion (Fe^{3+}) as an oxidising agent. This chalcopyrite dissolution process is an oxidative process and the ferric ion is the oxidising agent. Figure 2.10 shows that the dissolution of chalcopyrite in the acid medium takes place through a solid transformation into different intermediate sulphides (Cu_5FeS_4, CuS, Cu_2S) (Córdoba et al., 2008a). According to the diagram, in order to dissolve chalcopyrite, the pH should be maintained below 4 and the oxidising redox potential should be higher than +0.4 V when using ferric ion as the oxidising agent. The preferable redox potential when leaching chalcopyrite using ferric ion is reported as being a small range between 400 and 450 mV vs. SCE (standard calomel electrode) (Barr et al., 1992; Córdoba et al., 2008b). Low Eh value can be achieved by adding ferrous ion. In

a sulphuric acid system containing both ferric and ferrous ions, Fe^{3+}/Fe^{2+} is the only significant redox couple. The Eh (V vs. SHE) can thus be calculated using the Nernst equation and the ferric and ferrous concentration can be calculated based on the solution potential (Hiroyoshi et al., 2008, 2000):

$$Eh = 0.670 + 0.059log(\frac{[Fe^{3+}]}{[Fe^{2+}]}) \tag{2.22}$$

$$[Fe_{total}] = [Fe^{3+}] + [Fe^{2+}] \tag{2.23}$$

where $[Fe^{3+}]$, $[Fe^{2+}]$ and $[Fe_{total}]$ indicate the concentration of ferric ion, ferrous ion and total iron, Eh is the redox potential (V vs. SHE). Figure 2.11 shows the relationship between the initial concentration ratio of ferric to ferrous ions and the initial redox potential E (mV vs. SHE) in 0.1M sulphuric acid. It can be observed that the value of Eh has a linear relationship with $log([Fe^{3+}]/[Fe^{2+}])$. However, many authors reported that ferrous ion can catalyse the chalcopyrite dissolution thus can enhance the chalcopyrite leaching and the optimum Eh for leaching is below 400 mV vs. SCE (Córdoba et al., 2008b; Hiroyoshi et al., 2001).

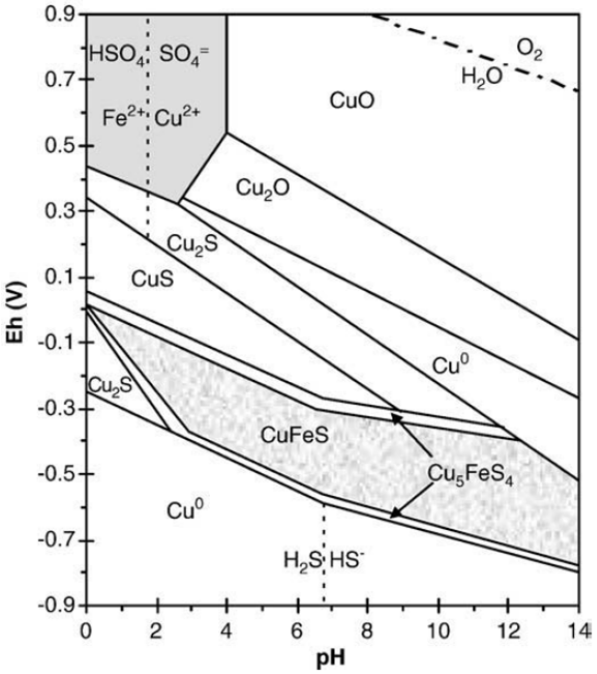


Figure 2.10.: Pourbaix diagram for the $CuFeS_2$-H_2O system at 25 °C (Córdoba et al., 2008a).

One well accepted chalcopyrite dissolution reaction with ferric ion is (Barriga Mateos

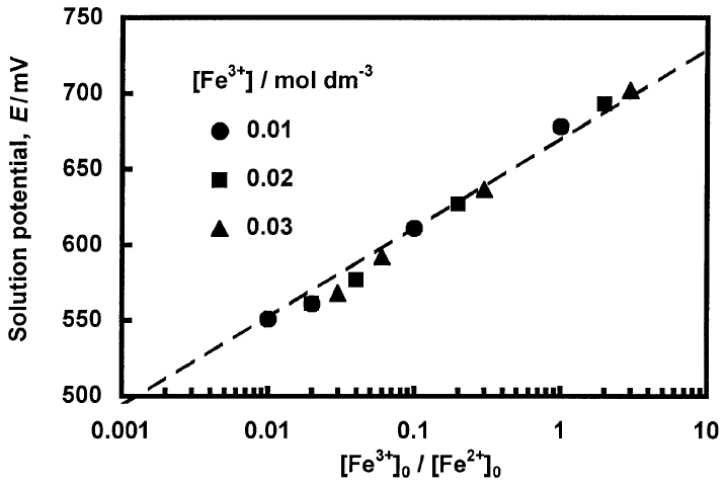


Figure 2.11.: The relationship between the initial concentration ratio of ferric to ferrous ions and the initial redox potential E (mV vs. SHE) in 0.1M sulphuric acid (Hiroyoshi et al., 2001).

et al., 1987):

$$CuFeS_2 + 4\,Fe^{3+} \longrightarrow Cu^{2+} + 5\,Fe^{2+} + 2\,S \tag{2.24}$$

At the same time, it has been proved that there is a parallel, non-oxidative reaction existing in chalcopyrite leaching in sulphuric acid medium (Watling, 2006):

$$CuFeS_2 + 4\,H^{+} \longrightarrow Cu^{2+} + Fe^{2+} + 2\,H_2S \tag{2.25}$$

Apart from the ferric ion, oxygen can be another active oxidant. The sources of oxygen can be the dissolved oxygen in solution or a separate air flow. When the oxygen is present, the H_2S can be further oxidised to S, following the reaction (Pradhan et al., 2008):

$$CuFeS_2 + 4\,H^{+} + O_2 \longrightarrow Cu^{2+} + Fe^{2+} + 2\,S + 2\,H_2O \tag{2.26}$$

When ferric ion and oxygen occur at the same time, it is reported that the ferrous ion is formed as a product that can be re-oxidised to ferric ion (Hiroyoshi et al., 2001; Koleini et al., 2011). This process can also be assisted by the occurrence of iron oxidising bacteria (Pradhan et al., 2008):

$$4\,Fe^{2+} + O_2 + 4\,H^{+} \xrightarrow{\text{bacteria}} 4\,Fe^{3+} + 2\,H_2O \tag{2.27}$$

According to Equation (2.26), the leaching of chalcopyrite when oxygen exists is an acid consuming process. The large acid consumption is one of the key issues limiting the application of hydrometallurgical method in copper extraction, which increase the cost

and raise environmental problems. By adding sulphur oxidising bacteria, this problem can be partially alleviated as this kind of bacteria can make a contribution in acid regeneration (Pradhan et al., 2008):

$$2\,S + 3\,O_2 + 2\,H_2O \xrightarrow{\text{bacteria}} 4\,H^+ + 2\,{SO_4}^{2-} \tag{2.28}$$

In the presence of ferric ion, two well accepted reactions expressing chalcopyrite dissolution are (Barriga Mateos et al., 1987; Córdoba et al., 2008a):

$$CuFeS_2 + 4\,Fe^{3+} \longrightarrow Cu^{2+} + 5\,Fe^{2+} + 2\,S \tag{2.29}$$

$$CuFeS_2 + 4\,Fe^{3+} + 3\,O_2 + 2\,H_2O \longrightarrow Cu^{2+} + 5\,Fe^{2+} + 2\,H_2SO_4 \tag{2.30}$$

It is reported that both Equation (2.29) and Equation (2.30) can happen during leaching process of chalcopyrite which depend on the availability of oxygen in the leaching solution (Córdoba et al., 2008a; Hackl et al., 1995).

2.3.4.3. Factors Affecting Chalcopyrite Leaching

As a typical primary sulphide mineral, chalcopyrite is highly refractory under most leaching conditions (Córdoba et al., 2008a). In order to achieve efficient leaching, many parameters need to be considered to enhance the dissolution of chalcopyrite. The parameters which can influence heap leaching are summarised in Section 2.2.2. Most chemistry related studies involve tank leaching experiments using milled samples. Several key parameters that significantly affect chalcopyrite leaching in the experiments are reviewed and discussed below:

- Particle size and mineral grain exposure

  In order to achieve efficient leaching of chalcopyrite, minerals must be effectively exposed to the leaching solution which makes ore preparation stage important. The leaching of chalcopyrite is usually slow and incomplete and this can be improved by grinding ores finely ($P_{80} < 15$ μm) because a larger surface to volume ratio increases dissolution (Watling, 2006). During the grinding and crushing process, pores and cracks can also be created and become new access points for leaching solution, which can also enhance leaching. Fine grinding can be an economic method when applying with moderate temperature rather than high temperature. Watling (2006) mentioned a successful example using this method in Mt Lyell and 96% of copper was extracted after 5 to 6 days. The leaching process was conducted under

moderate temperature, using moderate thermophiles (45 °C - 47 °C), and the pH was controlled between 0.8 and 2.0.

- Iron concentration

  It is widely accepted that the ferric ion concentration is a key parameter in chalcopyrite leaching. The effect of ferric ion concentration in chalcopyrite leaching is significant at low ferric concentrations but becomes negligible at high ferric concentrations. Hirato et al. (1987b) found out that the increase of ferric sulphate concentration could enhance chalcopyrite leaching at 70 °C within a range of 0.001 to 0.1M. It is estimated that Fe^{3+} and $FeHSO_4^{2+}$ species are responsible for chalcopyrite leaching and their concentration can increase when the total iron concentration increased, with an upper limiting value of 0.1M (Córdoba et al., 2008a). Córdoba et al. (2008b) conducted chalcopyrite leaching experiments at 68 °C and found similar positive effect results with an iron concentration range from 0.009 to 0.09M (0.5 to 5 g/L).

- Temperature

  When leaching chalcopyrite with ferric ion in acidic medium, temperature is a significant parameter that needs to be considered. Higher temperature can lead to higher leaching kinetic rate. Córdoba et al. (2008b) carried out an experiment to leach chalcopyrite in ferric sulphate medium and the results showed that after a 13-day leaching period, the percentage of copper extracted under 68 °C is more than 80% while the percentage dropped to lower than 3% when temperature is 35 °C.

  The activation energy is a measure of the energy needed to break down bonds in chalcopyrite crystal lattice and higher values mean higher temperature is needed (Córdoba et al., 2008a). The values of activation energy required in leaching chalcopyrite in the presence of ferric ion reported by different authors are summarised by Córdoba et al. (2008a), shown in Table 2.7. It can be observed that the activation energy in chalcopyrite leaching is quite similar for the first three cases using ferric sulphate medium. Córdoba et al. (2008a) states that the possible reason that makes 130.7 kJ/mol much higher than other cases is the different temperature range selected. Another important observation is that the activation energies are higher when using a sulphate medium than with a chloride medium, which indicates that the oxidising power of the ferric sulphate medium is lower (Córdoba et al., 2008a).

Table 2.7.: Effect of temperature during chalcopyrite leaching with ferric ion (Córdoba et al., 2008a).

Medium	Temperature	Activation energy	Kinetic control	Reference
$Fe_2(SO_4)_3$	50 °C - 94 °C	71 kJ/mol	Parabolic kinetics diffusion control	Dutrizac et al. (1969)
	60 °C - 90 °C	84 kJ/mol	Parabolic kinetics electrochemical control	Munoz et al. (1979)
	50 °C - 78 °C	88 kJ/mol	Parabolic-linear kinetics chemical control	Hirato et al. (1987b)
	35 °C - 68 °C	130.7 kJ/mol	Parabolic-linear kinetics chemical control	Córdoba et al. (2008b)
$FeCl_3$	60 °C - 90 °C	60 kJ/mol	Linear kinetics electrochemical control	Hirato et al. (1987a)
	55 °C - 84 °C	69 kJ/mol	Linear kinetics electrochemical control	Majima et al. (1985)
	50 °C - 100 °C	47 kJ/mol	Linear kinetics diffusion control	Dutrizac (1978)

- Ferric salt anion

  The ferric salt anions can also affect the leach behaviour. Ferric chloride is a better leaching agent compared with ferric sulphate, particularly at higher temperatures (Córdoba et al., 2008a). Ferric chloride also has stronger oxidising power than ferric sulphate in chalcopyrite leaching that can be reflected by the lower activation energy (Table 2.7). Dutrizac and MacDonald (1971) demonstrated that with a ferric sulphate medium, based on their experiment, the chalcopyrite dissolution rate could be enhanced by extra chloride ions at a higher temperature (>50 °C) but had a negligible effect at lower temperature. This phenomenon could possibly be due to the elemental sulphur formed in the ferric chloride medium which was more porous than with ferric sulphate medium (Córdoba et al., 2008a).

  However, in industry, ferric sulphate is used more widely than ferric chloride due to following factors (Córdoba et al., 2008a):

  - The affinity of the chloride ion towards many elements complicates the process of separating copper from the solution.
  - Chloride solutions are extremely corrosive.
  - Hydrochloric acid is more expensive than sulphuric acid, which is the prime reason.

- pH value

  The pH value can also affect chalcopyrite leaching and most chalcopyrite leaching

processes are carried out under acidic conditions with a relatively low pH values. Many authors conclude that the leaching rate of chalcopyrite is higher at higher pH as chalcopyrite can be oxidised by oxygen and ferric ion that are present in the leaching solution and the dissolution rate of chalcopyrite is quite low at low pH (<1.0) (Antonijević and Bogdanović, 2004; Córdoba et al., 2008a).

Antonijević and Bogdanović (2004) carried out an experiment of leaching chalcopyrite under different pH values from 0.5 to 2.0 and the copper content in output solutions were from 0.076 to 0.116 g/dm^3, reflecting that the values of pH did not significantly affect the dissolution rate. They concluded that the dissolution rate at pH of 0.5 was the lowest and could be explained as chalcopyrite at low pH value (<0.5) could be in passive state where a layer of chalcopyrite with insufficient iron is formed on the surface of this mineral (Antonijević and Bogdanović, 2004; Lu et al., 2000). Córdoba et al. (2008a) also proved that the dissolution of chalcopyrite with ferric sulphate decreases with declining pH but also showed that the dissolution rate at pH = 2.0 (>500 mg/L) was much higher than the rate at pH = 0.5 (<150 mg/L) and pH became an important factor in their case. Córdoba et al. (2008a) also estimated that $Fe(SO_4)_2^-$ could be the possible species responsible for oxidisation of chalcopyrite rather than ferric ion because it is the only species increasing in concentration within that pH range (0.5<pH<2.0).

However, lower pH is also necessary as it can prevent the occurrence of ferric hydrolysis and its precipitation which can cause passivation and a loss of permeability in the heap system (Córdoba et al., 2008a; Dutrizac et al., 1969; Habashi, 1999). According to Figure 2.8, the precipitation of ferric salts can happen even when pH is as low as around 1, which means that the value of pH needs to be maintained quite low, probably lower than 1.0, to avoid precipitation.

2.4. Ore Particle Effects in Heap Leaching

One of the key differences between heap leaching and conventional pyrometallurgy methods is that heap leaching uses ores with larger particle size, typically 12-25 mm after crushing. Therefore, the research at the particle scale becomes important in understanding the leach behaviour under such condition. At this scale the effect of both mass transport and surface reaction are important. Research has been carried from macro scale to mineral grain scale (Bartlett, 1998; Klauber, 2008; Padilla et al., 2008), however, few studies have been carried out looking at the individual particle scale and particularly,

leach behaviour within individual ore particles.

2.4.1. Scales in Heap Leaching

The study of heap leaching process can be divided into different research scales, including macro scale (heap scale), meso scale (stagnant cluster), particle scale (within a single particle) and grain scale (mineral surfaces), shown in Figure 2.12 (Ghorbani et al., 2011a; Dixon and Petersen, 2003).

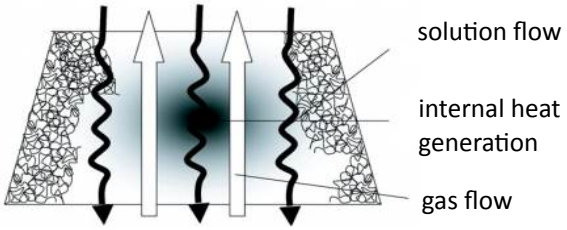
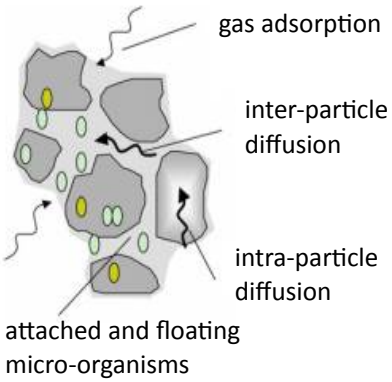
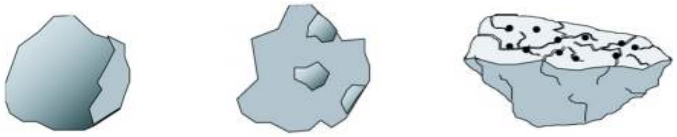
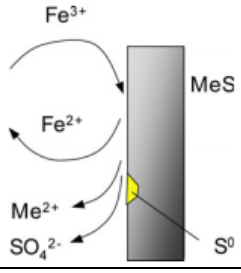
Scale	Sub-processes	Illustration
Macro scale (Heap)	Unsaturated solution flow Gas advection Water vapour transport Heat balance	
Meso scale (Stagnant cluster)	Gas adsorption Inter-/ intra-particle diffusion Microbial growth Microbial attachment Microbial oxidation	
Particle scale (Ore particle)	Topological effects Intra-particle diffusion Particle size distribution	
Grain scale (Mineral grain)	Ferric reduction Mineral oxidation Sulphur oxidation Surface processes	

Figure 2.12.: Illustration of different sub-processes scales in heap leaching (Dixon and Petersen, 2003).

The main processes involved at the macro scale is the transmission of mass (gas and

solution flow) and energy (heat) within the heap. Mass and energy balances are essential at this scale (Ghorbani et al., 2011a). The macroscopic behaviour such as fluid dynamics and liquid hold up can be understood.

The meso scale involves clusters of ore particles and the reaction kinetics are governed by the processes including gas adsorption, inter and intra particle diffusion, bacteria growth, attachment and oxidation (Ghorbani et al., 2011a). Ghorbani et al. (2011a) pointed out that oxygen is a key reactant in heap bioleaching as microbes need oxygen to oxidise ferrous ion to ferric ion and reduce sulphur species. Small scale column leaching can be carried to understand the overall leach behaviour under different leaching condition such as temperature, different ores, different leaching reagents, etc..

At the ore particle scale, the leaching process is significantly influenced by the distribution and accessibility of the mineral grains, both of which directly affect the efficiency of the leaching process. Another important factor that can influence the leachability, especially in low grade ores, is the effect of gangue minerals as they can interfere with leaching and biological phenomena (Ghorbani et al., 2011a).

At the grain scale, leaching kinetics are governed by chemical and electrochemical reactions at the grain surface (Ghorbani et al., 2011a). The reactions may also be influenced by temperature and activation energy and a typical example is chalcopyrite leaching with ferric ion (Table 2.7).

2.4.2. Leaching Behaviour at Individual Ore Particle Scale

As shown in Table 2.3, there are many aspects affecting the overall behaviour and kinetics of heap leaching. A suitable leaching condition involves correct physical and chemical conditions.

2.4.2.1. Ore Particle Size

For ore particles, the leaching kinetics are influenced by the surface area to volume ratio, and the higher the ratio the faster the kinetics. In this case, both ore particle size and shape are factors determining the ratio. The leaching kinetics follows the general trend that a smaller particle size gives higher leaching rates.

When simulating and modelling the leaching process, the shrinking core model is a common model for mineral dissolution. The details of shrinking core model are explained in Section 2.4.3. Ogbonna et al. (2006) carried out a simulation of leaching ore particles containing chalcocite and pyrite, with different particle sizes (Figure 2.13). The results indicated that particles in the 0.5 mm radius size class achieve an overall 90%

dissolution of chalcocite and covellite after 250 days and the dissolution rate of three minerals were quite different. However, it took 1000 days for the particles in 5 mm size class to achieve the same percentage with a much lower dissolution rate, and the rates for the three minerals were quite similar. This can be explained by the rim effect. For larger particles, after the depletion of chalcocite and pyrite that are close to the surface following Equation (2.9) and Equation (2.17), both pyrite and covellite (by product) left in the outer rim can significantly prevent ferric ion diffusing deeper into the particle to contact unreacted chalcocite (Ghorbani et al., 2011a; Ogbonna et al., 2006). However, if the particle size is smaller, this effect can be negligible because of the much shorter diffusion distance.

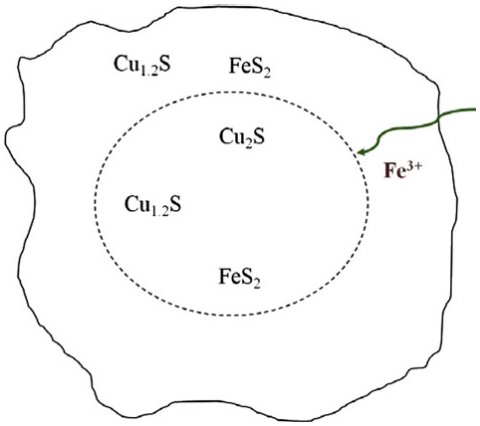


Figure 2.13.: Ferric diffusion through rim leach in large particles (Ogbonna et al., 2006).

For real ore particles, it is observed that initially a higher leaching rate (Figure 2.7) can occur in almost all size categories, which then slows down significantly. This rapid leaching can dissolve the majority of minerals if the particle size is small but can only partially dissolve minerals if the particle size is larger. It can be explained that after the depletion of easy-to-leach surface minerals, the leaching solution has to access deeper via the porous network or cracks and then return dissolved species to the surface (Ghorbani et al., 2011a; Ogbonna et al., 2006).

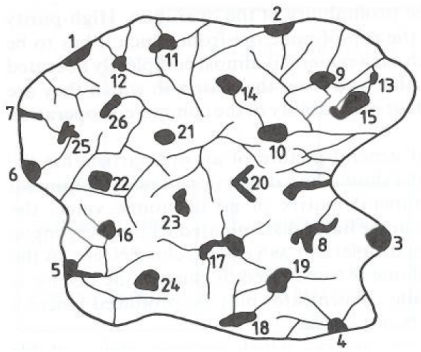
2.4.2.2. Grain Distribution and Accessibility to Leaching Solution

The leaching process is a complex dissolution process that requires the leaching solution to come into contact with the target minerals. As it is impractical to dissolve the entire ore particle, leaching solution comes into contact with minerals by penetration through the unreacted gangue minerals via pores and cracks, or partially reacted gangue

minerals, before reaching the target minerals (Rossi, 1990). Therefore, the analysis of mineral grain distribution and accessibility to leaching solution becomes significant.

According to the accessibility to leaching solution, Rossi (1990) classified the mineral grain distribution into five categories (Table 2.8). A two dimensional model of a low grade ore particle was developed where the reactive and valuable minerals are marked in black, gangue minerals are marked in white, and pores and cracks are illustrated using lines. Type (d) and (e) grains do not contribute to the dissolution rate at the early stage, but are involved when new cracks and fissures are generated in gangue minerals and make the grains accessible to leaching solution (Rossi, 1990). This is due to prolonged contact with leaching solution. Four rate regimes are defined according to the particle sizes and characteristics, shown in Table 2.8.

Table 2.8.: Mineral grain distribution based on accessibility to leaching solution (Rossi, 1990).

Categories	Illustration
a) Grains exposed to the leach solutions at the surface of particles (e.g. grain number 1, 2, 4) b) Grains exposed to the leach solutions via pores or cracks (e.g. grain number 9, 10, 11) c) Grains which become exposed to the leach solutions only after other grains have reacted (e.g. grain number 14) d) Grains from which pores or fissures that do not debouch to the particle surface depart (e.g. grain number 18, 19) e) Grains located inside the particles and not connected to a pore (e.g. grain number 21, 24)	

For the particles of the type shown in Table 2.8, four rate regimes can be identified according to their size (Rossi, 1990):

1. The particle size is comparable with the size of the mineral grains; this is the case of very high-grade ROM ores or of concentrates. In this case, the reaction rate is close to that of the fully liberated grains and the inert matrix plays a minor role. Leaching is surface-chemical reaction- controlled. This regime is characterised by a shrinking of the particle as the reaction proceeds.

2. The particle size is larger than that of the mineral grains, although the latter are all accessible to the leach solutions from the start of the reaction. Most of the surface of the mineral grains is surrounded by impervious inert gangue and leach solution can only gain access to through the pores and/or cracks. Leaching is therefore still

surface-chemical reaction-controlled, but the gangue reduces the rate by blocking access of the leach solutions to most of the surface. Thus, diffusion control comes into play. In this case, particle size does not significantly affect reaction rate.

3. The ratio between particle radius and embedded mineral grain radius is even larger than in the two preceding cases. The characteristic feature of this situation is that not all the grains are accessible at the start of leaching, although the overall rate is still controlled by the surface chemical reaction. Accessibility to the inner grains is hindered by the outer mineral grains and the inert gangue. The rate exhibits a further reduction.

4. In the largest particles sizes the kinetics is diffusion-controlled or mixed (diffusion and surface- chemical reaction-controlled). The effect of the gangue is to increase the diffusion path length-thereby reducing the overall rate still further.

The locations and sizes of individual mineral grains are a key factor in leaching and this is one of the main objectives in this study when trying to quantify and understand leach performance.

2.4.2.3. Porosity

The leaching kinetics for small particles at the particle scale is usually controlled either by molecular diffusion through a boundary layer extending into the fluid or by the reactions occurring at external surface (Ghorbani et al., 2011a). For larger particles, it is mainly controlled by internal diffusion. When porosity is low, the particle size which determines surface area to volume ratio is a major factor. If the porosity is relatively high or there are micro cracks and pores which are accessible, leaching solution can diffuse into the internal particle and dissolve minerals there.

Under the steady state condition, the diffusion rate and reaction rate are the same and the state is maintained by a concentration gradient from higher concentration in bulk solution to lower concentration in solution inside the particle via pores and cracks (Ghorbani et al., 2011a). If the reaction rate is slow, such as leaching primary copper sulphides, the concentration gradient becomes much shallower than that in the bulk solution. The reactions take place at both external surface of the ore particle and the surfaces of cracks, holes and pores inside the particle, and the reaction rates at all surfaces are virtually the same (Cariaga et al., 2005; Ghorbani et al., 2008). In contrast, if the reaction rate is fast at the surface when leaching copper oxides and secondary sulphides, the concentration gradient becomes steep and the leaching solution is consumed before it penetrates into the particle via pores and cracks.

2.4.2.4. Gangue Minerals

An ore particle can be regarded as a dispersion of reactive and valuable mineral grains throughout a mass of gangue mineral which has no economic value but increases costs. This characteristic is significant when treating low grade ores where a large proportion of the volume is gangue minerals. One of the most significant influences caused by gangue minerals is the reagent consumption, especially the acid consumption, which can directly affect the operation costs.

2.4.3. Ore Particle Level Modelling

The leaching process related to a single ore particle is widely assumed to follow the shrinking core model. The shrinking core model typically assumes that the ore particles are spherical, with an unreacted core and an outer leached region through with the reactants must be transported (Bartlett, 1998; Ghorbani et al., 2011a; Liddell, 2005). Figure 2.14 shows a shrinking core example through time.

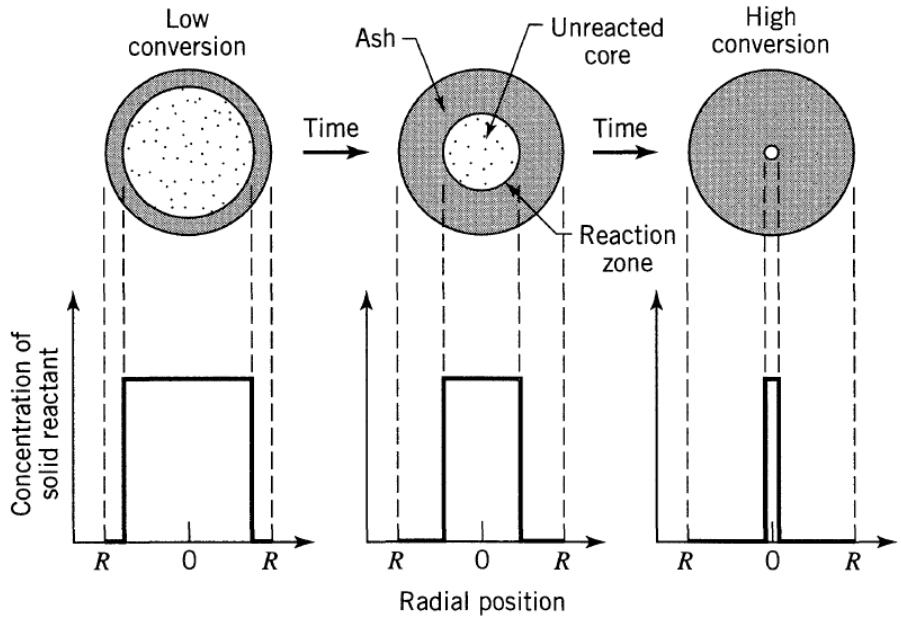


Figure 2.14.: Schematic diagram showing the principle of shrinking core model: reaction proceeds at a narrow front which moves into the solid particle. Reactant is completely converted as the front passes by (Levenspiel, 1999).

The transport through the unreacted outer region is governed by an effective diffusion coefficient, D_{eff} (Bartlett, 1997):

$$D_{\text{eff}} = D\varepsilon/\tau \tag{2.31}$$

where D is the intrinsic diffusion coefficient, ε is the particle voidage and τ is the void tortuosity. Hence, by assuming the shape of a single ore particle is a sphere, the diffusion controlled fractional extraction, $F_{t,r}$, can be simplified and expressed as (Bartlett, 1997, 1998; Miller, 2003):

$$F_{t,r} = 1 - \frac{6}{\pi^2} \sum_{n=1}^{\infty} \frac{1}{n^2} \exp\left(\frac{D_{\text{eff}}\, n^2 \pi^2 t}{r^2}\right) \tag{2.32}$$

where $F_{t,r}$ is the fractional extraction in time t for a single ore particle of radius r. Based on this model, it is obvious that particle size has a squared effect on required leaching period, t, to achieve same fraction extraction.

Although the shrinking core model has been widely applied as an assumption when studying leaching (e.g. (Safari et al., 2009)), a large amount of experimental results suggest that the leaching reactions occur not only from outer rim surface to inner rim, but also occur quickly in inside particle because it is accessible by leaching solution via cracks and pores (Liddell, 2005; Strömberg and Banwart, 1999). These behaviours make the study of leaching process related to single ore particles complex as it is affected by many aspects. Table 2.9 shows some of the limitations of the shrinking core model comparing with the real situation.

Table 2.9.: Some limitations of the shrinking core model (Levenspiel, 1999).

Assumptions	Reality
Spherical particle	The shape of ore particle is relatively random.
Unreacted core	The unleached mineral is distributed randomly. The minerals in the core can be leached when the leaching solution arrives via pores, cracks or diffusion.
Sharp interface between leached rim and unleached part	As minerals have their own size, when leaching solution reaches the core part the larger minerals in the leached part may not necessary disappear completely.

2.5. XMT application in heap leaching

The rate and extent of leaching of a mineral grain within an ore particle will depend on three main factors, namely the conditions and concentrations in the fluids around the ore particle, the mass (and heat) transport within the ore particle and surface reaction kinetics. Most studies of heap leaching have either concentrated on the first or last of these factors. The apparent kinetics as a function of the effluent and/or feed conditions can be studied using particle sizes representative of real heaps (e.g. van Hille et al. (2010)).

Hydrodynamic related research can also be carried out to understand how fluid flow and liquid holdup affect the system from column scale experiments (Ilankoon and Neethling, 2013). The surface reaction kinetics can also be obtained by studying the dissolution of finely milled ores or pure mineral particles in stirred tank experiments (Córdoba et al., 2008b, 2009; Hiroyoshi et al., 2001; Koleini et al., 2011). A lack of information and understanding of the transport processes within the ore particles makes it very hard to predict heap or even particle scale leach performance based on surface reaction kinetics. Some of this information can be obtained by comparing thin sections through leached and unleached materials, though this is destructive and requires assumptions to be made about how representative the chosen particles are. Therefore, the understanding of leach behaviour is actually limited by the analysis techniques.

High resolution X-ray Computed Microtomography (also called micro-CT or XMT, which is reviewed in details in Section 2.6) is an accurate, fast, non-destructive and non-invasive three dimensional imaging based technique for materials characterisation at micron level in engineering (including earth science and geological science) (Stock, 1999, 2008; Ketcham and Carlson, 2001; Puncreobutr et al., 2012). XMT therefore provides a method for carrying out analysis in 3D in a non-destructive manner that allows the same ore particles (or volume) to be repeatedly scanned and analysed over the course of an entire leaching experiment, which can possibly fill the gap in leaching research looking inside particles. This is also the key motivation to study leach performance in mineral processing using this technique.

Within the context of heap leaching, XMT has been used to track the extent of leaching within the ore particles (Kodali et al., 2011). Morphological parameters such as the size and shape of particles (Lin and Miller, 2005), mineral grain exposure and related technique such as high-pressure grinding rolls (HPGR) (Kodali et al., 2011; Miller et al., 2003) and the particle size distribution of the mineral grains within ore particles (Miller et al., 2003), especially their relationship to features such as internal porosity and fractures (Dhawan et al., 2012; Yang et al., 2008; Ghorbani et al., 2011a).

Although XMT and imaging techniques have been used to quantify and understand the leaching process, one of the main existing barrier to extend XMT and imaging techniques in leaching related studies is the limited application of image processing techniques. Most of this work has either been relatively qualitative in nature or, in quantitative terms, have tracked the overall mineral volume reduction. It also makes the measurement error difficult to be fully understood. Having consistent algorithms with known error is crucial when using image analysis to quantify leach behaviour and this becomes one of the key objective when developing algorithms to automatically process the XMT data. Moreover,

by using high resolution XMT data, it has a big potential to quantify and analyse leach behaviour at much smaller scale, such as individual ore particle scale and mineral grain scale (shown in Figure 2.12), rather than simply studying the overall leach behaviour for the entire system. This can be achieved by developing and applying ore particle tracking and mineral grain tracking algorithms. By improving the imaging techniques (Chapter 4), the leach performance can be analysed much more quantitatively (Chapter 5). This is another key motivation in this thesis,

On the modelling side, there has, though, been very limited work on the use of XMT to form the basis of modelling of heap leach behaviour. Ghorbani et al. (2013) simulated the dissolution of mineral grains within an ore particle and compared their results to that obtained from XMT. The modelling assumed that the ore particles were spherical and that the mineral grains were uniformly distributed within the particle. The model itself included terms to represent diffusion and surface reaction, with semi-empirical adjustments to the model to account for fracturing. While this modelling was able to produce good fits to the data once the parameters had been optimised, what it did not do was make use of the initial shape of the particle, mineral grain distribution or measured porosity as part of the modelling input. Therefore, a new model which takes the initial XMT images before leaching as part of the inputs has been developed. This work is introduced in Chapter 6.

2.6. X-ray Computed Microtomography (XMT)

2.6.1. Essentials of XMT

A typical XMT system includes three main aspects, namely the sample, the X-ray source and the detector. The sample is placed in an X-ray beam, and rotated through 360° while a series of micron level 2D radiographs are taken. The attenuated X-rays can be converted to visible light by a scintillator and are collected by a CCD collector (Stauber and Müller, 2008; Landis and Keane, 2010). By using mathematical principles of tomography, these 2D images, which record the variation of X-ray attenuation within the sample, can be used to compute tomograms and can be further reconstructed to produce a 3D volume where each voxel (smallest volume element, equivalent to a 3D pixel) represents the X-ray attenuation at each point (Landis and Keane, 2010). Hence, the internal structure of the material can be visualised according to the relationship between X-ray attenuation and atomic number and density. A schematic diagram illustrating this process is shown in Figure 2.15.

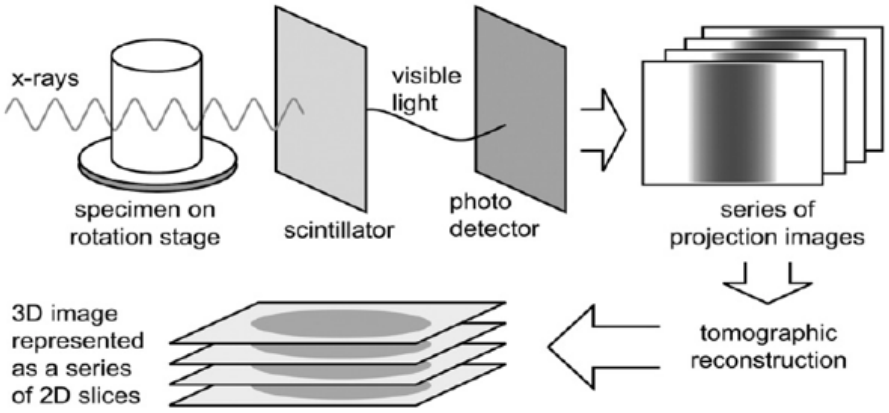


Figure 2.15.: Schematic illustration of X-ray CT acquisition and reconstruction processes. A series of X-ray projection images is acquired and mathematically reconstructed to produce a 3D map of X-ray absorption in the volume. The 3D map is typically presented as a series of 2D slice images (Landis and Keane, 2010).

The principle of XMT is the attenuation of X-rays along the object due to scattering and absorption when it passes through an object. The amount of attenuated radiation on an infinitely small distance is characterised by a linear attenuation coefficient, and the final attenuation reflects the sum of all local attenuation along the X-ray path (Stauber and Müller, 2008).

Photoelectric absorption, compton scattering and pair production are the three dominant physical processes making contribution to attenuation of X-rays, being dominant in different energy range (Ketcham and Carlson, 2001). In photoelectric absorption, the electron is ejected and released when the entire energy of an incoming X-ray photon is transferred to an inner electron. Compton scattering occurs when the incoming X-ray photon interacts with an outer electron, causing an electron to be ejected and lose part of the energy due to the deflection in a different direction. In pair production, the photon interacts with a nucleus and is transformed into a positron-electron pair, with any excess photon energy transferred into kinetic energy in the particles produced. Photoelectric effect becomes the dominant attenuation mechanism at low X-ray energies, up to approximately 50-100 keV, followed by up to 5-10 MeV for Compton scatter, after which pair production predominates (Ketcham and Carlson, 2001).

The attenuation by the photoelectric effect is the dominant attenuation mechanism for geological materials when a relatively low range of the energy spectrum is applied (Ketcham and Carlson, 2001; Stauber and Müller, 2008). A trend of the photoelectric effect is that the mass attenuation coefficient is approximately proportional to the third power of the attenuating material atomic number while being inversely proportion to the third power of the photon energy (Curry et al., 1990; Lin, 2008):

$$\text{photoelectric effect} \sim \frac{(\text{atomic number})^3}{(\text{photon enegy})^3} \tag{2.33}$$

One of the best methods to get insight into the expectation of scanning a geological sample is to plot the linear attenuation coefficients of the materials over the range of X-ray energy spectrum (Ketcham and Carlson, 2001). The linear attenuation coefficients can be obtained by multiplying mass attenuation coefficient by mass density (Berger et al., 2010). Figure 2.16 shows the relation between linear attenuation coefficients and incident X-ray energy for four common minerals examples including chalcopyrite, bornite, quartz and pyrite. It can be seen that the linear attenuation coefficients for chalcopyrite, bornite and pyrite are very similar but quite different from quartz. The average mass density for chalcopyrite, bornite and pyrite are 4.19 g/cm^3, 5.09 g/cm^3 and 5.01 g/cm^3 respectively while the average mass density of quartz is 2.62 g/cm^3. Linear attenuation coefficient as a function of X-ray energy allows predictions for the ability to differentiate between minerals in XMT images to be made. According to Figure 2.16, quartz can be easily differentiate from other minerals whereas chalcopyrite, bornite and pyrite are hard to distinguish from one another.

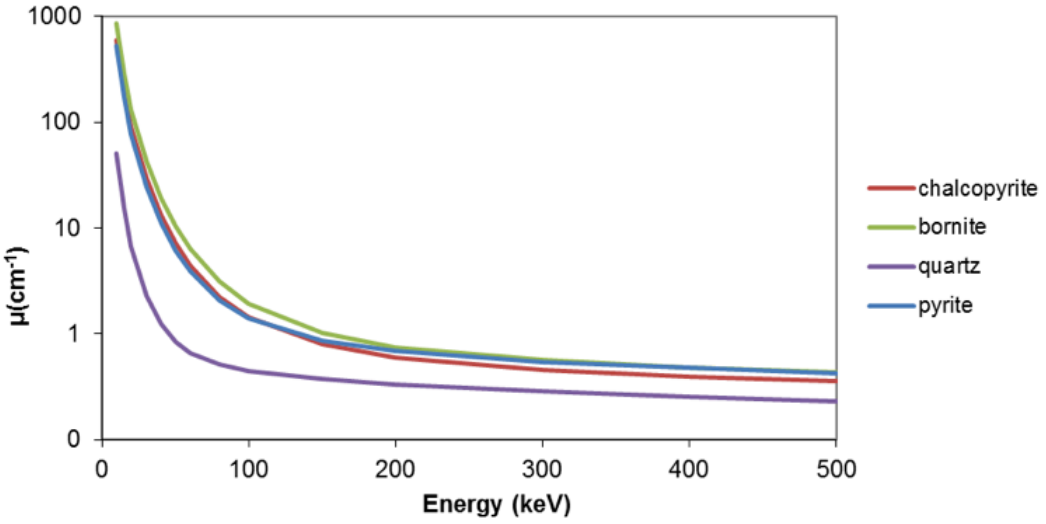


Figure 2.16.: Linear attenuation coefficient as function of incident X-ray energy of four different minerals (Berger et al., 2010).

The intensity of attenuated transmitted X-ray beam (I) through a homogeneous material can be expressed using Beer's Law (Ketcham and Carlson, 2001; Stock, 1999):

$$I = I_0 \exp(-\mu x) \tag{2.34}$$

where I is the attenuated intensity of X-ray beam, I_0 is the initial intensity of the X-ray beam, x is the thickness of the object material and μ is the linear attenuation coefficient with units of inverse distance. If the sample is composed of different materials, the equation becomes (Ketcham and Carlson, 2001):

$$I = I_0 \exp[\sum_i (-\mu_i x_i)] \tag{2.35}$$

where each increment i reflects a single material with attenuation coefficient μ_i over a linear extent x_i. Equation (2.35) can be written by applying mass attenuation coefficient given as μ/ρ with unit of $\mathrm{cm}^{-2}\mathrm{g}^{-1}$ (Hubbell, 1996):

$$I = I_0 \exp[(\frac{-\mu}{\rho})\rho x)] \tag{2.36}$$

$$\frac{\mu}{\rho} = -(\rho x)^{-1} \ln(\frac{I}{I_0}) \tag{2.37}$$

where ρx is a term called mass thickness that can be defined as the mass per unit area, being obtained by thickness x times density (Hubbell, 1996). The attenuation to each small thickness, dx, can be obtained by differentiating Equation (2.36):

$$\frac{dI}{I} = -\frac{\mu}{\rho}\rho dx = -\mu dx \tag{2.38}$$

There is a more general expression to define attenuated intensity of X-ray beam by adding the increments of attenuation along the direction of X-ray propagation yields:

$$I = I_0 \exp[-\int \mu(s) ds] \tag{2.39}$$

where $\mu(s)$ is the linear absorption coefficient at position s along ray s. One of the key problems in computed tomography is to assign the correct value of μ to each position along the ray (and along all the other rays traversing the sample) knowing only the values of the line integral for the various orientations of s. This process is called reconstruction (Stock, 1999):

$$\int \mu(s) ds = \ln(\frac{I_0}{I}) \tag{2.40}$$

Reconstruction is the mathematical process for converting 2D projections into stacked 2D images as a 3D volume and the most common method used is called filtered backprojection, in which the data are first convolved with a filter and each view is successively superimposed over a square grid at an angle corresponding to its acquisition angle (Feld-

kamp et al., 1989; Ketcham and Carlson, 2001). A 3D volume is produced by the reconstruction process and its quality is usually determined by contrast and spatial resolution, depending on the source and energy used.

The choice of the X-ray energy is mainly influenced by the object attenuation, including material, thickness. The X-ray energy needs to be decided properly as it has a significant influence on the image quality, particularly the contrast of the images. Contrast can be defined as the ratio of the difference in signal between feature (sample) and background to the signal from the background (Stock, 1999). It can also be expressed in a similar way but using the intensity of X-ray beam, shown in Equation (2.41). The higher the contrast, the better the distinction between two phases in the image:

$$\text{Contrast} = \frac{|sig_f - sig_b|}{sig_b} = \frac{|I_f - I_b|}{I_b} \tag{2.41}$$

where sig and I refer to the signal observed and intensity respectively and f and b refers to feature (sample) and background. Higher energy allows better penetration through materials with higher density while lower energy can lead to better contrast and image quality. Therefore, to determine the optimal energy of X-rays, contrast and the intensity need to be balanced.

The spatial resolution describes how well details of the sample can be imaged and it can be defined as the smallest separation at which two points can be perceived as discrete entities (Stock, 1999). In a 3D volume, the resolution is close to the voxel size.

2.6.2. Types of XMT

XMT can be divided into two main types, namely Micro/Nano focus X-ray cone beam tube sources (Figure 2.17 top) for lab based usage and parallel beam synchrotron radiation sources (Figure 2.17 bottom). Micro focus X-ray tubes generate X-ray by having a stream of electrons with high speed directed at a target material with a high atomic number (Lifshin, 1999; U.S. Geological Survey, 2001). In this system, a projected cone beam is normally used as the point source. The spot size of the X-ray source plays a significant role in a cone beam system. Smaller spot size leads to a more accurate image while larger spot size means that photons hitting a particular pixel can be traced back through different ray paths through the specimen and adds more noise thus reducing image quality (Landis and Keane, 2010). Therefore, the spot size for a commercial CT system is usually a few microns or even smaller.

Using synchrotron radiation as an X-ray source was a significant development to

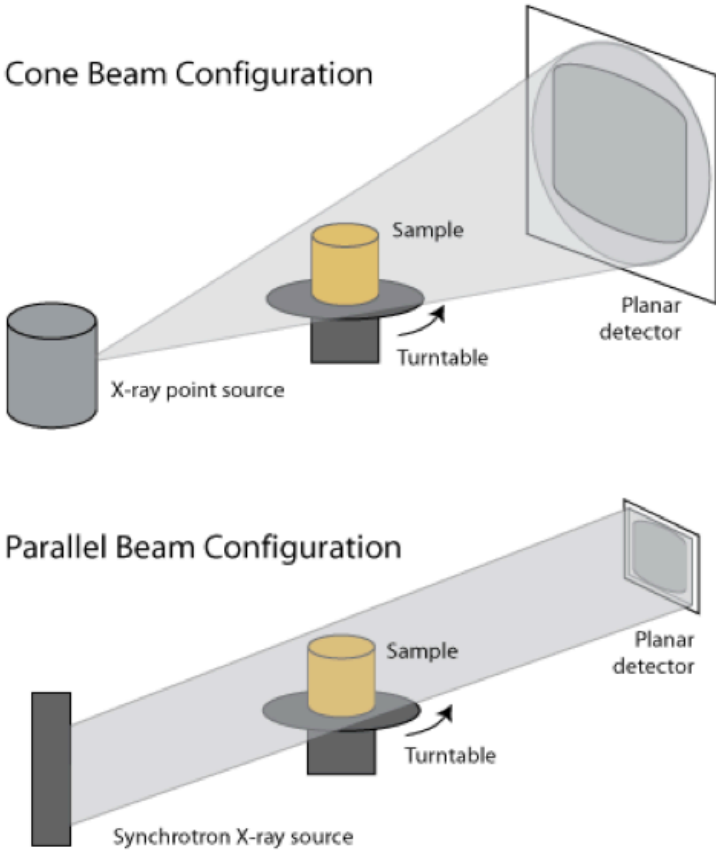


Figure 2.17.: Illustration of two primary experimental approaches to XMT data collection: (a) cone beam and (b) parallel beam (Ketcham, 2011).

enhance image quality (Kinney et al., 1994; Landis and Keane, 2010). Rather than a point source, synchrotron radiation takes the form of a parallel beam of finite cross-section and is produced by using magnets to bend a beam of fast moving electrons (Donath, 2006; Lifshin, 1999). Due to the higher beam flux, the emitted light is many orders of magnitude greater in brightness than a conventional X-ray source, which leads to much higher image contrast. Additional benefits of using synchrotron radiation can include significantly reduced scanning times comparing with a normal laboratory XMT system and a simplified tomographic reconstruction algorithm due to the use of parallel beam, and the tunability of the X-ray energy to a narrow energy band (Donath, 2006; Landis and Keane, 2010).

2.6.3. Artefacts and Partial Volume Effects in Geological Applications

Although the reconstructed 3D volume makes it possible to visually see the internal structure of a material, there are several artefacts and effects that can render the data more problematic and make any quantification more difficult. These include beam hardening, ring artefacts and partial volume effects. Figure 2.18 shows scans through 6-in diameter column of saprolite encased in a PVC pipe, showing scanning artefacts and results of various strategies for remedying them (Ketcham and Carlson, 2001).

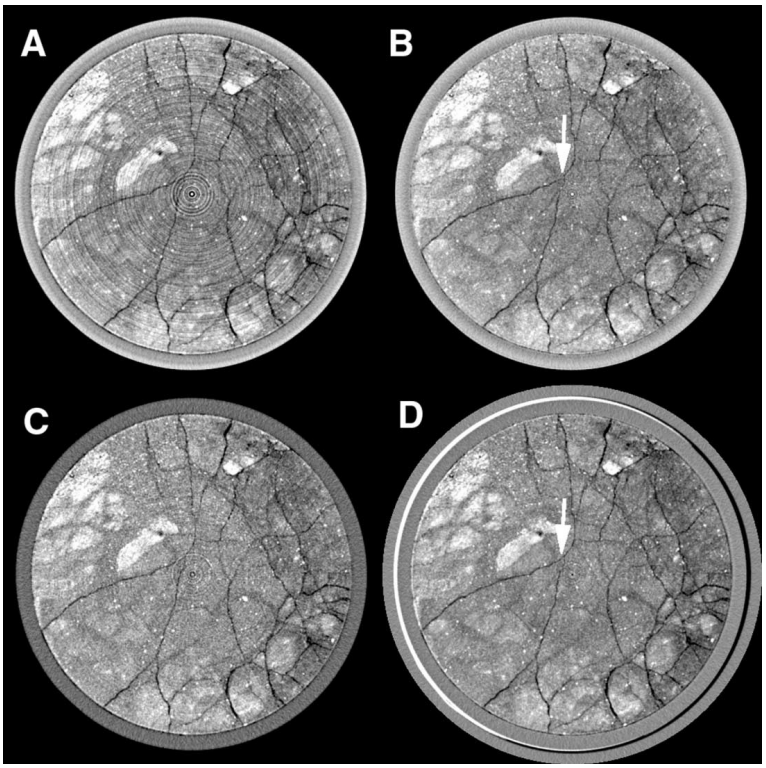


Figure 2.18.: Scans through 6-in diameter column of saprolite encased in PVC pipe, showing scanning artefacts and results of various strategies for remedying them. Scans all represent 1-mm thick slices collected with X-ray source at 420kV and acquisition times of 3 minutes. Scan (A) shows both ring- and beam-hardening artefacts. Latter is visible most obviously as bright ring around outer part of PVC. Image (B) is result of software correction of ring artefacts in (A). Image (C) shows the result of pre-filtering the X-ray beam by passing it through 6.35 mm of brass. Beam-hardening and ring artefacts have been reduced markedly but not totally, and image noise has increased considerably. Scan shown in (D) was done using self-wedge calibration through relatively homogeneous portion of column. Bright rim on left was caused by imperfect centring of column; image of saprolite itself, however, has only very minor ring artefacts and no beam hardening. (Ketcham and Carlson, 2001).

2.6.3.1. Beam Hardening

Beam hardening is one of the most common artefacts encounted in XMT scanning and depends on the incident beam energy spectrum, material composition, shape and dimensions. Beam hardening is caused by the different energy absorption rate within the X-ray energy spectrum. Based on the photoelectric effect, the X-ray absorption is approximately inversely proportion to the third power of the photon energy, which means that lower-energy X-rays are attenuated more readily and absorbed much more easily than higher-energy X-rays (Ketcham and Carlson, 2001; Stauber and Müller, 2008). Figure 2.19 shows a sketch of an example of the beam hardening problem (Stauber and Müller, 2008). Higher energy photons are more difficult to absorb than low energy photons and the mean value of the energy spectrum may shift to a higher value, leading to a higher average energy than the incident beam, which means that the actual attenuation coefficient of any material reduces and makes short ray paths relatively more attenuating than long X-ray paths (Ketcham and Carlson, 2001). It also needs to be noted that in beam hardening, the peak energy always remains the same, but the overall beam intensity is reduced due to the fact that the energy spectrum is changing because of different absorptions along the beam (Stauber and Müller, 2008). In an XMT image, this process can be seen as an artificial darkening at the centre and a brightening near edges, especially when the scanning sample has a roughly circular cross section, shown in Figure 2.18A where a bright ring around the outer part of the PVC tube. In Figure 2.19, line A and line B show the energy spectrum before and after the X-ray beam passed the object, respectively. The peak energy (80 kVp) and the place of the characteristic radiation remain at the same position. The preferential absorption of low energy photons causes the effective energy to shift toward higher values.

Beam hardening is a serious artefact when doing quantification because the apparent attenuation of a material is changed depending on its location. There are several ways to alleviate this artefact. The simplest method is to use a high energy to make the beam hardening effect negligible. However, most geological samples are attenuating enough that beam hardening is noticeable unless the sample is quite small (Ketcham and Carlson, 2001). Selecting a higher energy X-ray beam also needs to be balanced if the phase identification is important. This is because the linear attenuation coefficients for different minerals becomes similar and converge when the energy is high and different phases for different minerals become indistinguishable.

Another possible method is to let the X-ray beam pass through an attenuating filter before it reaches the sample. Filters are normally a piece of metal such as copper and

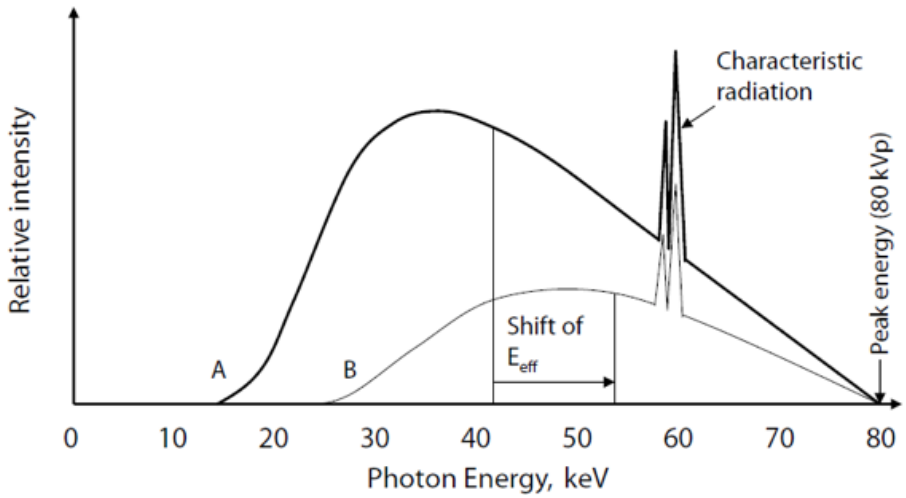


Figure 2.19.: The phenomenon of beam hardening (Stauber and Müller, 2008).

aluminium which can be used to absorb X-ray with low energy and improve the quality of the image by reducing the energy spectrum. The disadvantage of using a filter is that it reduces the overall beam intensity and increases the noise unless much longer acquisition times are used (Ketcham and Carlson, 2001; Stauber and Müller, 2008). Figure 2.18B shows the result of pre-filtering the X-ray beam by passing it through 6.35 mm of brass. Beam-hardening has been reduced markedly but image noise has increased considerably.

Employing a reference material, or a wedge material, of similar attenuation to the sample to calibrate the image is another effective method for alleviating beam hardening artefacts, shown in Figure 2.18D. The reference material should be cylindrical or packed in an attenuating material to achieve an overall cylindrical form to make this method effective (Ketcham and Carlson, 2001). In the latter case, the images could be more noisy due to the packing material. By using the reference material, the XMT image can be corrected by image processing techniques. The polynomial correction method is commonly used (Hammersberg and Mångård, 1998). The scan shown in Figure 2.18D was done using a self-wedge calibration through a relatively homogeneous portion of the column. The bright rim on the left was caused by imperfect centring of the column. The image of the saprolite itself, however, has almost no visible beam hardening artefacts. Note that although centres of Figure 2.18B and Figure 2.18D are similar, the edges of the saprolite are brighter in Figure 2.18B. Thus it is evident that beam-hardening artefact in Figure 2.18B was not confined strictly to edge of the PVC casing, but was a continuous feature within the saprolite as well. Another important advantage of employing a reference material is to normalise the pixel values among different scans, known as image normalisation. This needs to be considered carefully in this work as different scans need

to be compared over the whole leaching period.

2.6.3.2. Ring Artefacts

Ring artefacts can be observed as full or partial circles in the 3D volume around the centre of the rotational axis (Figure 2.18A). The ring artefacts can be caused by a defective pixel on the CCD detector, a defect in the scintillator which converts X-rays to visible light, or dust on the detector (Stauber and Müller, 2008). Among these possible reasons, the defective pixel on the CCD detector, which is normally caused by shifts in output from the detector and finally leads to anomalous values, is the most problematic source (Ketcham and Carlson, 2001).

There are several methods to avoid ring artefacts. If the rings are caused by dust on the detector, it can be easily solved by cleaning the detector. For defective pixels, most ring artefacts can be detected and removed by the software. This method can be achieved before reconstruction where a series of anomalous readings from a detector occurs on a sinogram as a vertical line (Ketcham and Carlson, 2001). In a sinogram, any single point in the scanned object corresponds to a sinusoidal curve. Similarly, ring artefacts can also be detected and removed after reconstruction where the image is converted to polar coordinates and vertical lines can be detected and removed (Ketcham and Carlson, 2001). An example is shown in Figure 2.18B. The main disadvantage of using software to detect and remove ring artefacts is that any roughly linear feature other than real ring artefacts in the sample, which is tangential to a circle centred on the rotational axis, can be removed, blurred or changed (Ketcham and Carlson, 2001). One potential problem caused from this in scanning geological samples is the fractures tracing. This can cause problems in, for instance, identifying fractures in some geological samples. Moreover, as ring artefacts are related to beam hardening, the methods used for alleviating beam hardening, including applying filter, using high energy X-ray beam and applying reference materials, are also helpful in dealing with ring artefacts.

2.6.3.3. Partial Volume Effects

The main cause of the partial volume effect is that the voxel grid does not perfectly align with feature/phase boundaries. Therefore, the actual value for each voxel in the XMT image represents the average of the attenuation of all phases within the voxel. The resolution can also significantly influence the partial volume effect. It is always the case in geological samples where several different phases such as quartz, pyrite and chalcopyrite can exist at the same time. The large size of large geological samples can also

lead to relatively poor resolution. It means that the surfaces and boundaries of different phases cannot be sharply defined. An example of partial volume effects is shown in Figure 2.20, where a core of limestone was scanned and subsequently cut for petrographic analysis (Ketcham and Carlson, 2001). Individual fractures that appear on the scan were measured petrographically and found to have widths that were significantly smaller than the pixel dimensions. After scanning the entire volume, the sample was cut and fractures were measured in thin section. Fractures are visible despite being considerably thinner than pixel width, because of the partial volume effect. Partial volume is one of the most significant artefacts causing uncertainties and errors in analysis. When rescanning the same sample, the location of features relative to the voxel grid can change, resulting in different partial volume effects and associated errors. The errors can be negligible when studying at ore particle scale, but it becomes crucial when studying at metal sulphide grain scale. Understanding these errors us a major area of study in this thesis (see Section 4.5).

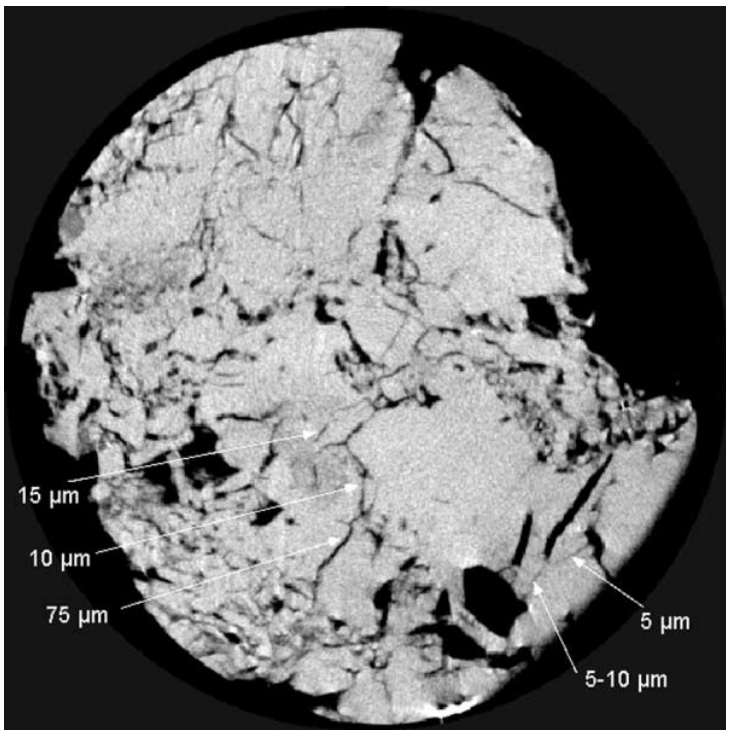


Figure 2.20.: An example showing partial volume effect where cracks with a width of 15 µm or less can not be seen due to blurring of edge voxels. Only the 75 µm crack looks open. Scan field of view is 21.5 mm, and individual pixels are 42 µm on a side. (Ketcham and Carlson, 2001).

2.7. General Image Processing

Image processing can be complex with application-specific procedures, but there are a number of general procedures to treat images before carrying out quantification and data analysis:

- Data conversion
- Intensity normalisation
- Filtering
- Thresholding
- Segmentation/separation

The first three items can also be regarded as image pre-processing. This section briefly introduces the general principle of three image processing steps. Detailed descriptions of some of the specific techniques adapted and developed for this project are described in later chapters.

2.7.1. Data Conversion

The data format of the 3D volume data from the reconstruction process can be float (32 bit), 16 bit signed/unsigned, or 8 bit unsigned. Data conversion is normally carried out to change the data format to a suitable and workable format. The consideration is the size of the image, which can significantly affect the computational time, memory consumption and storage space. Changing a float image to 16 bit unsigned or 8 bit unsigned can speed up processing significantly. However, by choosing images with fewer bits per pixel, the precision is reduced. In this project, the image format after reconstruction is float (32 bit) and all the data sets were converted to 16 bit unsigned for data analysis.

2.7.2. Intensity Normalisation

In image processing, intensity normalisation is a process that changes the range of voxel intensity values according to some rule, for example some reference values. Intensity normalisation of images is an important step when doing image processing analysis. Sometimes, it is difficult to make comparison between two scans due to unstable beams and artefacts. Therefore, image normalisation becomes important to normalise images to the same condition for comparison and quantification.

The intensity normalisation can be achieved if the same reference materials are used for several XMT scans. When normalising an image (Image 2) against a reference image (Image 1) using two reference materials, the image normalisation can be achieved by using the equation:

$$\frac{I_1 - I_{low1}}{I_{high1} - I_{low1}} = \frac{I_2 - I_{low2}}{I_{high2} - I_{low2}} \tag{2.42}$$

where I_1 and I_2 are the voxel intensity of image in Image 1 and Image 2 respectively, I_{low1} and I_{low2} are the intensity of the low attenuating reference material in Image 1 and Image 2, and I_{high1} and I_{high2} are the intensity of the high attenuating reference material in Image 1 and Image 2.

In order to get the intensity of the reference materials, an initial segmentation of the reference materials needs to be carried out. After successful segmentation, the intensity value of the references materials can be obtained using a suitable average for the intensity value within the reference material.

2.7.3. Image Filtering

The XMT data is normally noisy due to many factors, such as low energy or flux, etc., or limited number of projections. Image should be filtered to reduce the noise or enhance the contrast. There are many filtering methods available to adjust these kinds of noise for further analysis. These filters can be divided into two common groups, namely low pass filters to remove high frequencies and high pass filters to remove low frequencies (Stauber and Müller, 2008). A low pass filter is normally used for noise reduction but it also blurs edges. A high pass filter can be used for feature and edge enhancement, but it can increase noise. If the image contrast and resolution is good enough, a low pass filter such as a median filter, is normally good enough for data processing. There are also some more advanced, but more computational expensive filters, such as Gaussian or anisotropic diffusion filters (Stauber and Müller, 2008).

2.7.4. Thresholding

Thresholding, which is a basic but important step in image quantification, is an initial step of segmentation. Thresholding divides the original image into different groups according to voxel intensities or specific functions. It is also sometimes called binarisation, as it sets all voxel values below a threshold value to zero (black) and those above to one (white). The threshold value can significantly affect the accuracy of the quantification.

Global and local thresholding are the two common thresholding categories. One

of the most valuable tools for global thresholding is the voxel intensity histogram. It plots the number of voxels against corresponding intensities. By selecting a threshold value, two target phases can be separated. Histogram based methods usually require distinct separation in the intensity of different phases. Figure 2.21 shows an example of a material made up of aggregate particles, a hydrated and unhydrated cement matrix, and pore space (Landis and Keane, 2010). The peaks of air and solid phases can be easily distinguished. By selecting the threshold value of around 80, a binary image can be created. This simple method is also called global thresholding. There are also several automated thresholding methods based on the histogram. One of the most widely used methods is called the Otsu method (Otsu, 1979).

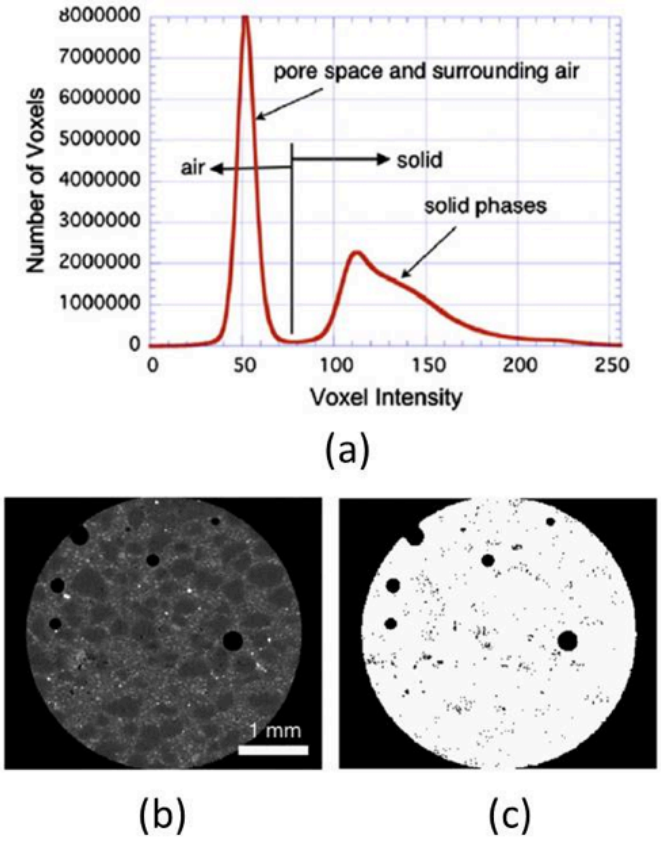


Figure 2.21.: Illustration of a simple image segmentation procedure. The voxel intensity histogram (a) shows peaks corresponding to lower absorption and higher absorption voxels. Recognizing that the lower absorption corresponds to surrounding air and internal void space, a threshold can be set, above which the voxel is associated with solid material. The resulting black and white image, (c), clearly identifies void space in the region delineated in the grayscale image of (b) (Landis and Keane, 2010).

Although global thresholding is commonly used, it becomes problematic when the

contrast of the image is poor or the volume of one phase is far less than the others, which means that the peaks in the histogram cannot be distinguished. This is caused by the overlapping of intensity distributions. Figure 2.22 shows the same example using global thresholding to try to separate aggregate particles, hydrated and unhydrated cement matrix phases using the same data as before. It can be observed that the intensity distributions of the three phases are overlapping. In this case, if the contrast of one phase whose distribution is under another phase's distribution is good enough to locate the phase boundary, global thresholding can still be used but a more complex algorithm is needed to calculate the threshold value (Figure 2.22a).

Another common solution is to use local thresholding methods. The basic theory of local thresholding methods is to have many small volume windows covering the entire image. In each volume window, the threshold value can be calculated individually. Applying gradients or local variance are the most common methods in local thresholding.

2.8. Summary

In this chapter, the heap leaching technique to extract valuable metal, especially copper, has been reviewed. The principles of heap leaching including chemistry and different factors that can affect leach performance have been reviewed and summarised. Most studies of heap leaching have either concentrated on the large scale to understand the macroscopic behaviour or grain scale to study the surface chemistry. A lack of information and understanding of the transport processes within the ore particles makes it very hard to predict heap or even particle scale leach performance based on surface reaction kinetics.

Having a better understanding of leach performance in heap leaching application by applying alternative techniques is the main objective in this study and the application of X-ray micro computed tomography (XMT) has a good potential to achieve this goal. The main advantage of applying XMT is its non-destructive nature, which makes it possible to monitor leach behaviour over the entire leaching period. The fundamentals of XMT and the relevant artefacts with possible solutions are reviewed and discussed. The general principles of image processing before quantification of leach performance have also been introduced with examples.

The current research about heap leaching using XMT and imaging techniques has also been reviewed. The existing barrier is that the imaging quantification is more qualitative and most of the studies did not mention the actual imaging techniques applied. This makes it difficult to fully parametrise the leach behaviour. This can be overcome by

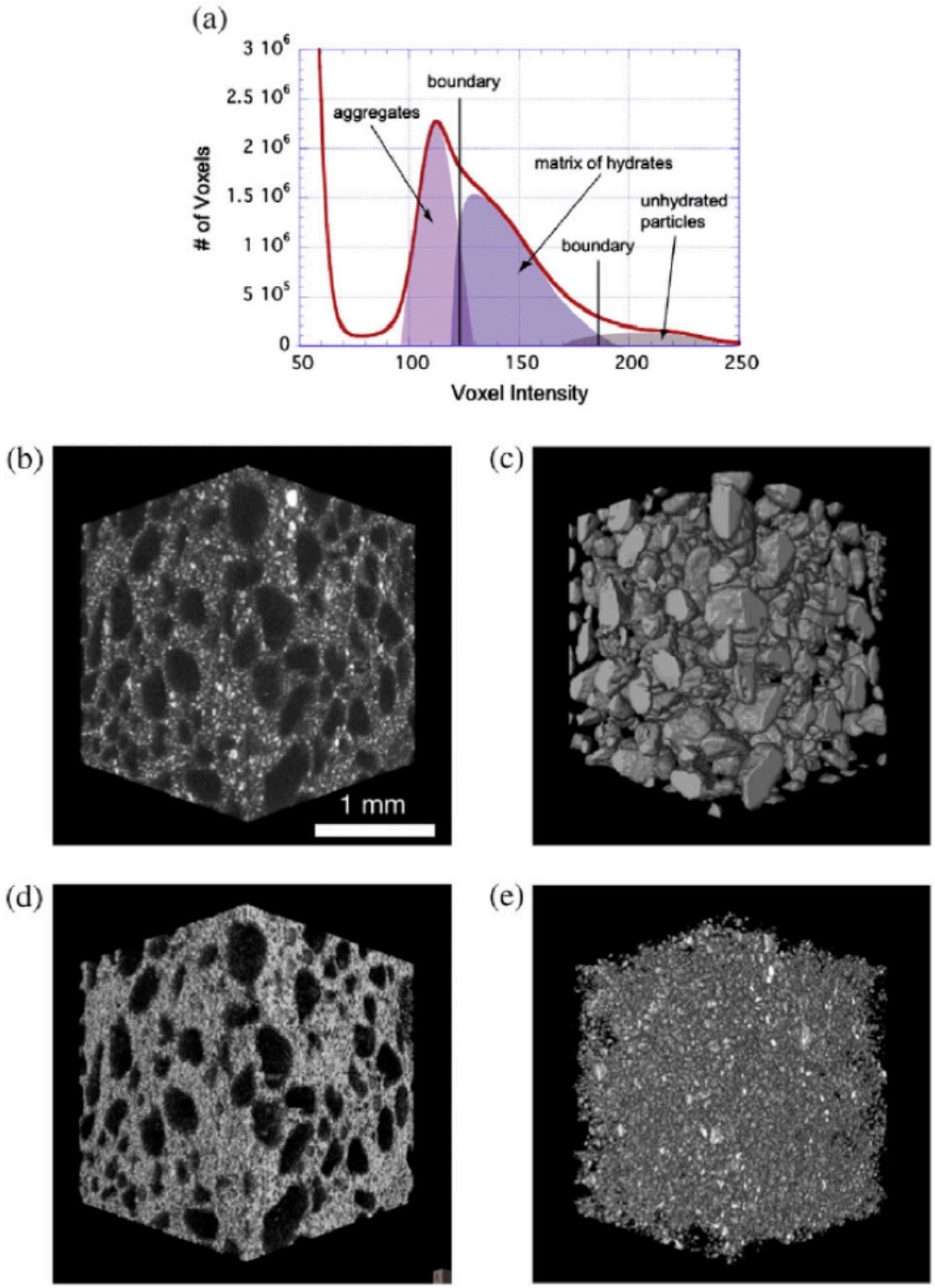


Figure 2.22.: Segmentation of solid phases. The histogram (a) illustrates the approximate overlapping intensity distributions of three different phases. Boundaries are set at voxel intensities where overlap is a minimum, and all voxels with intensities between the boundaries are assumed to be of the particular phase. A 3D rendering of a grayscale volume is shown in (b), and the corresponding aggregates, cement hydrates, and unhydrated particles are shown in (c), (d), and (e) respectively (Landis and Keane, 2010).

developing and applying more advanced algorithms to process and XMT data consistently and analyse the leach behaviour more accurately. The leach performance analysis can also be carried at smaller scales such as individual ore particle scale and mineral grain scale.

Chapter 3

Experimental Methodology for Column Leaching

3.1. Introduction

In order to understand the leach performance by using XMT imaging and quantification, three small scale column leaching experiments were carried out inside an incubator with temperature control in the thesis. The entire leaching period was about 200 days. Each column was scanned frequently using XMT to track the leaching performance followed by image quantification and analysis. In this chapter, the detailed experimental methodology is introduced including sample information, design of experiment, experimental rigs and the leaching solution preparation. In later Chapters, these columns were used as examples demonstrating the development of the 4D automatic quantification algorithms to be used on the reconstructed 3D data sets and the leaching performance analysis.

3.2. Ore Samples

The leaching columns were loadad with ores from the Kennecott Utah Bingham Canyon mine (called Sample K). The ore samples were supplied by the sponsor Rio Tinto (www.riotinto.com). This sample is useful in leaching related study as is a low grade copper ore deposit, containing finely disseminated sulphide minerals, primarily copper (e.g. chalcopyrite) and iron sulphides within a predominantly quartz monzonite host rock (Ilankoon and Neethling, 2013; Lufkin, 2010; Rio Tinto, 2009). The ore body contains both primary copper sulphides such as Chalcopyrite ($CuFeS_2$) and copper

secondary sulphides such as Chalcocite (Cu_2S) and Bornite (Cu_5FeS_4), and the current average copper content is approximately 0.75% (Ilankoon and Neethling, 2013; Lufkin, 2010). Other sulphide species like pyrite (FeS_2) also exist. From a mineral volume perspective, the amount of Fe is much greater than Cu, containing pyrite (4.5 vol%) and chalcopyrite (0.5 vol%), with minor amounts of covellite, chalocite and other Cu-bearing phases (0.6 vol%). The ore particle size for both samples are between 8 and 11.2 mm.

3.3. Copper Content from Sample Decomposition

In order to get the initial copper content of Sample K, representative samples were crushed and milled to a size range of 75 µm to 125 µm. 0.25 g sub samples with two duplicates were taken from the milled samples for decomposition, followed by Inductively Coupled Plasma Optical Emission Spectrometry (ICP-OES) analysis (iCAP 6000 Series ICP-OES Spectrometer from Thermo Scientific). The milled ore samples were decomposed using nitric and perchloric acid. The detailed experimental procedure for sample decomposition process is in Appendix A.1. Table 3.1 shows the results of measured copper content. The details of carrying out ICP-OES measurement is introduced in Section 3.5.3.

Table 3.1.: Measured copper content from ICP-OES.

	Mass	Average copper concentration from ICP	Dilution factor	Total Cu	Cu%
Sample K	0.25 g	195.55 ppm	0.04	0.0020 g	0.78%

The initial Cu content is highly variable from one ore particle to another. The average initial copper content is around 0.7% to 0.8% (Table 3.1). It needs to be noted that this value can only be used to estimate the copper recovery. The actual recovery can be calculated after the experiment finishes. The residue samples need to be decomposed to get the amount of copper that remains in the ore samples. The initial amount of copper is the sum of copper from collected leachate and the copper in residue. The actual copper recovery can then be calculated. However, residual decomposition has not been fully completed in this thesis. All the mineral recovery in later Chapters based on ICP-OES measurements are estimated recovery by assuming the initial copper content is 0.78% (e.g. Recovery shown in Figure 5.2).

3.4. Design of Experiment

3.4.1. Controlling Parameters

Flow rate is the main parameter assessed in this series of experiment. The flow rate of 8 L/m^2/hr (equivalent to ∼80 µL/min in the column system) is a typical flow rate used in industry. This flow rate was halfed and doubled to see the influence. Ferric ion is the main oxidising agent wihch dissolves copper sulphides including chaocopyrite. In order to have a relatively high reaction kinetics wihch allows XMT to capture the leach performance over a relatively short period, the initial Fe^{3+} concentration was designed as 5 g/L. This high Fe^{3+} concentration can also alleviate the bacteria activity. The pH value was designed to be 1 and the details about pH and acid concentration can be found in Section 3.5.

Table 3.2.: Design of column leaching experiment.

Column No.	Rock	Flow rate		Eh (feed)	Temperature
		µL/min	L/m^2/hr		
1	Sample K	160	∼16	700 mV (pure $Fe_3{}^+$)	60 °C
2		80	∼8		
3		40	∼4		

3.4.2. Leaching Solution

In industry, the most common leaching solution is dilute sulphuric acid (H_2SO_4) which can dissolve most copper oxides and secondary copper sulphides. Primary copper sulphides, especially $CuFeS_2$, need a strong oxidising agent in order to be dissolved. In real systems, the main oxidising agent is ferric ion (Fe^{3+}), which is generated by bacterial consumption of pyrite. In this experiment, ferric and ferrous ion sulphate were added into H_2SO_4 as the feed leaching solution to simulate the real heap leaching. According to Córdoba et al. (2008b), acidic leaching solution with more than 5 g/L total iron have been shown to give a relatively fast leaching kinetic.

The 98% AnalaR NORMAPUR analytical reagent H_2SO_4 from VWR International, reagent grade ferric ion sulphate hydrate ($Fe_2(SO_4)_3 \cdot nH_2O$) from Alfa Aesar and de-ionised water were used to prepare the leaching solution. In order to prepare leaching solution with specific range of iron concentration, pH and Eh to give a decent reaction kinetic, the iron content from the raw chemicals ($Fe_2(SO_4)_3 \cdot nH_2O$) needs to be measured

for feed preparation. Iron content from raw $Fe_2(SO_4)_3 \cdot nH_2O$ has been measured using Inductively Coupled Plasma Optical Emission Spectrometry (ICP-OES). The measured Fe% for $Fe_2(SO_4)_3 \cdot nH_2O$ awas approximately 17% (Details shown in Section 3.5.2).

The chemical composition for the high Eh feed is 0.1M H_2SO_4 with calculated 5 g/L total Fe. The target Eh value for the high Eh feed solution is about 700 mV which is contributed by 5 g/L pure Fe^{3+}. The amount of Cu (impurity in the feed solution) and Fe in the prepared feed solution were measured using ICP-OES. Eh values were also recorded. Although the initial Cu (due to impurity), total Fe and Eh can vary among different feed prepared, all the feed data was recorded individually and generally the average total amount of Fe^{3+} for high Eh feed was 5.6 g/L and the average measured Eh values was 680 mV. Table 3.3 shows the recorded pH, Eh, initial Cu and Fe concentrations for feed solutions used in the experiment. The pH and Eh were measured using Mettler Toledo SevenGo portable meter with Mettler Toledo InLab Power Pro pH meter and Mettler Toledo InLab Redox Pro Eh meter.

Table 3.3.: Recorded pH, Eh, initial Cu and Fe concentrations for feed solutions.

Feed No.	pH	Eh (mV)	Cu concentration (ppm)	Fe concentration (ppm)
Batch 1	1.20	700	1.185	5845
Batch 2	1.15	690	1.082	5791
Batch 3	1.18	676	1.075	5663
Batch 4	1.26	678	0.942	5389
Batch 5	1.25	668	0.984	5527
Batch 6	1.25	690	1.158	5313
Batch 7	1.25	675	1.184	5347
Batch 8	1.21	681	0.897	5834
Batch 9	1.21	673	0.942	5711
Batch 10	1.20	671	1.018	5452

3.4.3. Experimental Rigs

A Perspex incubator with heater was designed for the column experiment (Figure 3.1 and Figure 3.2). Insulation was used to maintain the temperature at 60 °C. The temperature controlled heater (Figure 3.3a) can maintain inside temperature at 60±0.5 °C. The feed solution was pumped at prescribed flow rates controlled by a multi-channel Masterflex Peristaltic pump (Figure 3.3b). The leachate from each column was stored in a separate collection vessel. The leachate was not recycled.

The leaching column, shown in Figure 3.4, is made of a glass tube with 28 mm internal diameter and 190 mm height. 500 microns aperture size polypropylene mesh was used on both ends to filter fines and any precipitation which may block tubes. All the

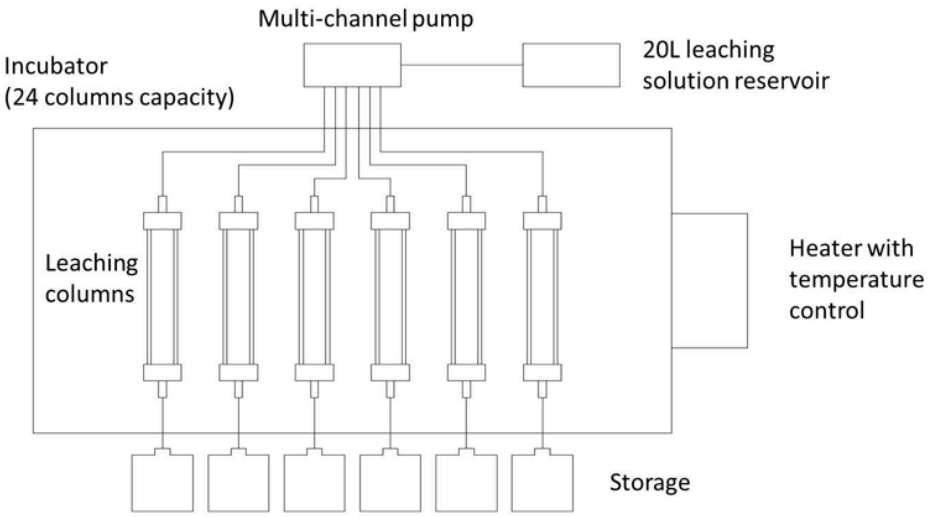


Figure 3.1.: Schematic diagram of the experimental rig for column leaching experiment.

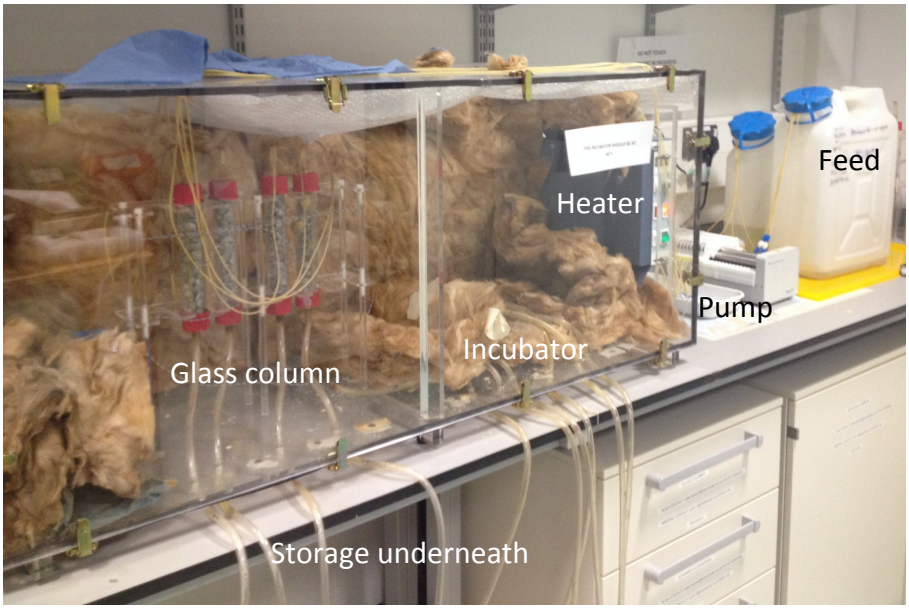


Figure 3.2.: Experimental rig for column leaching experiment.

materials used to make the columns are suitable for dilute acid at 60 °C. Each column was filled with 136 g samples (Figure 3.5). At each scanning time point (sampling point), pH, Eh and total volume of solution collected from each column were measured and recorded.

3.4.4. Multi-channel Peristaltic Pump for Flow Rate Control

Figure 3.3 shows the 24 channels pump used for flow rate control. All the channels were controlled by a single roller and the flow rate range for each channel was between

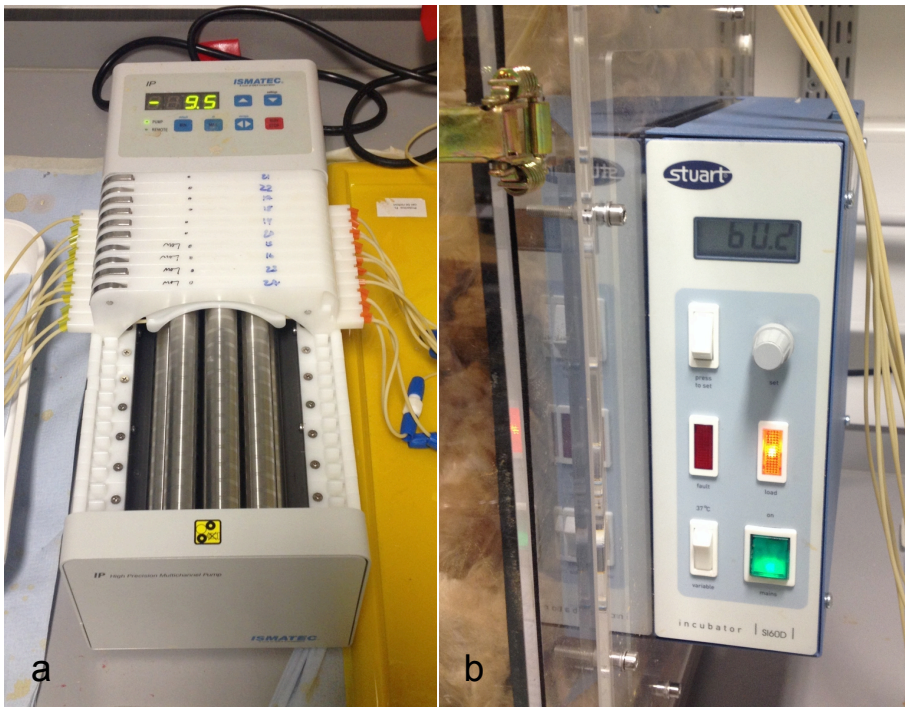


Figure 3.3.: Temperature controlled heater and multi-channel peristaltic pump for column experiment.

0.0004 ml/min and 11 ml/min. In order to achieve three different rates, the flow rates were calibrated to 40 µL/min. High flow rate can be achieved by having more than one tube. After calibration, the RPM was fixed at 9.5 and the flow rate for the 14 channels are listed in Table 3.4. It can be observed that the differences among different channels were around ±1.5 µL/min. The material of tubing connecting the pump and the leaching columns was PharMed BPT, which had excellent acid resistance and is suitable for 60 °C working environment. In the actual experiment, each time when reloading the columns back into the incubator after XMT scanning, the channels for each column were randomly selected.

3.5. Feed Composition for the Leaching Experiment

This section outlines the procedure for producing the feed solutions, which need to have a pH of close to one and Eh value close to ∼700 mV vs. SCE.

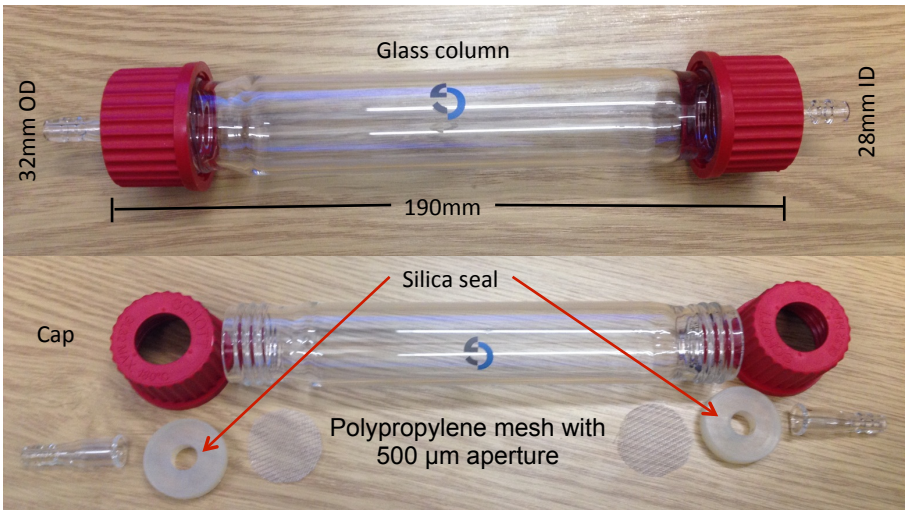


Figure 3.4.: Glass leaching column.

Table 3.4.: Calibration of multi-channel peristaltic pump.

Channel	RPM	Time period (min)	Water mass (g)	Flow rate (µL/min)
1	9.5	60	2.503	41.72
2			2.423	40.38
3			2.398	39.97
4			2.454	40.90
5			2.439	40.65
6			2.438	40.63
7			2.425	40.42
8			2.387	39.78
9			2.376	39.60
10			2.365	39.42
11			2.471	41.18
12			2.39	39.83
13			2.474	41.23
14			2.421	40.35

3.5.1. pH and Acid Concentration

In order to achieve a pH of around 1 using sulphuric acid, 0.1M sulphuric acid solution was produced by diluting 98% analytical grade sulphuric acid solution (Molar mass: 98.08 g/mol, density: 1.84 g/cm^3). 5.439 ml of 98% sulphuric acid was taken by pipette and diluted with de-ionised water to produce 1 L of solution. The pH of the solution was

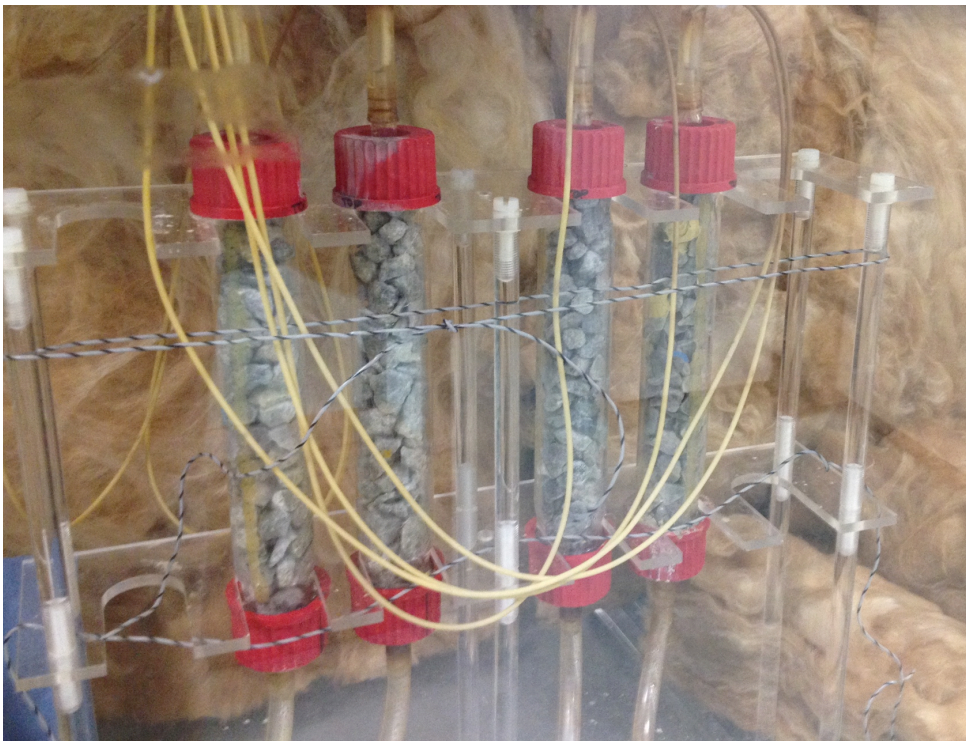


Figure 3.5.: Glass leaching column with ore samples.

measured by a pH meter. After making 0.1M H_2SO_4, 1 ml of 0.1M H_2SO_4 was taken for acid titration, using 0.5M sodium hydroxide (NaOH with molar mass 40 g/mol) solution and methyl orange as indicator, to ensure the 0.1M is correct. The procedure for this titration can be found in Appendix A.2.

Each time, the initial volume (V_1 ml) and the final volume (V_2 ml) were recorded when the colour changes from red to orange. It needs to be noted that when using methyl orange as an indicator for strong acid and base, the titration should be stopped when the very first trace of orange occurs in the solution to avoid getting further from the equivalence point. The reaction is:

$$H_2SO_4(aq) + 2\,NaOH(aq) \longrightarrow Na_2(SO_4)_3(aq) + 2\,H_2O(aq) \tag{3.1}$$

Every 2 moles of NaOH reacts with 1 mole of H_2SO_4. The molar concentration of H_2SO_4, C, can be calculated according to equation:

$$C = \frac{0.5M \times (V_2 - V_1)\text{ml}}{1\text{ml} \times 2} \tag{3.2}$$

The results of making 0.1M H_2SO_4 is shown in Table 3.5.

The sulphuric acid concentration can be ensured as 0.1M and 0.105M in test one can

Table 3.5.: Results of sulphuric acid titration using sodium hydroxide solution and methyl orange as indicator.

Test number	pH before titration	Volume of sulphuric acid (ml)	V1 (ml)	V2 (ml)	C (M)
1	1.01	1	2.5	2.92	0.105
2			3	3.4	0.1
3			3.6	4	0.1

be caused by the error of reading volume in burette. It also needs to be noted that the pH measured here was pure H_2SO_4, when preparing leaching solution by adding ferric and ferrous sulphate, the pH may change slightly. However, the pH should still be controlled to around 1 and the composition of chemicals needs to be fixed.

3.5.2. Calibration of Iron Concentration from Raw Chemical Reagents

The specifications of the iron content of ferric sulphate hydrate based on the catalogue is shown in Table 3.6. However, both $Fe_2(SO_4)_3 \cdot nH_2O$ and $FeSO_4 \cdot 7\,H_2O$ can absorb water when they are exposed to the atmosphere. The actual iron percentage can thus be lower than the theoretical calculation. Therefore, in order to get a more accurate result, the actual iron concentration from the raw materials needs to be validated. The way to validate this value is to pick a certain amount of raw material and dilute to a suitable iron concentration range for ICP-OES measurement according to the nominal iron content shown in the catalogue, followed by ICP-OES measurement to measure the actual iron contained in the solution. As ICP-OES is accurate when the concentration is between 0 and 20 ppm, the samples were diluted to approximately 15 ppm (0.015 g/L). Based on the nominal iron percentage from catalogue, the calculated amounts ferric sulphate hydrate was 0.07 g/L. The validation is also duplicated to ensure the results are repeatable. The experimental procedure for this validation can be found in Appendix A.3. The actual measured iron concentration from the raw chemicals was 17.65%, shown in Table 3.7.

Table 3.6.: Iron concentration based on VWR catalogue.

	Nominal percentage	Iron percentage	Selected Fe% for calculation
$Fe_2(SO_4)_3 \cdot nH_2O$	21.0 to 23.0% (Based on Fe^{3+})	21.0 to 23%	22%

Table 3.7.: ICP-OES results for iron concentration in analytical reagents.

Sample	Description	Iron concentration	Iron percentage in reagent	Average iron concentration
1	0.07 g $Fe_2(SO_4)_3 \cdot nH_2O$ in 2 L in nitric acid (2M)	6.12 ppm	17.48%	17.65%
2	0.14 g $Fe_2(SO_4)_3 \cdot nH_2O$ in 2 L in nitric acid (2M)	12.47 ppm	17.81%	

3.5.3. Inductively Coupled Plasma Optical Emission Spectrometry

Inductively Coupled Plasma Optical Emission Spectrometry (ICP-OES) is an analytical technique used for metal detection to measure the metal concentration within the solution. The ICP-OES facility can be easily accessed within Imperial College.

The copper and iron concentration within the solution is measured using iCAP 6000 Series ICP-OES Spectrometer from Thermo Scientific. When measuring multiple elements concentrations, chemical and spectral interferences can affect the accuracy of the result as they can present as a suppression or enhancement of the detected signal. One of the most common methods to alleviate or negate the interferences is the background correction. This background interferences can be defined by the wavelength of each element. As Cu and Fe are the two elements being measured, it needs to be ensured that the presence of both metals will not interfere with the measurements and that the intensity for each measured element is high enough. Appendix A.5 shows the interferences for the selected Cu (Cu2247) and Fe (Fe2382). It can be seen that the intensity for the measured elements are much higher than the others and each of the measured elements does not exist in the interference table.

ICP measurements use calibration standards with known elements' concentrations to calculate the concentration for the prepared solution. In order to get accurate results, the most important steps is to prepare accurate calibration standards. In ICP-OES measurements, in the solution with relatively low concentration there is a linear relationship between measurement intensity and concentration (ppm). Figure 3.6 shows the actual ICP-OES calibration curves for both Cu and Fe measurements for the leaching experiment. During the measurement, the calibration standards are measured and plotted first, the element intensity for the prepared solutions are then measured and the concentration (ppm) calculated according to the plotted linear relationship. In this experiment, the calibration standards are made with 1000 ppm Cu and 1000 ppm Fe solution from VWR,

both in a HNO_3 matrix. The calibration standards are diluted and prepared with 2M HNO_3 (prepared using analytical grade 70% HNO_3), the standards are (recipe shown in Table 3.8):

- Blank solution (2M HNO_3 only)
- 1 ppm (both 1 ppm Cu and 1 ppm Fe in 2M HNO_3)
- 5 ppm (both 5 ppm Cu and 5 ppm Fe in 2M HNO_3)
- 20 ppm (both 20 ppm Cu and 20 ppm Fe in 2M HNO_3)
- 50 ppm (both 50 ppm Cu and 50 ppm Fe in 2M HNO_3)

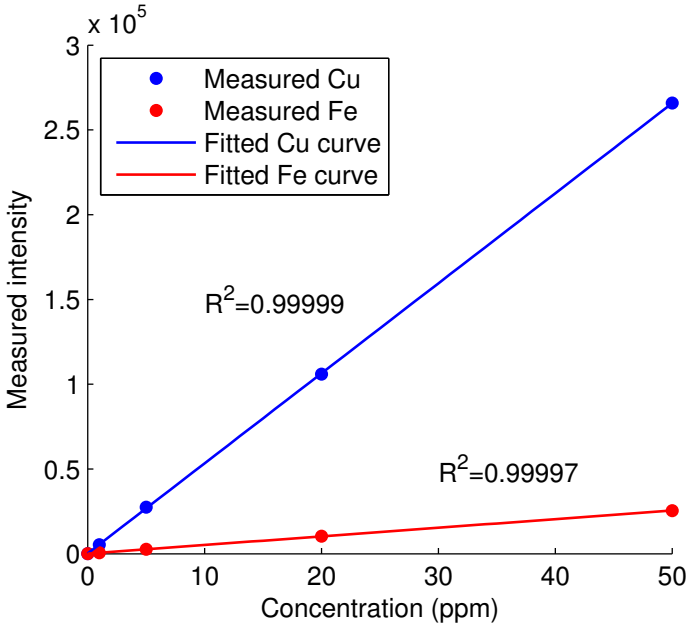


Figure 3.6.: Plot of linearity relationship in ICP-OES calibration standards measurements.

Table 3.8.: Amount of 1000 ppm Cu/Fe solution for ICP-OES calibration standards.

Standards	Amount of Cu (1000 ppm)	Amount of Fe (1000 ppm)	Total volume
Blank	0 µL	0 µL	
1 ppm	50 µL	50 µL	
5 ppm	250 µL	250 µL	50 ml
20 ppm	1000 µL	1000 µL	
50 ppm	2500 µL	2500 µL	

3.6. Summary

In order to use XMT to quantify leaching behaviour, a number of leaching columns were set up inside an incubator with temperature control. Three columns with different flow rate values were used in this thesis. The leaching solution is the 0.1M H_2SO_4 with a certain amount of Fe to achieve the target Eh value. The total amount of Fe was set as a higher value to give a reasonably fast reaction kinetics. All the metal concentration within the collected solution is measured by ICP-OES.

Chapter 4

4D Automatic Quantification of Ore Particles

4.1. Introduction

To understand leach behaviour in a more quantitative way, it is crucial to have a consistent methodology for processing the image data sets and an understanding of the errors and uncertainties. Table 4.1 shows the main steps and difficulties in carrying out efficient and consistent 4D image quantification (time series of three-dimensional images), as well as the platform used. For instance, the individual ore particles need to be identified, which is easy early in the leaching cycle, but became more challenging as deposits of, for instance, Jarosite appeared between the particles. The particles in the column also shifted and rotated over the course of the leaching period, which needed to be accounted for in the comparisons between time steps. The same mineral grains across different images also needed to be identified, which is complicated by the fact that they change size and can even disappear.

In this chapter, after describing the XMT system and scanning settings used for the leaching experiment (see Section 4.2), a full series of image processing steps for 4D quantification were developed to fully quantify the leach performance at mineral grain scale within ore particles (see Section 4.3). In particular, a novel mineral grain tracking algorithm (see Section 4.4) was introduced showing how the evolution of the thousands of individual mineral grains within the ore particles can be tracked over time. By using the mineral grain tracking algorithm, the studies of imaging based measurement errors and its related uncertainties can be carried out to have a better understanding of the relevant errors (see Section 4.5). A novel method for threshold value correction and

Table 4.1.: Main steps and difficulties in order to carrying efficient and consistent 4D image quantification.

Main image processing steps	**Challenges**	**Platform**
Thresholding, segmentation and labelling of each ore particle	Identifying separate ore particles when there is deposition between ore particles (e.g. Jarosite or elemental sulphur).	Matlab & Avizo
IDL centroid tracking to identify same ore particle in different scans	Ore particles move and rotate between scans.	Matlab
Registration of same ore particle in different scans		Avizo
Thresholding of mineral grains	No clear peaks in histogram, a more advanced algorithm needs to be used. The uncertainty and error are difficult to be quantified, which affects small particles a lot.	Matlab
Connectivity analysis and labelling of each mineral grains		Matlab
Quantification of each ore particles	Fast algorithms are needed for calculating metal sulphide particle size distribution (3D volume, 3D surface, etc.), distance map, particle tracking, etc..	Matlab
Grain tracking and quantification	Large number of particles need to be checked: need fast algorithm. Particles shape will change due to leaching, part of them will be completely dissolved.	Matlab

image calibration was developed and introduced based on the error analysis from the grain tracking results (see Section 4.6). Different threshold methods can also be compared quantitatively (Section 4.7).

4.2. X-ray Computed Microtomography (XMT)

4.2.1. X-ray CT Systems

All the the columns were scanned using a Nikon Metris Custom Bay (Figure 4.2). Figure 4.1a illustrates the XMT system. The X-ray source is a 225 kV microfocus with 3 µm reflection target. The XMT system is configurable with high resolution 2000×2000 pixel Perkin panels as detector Figure 4.1. The actual system uses a room as a cabinet instead of a small cabinet (Figure 4.2).

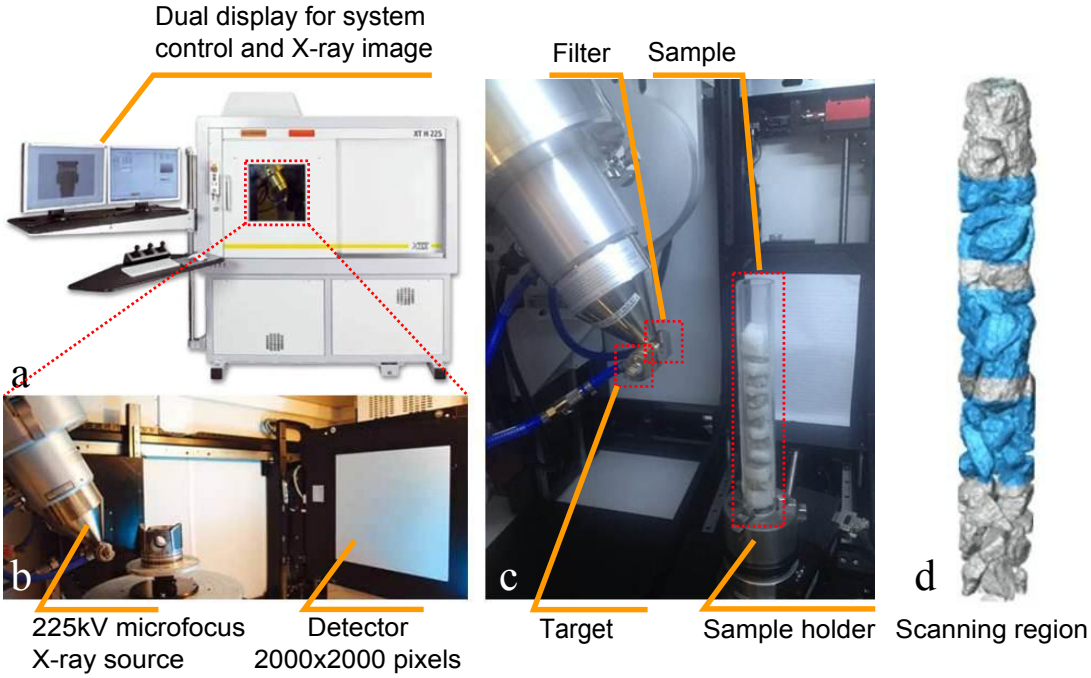


Figure 4.1.: Illustration of XMT system: (a) Picture of the XMT system with small cabinet. (b) Internal view of the XMT system. (c) X-ray source with samples on the sample holder. (d) Schematic figure showing the scanning region (blue) for each column.

Three volumes (top, middle and bottom) were scanned for each column. Figure 4.1d Each column was scanned frequently over the entire leaching period. Table 4.2 shows the actual scanning time points for the column leaching experiment. It needs to be noted that any day number used in the chapter, as well as in later chapters, is the total number

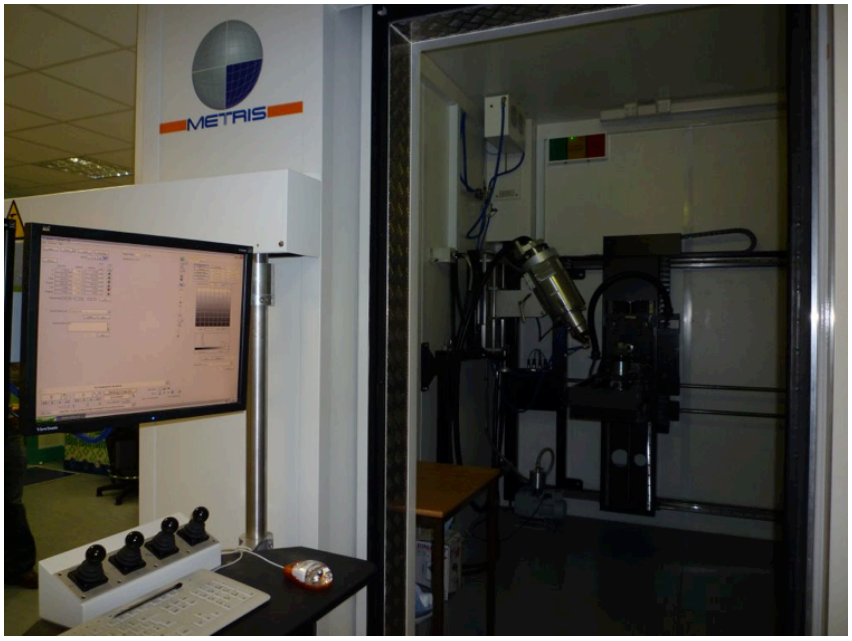


Figure 4.2.: Photo of Nikon Metris Custom Bay.

of leaching days (end of the last day) before the XMT scanning. The scanning settings are summarised in Table 4.3. The 1 mm aluminium filter was used to reduce the effect of beam hardening and noise caused by low level energy. The resolution is approximately equal to the size of the object divided by the number of pixels across the detector which gives a linear resolution of approximately 17 microns for the columns with a 28 mm internal diameter.

Table 4.2.: Scanning time points for the column leaching experiment.

Column No.	Scanning point (end of leaching day)												
1													
2	0	1	5	11	16	23	33	43	53	83	118	136	168
3													

4.2.2. Centre of Rotation Determination and Image Reconstruction

The reconstruction algorithm expects the projection images to be perfectly aligned vertically and centred on the rotation axis, but this is not always possible to achieve. Therefore, before generating a 3D volume image from the acquired series of 2D projections, one of the main steps is calculating the centre of rotation of the image series

Table 4.3.: The main scanning settings for column leaching.

Energy	89 kV
Exposure time	0.708 s
Projections	2001
Filter	1 mm Al
Detector size	2000×2000 pixels
Resolution	~17 microns (consistent magnification)

accurately as this is the most important step determining the image quality (Figure 4.3). Centre of rotation problems arise due to the rotation of the object not being exactly on the X-ray source to detector midpoint axis. Therefore, the 2D projection images need to be shifted and sheared correctly before applying the reconstruction algorithm. In the reconstruction software supplied by Nikon, two test slices are reconstructed and the sharpness of the reconstructed images are assessed to determine the centre of rotation. The projections are then shifted to one side by a pixel and the test slices are reconstructed again. The sharpness of the slices is reassessed to estimate the next required shift. This iterative movement and reconstruction are repeated until the slices have reached the desired quality.

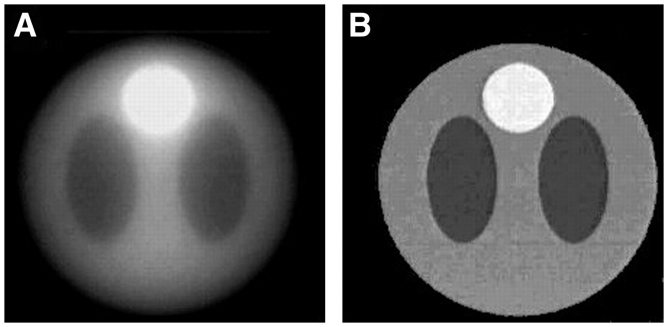


Figure 4.3.: Examples of two slices reconstructed with different centre of rotation (Goldman, 2007).

Normally, the two test slices selected are near the top and bottom of the region of interest. The calculated value for these two slices thus indicate the misalignment at the top and bottom of the image, and thus the shift and shear needed to correct all of the projections for the entire volume can be calculated. For the column leaching experiment, the centre of rotation determination process for all the scans was done automatically using the software supplied by Nikon.

In the final reconstruction stage, the entire volume with dimension of 2000×2000×2000

pixels was reconstructed at full resolution. Figure 4.4 shows an example slice for a scanned leaching column from the reconstruction data.

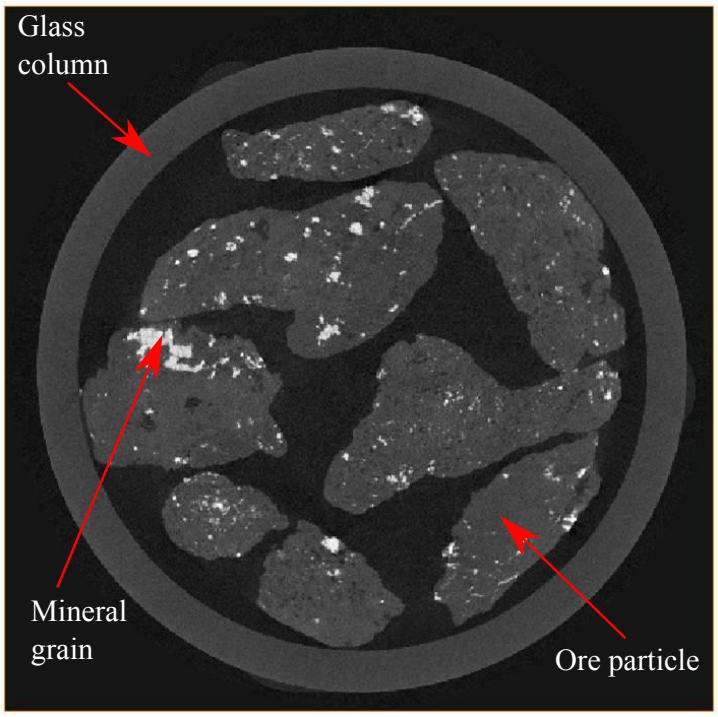


Figure 4.4.: Example slice of a scanned leaching column from a reconstruction image.

4.3. Image Processing

One of the main advantages of using XMT for leaching related research is that it allows the leach behaviour to be quantified and tracked through time based on a large number of 3D volume data sets. As each 3D volume data set has to be processed separately, the consistency of image processing becomes important to make individual result from image processing comparable. Therefore, consistent algorithms need to be applied to each image processing steps. Moreover, to deal with large numbers of 3D data sets efficiently, all the algorithms need to be fully automated. In this section, detailed algorithms and methods for each image processing step are introduced with examples.

4.3.1. Image Pre-processing

After each 3D volume was produced, the data had a 3×3×3 median filter to reduce the noise level. The data sets were then normalised based on the intensity of the back-

ground peak, I_1, and the intensity of the ore peak, I_2 (the intensity of background peak is always smaller). The normalised intensity for each pixel, I_{New} can be calculated as:

$$I_{\text{New}} = \frac{(I_2 - I)\, I_{\text{Low}} + (I - I_1) I_{High}}{I_2 - I_1} \tag{4.1}$$

where I is the original voxel (smallest volume element, equivalent to a 3D pixel) intensity, I_{Low} is the reference intensity for the background peak and I_{High} is the reference intensity for the ore peak.

In this particular case, the normalisation process is mainly for better visualisation. The analysis, especially the thresholding, will not be affected as the threshold values calculated from the algorithms represent the threshold position relative to the entire histogram range.

4.3.2. Thresholding, Segmentation and Labelling of Ore Particles

Global thresholding based on the histogram can be used to threshold between different phases when there are distinct peaks in the histogram. This is the case for the air and the gangue within the ore particle (the glass column has essentially the same grey value as the ore particles), where the peaks are quite distinct (Figure 4.5). However, there is no clear peak for metal sulphide grains as its peak value has similar counts to the noise within the ore phase. More advanced methods need to be used to distinguish the sulphide grains, which will be discussed in later sections.

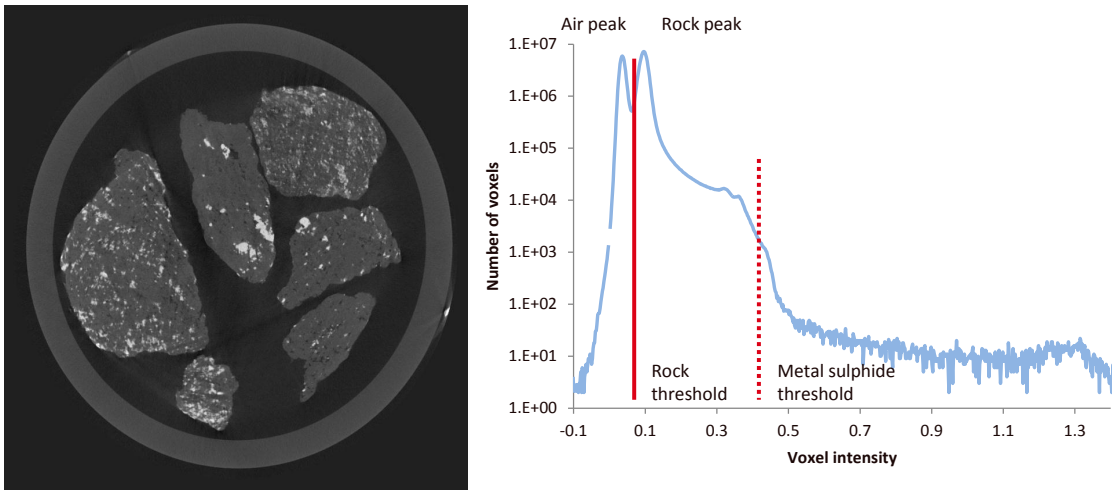


Figure 4.5.: The histogram of a typical scanning volume with estimated thresholding values for ore and metal sulphide grains.

Histogram based global thresholding using the Otsu algorithm (Otsu, 1979) was used to threshold the rock phase within the ore particles from the background air, followed by a hole filling algorithm. After thresholding, there are voxels (with value of 0) surrounded by white voxels (with value of 1) inside rock phase, this is mainly due to noise within the image. Those voxels can cause problems in later particle separation as it can dramatically change the 3D gradient map. The hole filling algorithm fills the holes inside particles after thresholding. A binary image was then generated for all the ore particles (Figure 4.6a and Figure 4.6b). The Otsu algorithm minimises within-class variances, which is the same as maximising between-class variances (Gonzalez et al., 2003). Within-class variances, σ_W^2, can be defined as:

$$\sigma_W^2(T) = \omega_B(T)\sigma_B^2(T) + \omega_O(T)\sigma_O^2(T) \tag{4.2}$$

$$\omega_B(T) = \sum_{i=0}^{T-1} p(\mathrm{i}) \tag{4.3}$$

$$\omega_O(T) = \sum_{i=T}^{N-1} p(i) \tag{4.4}$$

$$\sigma_B^2(T) = \text{the variance of the pixels below the threshold} \tag{4.5}$$

$$\sigma_B^2(T) = \text{the variance of the pixels above the threshold} \tag{4.6}$$

where $p(i)$ is the probability of the two classes being separated by intensity level i and [0, N-1] is the range of intensity levels. Between-class variances, σ_O^2 can then be defined by subtracting the within-class variance from the total variance of the combined distribution. The optimal threshold value can be determined by maximising σ_O^2.

$$\sigma_B^2(T) = \sigma^2 - \sigma_W^2(T) = \omega_B(T)[\mu_B(T) - \mu]^2 - \omega_O(T)[\mu_O(T) - \mu]^2 \tag{4.7}$$

where

$$\mu_B(T) = \sum_{i=0}^{T-1} i[p(i)]/\omega_B \tag{4.8}$$

$$\mu_O(T) = \sum_{i=T}^{N-1} i[p(i)]/\omega_O \tag{4.9}$$

$$\mu(T) = \sum_{i=0}^{N-1} i[p(i)] \tag{4.10}$$

After the rock phase thresholding and hole filling steps, some of the ore particles were

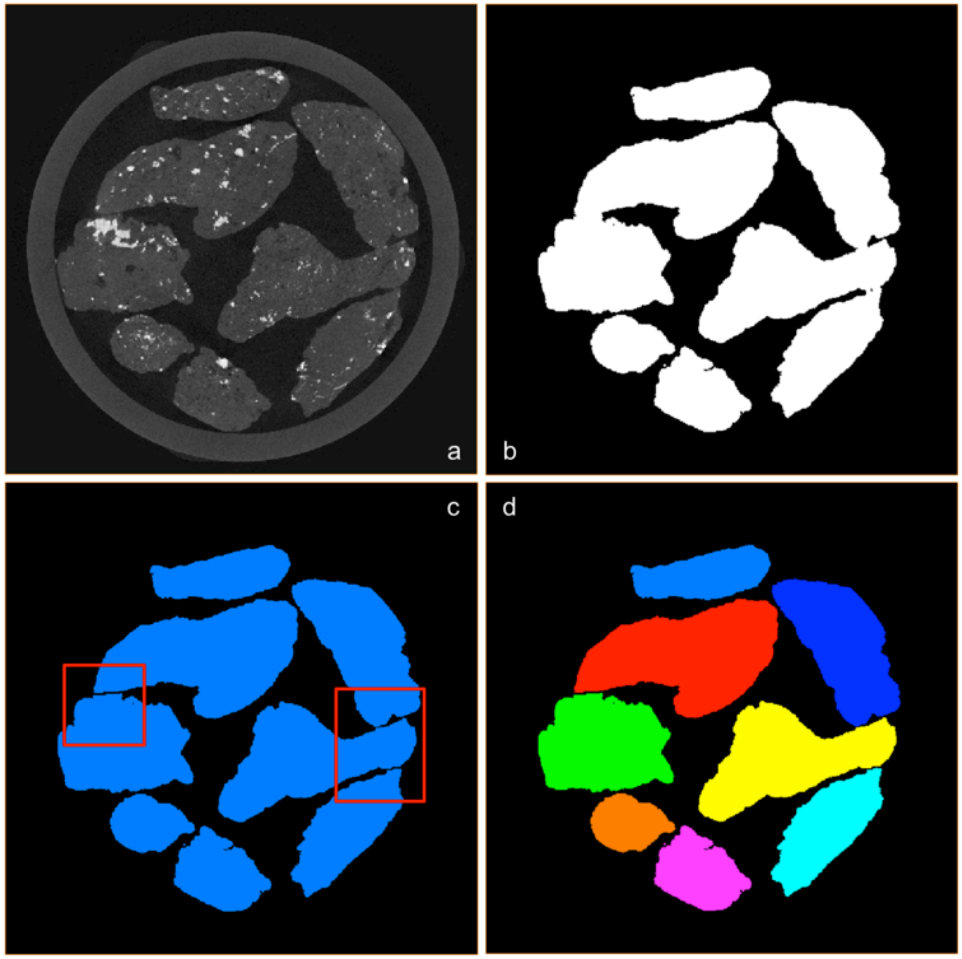


Figure 4.6.: An example slice from a volume data showing the results of thresholding, separation and labelling: (a) A slice showing the raw image from reconstruction. (b) The same slice showing the extracted rock phase after applying Otsu algorithm. (c) The same slice showing separated individual ore particles based on watershed and marker control based algorithm. (d) The same slice after labelling individual ore particles.

connected (Figure 4.6b). In order to label individual particles, the connected ore particles were then separated by applying a distance map and marker control based 3D watershed algorithm. This step is crucial in the automation as after rock phase thresholding there will be particles in contact with others (Figure 4.6c), which is due to the actual physical contact and the deposition (e.g. Jarosite) that occurs during leaching between particles. After particle separation, flood-filling was then used for connectivity analysis in order to identify individual ore particles which are not connected with others. Each particle is then assigned a unique label (Figure 4.6d). The flood-fill based connectivity analysis was applied with 18 neighbours.[1].

[1] 3-dimensional connectivity: 6-connected pixels are neighbours to every pixel that touches one of their

Figure 4.7 shows an example of particle separation using the watershed separation method. A 3D distance map can be calculated from the binary image of the ore particle by assigning a value depending on the distance between each pixel and the nearest nonzero-valued pixel. The boundary voxels of the object are assigned a value of zero and the assigned value increases as the distance increases. The watershed algorithm is a widely used and powerful technique in image processing, especially for automated separation (Visualization Sciences Group, 2011). It expands the region according to the 3D distance map, until the regions touch the watershed lines (Figure 4.8). One of the common problems using watershed separation is over segmentation (normally indicated by straight lines within the particle). This problem can be overcome by applying local markers (Figure 4.9), which calculate and merge local maxima values to ensure a single object will not be split. Figure 4.6d shows the separated ore particles after watershed separation. Note that while Figure 4.6 and Figure 4.7 show 2D slices, all these algorithms are carried out in 3D.

4.3.3. Particle Tracking and Registration of Ore Particles

To make all the quantification algorithms fully automated, one of the most difficult aspects is the ore particle tracking. When scanning the same volume at different time points, the particles change location due to both the ore particle movement as they settle over time and slightly different orientations of the column when placed onto the sample holder. The location of each particle may be rotated and/or shifted between time points. After labelling, the same particle in different scans may therefore have different label numbers (Example shown in Day 0 and Day 136 in Figure 4.10). Therefore, ore particle tracking needs to be carried out to find the same ore particle in different scans so that it can be relabelled to have the same label number across the entire time sequence.

The centroid tracking algorithm, which is based on the calculation of the mass centre (centroid) for all the ore particle, was used to identify the same ore particle in different scans (Blair and Dufresne, 2008; Crocker and Grier, 1996). The mass centroids of individual ore particles in different scans were calculated separately. By setting up an estimated maximum distance for centroids to move, the new location of each centroid was matched up by looking for the most likely correspondence in later scans. Figure 4.10 shows an example of a leaching column scanned after 136 days to compare to its initial condition. Different colours represent different particle labels. It can be seen that after particle tracking and relabelling, all the particles have been identified correctly. How-

faces. 18-connected pixels are neighbours to every pixel that touches one of their faces or edges. 26-connected pixels are neighbours to every pixel that touches one of their faces, edges, or corners.

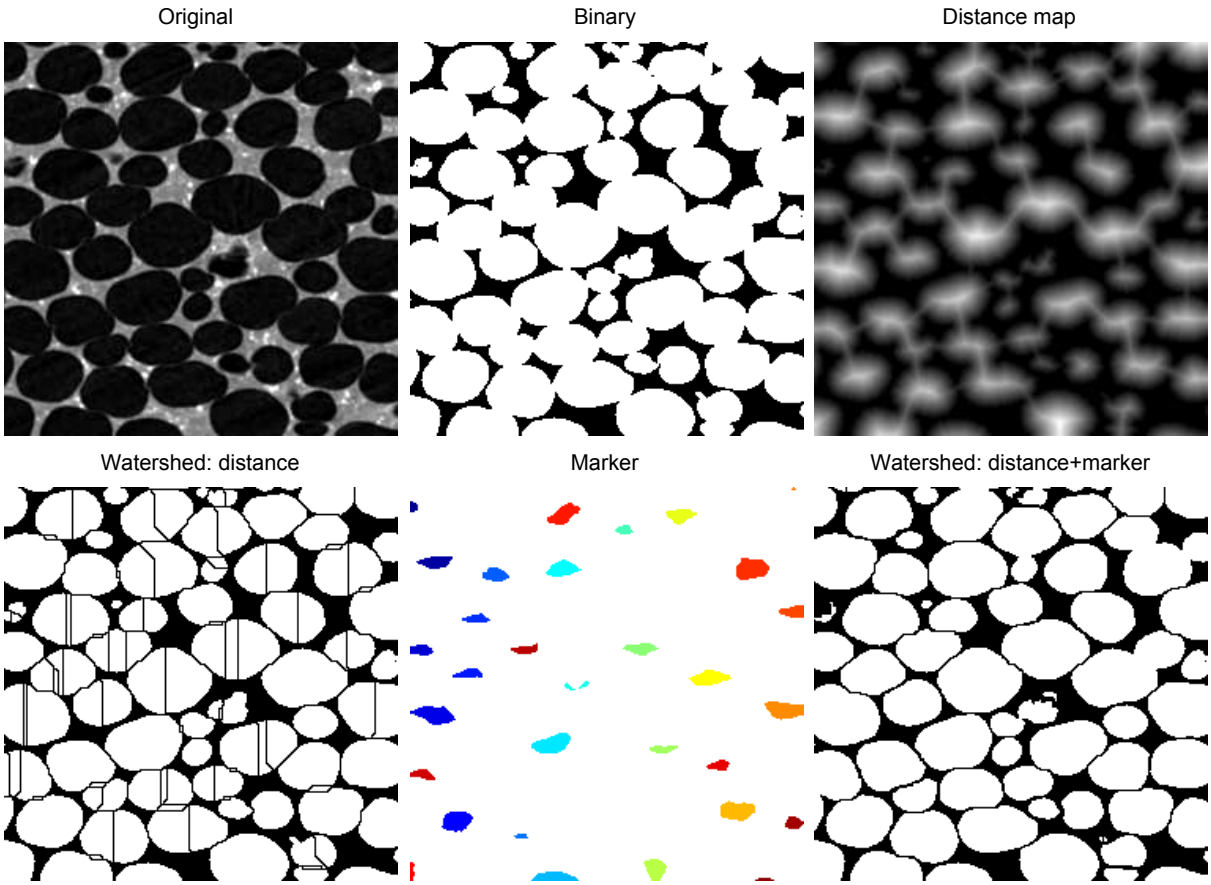


Figure 4.7.: The principle of distance map and marker control based watershed algorithm to separate connected objects.

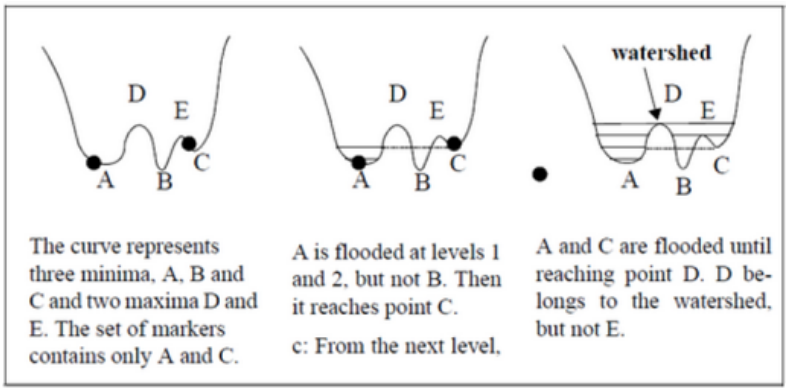


Figure 4.8.: Principle of watershed algorithm.

ever, it needs to be noted that the tracking code only allows a certain movement of each centroid.

Registration, or alignment of images is a process of transformation of different images into the same coordinate system. Each tracked ore particle in different scans was

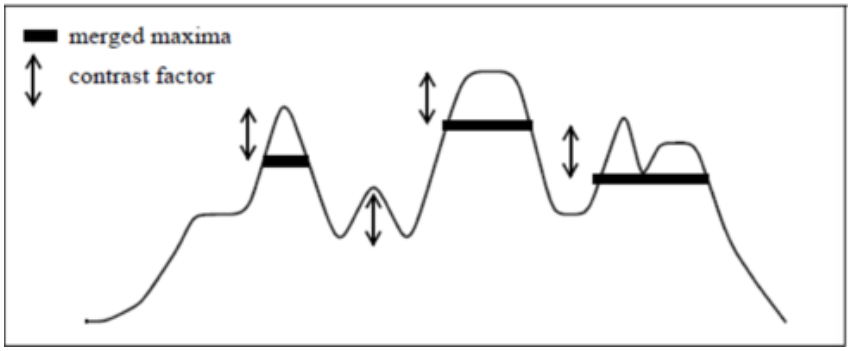


Figure 4.9.: Principle of merging local maxima for maker control watershed separation.

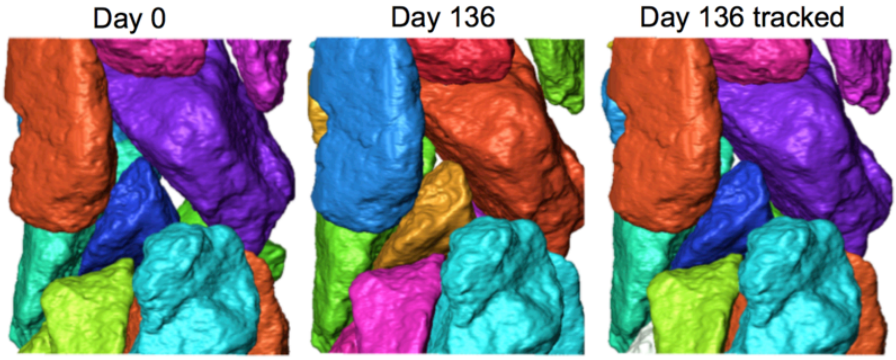


Figure 4.10.: An example of ore particle tracking and relabelling of a volume in two different scans.

registered (or aligned) to the same orientation using its Day 0 scan as the reference (Studholme et al., 1999). This procedure is shown in Figure 4.11. Registering the same particle in different scans means that particle always have the same orientation even if it is scanned at different positions. It needs to be noted that making the same ore particle have the same orientation by applying the registration and the resampling algorithms can make the data analysis much easier. The registration was achieved automatically by using Avizo 7. However, the resampling of the raw data can introduce extra errors. The solution to this is to extract the transformation matrix from the registration for future analysis without rotating any raw data sets. Extracting and applying the transformation matrix to complete grain tracking and achieve more accurate quantification is covered in Section 4.4.

4.3.4. Thresholding of Metal Sulphide Grains

From Figure 4.5, it can be seen that there is no distinction between the metal sulphide grains and rock phase peaks in the histogram and thus no obvious threshold value can

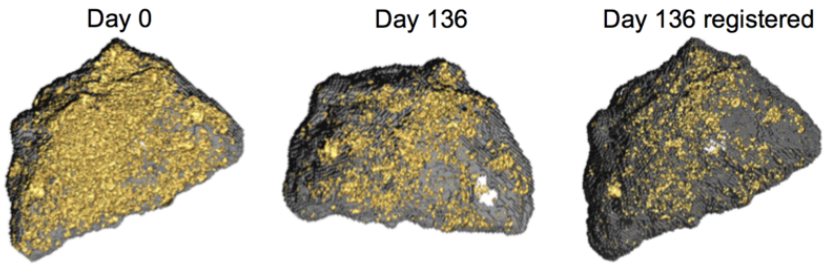


Figure 4.11.: Registration example of an ore particles after 136 days leaching.

be selected. The main reason for no clear peak for the mineral grain phase is that the total volume of metal sulphides compared with the volume of the ore particle is very small (approximately 5%) and the peak is actually hidden in the tail of the ore peak. Global thresholding adopting a more complex algorithm to determine the optimal threshold value is still an attractive method because it is much faster compared to local thresholding methods. A number of different global thresholding methods were tested using the auto threshold plug-in in ImageJ (Fiji, 2013). It was found that the algorithms based on the measurement of entropy (e.g. Maximum entropy (Kapur et al., 1985), Renyi entropy and Yen's methods (Yen et al., 1995)) give give reasonable mineral grain phase segmentation. Entropy is a statistical measurement of randomness that can be used to characterise the texture of the input image (Gonzalez et al., 2003; MathWorks, 2013). Mathematically, the entropy of an image can be defined as:

$$H = -\sum_{k=0}^{M-1} P_k \log P_k \tag{4.11}$$

where M is the total number of grey value levels and P_k is the probability at grey value k. According to Kapur et al. (1985), for a histogram:

$$\sum_{i=0}^{i_{\max}} h(i) = 1 \tag{4.12}$$

where $h(i)$ is the histogram and i is an integer within the histogram range (e.g. 0 to 255 for an 8 bit histogram and 0 to 65535 for a 16 bit histogram). The entropy of black pixels (dark part) and white pixels (bright part) can be calculated as:

$$H_B(t) = -\sum_{i=0}^{t} \frac{h(i)}{\sum_{j=0}^{t} h(j)} \log \frac{h(i)}{\sum_{j=0}^{t} h(j)} \tag{4.13}$$

$$H_W(t) = -\sum_{i=t+1}^{i_{\max}} \frac{h(i)}{\sum_{j=t+1}^{i_{\max}} h(j)} \log \frac{h(i)}{\sum_{j=t+1}^{i_{\max}} h(j)} \tag{4.14}$$

The optimal threshold can be calculated by finding the value of t that maximises the sum of black and white entropy:

$$T = \underset{t=[0,65535]}{\text{Arg Max}} \; H_B(t) + H_W(t) \tag{4.15}$$

Local thresholding algorithms (e.g. 3D watershed based) can also be used to threshold mineral grains. Figure 4.12 shows a comparison between Maximum entropy and 3D watershed algorithms for identifying sulphide grains. The 3D watershed algorithm sometimes cannot pick small particles (Shown in red) and, due to its strong gradient sensitivity, it will also tend to over-estimate the size of very bright particles. Local methods are also typically computationally more expensive than global methods. On the other hand, local methods are less sensitive to artefacts such as beam hardening and can be more easily tuned to ignore noise in the image.

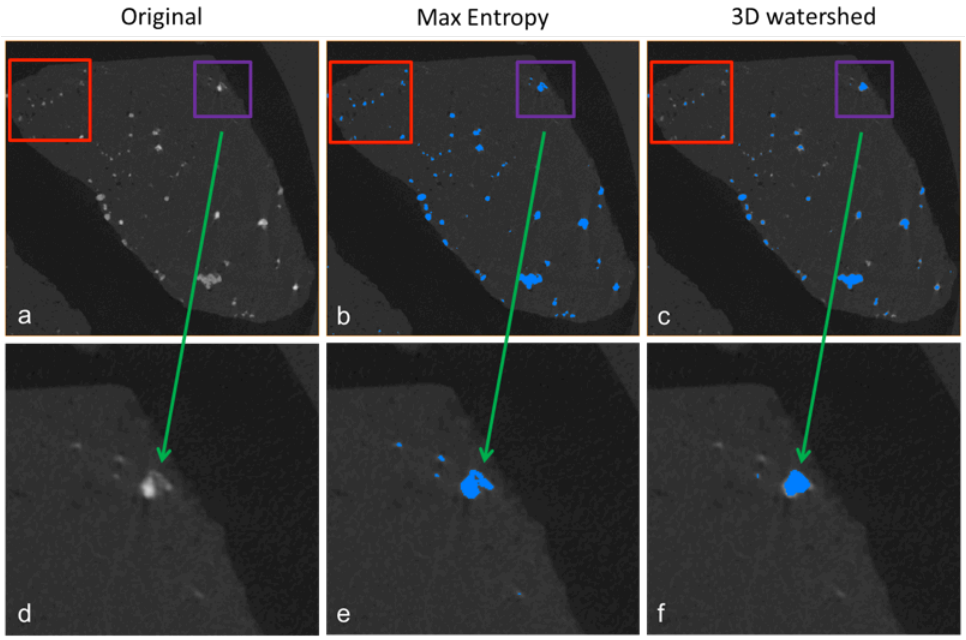


Figure 4.12.: The comparison of different methods to threshold metal sulphide grains using Max Entropy and 3D watershed.

4.3.5. Connectivity Analysis and Labelling of Mineral Grains

Similar to dealing with the ore particles, each mineral grain within an ore particle can also be tracked and labelled. This step makes quantification of individual grains possible and detailed quantification can be carried out based on this. However, when doing connectivity analysis and labelling for all the grains within an ore particle in different scans, the labels for the same grain in different scans were different. This is because due to the leaching process, the total number of grains and the volume of each grain changed with time. A mineral grain tracking algorithm is thus needed and will be discussed in Section 4.4.

4.3.6. Preliminary Quantification of Ore Particles

The main image quantification for leach behaviour involves the average leach behaviour, the mineral grain size distribution within an ore particle and the distance map related analysis. The average leach behaviour, which is obtained from the volume reduction in sulphides, can give both the macroscopic leach performance for the larger system (e.g. a leaching column) and the average leach performance for individual ore particles within the system. The volume measurement in image quantification is obtained by counting the total number of voxels that are identified as sulphides. Surface area is also calculated using the voxel counting method. The Marching cube method is better for surface area calculation but it is not crucial in this case.

The mineral grains size distribution within the ore particles and the relevant distance map analysis are more advanced quantification techniques to understand the leach performance. The size distribution can be carried out based on the volume measurements for individual grains based on the connectivity analysis for the minerals grains. The distance map is a more advanced imaging technique to analyse the data. The distance transform of a binary image calculates the distance from every white pixel to its nearest black pixel (Gonzalez et al., 2003). In the ore sample case, after applying the 3D distance map to the binary image of the ore particle, the locations of all the minerals can be obtained and these locations can be defined by the distance values (Figure 4.13). By applying the 3D distance map, the leach behaviour against distance within the ore particle can be quantified (Figure 4.14 and Figure 4.15). It can be seen that there is a clear trend that leaching kinetics drop when the distance between metal sulphide grains and the nearest surface increases. This indicates that the mass transport is an important factor in the apparent leaching kinetics.

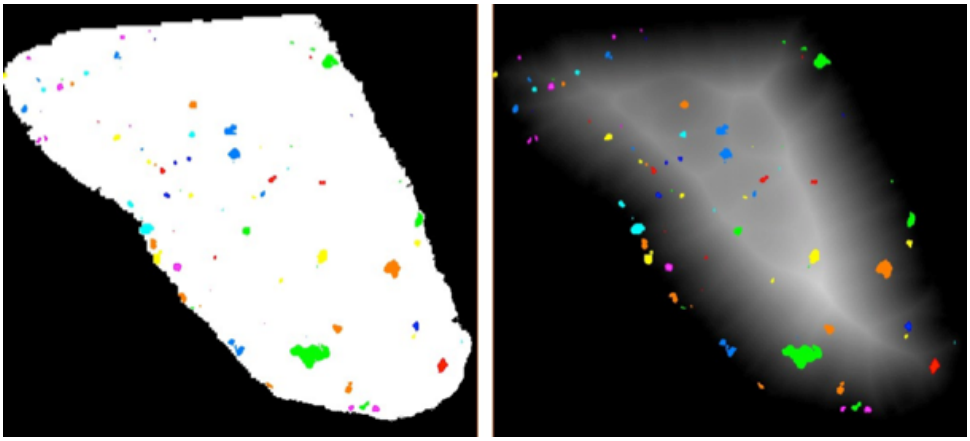


Figure 4.13.: An example slice of distance map of ore particles and inside metal sulphide grains for an example ore particles.

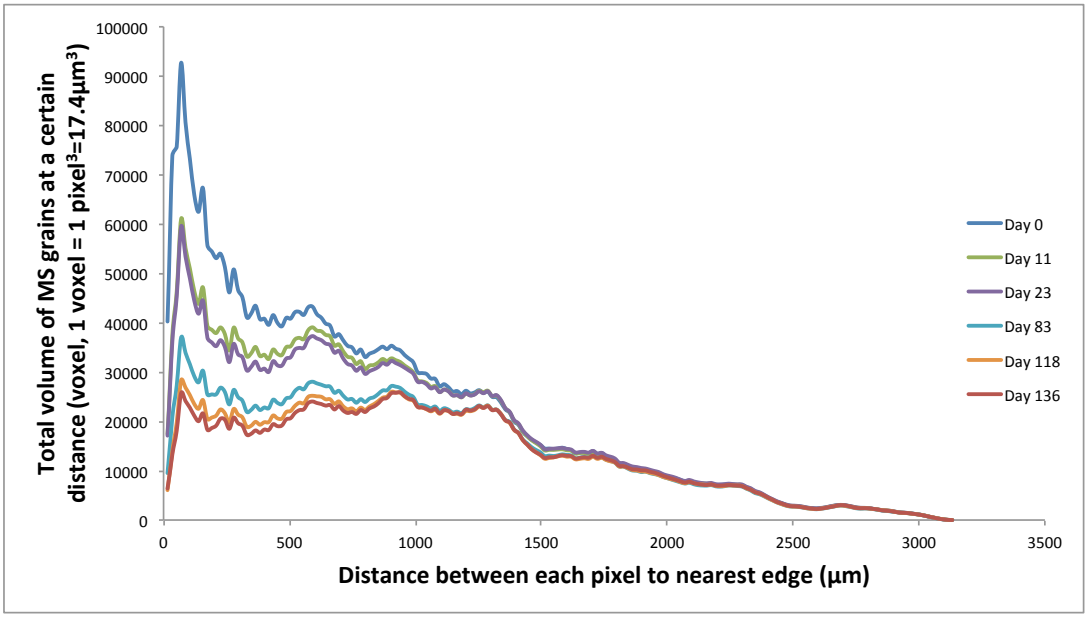


Figure 4.14.: Plot of total volume of metal sulphide grain at a specific distance against distance for different leaching days for an example ore particles.

4.4. Mineral Grain Tracking

According to the preliminary quantification, there is a strong distance dependency affecting the leach behaviour within the ore particles. It is still difficult to understand the mass transport for individual grains during leaching, although some of the information can be gathered by analysing the grain size distribution based on the 3D distance map. Tracking individual grains within the ore particle is important in further understanding the leach performance and potentially trying to simulate and model the leaching process.

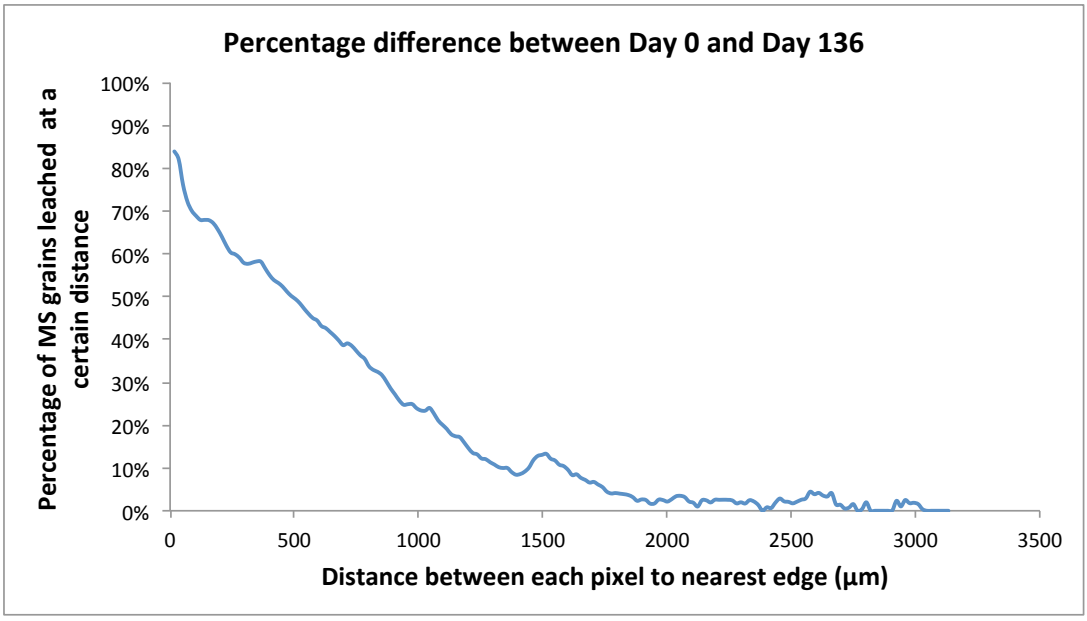


Figure 4.15.: Percentage leaching after 136 leaching days based on distance map for an example ore particles.

4.4.1. Mineral Grain Tracking Methodology

The tracking of the mineral grains is not done using the same centroid tracking algorithm that was used to track the individual ore particles. There are a number of reasons for not using this algorithm:

- Firstly, the sizes of each mineral grains change over the course of the experiments due to leaching (it is actually this change in size that is of most interest to us). The location of the centroid of the grains, which is the input for this tracking algorithm, can thus change due to leaching.

- The mineral grains not only shrink, but can also disappear. This causes problems for the centroid based algorithm, which will typically identify another grain that has not disappeared as the matching grain.

- A final consideration is the speed of the algorithm, which needs to be fast given the very large number of mineral grains involved (approximately 100,000 grains per scan, 6,000 grains per ore particle).

The main requirement of this fast tracking algorithm is that it assumes that after registration (or alignment), the matching of location and orientation of the sample with that at the reference scan, is accurate enough.

The algorithm starts by identifying all the mineral grains of interest in the reference image. The connectivity of the grains are analysed so that each isolated grain is given a unique identifier (Figure 4.16a). On subsequent images, voxels that are identified as mineral grains (Figure 4.16b) need to be given the same identifier number as they had in the original image. This is achieved by using a mask based on the reference image. It should be noted that in this algorithm it is the mask that is rotated and translated and not the data itself. Rotating the data would have an effect on the measured volume of the grains and thus also the error associated with the volume measurement as the interpolation required to project the rotated and translated data back onto a grid will cause the boundaries to become even more diffuse. Translating and rotating the mask will cause slight changes in the size and shape of masked regions, but this will have virtually no impact on the algorithm as the rims that result from slight errors in the mask are accounted for. Figure 4.18 shows an example of a reference and subsequent image as well as the original and transformed mask. Note that, while the figure shows a 2D slice, the rotations and translations were all 3D. The input reference mineral grain label in Figure 4.16a is the output label after applying the transformation matrix in Figure 4.18d. The mask is then applied to the mineral grains in the subsequent images (Figure 4.16c).

Since the grains theoretically do not grow through time between images, this mask would be all that is required if the thresholding of the images and the translation and rotation of the mask were perfect. In general this is not the case and unassigned rims can remain around the masked grains (Figure 4.17, or Figure 4.16d). This problem is resolved by assigning these rim voxels the identifier of a neighbouring voxel which has an identifier. This process is repeated until no more voxels gain an identifier (Figure 4.16e).

This tracking method has a few assumptions and limitations. Firstly, any objects that do not appear in the initial image but exist in later scan are not counted. This issue can occur for objects that are of a size very close to the voxel resolution or due to phantom particles caused by noise in the image, which can be ameliorated by the use of a median filter. Another potential issue with this algorithm is if the mask does not overlap any portion of the object in a subsequent images. Again this is only really an issue for objects that are approximately the same size as the voxel resolution. Objects that appear in the reference scan, but are not observed in the subsequent scan are included in the statistics, though objects that are not in the reference scan, but appear in a subsequent scan are not counted. These objects make up about 5% of the total number of objects in the subsequent scan, but as their sizes are all close to the scan resolution they account for only 0.05% of the total volume of the identified objects.

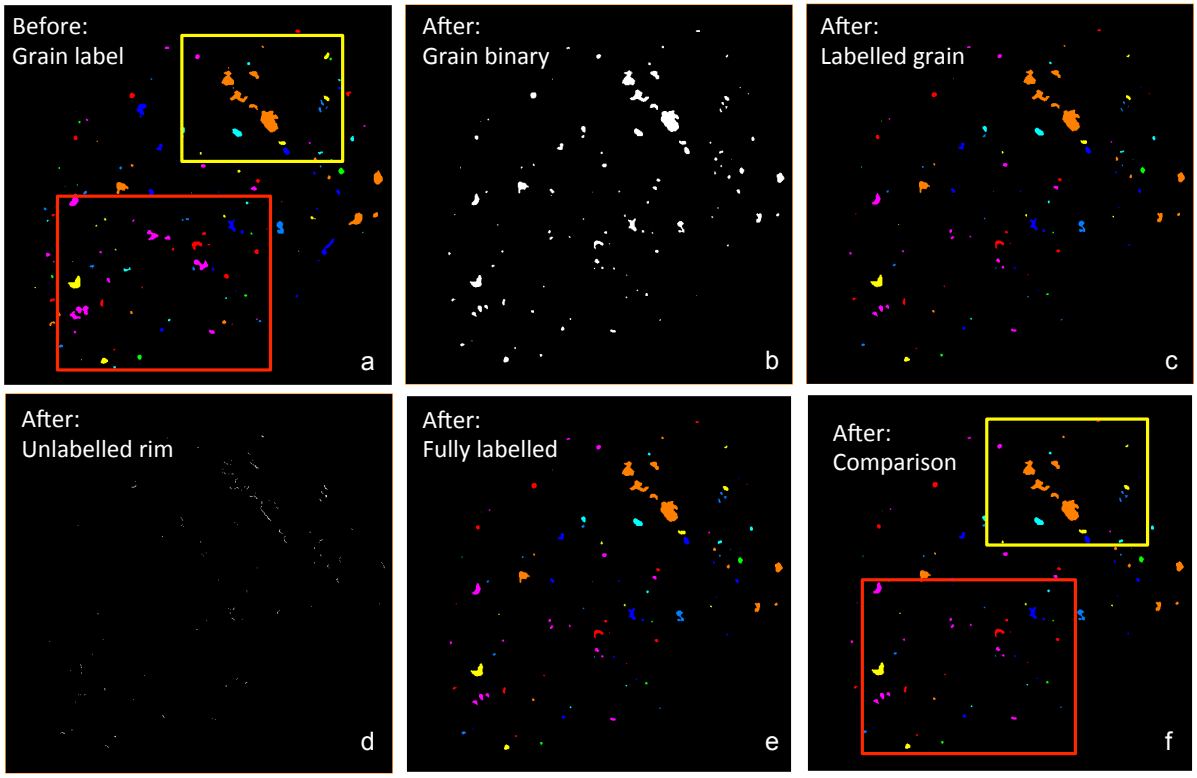


Figure 4.16.: A slice through a 3D tomogram of an ore particle showing the different stages in identifying the same grains in different images. (a) Reference image with grains identified and labelled. (b) Mineral phase identified in subsequent image. (c) Mask based on reference image applied to subsequent image. (d) Unassigned rims not covered by the mask, (d) is calculated by subtracting (c) from (b). (e) Labelled subsequent image with rims assigned to appropriate grains. (f) Comparison with reference highlighting regions.

Figure 4.19 shows the 3D visualisation of grain tracking for an example ore particle and Figure 4.20 shows a series of isosurface images for a relatively large example grain as it undergoes leaching. These examples show how the algorithm successfully tracks the grain as it both changes size and splits into smaller grains. The advantages of this algorithm is that grains that disappear can be easily identified and, where leaching causes a grain to split into a number of smaller child grains, each of these grains will have the same identifier as the initial grain.

4.4.2. Preliminary Quantification of An Ore Particle Based on Mineral Grain Tracking

Based on the grain tracking algorithm, the study of leach performance can reach grain level by investigating the behaviour for individual grains and more advanced quan-



Figure 4.17.: Unassigned rims not covered by the mask.

tification analysis can be carried out. After measuring the volume reduction for individual grains through time, 4D quantification can then be achieved. Figure 4.21 shows an example of recovery of an ore particle when grain size and distance to nearest surface change. The colour transition, especially in Day 1, shows that smaller grains have much faster and higher recovery. The change of the shape of the plots also indicates the distance dependency where grains having shorter distance to surface leach faster than the grains in the centre of the ore particle. This kind of plot can be used to investigate the trend of leach performance, but it is still quite difficult to understand the leach performance variation within the ore particle. There is also variation in recovery for grains with similar initial size and distance to nearest outside surface. Moreover, the measurement error, which is indicated by the negative recovery, can have a huge impact for the grains. This impact becomes more significant when the measured size decreases. Therefore, in order to have a more accurate leach performance quantification, it is better to combine a certain amount of grains with similar initial conditions (e.g. size, distance) and then carry out statistical analysis to minimise the impact from the measurement error. More detailed analysis including the error analysis and the leach performance analysis is covered in Section 4.5 and Section 5.4 respectively.

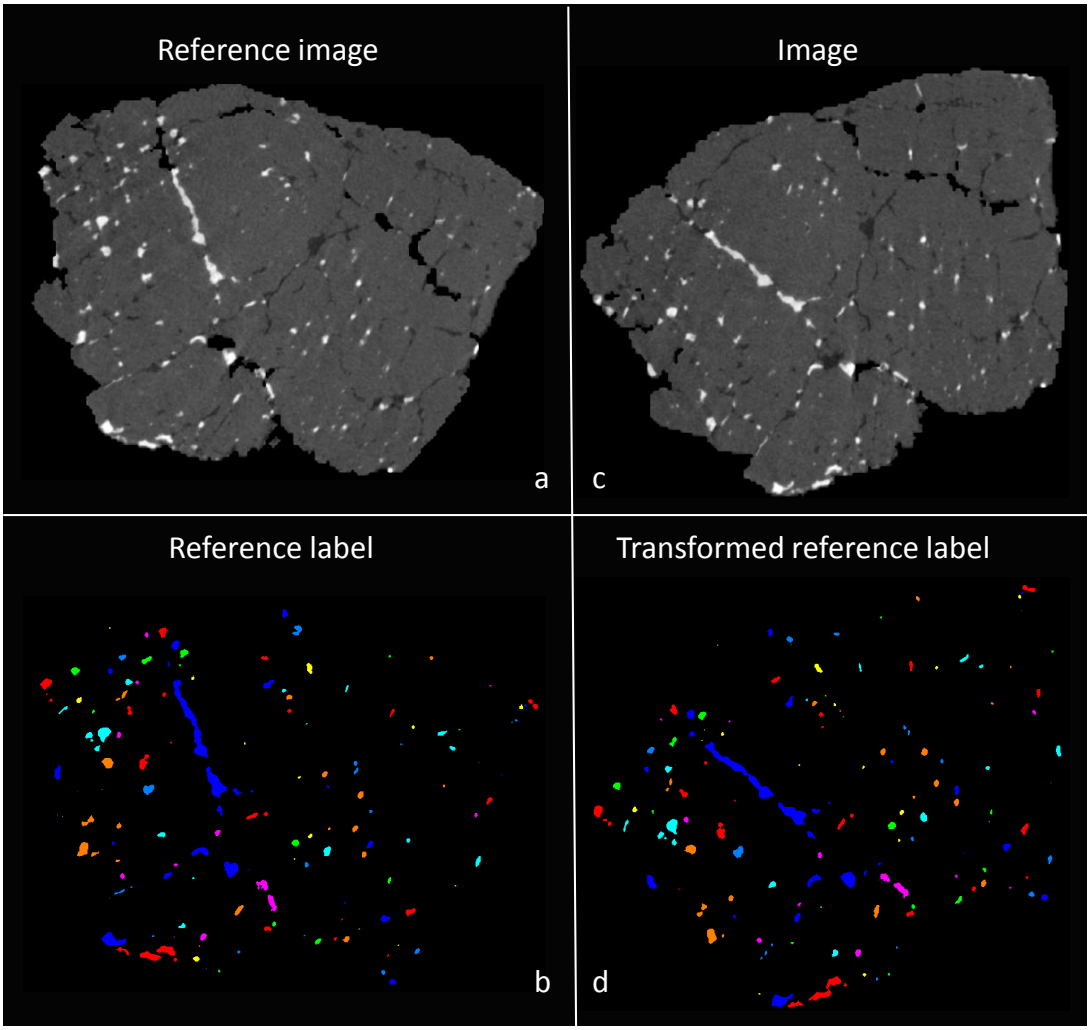


Figure 4.18.: Example of reference label transformation. (a) Reference image. (b) Label mask for reference image. (c) Image in subsequence scan. (d) Transformed reference label after applying 4×4 transformation matrix. The transformation matrix is calculated using (a) and (c).

4.5. Quantifying and Minimising Systematic and Random Errors in Volume Measurements

For the measurement of object or feature volumes from XMT images, each voxel belonging to a feature or object is obtained using a thresholding algorithm, and the volume obtained by counting the relevant voxels. However, the boundaries of features rarely coincide with the boundaries of the regular voxel grid, leading to the partial volume effect at the interface, where voxels have an intermediate bulk composition, and there is some uncertainty in the exact boundary location (Ketcham and Carlson, 2001; Stock,

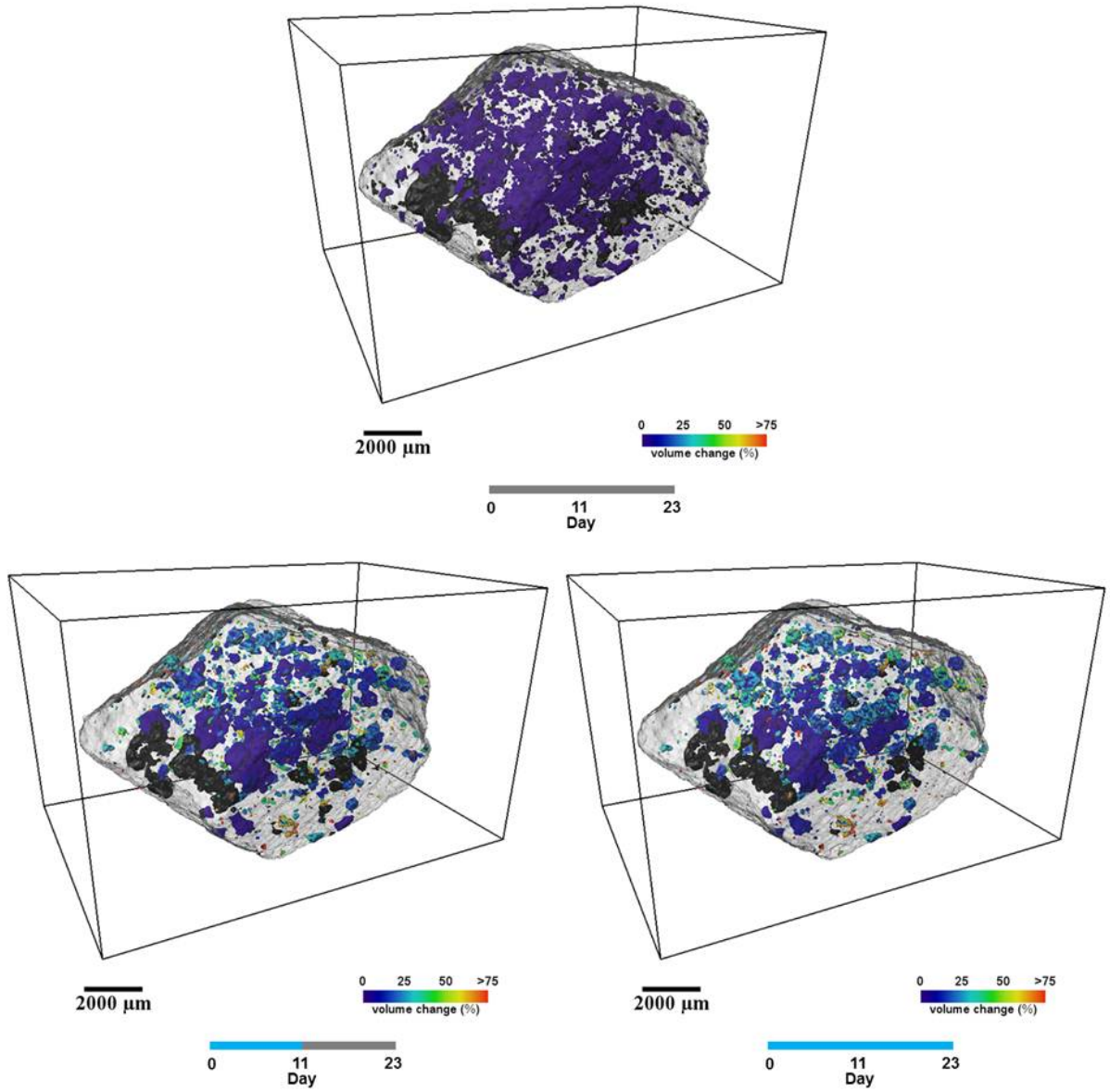


Figure 4.19.: 3D visualisation of grain tracking for an example ore particle.

1999). Theoretically the partial volume effect should only affect a narrow (few voxels) region when the boundary is planar, smooth and sharp, but in certain systems boundaries can be uneven and diffuse (Figure 4.22).

Before the volume data can be used with confidence the systematic and random errors in the measurement need to be understood. Systematic errors are those in which the error is the same for all similar objects and, for volume measurement, will typically be a function of the size of that object. Correction of systematic errors is possible using appropriate standards and calibration. Random errors are those that are not the same

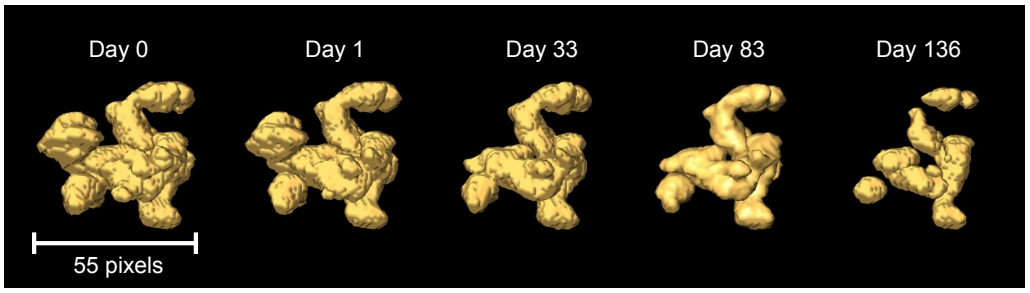


Figure 4.20.: Isosurface images for an example grain after identification.

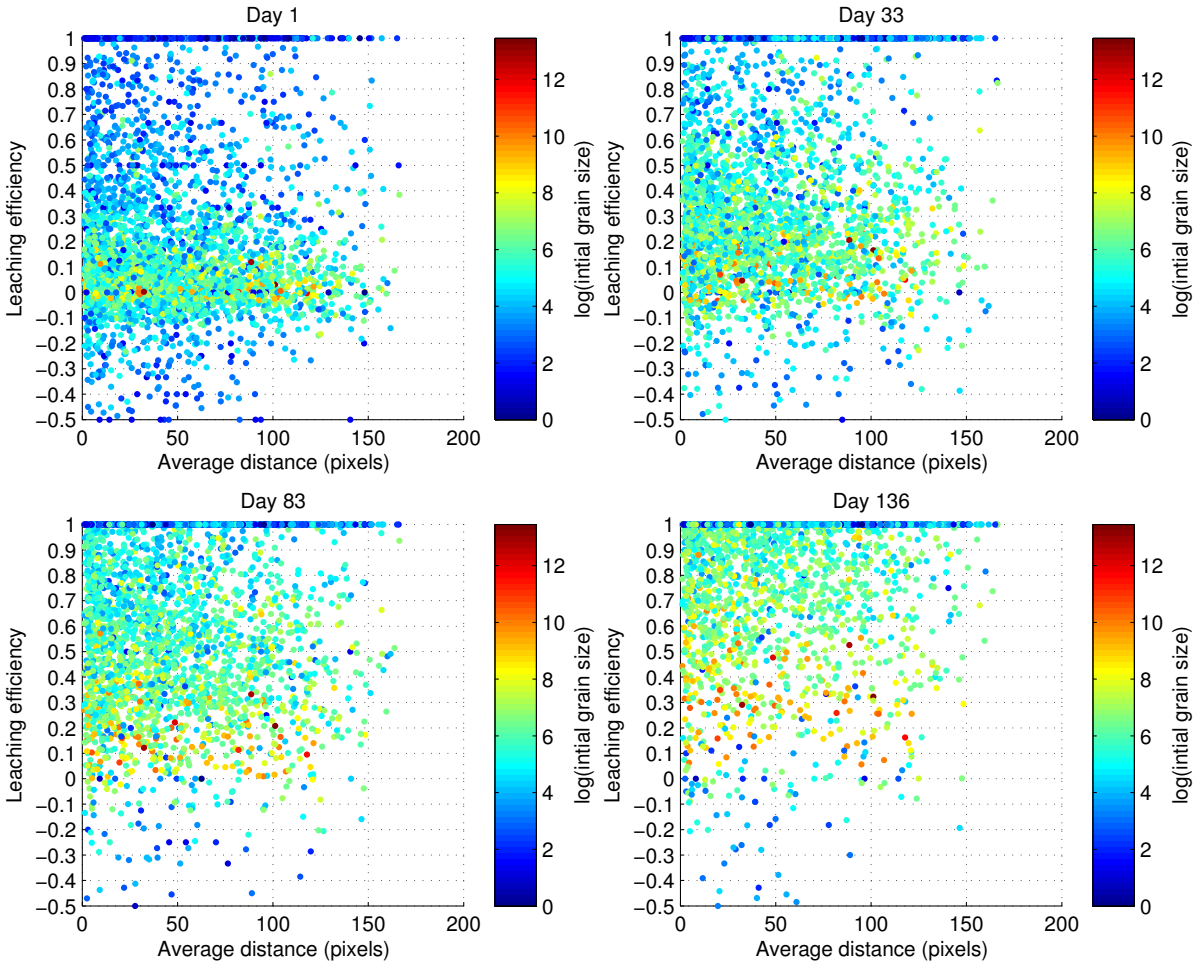


Figure 4.21.: An example quantification of an ore particles with four scanning points combining individual grain leaching efficiency with particle size and distance to nearest surface. The colour is defined by the logarithm value of the size in volume.

for similar objects or between scans and thus add an uncertainty to measurements that cannot be eliminated by calibration. However, unlike systematic errors, random errors do not influence the average measured volume if enough volume measurements have been used.

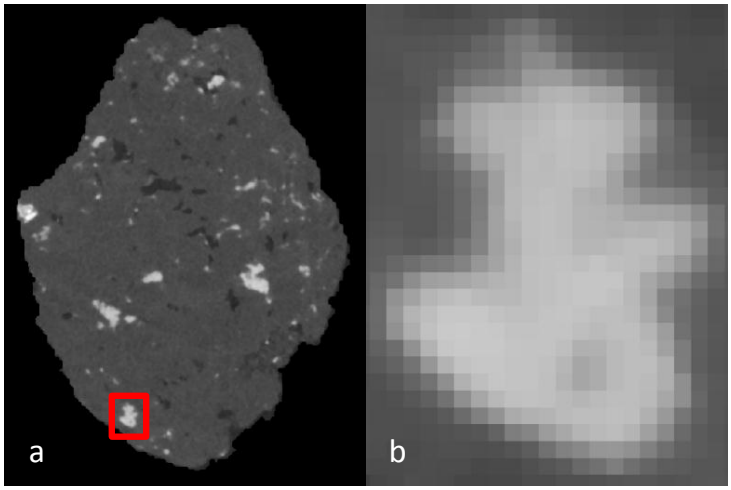


Figure 4.22.: a) A 2D slice through a 3D tomography volume of example data showing mineral grains within an ore particle. b) A region of interest demonstrating diffuse boundaries.

The systematic error in the grain volume will come about from effects such as an error in the threshold used, while the random error will come about due to effects such as the change in the partial volume effect due to the specific location of the mineral grain relative to the voxel grid, which will change from scan to scan and from grain to grain.

The choice of thresholding algorithm or threshold value will have a systematic effect on the measured volume, while variability in the exact location of the object relative to the voxel grid will cause a random variation in the measured volume. Typically an algorithm is used to choose the threshold to reduce subjectivity in the identification of the objects within the image, but this does not mean that systematic errors due to thresholding are eliminated, and it might well be appropriate to adjust the threshold value to minimise these systematic errors if an accurate, rather than simply consistent, volume measurement is required. The relative impact on the measured volume of both these systematic and random errors will be strongly dependent on the size of the object relative to the voxel size, as the proportion of the volume that is within the uncertain region at the boundaries of objects will decrease as the object size increases.

In this section a procedure for quantifying both the systematic and random components of this uncertainty in volume is introduced. In particular, how to ascertain how many times an object needs to be scanned (or how many similar objects in the same scan need to be combined) to achieve a given level of accuracy in the measured volume, assuming that any systematic error has been eliminated, is assessed. Repeatability will also be influenced by both the random and systematic components of the error as the systematic error is likely to change from scan to scan, while the random component will

add uncertainty to the measurement. While the methodology described in this section is applied for the identification of the valuable mineral phases within ore particles, the methodology itself is more generally applicable and relevant to other systems in which volumes are obtained from XMT data.

The samples used is this section do not come from any of the columns in Chapter 3, but come from a separate volume being scanned twice with slightly different orientations without any leaching. This data is also used in Section 4.6. The image processing for these scans are the same as the procedure mentioned in and Section 4.2 and Section 4.3 and thus the same as is what is applied to the leaching columns.

4.5.1. Sensitivity of Measured Volume to Threshold Changes

The initial threshold values used to identify the mineral grains were obtained by applying the maximum entropy global thresholding algorithm to each rock (Kapur et al., 1985). The threshold was then adjusted from these values and the percentage change in the measured total volume of all the mineral grains calculated (Figure 4.23). The shift in threshold value is calculated as the ratio between absolute value shift ($T_{\text{shift}} = \pm 50$, ± 100, ± 200, ± 300, ± 400, ± 500) and the difference between the rock and mineral grain phase thresholds:

$$T_{\text{shift}}\% = \frac{T_{\text{shift}}}{T_{\text{grain}} - T_{\text{rock}}} \tag{4.16}$$

where T_{grain} is the threshold for the metal sulphide grain and T_{rock} is the threshold for the rock phase. The reason for using the change relative to this difference is that the appropriate threshold value must lie between the intensity of the grains and the matrix.

There is an approximately linear change in measured total volume as the threshold value is changed (Figure 4.23), though the magnitude of the change varies somewhat from sample to sample. This variability is probably due to differences in the size distribution of the grains within the three ores.

The sensitivity of a grain volume measurement to a change in threshold is very dependant on its size relative to the voxel resolution. Smaller grains are more sensitive to a change in threshold because this is mainly a surface effect and smaller grains have a larger specific surface area. Assuming that a small change in the threshold produces a small change in the location of the boundary (this analysis does not require that the relationship between the change in the position of boundary and the threshold be a simple one, only that the change in position is approximately the same at all boundaries), the

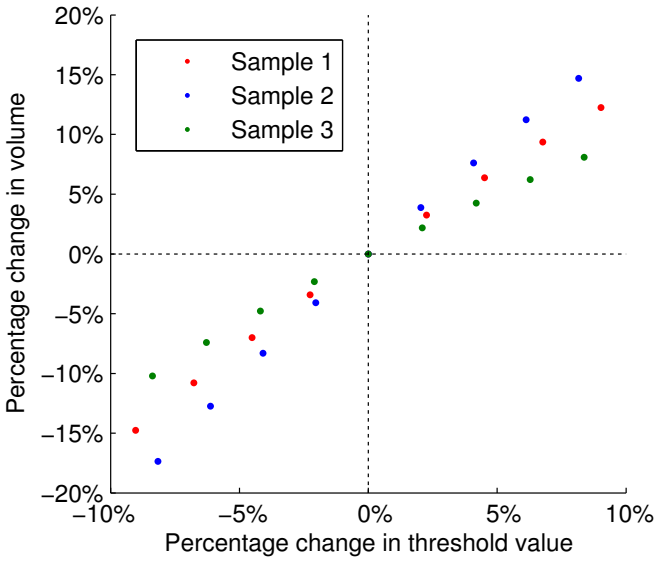


Figure 4.23.: The relationship between the change in mineral grain volume and the variation in the threshold value.

fractional change in volume can be expressed as:

$$\frac{\Delta V}{V} \propto \frac{r^2 \Delta r}{r^3} = kV^{-\frac{1}{3}}\Delta r \tag{4.17}$$

where V is the volume of the grain, r is a linear dimension of the object (proportional to $V^{1/3}$) and k is a dimensionless constant. Δr mainly depends on the change in the threshold value, but it can also depend on the shape and size of grains. This power law exponent of -1/3 implies that the relative change in volume is inversely proportional to the grain radius and proportional to its specific surface area.

Plotting $\Delta V/V$ against grain volume for different threshold (Figure 4.24) values shows that the larger grains follow Equation (4.17), but that the smaller grains have a more negative slope, with $\Delta V/V = kV^{-2/3}$ (a power law exponent of -2/3) producing a better fit. An exponent of -2/3 implies that the change in the volume upon a threshold change scales with the radius of the grains rather than its surface area for the smaller grains. This is somewhat unexpected, but one possible explanation for this is that either the reconstruction algorithm or the imaging itself is producing more uncertainty in one of the axes than the others. Another possible explanation is that the apparent shape of some of the objects are strong functions of the threshold value chosen. This is not much of an issue for convex objects, but is likely to be important for more complex objects. For such objects simple thresholding might not be sufficient and more complex techniques may need to be applied. An example of such a method is de-convolution based on an

the assumption that the blurring of the edges takes the form of a point spread function (Ketcham, 2006; Ketcham and Hildebrandt, 2014).

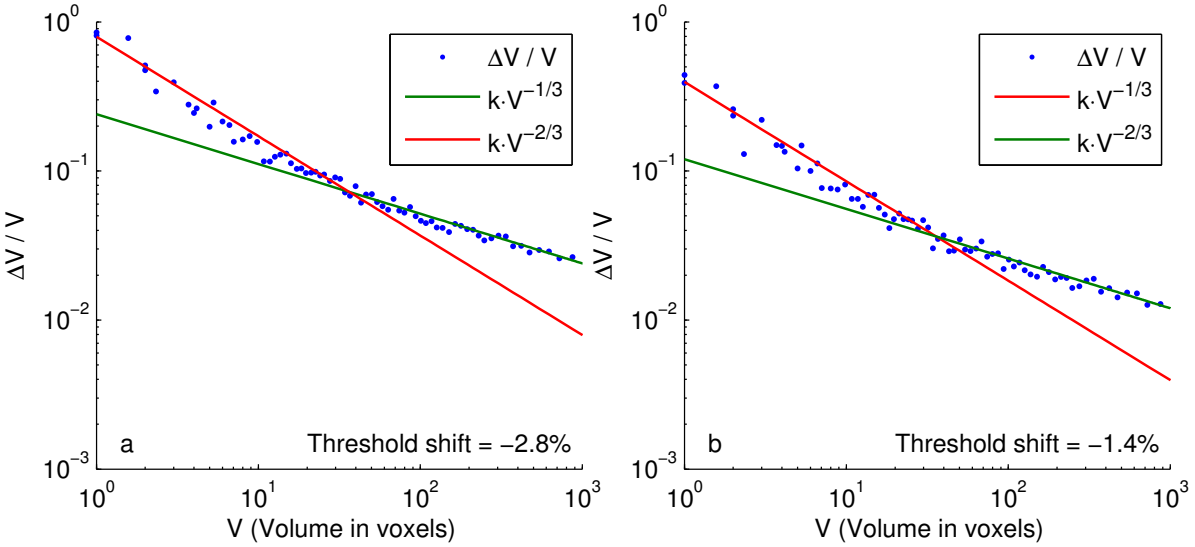


Figure 4.24.: The plot of the relative change in grain volume as a function of the volume for two different threshold changes. a) 2.8% b) 1.4%. The power law relationships for large (-1/3) and small (-2/3) grains are also shown.

While the relative change in the average measured grain volume is of a similar magnitude to T_{shift}, (Figure 4.23), for individual grains the difference is strongly size dependant (Figure 4.24). Since the small grains are more sensitive to changes in threshold than the larger grains, it is this region of the curve that is most important.

In Figure 4.25, the prefactor in the best fit to smaller grains (less than 100 voxels) for a power law relationship with an exponent of -2/3 is plotted against the change in the threshold value. Since the k value and the magnitude of the average change in volume are directly related, there is also a near linear change in k with the change in the threshold value. This curve will be used later in the correction of the systematic errors (Section 4.6).

4.5.2. Estimation of Grain Volume Uncertainty

While the effect of changing the threshold can be obtained from a single image, repeat scans of the same volume are required to determine the random component of the error. As the scanned volume contains a number of ore particles and each ore particle contains thousands of grains, the identification procedure outlined in Section 4.4.1 allows us to look at the variability in the measured volume of tens of thousands of individual objects. The same analysis can be carried out for systems containing fewer objects, but

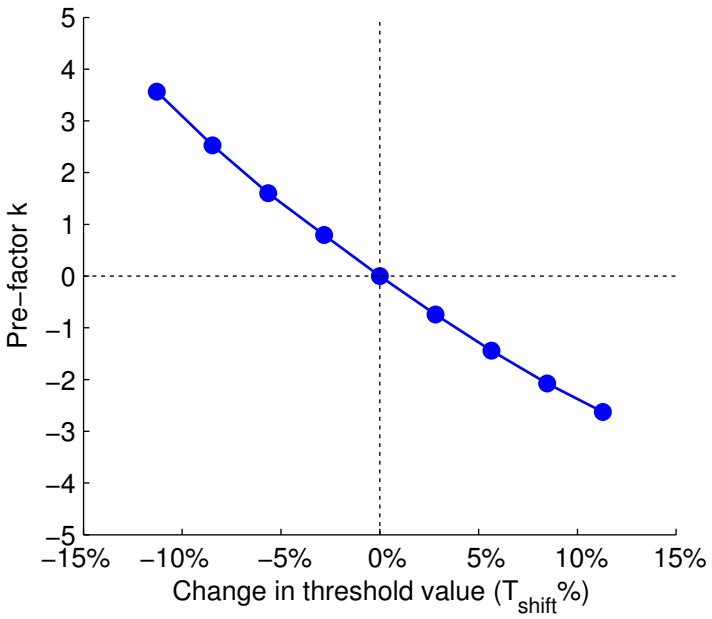


Figure 4.25.: Plot of prefactor k as threshold value changes.

in order to generate sufficient statistics on which to base the analysis, repeated scans of the same objects may need to be carried out.

Taking two images of the same sample volume, the relative error in volume measurement for each individual grain was calculated. The grain volumes were then ordered according to size and the standard deviation in the relative error was calculated for sets of 500 grains of similar volume and plotted against the mean volume of the set of grains (Figure 4.26).

For a single grain the uncertainty (expressed as the standard deviation of the measurement) in the size of the grain is as large as the grain itself for any grain less than approximately 7 voxels. For an uncertainty of less than 10% the grain needs to be larger than about 260 voxels in volume. However, statistically relevant information on the change in volume of the smaller grains can be achieved by combining data from a number of similar grains. Figure 4.26 shows that there is a power law relationship between the standard deviation in the relative error and grain volume, with an exponent of close to -2/3, which is consistent with the scaling for the systematic error[2] (Figure 4.24). This means that the magnitude of the random component of the error is approximately proportional to the radius of the grain, which is again surprising as the naive expectation would be that this error would be related to the surface area of the grain.

The uncertainty in the measured volume can be reduced by either repeated scans

[2]While they have similar volume scaling in this system, there is no fundamental reason why the systematic and random components of an error need to have the same dependencies.

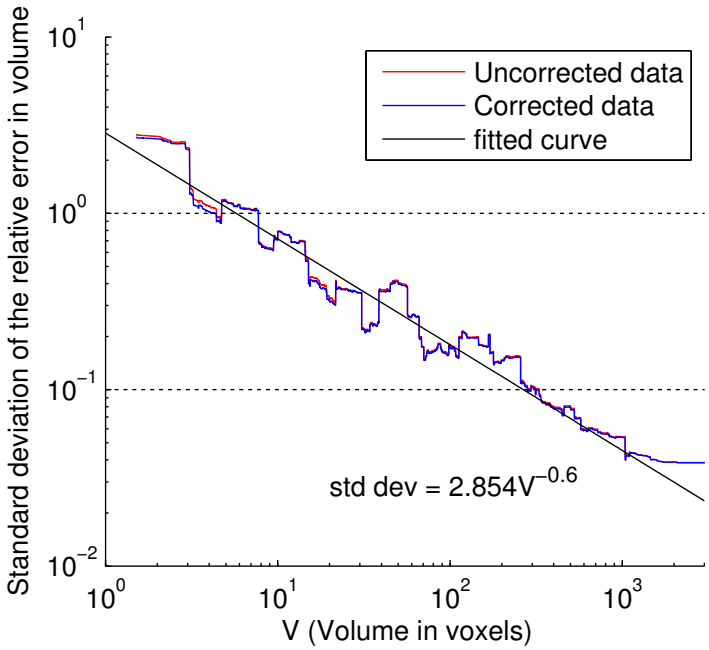


Figure 4.26.: Standard deviation in the relative error in the grain volume as a function of the grain volume.

of the same object or by combining the results from a number of similar objects. As the uncertainty for an individual object is a function of the object volume, the number of similar objects, N, of volume V that need to be combined to achieve an acceptable relative error, ε, in the measured volume can be calculated (or, alternatively, N is the number of times that the same object needs to be scanned):

$$N = \frac{(\kappa V^n)^2}{\varepsilon^2} \tag{4.18}$$

where κ is the prefactor in the relationship between the relative standard deviation in the measure volume of a single grain and n is the power law exponent. For example, based on the scans used to produce Figure 4.26, to reduce the random component of the uncertainty when measuring volume to less than 5% you would need to combine the measurements from approximately 600 grains with a volume of 4 voxels, approximately 12 grains with a volume of 100 voxels objects, or one object of 1000 voxels (see Figure 4.27). This will not account for any genuine variability in the behaviour of nominally identical objects, and it is important to note that it is only the random component of the error that is reduced by averaging repeat results. By definition, combining results will have no impact on any systematic error. Figure 4.27 can only be used as an indication of the error expected as the error will depend upon the particular material and its scanning conditions. The procedure presented is relatively straight forward, and is recommended

whenever precise quantitative data for the volume or volume change is required.

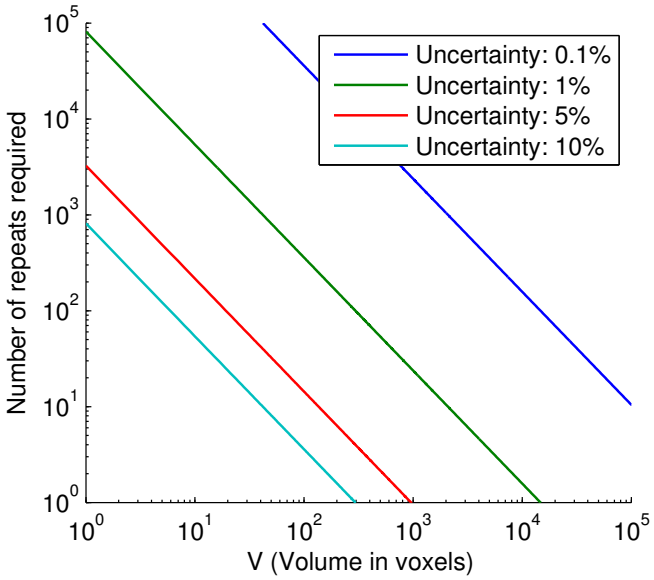


Figure 4.27.: Number of repeats required to reduce the random component of the uncertainty (relative standard deviation) in the volume to a given level as function of the object volume.

4.6. Obtaining Consistent Results in The Face of Systematic Errors by Changing Threshold Values

It is common practice to use intensity standards (usually introducing the same objects of known attenuation into all scans) when carrying out XMT measurements, and this is usually sufficient for samples containing large features with high contrast. The intensity normalisation can be achieved by normalising phase peaks in the histogram. When normalising an image (Image 2) against a reference image (Image 1) using two phase peaks, the image normalisation can be achieved by Equation (4.1). For example, Yue et al. (2011) applied a global thresholding algorithm to the normalised images and the threshold values were determined by picking the value equidistant between the two peaks. However, this method has some limitation. Firstly, the fundamental assumption for this normalisation is that it assumes that the change between the two peaks is linear which is not true in reality. Secondly, this method only works for histograms with two clear peaks. Moreover, the assumption of linearity can also end up with some systematic error when applying the global thresholding method.

In these cases, variations in machine behaviour or beam energy over time (which is equivalent to variations in the threshold value) will be small. However for small objects, especially in low contrast materials or when volume changes can alter the bulk attenuation along the beam path, simple intensity calibration is unlikely to be sufficient. In this case having both volume and intensity references were recommended, especially for smaller grains. The number of reference features needs to be sufficient for suitably accurate volume determination, and the features for should not change between scans over a time series experiment. In this particular example of grain dissolution, an appropriate standard could consist of an unaltered particle of the ore that is present in all scans. Ideally this procedure will be carried out using a reference image containing sufficient reference features which the individual volumes are known, as this will allow not only consistent, but also accurate results. In this specific example the volumes in the reference image are not known and thus it is only consistency that is achieved by using this method.

The reason why the correction of systematic errors has been after that of the random errors is that it is important to know which errors or discrepancies can be eliminated by appropriate adjustment of the thresholds and which errors are random.

In Figure 4.28 the relative difference in volume ($\Delta V/V$) of the grains in two independent scans of the same volume collected under identical machine settings and analysed using the same thresholding algorithm (the maximum entropy algorithm) should be negligible and yet plotting the $\Delta V/V$ as a function of grain volume shows a systematic error in the volume, especially for smaller grains. The discrepancy between the two scans will contain both systematic and random components and therefore this is reduced by combining measurements from 100 similar sized grains. This virtually eliminates the random component of the error for the larger particles, but it is still significant for the smaller particles (below about 100 voxels).

It is expected that much of the difference will be caused by small inconsistencies in the threshold value and it is the smallest grains that have the largest discrepancy. The same equation form that fitted the smaller particles in Figure 4.28 is therefore fitted to this data, namely a power law relationship with an exponent of -2/3.

When trying to eliminate errors, it is important to consider the grain distribution within the ore particles. For example, Figure 4.29 shows the proportion of grains in different size categories with their volumes in percentage covered in the reference scan. Although the grains with volume smaller than 100 voxels cover more than 50% of the total number of grains, the total volume for these grains is only around 5%. Based on the grain tracking algorithm, the total volume of grains in each scan (Reference Scan 1 and Scan 2) were calculated. Although the percentage difference is approximately 2% in

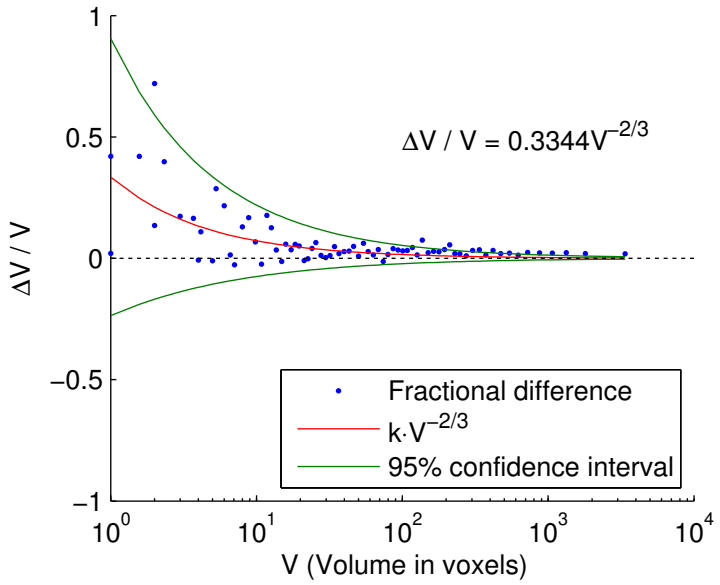


Figure 4.28.: The discrepancy in volume between reference scan and repeated scan.

total but this global difference is mainly contributed by large grains because the relative errors and uncertainties for smaller grains are much larger than larger grains. Thus, different portions of grains need to be considered differently depending on the objective of error elimination. When investigating the average behaviour, the threshold value needs to be corrected based on the larger grains as they cover the majority of the volume. On the other hand, when trying to understand the grain level behaviour against grain size, smaller grains need to be considered more as they covers the majority of the grains. In this case, the threshold value is corrected based on the grains larger than 10 voxels which over come the majority of the system error for the average behaviour, but also considered approximately 85% of the tracked grains.

Since the expected standard deviation in the average of the 100 grains used to generate each of the points in Figure 4.28 is known from Figure 4.26, the 95% confidence interval for the fitted equation can be plotted. For the smaller grains virtually all the points fit within this confidence interval, which would be expected if the assumed form for the data is correct. The difference in volume for the larger grains lies outside the confidence interval, but the power law relationship with an exponent of -2/3 is only expected to fit the data for the smaller particles.

If there were no systematic error there should be no trend in the discrepancy and the data should be scattered around zero, with a larger scatter at smaller sizes. To try and achieve this, the correction to the threshold required to eliminate the systematic error

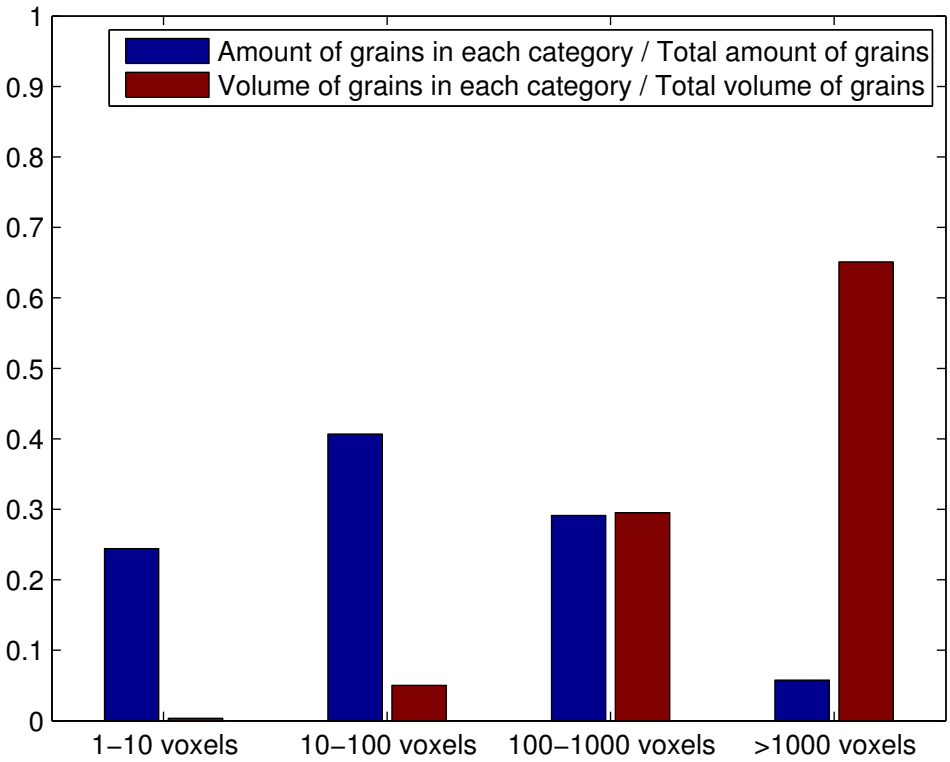


Figure 4.29.: Amount of grains at specific size range with volume percentage in Scan 1 (reference).

can be estimated based on the prefactor, k, in the fitted power law (Figure 4.28). In this case an increase in the relative threshold value of about 1.5% (from Figure 4.25) was required[3]. The power law relationship between the change in volume and the volume when the threshold is adjusted means that even this small change has quite a large effect on the smallest grains. If this change in threshold has the same relative effect on the measured volume in the subsequent image as it did on the reference image, then the systematic error should be eliminated.

Figure 4.30 shows the discrepancy in the volume once this change in threshold has been applied. It can be seen from the 95% confidence intervals that this correction has resulted in discrepancies in volume that are consistent with no systematic error in the size of the smallest grains. While the correction was not based upon the size of the largest grains, the systematic error in their size was reduced from about 2% before correction to 0.8% after correction.

The correction has virtually no impact on the random component of the error, with

[3]The prefactor in the power law fit to the data in Figure 4.28 (0.3344) is used to read off the required shift in threshold from Figure 4.25 (1.5%). Note that a positive prefactor implies that the measured volume is too large and that the threshold must thus be increased.

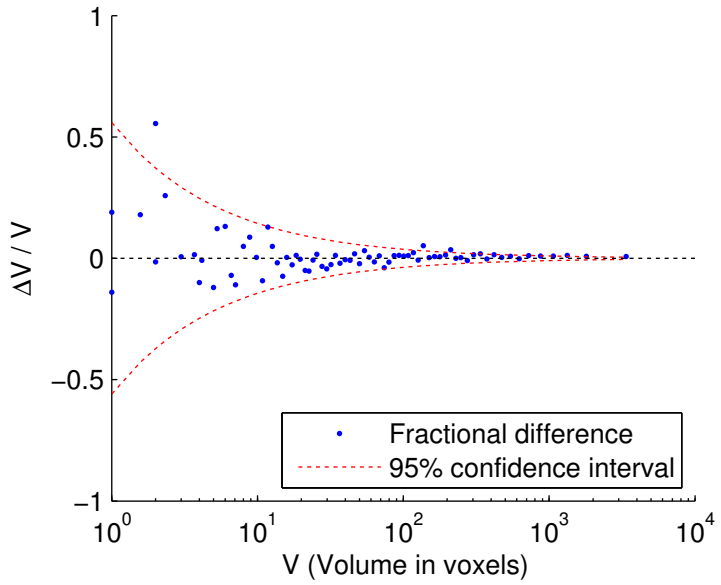


Figure 4.30.: Mean relative error in metal sulphide grain volume as a function of the grain volume.

the relationship between the standard deviation in the measured volume and volume itself for the corrected and uncorrected data being virtually the same (Figure 4.26). This indicates that the random and systematic errors are independent of one another in this system. It also means that the random error can be accurately assessed without using a size standard as this component of the error is very insensitive to the specific threshold value used.

4.7. Comparing Different Thresholding Methods and Their Consistency

Thresholding is one of the most important steps in image processing and quantification. Normally, there is more than one method available to achieve phase thresholding when thresholding mineral grains from ores. The most accurate way to evaluate how accurate a thresholding algorithm is is by comparing the measurements from image analysis with the physical measurements. For example in Figure 2.20, after extracting the feature, which are pores, the measured width of pores can be compared with the physical measurements from the thin section (Ketcham and Carlson, 2001). However, in many cases, it is difficult to obtain physical measurements as reference values to evaluate the accuracy of the algorithms. In this situation, the important aspect of doing image quantification is to make sure that the algorithm used for analysis is consistent. In this section, a method

based on the mineral grain tracking algorithm (Section 4.4.1) is used to evaluate the consistency of different algorithms when thresholding mineral grains from ore particles. The Max Entropy (Kapur et al., 1985) and Moments (Tsai, 1985) algorithms are compared in this section.

The easiest way to evaluate whether a thresholding algorithm is appropriate or not is achieved by visual inspection. However, in many cases, visual inspection is not accurate enough to evaluate the accuracy of the algorithm. In the following example, the histogram of an ore particle was plotted in Figure 4.31. The air phase of the image has been extracted using the Otsu algorithm (Otsu, 1979) and all the pixel values of the air phase have been replaced with 0 (black) and was excluded in Figure 4.32. Therefore, the rock phase and the mineral grain phase are the only two phases in the image and the peak point in the histogram (red dashed line) indicates the intensity of the rock phase. The Max Entropy and Moments algorithms are both global thresholding methods, but when calculating the threshold value for the mineral grains, the Max Entropy uses the entire histogram as input, while the Moments algorithm only takes part of the histogram (the pixel values larger than the rock phase peak) to give reasonable thresholding results (Figure 4.31). Figure 4.32 shows the comparison of binary images of extracted mineral grains using the two methods described above.

According to Figure 4.32, both methods can extract mineral grain phase from the background (rock phase) and there is not a big difference from visual inspection. In this case, to further investigate the algorithm consistency, the mineral grain tracking algorithm needs to be applied, followed by statistical analysis. It needs to be noted that in this particular case, the data used are not rescanned samples (Same sample scanned twice, which was the case when studying measurement error in Section 4.5). The main reason is that global thresholding is potentially sensitive to change in the object, as well as the change in the histogram. Leaching of minerals closer to the ore particle surface could thus influence the shape of the histogram and the calculated threshold value. Therefore, the best way to evaluate the consistency of threshold algorithms is to analysis unleached grains while the histogram has changed.

The images of the ore samples before leaching (Day 0) and after one day leaching (Day 1) were used. The mineral grains for those time points were thresholded using both Max Entropy and Moments algorithms. All the grains within the ore particles in Day 1 were tracked according to the reference scan (Day 0). In theory, after one day leaching, the mineral grains in the centre of the ore particles should not be leached and the grains left should have almost the same volume as in Day 0 image but the shape of the histogram has been changed due to the one day leaching. Therefore, grains with distance to nearest

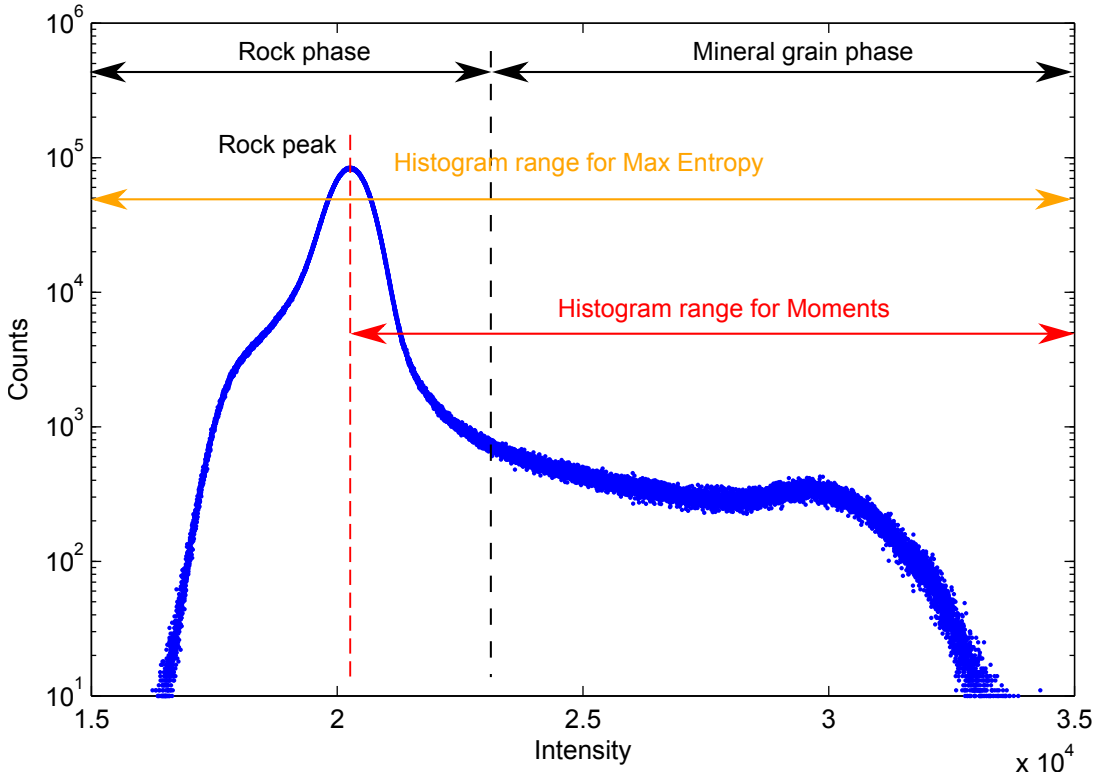


Figure 4.31.: Histogram plot of the example ore particle with indication of threshold calculation using Max Entropy and Moments algorithms.

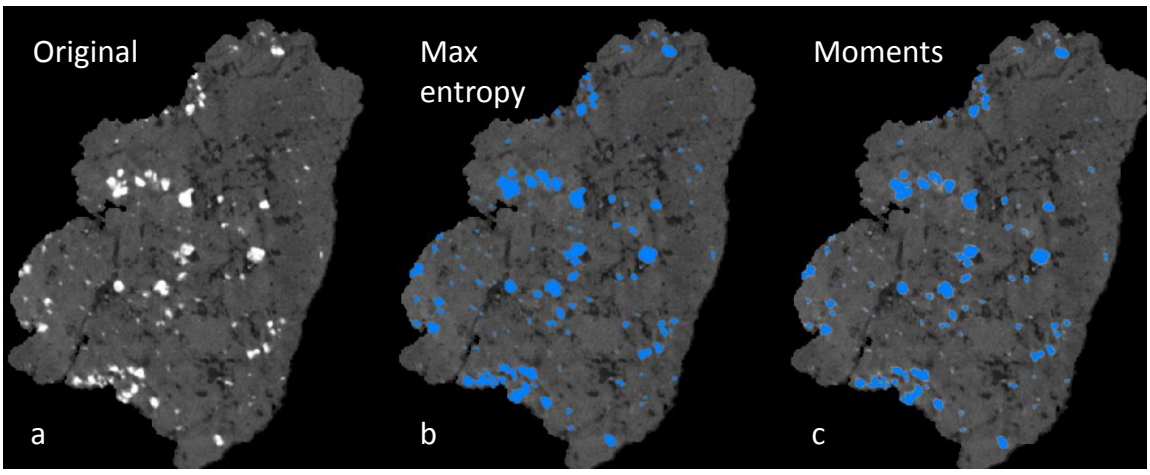


Figure 4.32.: Comparison between Max Entropy and Moments algorithms to threshold mineral grains within an ore particle: a) Original example slice. b) Mineral grains thresholded using Max Entropy algorithm. c) Mineral grains thresholded using Moments algorithm.

outside surface less than 70 pixels were filtered. Three random selected ore particles, namely Sample 1, 2 and 3 from the same scanning volume, were used to further compare the two methods. The standard deviation of the relative error for the grains after filtering

within these particles between Day 0 and Day 1 can then be plotted as a function of the volume (Figure 4.33). There are two common criteria to evaluate whether the algorithm is consistent and accurate:

1. The standard deviation of the relative error in volume should decrease when grain size increases. As the leaching period is only 1 day and the plotted data are grains having more than 70 pixels from the surface, the volume change should be negligible. Therefore, for larger grains the standard deviation of the relative error should be small.

2. For a consistent algorithm, the plots for different samples (from the same scanning volume) should be similar. If the plots for different samples from the same scanning volume are very different, it means that the thresholding algorithm is not ideal for the data sets.

Figure 4.33a shows that the standard deviation of the relative error against grain volume plots for three samples have very similar trend using the Max Entropy algorithm and the three plots almost overlap, which indicates that the threshold results from the Max Entropy algorithm give consistent results for later quantification and analysis. For larger grains, the standard deviation values between Day 1 and Day 0 reach about 2% for all the three samples, which is reasonable. However, the Moments algorithm shows very different behaviours (Figure 4.33b). For Sample 1 and Sample 2, Moments algorithm still gives about 10% error even the larger grains, but the plot for Sample 3 gives reasonable result. The trends for three samples are quite different which means that the Moment algorithm is quite sensitive to the images and the shape of the histogram and it is really likely to give inconsistent results. For Sample 1 after using the Moments algorithm, the standard deviation is consistently 100% (not able to show in log-log axes) for grains smaller than 10 voxels. The reason is that in Sample 1, comparing to Day 0, the threshold value in Day 1 is too large to pick smaller grains which can be seen in Day 0 image. The smaller grains therefore look like they are disappearing.

Plotting standard deviation of the relative error against grain volume by applying grain tracking algorithm cannot really tell why an algorithm is not consistent and accurate, but it is a fast and effective way to evaluate if an algorithm is appropriate for the data. By using the grain tracking algorithm, different thresholding algorithms can be tested at the early stage of image processing and quantification to select an appropriate algorithm.

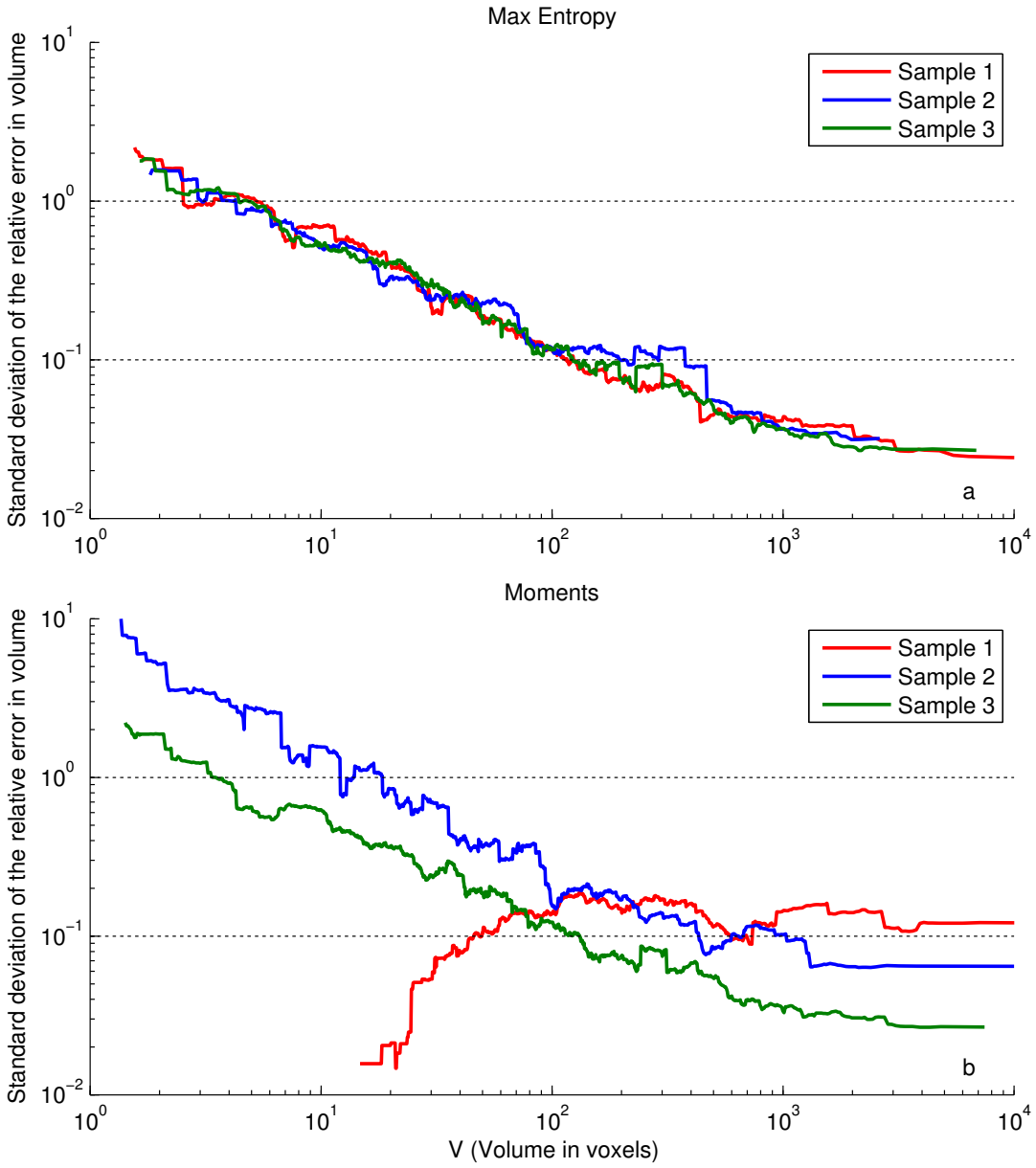


Figure 4.33.: The plot of percentage difference for grains having minimum distance to nearest surface of 70 pixels when between Day 0 and Day 1 using: a) Max Entropy. b) Moments.

4.8. Summary

The details of a series of automatic quantification algorithms for tracking particles undergoing leaching have been introduced in this chapter. Each quantification step, including thresholding, tracking, labelling and registration for both the ore particles themselves as well as the mineral grains has been introduced and explained. The rock phase

was thresholded using the Otsu algorithm while the metal sulphide grains were thresholded using the Maximum Entropy algorithm. For the ore particle tracking, the same ore particles in different scans can be tracked using the centroid of each particle as input. In order to fully understand the leach performance, the mineral grain tracking needed to be developed to track individual grains and their dissolution through time. A novel fast masking based tracking algorithm was developed using the transformation matrix from image registration. The algorithm can track individual grains even when they were fully leached or split into multiple smaller parts.

Based on the mineral grain tracking algorithm, the systematic and random errors and uncertainties in the volume measurement were also quantified. In particular, it showed the strong dependency on volume relative to voxel size that these errors have. To achieve a desired level of uncertainty due to random errors, the results from repeat scans or scans of similar objects need to be combined. It was shown that in the system studied in this work a single object of a thousand voxels has an uncertainty of about 5% in its volume, while 12 objects of a hundred voxels would need to be combined to achieve the same level of uncertainty. A methodology for eliminating systematic errors based on knowledge of how changes in threshold effect the measured volume and its dependency upon size was also developed. Moreover, based on the statistical analysis, the consistency for different thresholding algorithms can be compared quantitatively.

Chapter 5

Leaching Analysis Based on XMT

5.1. Introduction

In leaching experiments, the most common way to obtain the leach recovery comes from the measurements of the copper concentration in the collected solution using ICP-OES. The main disadvantage of this method is that it can only give the average recovery for the entire system. On the other hand, the use of XMT and image processing techniques make it possible to track and quantify leach performance at different scales by tracking individual ore particles, as well as individual mineral grains. However, for the image measurement, which is mainly volume measurement of mineral grain dissolution, the linear attenuation coefficients for the main sulphide minerals (e.g. chalcopyrite, bornite, pyrite etc.) over the range of X-ray energy spectrum shown in Figure 2.16 in Section 2.6.1 indicates that the different sulphide mineral phases in an XMT image are indistinguishable. Understanding the relationship between conventional chemistry measurements and image measurements is important when using XMT to quantify and understand the leaching process.

Moreover, as reviewed in Section 2.5, the majority of leaching related studies are focusing on the average leach recovery for the entire system. There is a lack of information about the leach performance and its variability for the individual ore particles as well as the mineral grains within the system. This barrier makes it difficult to understand and predict heap or even particle scale leach performance based on surface reaction kinetics. Analysing is thus becomes necessary and important.

In this chapter, the relationship between chemistry and image measurements is investigated by comparing the average leach recovery for the three columns (Table 3.2 in Section 3.4.1) with different flow rate values (see Section 5.2). By applying the image

quantification algorithms, including the mineral grain tracking algorithm, developed in Chapter 4, the leach performance can be analysed at different scales (see Section 5.3). In particular, at the grain level, the preliminary analysis shown in Section 4.4.2 indicates that looking at leach performance for each grain is not meaningful. A new method to quantify the leach performance at grain level needs to be developed, as well as the associated image measurement error (see Section 5.4 and Section 5.4.2). Finally, the effects of leaching parameters at sub particle level can be studied (see Section 5.4.3).

5.2. Relationship between Image Measurement and Chemistry Measurement

The conventional chemistry measurement measures the actual copper recovery whereas the image measurement measures the total sulphide mineral recovery based on the mineral volume reduction measurement. A useful method that can assist our understanding of the relationship between the image measurement and the chemistry measurement is looking at thin sections for both the original ore particles before leaching and the ores after leaching. Although the thin sections for before leaching and for after leaching cannot be the same ore particles, it is still possible to obtain some useful information, especially as to which minerals are left after leaching and what is the amount for copper minerals. By using thin sections and combining the data with the XMT data, it is possible to estimate the relative leaching rate of different mineral species. Therefore, in pure image analysis without having thin sections, investigating the similarities and differences between the image measurements and the chemistry measurement becomes crucial in understanding the underlying leach behaviour.

Taking Columns 1, 2 and 3 (Table 3.2) as examples, the relationship between chemistry measurement and imaging measurement can be further investigated. Columns 1, 2 and 3 have the same ore type, leaching solution and temperature. The only difference is the flow rate. Theoretically, there should be an optimum flow rate giving highest leaching kinetics and recovery when applying continuous flow with different flow rates. A possible explanation is that when the flow rate is too high the amount of oxygen, which is one of the main reactants in sulphide leaching, becomes the limiting factor, while if the flow rate is too low, the amount of leaching solution becomes the limiting factor. The difference in leach behaviour can be reflected in both chemistry measurement and image measurement, which is used to investigate the relationship between the two types of measurement.

For the image measurement shown in Figure 5.1, all three columns had rapid leaching

for the first 15 days. During this period, the main reactions likely to be were oxide and secondary sulphide leaching with sulphuric acid and ferric ion, together with fast leaching of other minerals including primary sulphides like chalcopyrite which were near the ore surface. After this initial period the leaching kinetics start to slow down and become relatively linear. The column with medium flow rate reaches around 55% recovery after 168 leaching days, followed by 51% for low flow rate and 49% for high flow rate. Although the column with medium flow rate has the highest recovery, the differences compared with other columns are not very large. The main reason for the similar recovery in the image measurement is that X-ray cannot distinguish different sulphide minerals within the ore particles. The ore samples used in this experiment contains both copper minerals and pyrite. The amount of pyrite is more than 5 times that of the copper minerals in volume. In the sulphuric acid system, the pyrite leaching is much slower compared with that of the other minerals.

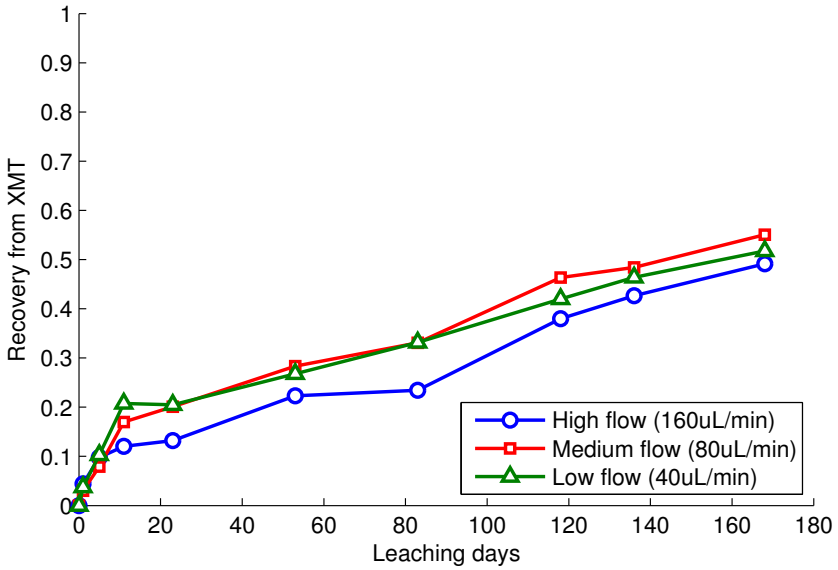


Figure 5.1.: Mineral recovery based on image quantification from XMT images.

However, an obvious difference in recovery with different flow rates can be seen when looking at the actual copper recovery based on the chemistry measurements from ICP-OES (see Figure 5.2). The column with medium flow rate reaches around 80% recovery, followed by 70% for low flow rate and 50% for high flow rate. Although there can be many reasons affecting the copper recovery, the result that the column with medium flow rate had the highest recovery followed by the column with low flow rate and high flow rate are consistent with the hypothesis that there is an optimum flow rate at which neither the oxygen in the air nor the supply of fresh reagent is the limiting factor.

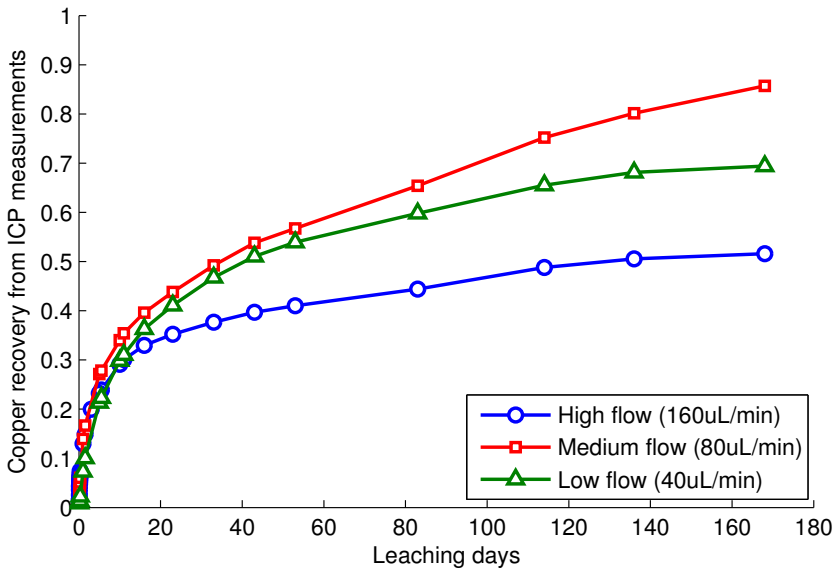


Figure 5.2.: Copper recovery based on chemistry measurements from ICP-OES. The copper recovery is estimated recovery by assuming the initial copper content is 0.78%, which is obtained from the raw material sample decomposition mentioned in Section 3.3.

From Figure 5.1 and Figure 5.2, it can also be observed that the magnitude of the recovery values for both methods are different but the trends are quite similar. The column with medium flow rate has the highest recovery followed by column with low flow rate and high flow rate. The fact that the difference is more pronounced in the actual copper recovery in the chemistry than in the total mineral recovery in the image measurement implies that the effect of the flow rate on pyrite leaching is lower than that on the copper species.

In the parity plot between the image measurement and the chemistry measurement from ICP-OES (Figure 5.3), it can be seen that the values for the slope for all three columns are larger than 1 (all points are above the dash line). This is again caused by the faster leaching of the copper containing minerals compared to the pyrite. In an acidic system with high ferric ion concentration (5 g/L), the bacteria activities generating sulphuric acid by consuming pyrite would be limited according to Equation (2.17) in Section 2.3.3.3. When comparing the three columns with different flow rates, it can be observed that the relationship between image measurement and chemistry measurement is quite similar for the first few points and starts to diverge after that. For the first few points (e.g. first five days), the main reactions were leaching of the oxide and secondary sulphide and minerals close to the ore surface for both copper and non-copper mineral species. The difference in flow rate did not affect the trend dramatically. However, after

this fast leaching stage, the leaching reactions can be affect by many different aspects such as the amount of oxygen and fresh leaching solution which can be affect by different flow rates. The shape of the curve in the parity plot was then controlled by the ultimate recoveries. It can be observed that the curves for three different columns with different flow rates diverge after the first five points. However, the parity plot can still be used to roughly estimate the the real copper recovery based on the image measurement.

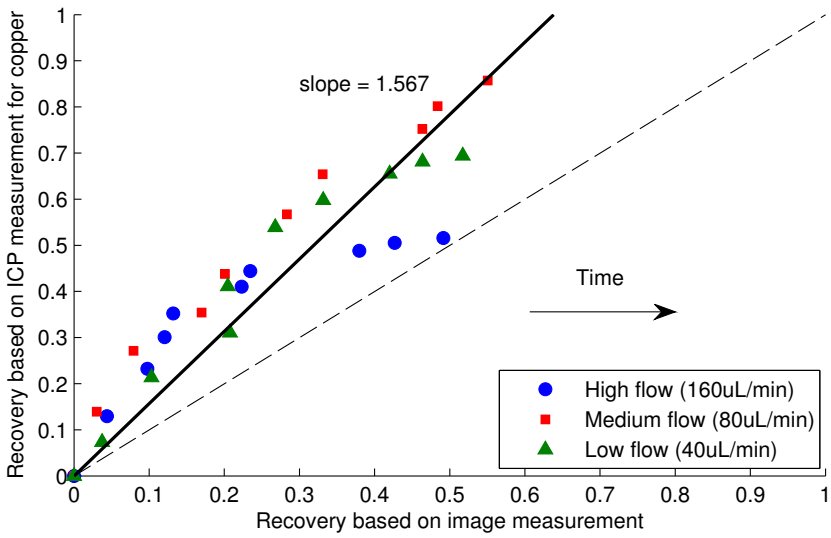


Figure 5.3.: Relationship of recovery between image measurement and chemistry measurement from ICP-OES.

5.3. Leach Performance Analysis at Larger Scales

The use of XMT allows us to investigate what is happening during leaching at both the individual ore particle scale and the mineral grain scale, providing a better understanding of leach behaviour. In this section, a leaching column (the column with high flow rate) is used as an example to demonstrate and investigate the leach behaviour to understand the leaching variability at different scales.

5.3.1. Column Scale Analysis

When studying the leach performance for columns at the column scale, the average mineral recovery can be compared to understand the macroscopic behaviour. This has been demonstrated when investigating the relationship between image measurement and chemistry measurement by comparing three leaching columns with different flow rates in the previous section.

Within a single column, the leaching variability at column scale can be investigated by comparing the overall leach performance for the three scanning volumes (top, middle and bottom) for each column. Figure 5.4 shows the recovery against the initial ore volume, mineral grain volume, and mineral content for the column (all top, middle and bottom volumes) after 168 leaching days for the high flow rate column. The error bar is calculated using ±2% which is the relative error when measuring the total volume of the minerals and it is mainly caused by the image processing algorithms. The value of ±2% is measured by comparing the total volume of tracked mineral grains for a rescanned volume to its reference volume Section 4.6. This error value is suitable for measuring the total volume of mineral grains with a wide size distribution rather than grains at a specific size (relative error against size can be obtained from Figure 4.26).

From Figure 5.4, it can be seen that all the three volumes within the column had quite similar initial ore volume, though the bottom volume had slightly higher initial sulphide mineral content. In a larger scale system, ore particles at the bottom normally have lower recovery due to the depletion of leaching solution. However, in this case, after 168 leaching days, all the three volumes reached approximately 45% recovery and the actual recovery for the bottom volume is slightly higher than the top and middle ones. The height dependency is not obvious and the main reason is that in this experiment the initial ferric ion concentration was high (5 g/L) and was enough for the entire column. Generally, the leach performance variability is not obvious at column scale. Therefore, it is important to study and understand the leach performance and its variability at the individual ore particle scale, as well as the grain scale.

5.3.2. Individual Ore Particle Scale

After ore particle segmentation and separation, the total number of tracked whole ore particles[1] is 26 for the example column. After particle tracking and leaching analysis based on image quantification, the recovery for these 26 particles can be calculated. Figure 5.5 shows the average recovery for the entire column, the average recovery for the three scanned volumes (top, middle and bottom) within the column and the recovery for the individual ore particles. It shows that at the scale of the individual ore particles, significant leach performance variation can be observed. Although the average recovery for the column is approximately 45%, the actual recovery range for all the 26 particles is between 18% and 96%. As the most significant barrier limiting the application of

[1] A whole ore particle means an ore particle that appears entirely in all the sequences. The ore particles, especially the particles located close to the edge of the scanning volume, were ignored when only part of the particles occurred in the scan.

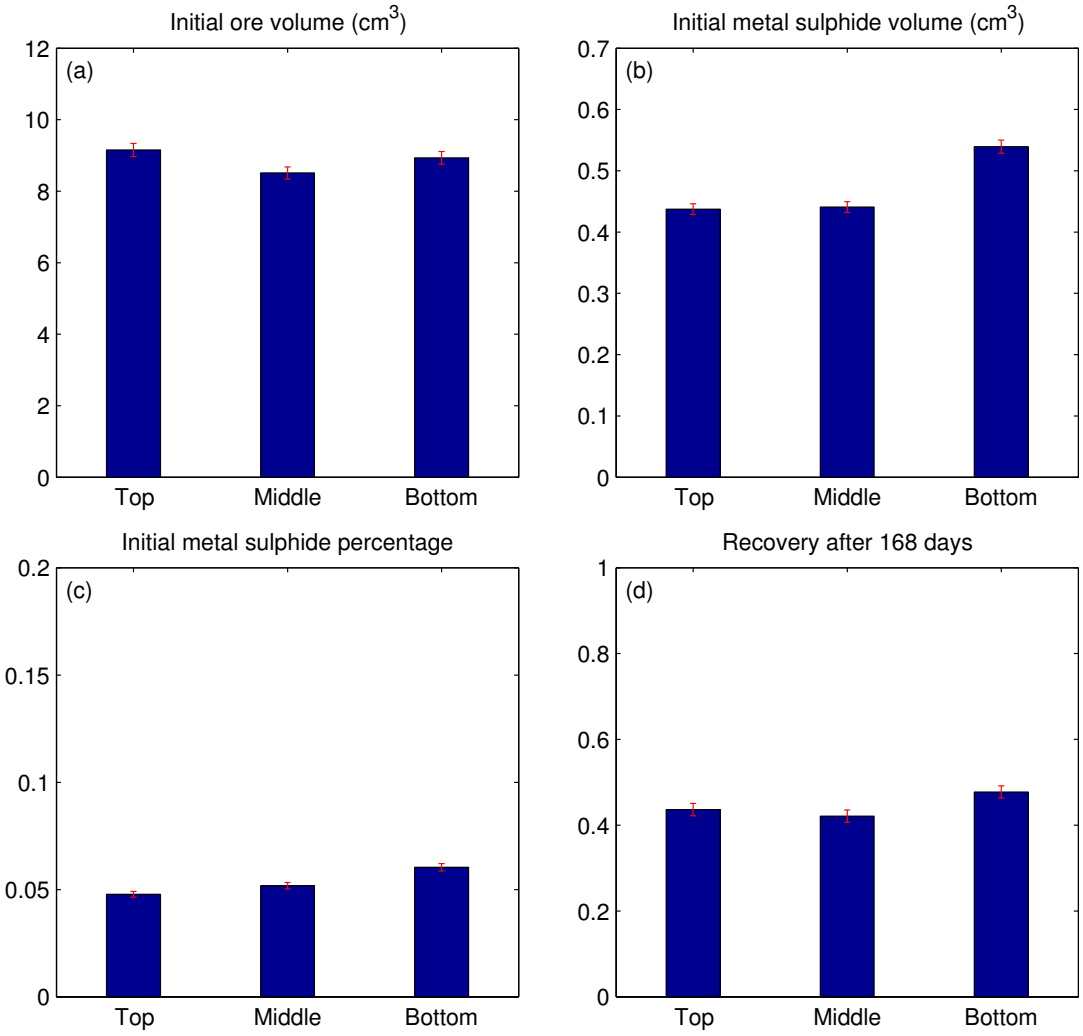


Figure 5.4.: The initial conditions of scanned volumes and their overall leach recovery. The error bar measures the uncertainty caused by the thresholding algorithm, which is ±2%. The resolution of the scanning is approximately 17 microns.

heap leaching is its long extraction time and relatively low recovery, especially for those ore particles with much lower recovery than the others, understanding what are the key aspects affecting the leach behaviour becomes important. In this small scale column leaching experiment, the initial ore particle size, the initial mineral grain content and the location of the individual ore particles are the main aspects which can affect the mineral recovery at this scale.

For each parameter, the linear correlation coefficient (r) and coefficient of determination (r^2) are also calculated. The linear correlation coefficient measures the strength and the direction of a linear relationship between two variables. A correlation closer to ± 1 is generally described as strong, whereas a correlation closer to 0 is generally described as

weak. The coefficient of determination gives the proportion of the variance (fluctuation) of one variable that is predictable from the other variable. This can be used to show how well the regression line represents the data.

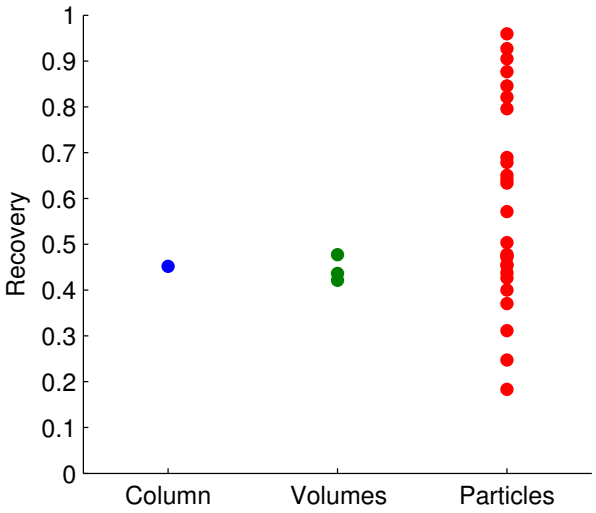


Figure 5.5.: Plot of the average recovery for the entire column, the average recovery for the three scanned volumes (top, middle and bottom) within the column and the recovery for the individual ore particles.

The total volume (in voxels) of each particle was measured using the voxel counting algorithm and converted into mm^3. Figure 5.6 shows the recovery against the initial ore particle size for all the tracked particles within the column. According to the linear correlation coefficient which is -0.40, a weak size dependency can be observed that the smaller ore particles generally having a higher recovery than the larger ones. There is, though, a lot of variability (with small coefficient of determination value of 0.16) in this trend that is likely to be due to other specific effects such as the distribution of the mineral grains.

The recovery for individual ore particles against the initial mineral grain content is plotted in Figure 5.7. Although there is a weak correlation with coefficient of -0.39, the majority of the ore particles have an initial mineral content less than 5%. The range of the initial mineral content is too narrow and the variability in recovery over this range is too high (with small coefficient of determination value of 0.15) for a clear trend to be observed.

Before investigating how grain distribution can affect the leach performance, the recovery of all the ore particles against their location was studied. The location of the ore particles is defined by the measured distance between the centroid of each particle and the centre of the column, which can be used to understand the variability related

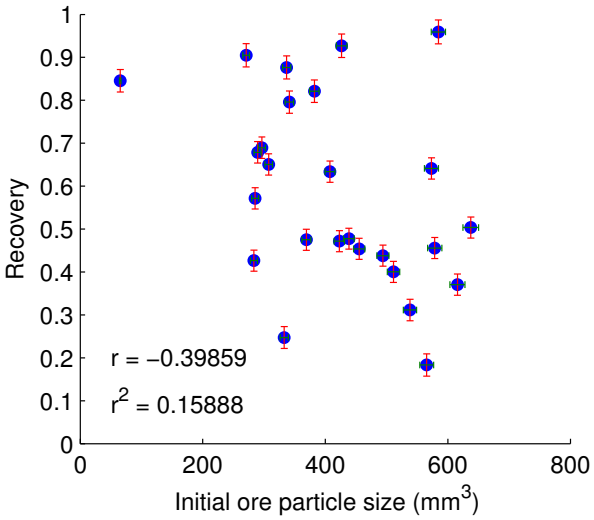


Figure 5.6.: The leach recovery for all the tracked ore particles against their initial ore particle sizes. The error bar measures the uncertainty caused by the thresholding algorithm, which is ±2%. The resolution of the scanning is approximately 17 microns.

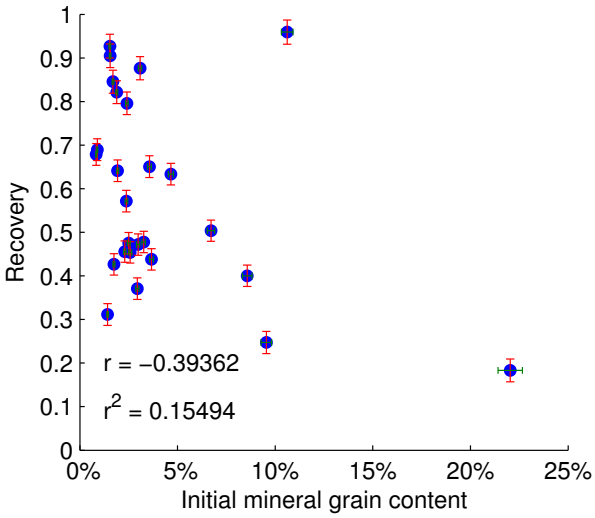


Figure 5.7.: The leach recovery for all the tracked ore particles against their initial mineral grain content. The error bar measures the uncertainty caused by the thresholding algorithm, which is ±2%. The resolution of the scanning is approximately 17 microns.

to the fluid flow and the wall effect in this small scale experiment. Figure 5.8 shows the individual recovery against the measured distance.

The fluid flow is one of the most significant aspects affecting the leach performance. After introducing the leaching solution on top of the heap, the flow pattern spreads out due to capillarity and dispersion. However, the ore particles far away from the main

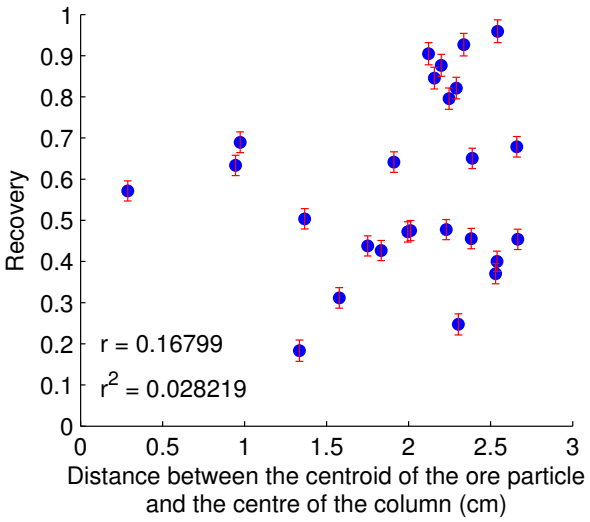


Figure 5.8.: The leach recovery for all the tracked ore particles against the distance between the centroid of the ore particle and the centre of the column (pixels). The error bar measures the uncertainty of caused by the thresholding algorithm, which is ±2%. The resolution of the scanning is approximately 17 microns.

flow pattern can be wetted, but the recovery can be much lower due to the inactive flow pattern and the slow ion exchange. However, in this experiment, a single drip feed located in the top centre of the column was used as feed for the small scale leaching column. Due to the scale of the column (internal diameter of the column was 28 mm), the flow can spread relatively evenly. Figure 5.8 also shows that there is no trend showing the ore particles located closer to the centre have better recovery, which is reflected by the very small correlation coefficient value of 0.17. However, high variability of leach recovery can be observed for those ore particles far away from the centre with larger distance values. This can be due to the wall effect in this small scale experiment. For the ore particles closer to the centre of the column, the variability cannot be observed due to the very limited number of particles located in that region.

According to the analysis above, the leach performance variability is more likely due to the grain distribution, which can be quantified by applying a 3D distance map. In the distance map analysis, each voxel is assigned a value depending on the distance to the nearest object boundary. The boundary voxels of the object are assigned a value of zero whereas the assigned value increases as the distance increases. During leaching the minerals close to surface should leach faster than the minerals locate in the centre of ore particle. Generally, the shorter the distance to the surface, the easier it is for the leaching solution to diffuse in and the dissolved species to diffuse out. Figure 5.9 shows a distance plot of an example particle after 168 days of leaching. A strong distance dependency can

be observed.

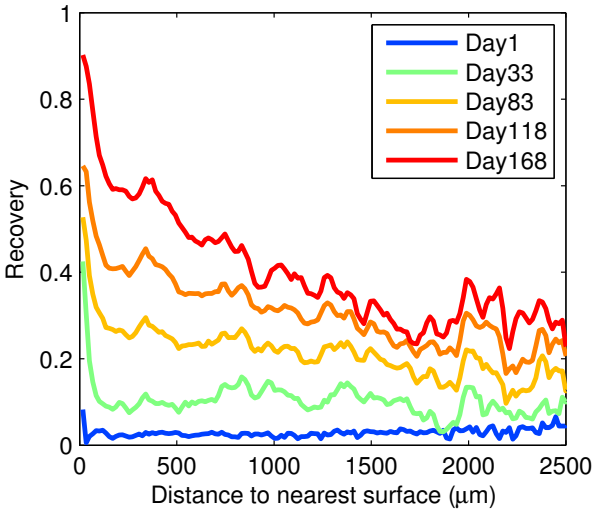


Figure 5.9.: Distance plot for an example ore particle along 168 days leaching period.

Among all the 26 particles, the majority of them have similar trends as shown in Figure 5.9. There are some ore particles that have high recovery even in the middle of the particle. The main reasons are probably the mineral species (e.g. oxides and secondary sulphides) and high porosity of the ore particles. If the porosity of the ore particle is high, the mineral grain size is small, or the minerals are oxides and secondary sulphides, the leaching can be significantly enhanced, even in the centre of the ore particle. Another possible reason can be that at the centre of the ore particle with higher distance value, the total number of grains and the total volume of grains are much smaller comparing with the region with small distance value. Even a small amount of grains with higher reaction rate can affect the average recovery significantly. The average recovery of all the mineral grains within those 26 tracked ore particles against distance can then be calculated, shown in Figure 5.10. A strong distance dependency can be observed showing that the mineral grain recovery can be significantly influenced by the spatial grain distribution.

5.4. Statistical Analysis at the Grain Scale

In the small scale column leaching experiment at the individual ore particle scale, there is a correlation between leach performance and ore particle size (Figure 5.6); but there is no clear trend with the initial mineral grain content, or with the location of the particles within the column. The mineral extraction is a strong function of its distance to the ore particle surface (see Figure 5.10), with a strong dependency seen in all the

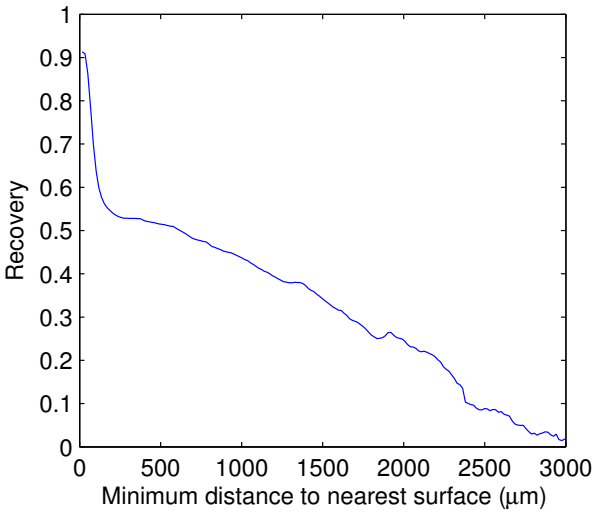


Figure 5.10.: The average leach recovery for all the tracked ore particles against the distance between grains and nearest surfaces after 168 leaching days.

studied particles. The differences in the initial distribution of the grains relative to the ore particle surface is thus a major source of the variability in the average leaching rates of the individual ore particles. In order to fully understand the leach performance and its variability, the analysis also needs to be carried out at the grain scale.

Within a single ore particle, Figure 5.11 shows the change in recovery for 25 mineral grains chosen randomly out of those that have an initial volume of between 500 and 1000 voxels (this corresponds to initial equivalent spherical diameters of between about 75 μm and 95 μm). As well as these 25 randomly chosen grains, the average behaviour of all 394 mineral grains within the single ore particle is also plotted. While the uncertainty in the size of the individual grains due to measurement error within this size range is small, it is not trivial (3 or 4 percent based on Figure 4.26), the effect of measurement error on the calculation of the average leach behaviour is tiny, though, due to the large sample size. The measurement uncertainty will be the reason why a small number of the recoveries for individual mineral grains are below zero (The trends for individual grains will be particularly sensitive to measurement errors in the initial scan as this influences every subsequent recovery value).

Not only is it important to understand the average leach behaviour of the grains, it is also important to understand the variability in these rates. This variability can be seen in the range of recoveries within the 25 randomly selected grains shown in Figure 5.11, but it is desirable to analyse this variability in a quantitative manner. The two main parameters are the initial grain size and its distance to the surface.

After applying the grain tracking algorithm, the total number of grains that were

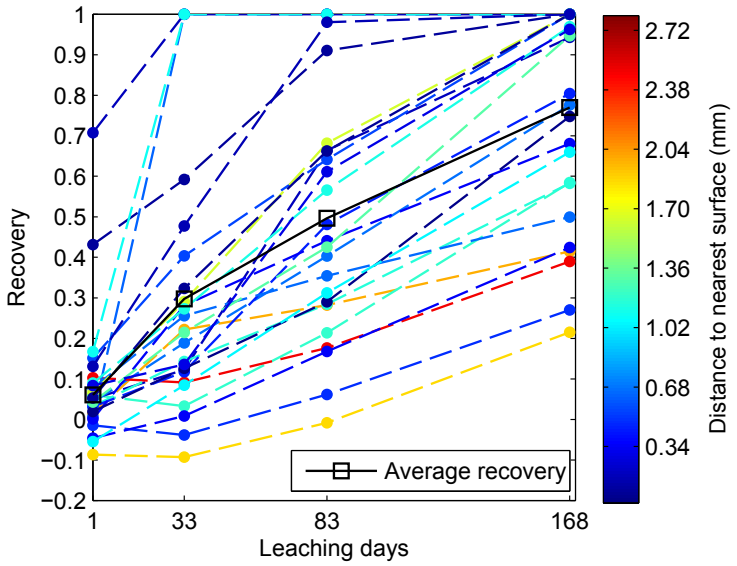


Figure 5.11.: The change in recovery of 25 example grains with initial volumes of between 500 and 1000 voxels over the 168 days of leaching. In addition, the average recovery behaviour for all 394 grains within this category is also plotted.

tracked within those 26 ore particles was 136443. Based on the preliminary investigation of the leach performance shown in Section 4.4.2, analysing tens of thousands of grains individually is not very meaningful and efficient, especially for smaller grains which have high measurement errors and uncertainties (see Figure 4.21). Therefore, it is more reliable to divide all the grains into different size-distance categories and study the average leach behaviour with its variability statistically for each category. The grains were divided into categories based on size and distance to the surface, with intervals chosen to give a reasonable distribution of the grains over the categories (see Figure 5.12). Without having, for instance, different size intervals for different distance categories it is impossible to perfectly balance the number of grains in each category. As they have smaller measurement errors associated with them, it is less important to have a large number of grains in the categories with larger grain sizes.

5.4.1. Leaching Performance Analysis for Different Categories

The average leach recovery for different size-distance categories is shown in Figure 5.13. The categories shown are those with average size larger than 100 voxels and sample size larger than 10. A clear colour gradient can be observed with increasing average initial grain size and average distance to the ore surface. The colour gradient indicates that the grains with smaller size and shorter distance have higher leaching kinetic rate as expected.

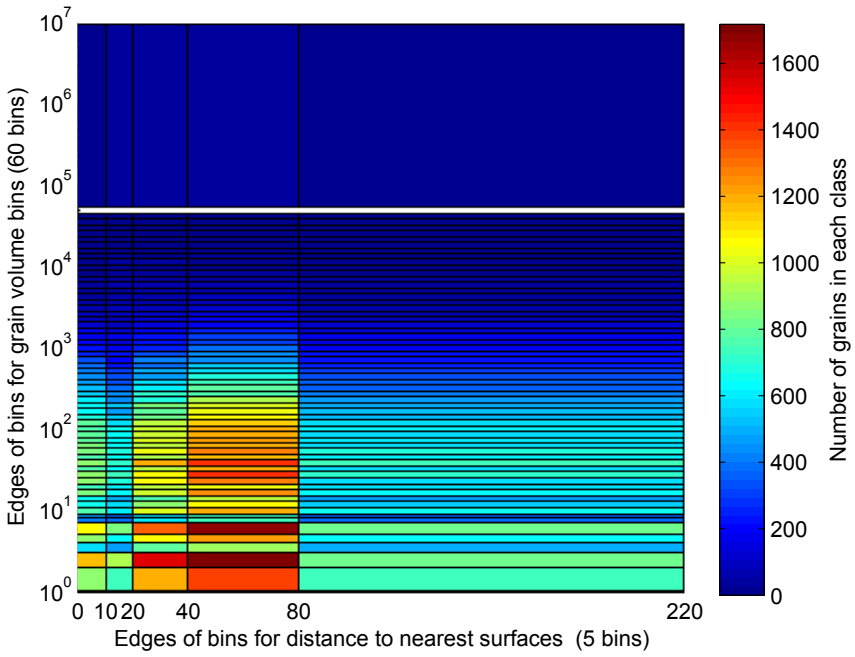


Figure 5.12.: Dividing tracked grain into different categories according to size and distance to surface. The colour indicates the number of grains in each category.

Before further investigating the leach performance for individual size-distance categories, it is important to understand how representative the average recovery value is for each category with narrow size and distance intervals after combing a large number of grains (example grains with quite different behaviour have been shown in Figure 5.11). Figure 5.14 shows the average mineral recovery for different size-distance categories at Day 11 and Day 168. The error bar on the average leach recovery is the 95% confidence interval, showing the leaching variability within the category. It can be observed that the majority of the categories have a quite narrow interval range at both early stage (Day 11) and late stage (Day 168) of the leaching. This indicates that after combining a large amount of grains, the average leach recovery for each category is representative. The observed leaching uncertainties increases at the larger gain sizes which is mainly due to the small sample sizes for those categories (Figure 5.12). The detailed quantification of the overall variability, the measurement variability and the underlying variability of the leach behaviour is described in Section 5.4.2.

Although the average leach recovery is representative for the majority of the categories, in Figure 5.14 the leaching variability at the late stage of leaching (Day 168) is much larger than the variability at the early stage of leaching (Day 11). This is mainly contributed by the actual leaching variation among different minerals, especially different mineral species.

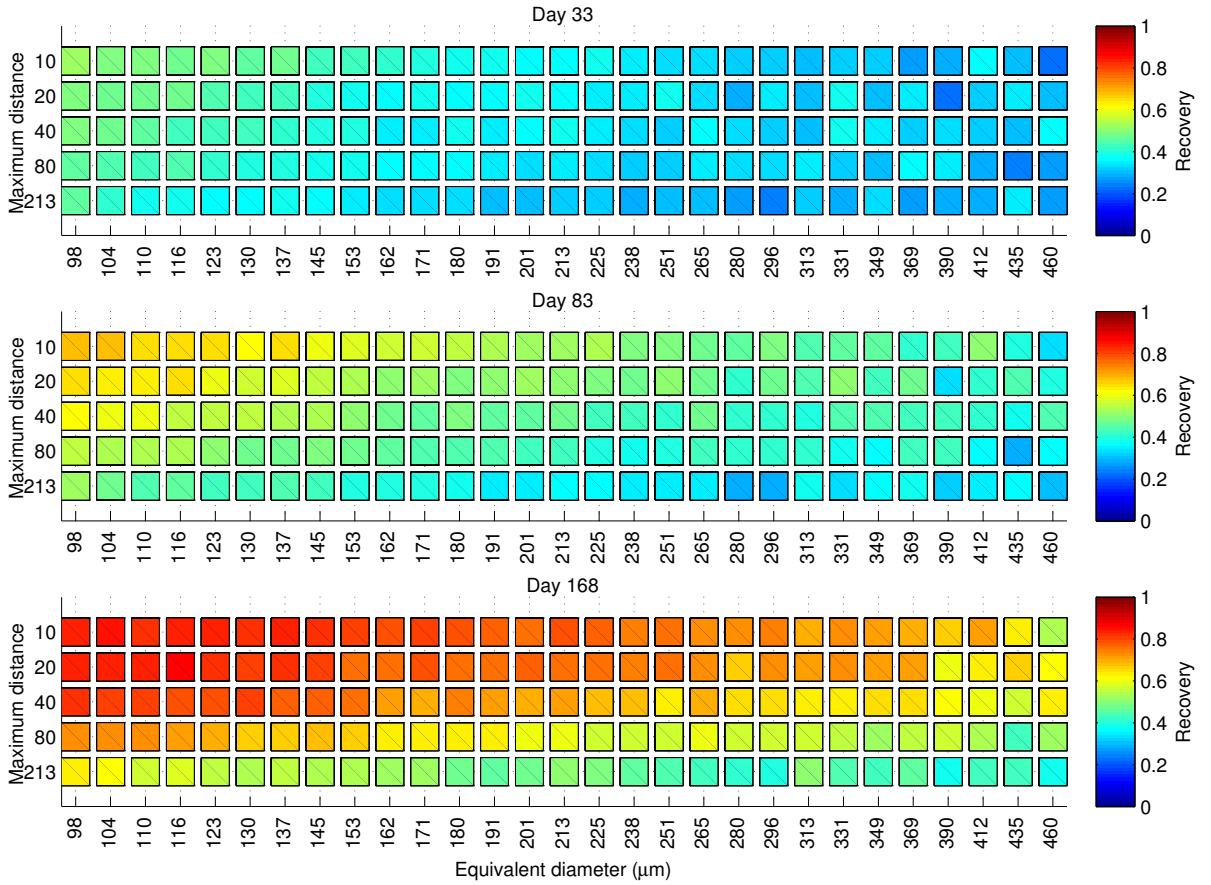


Figure 5.13.: Plots of average metal sulphide recovery in each size-distance category in three difference time points using colour map indicating percentage recovery.

The leach performance can be analysed statistically at the grain level by analysing the average recovery for different size-distance categories. As shown in Figure 5.14, the leach performance for each category is a function of the initial grain size and the distance to ore surface for the grains. Strong size and distance dependency can be observed. Figure 5.15 shows the average leach recovery for the categories, which have five different size and distance categories.

From Figure 5.15, two leaching periods for all the categories can be observed. The first stage is the fast leaching period for the first 30 days, followed by the slower leaching period after that. The fast leaching period existed for all categories. Approximately 15% to 20% of minerals were dissolved during this period for the majority of the categories, even the categories which have high initial grain volume and high distance value. At this period, the main minerals dissolved are likely to be oxides and secondary sulphides, as well as minerals closer to the ore surface and the minerals in the centre of the ore particles, but with accessibility for leaching solution via pores and cracks connected to

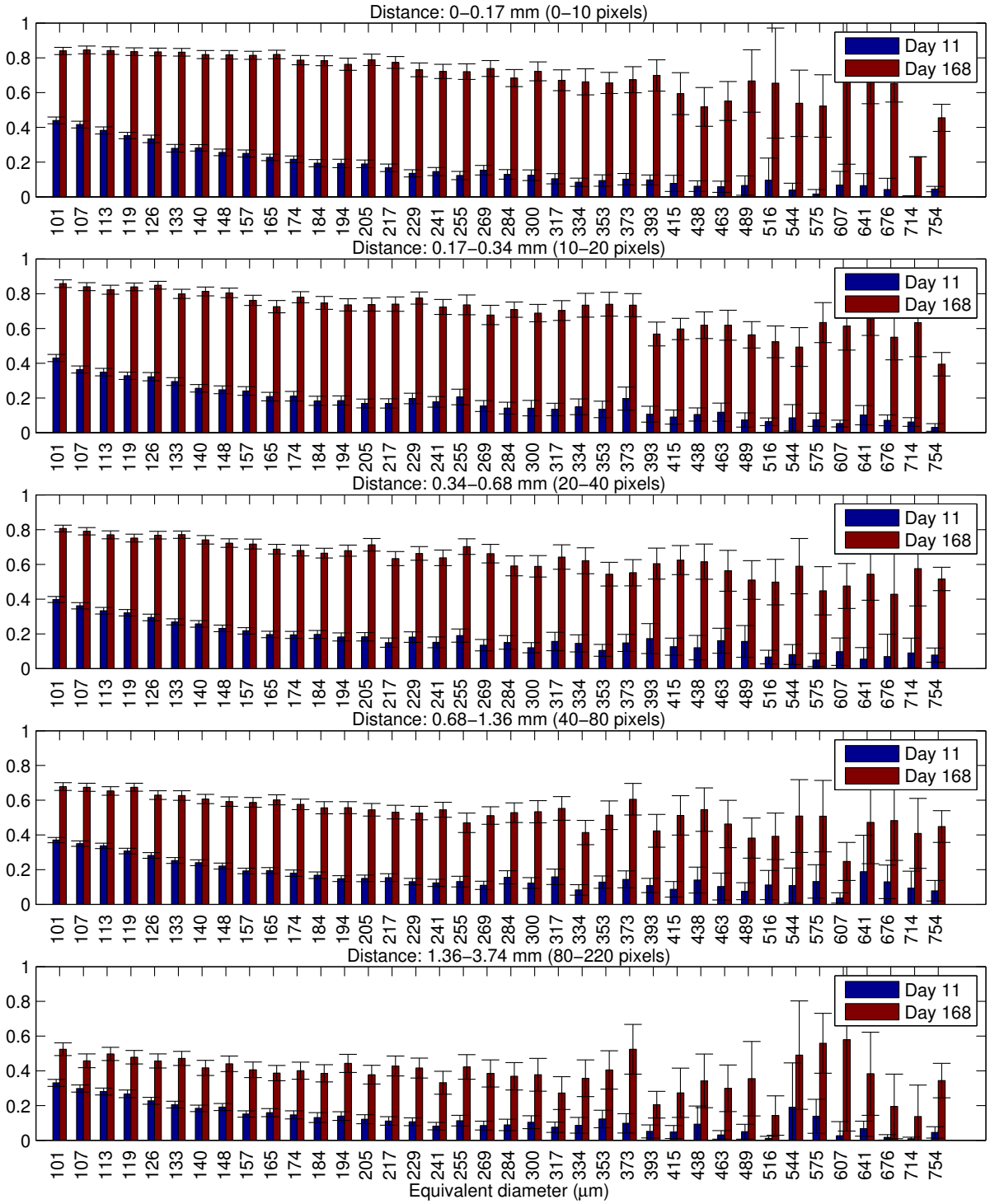


Figure 5.14.: The recovery for all the size-distance categories with average initial grain size larger than 100 voxels after Day 11 and Day 168. The error bar measures the 95% confidence interval.

the outside. The leaching rate subsequently started to slow down and became relative stable. After about 30 to 50 days leaching, the system started the second leaching period with much slower and steady leaching rates.

Although both size and distance dependency can affect the leach performance, the size dependency is more obvious at the early stage of the leaching (e.g. first 30 days). The ultimate recovery for the categories which have different sizes but similar distance to the ore surface are also similar. The gradually decreased size dependency can also been seen in Figure 5.16, which shows the recovery against leaching period at different distance values for categories with different sizes. A much clearer size dependency can be seen at Day 11 and it becomes weaker for all categories at Day 83 and Day 168. This probably because the initial rate is surface reaction limited while the system will become more diffusion limited as time passes.

On the other hand, the distance dependency is less significant at the early stage. The categories which have different distance to the ore surface values but same size have quite similar recoveries (see time points for the first 30 days in Figure 5.15 and Day 11 plot in Figure 5.16). However, while the size dependency becomes weaker, the distance dependency becomes much stronger and the ultimate recovery for all the categories is predominantly a function of distance (see both Figure 5.15 and Figure 5.16). At the late stage of the leaching period, the majority of the minerals remained within the shorter distance regions were non-leachable minerals and the recoveries in those regions was nearly completed and became relatively stable. However, the minerals in the centre of the ore particles was still undergoing leaching due to the long distance for the leaching solution to diffuse in and the dissolved minerals to diffuse out. This ends up with much lower recovery values for the categories with larger distance values. This indicates that distance to the ore surface is the dominant parameter controlling the ultimate recovery for a heap leaching system.

Although the grain size can significantly affect the fast leaching stage for the first one or two months, the size distribution is mainly controlled by the mineralogy and it is not very likely to be controlled and modified. Moreover, as a heap leach for primary sulphides can last at least 12 months or more, the ultimate recovery for the system is therefore likely to be mainly affected by the distance control. The distance values within ore particles is mainly contributed by the ore particle size, cracks (including micro cracks) and pores which are connected to outside.

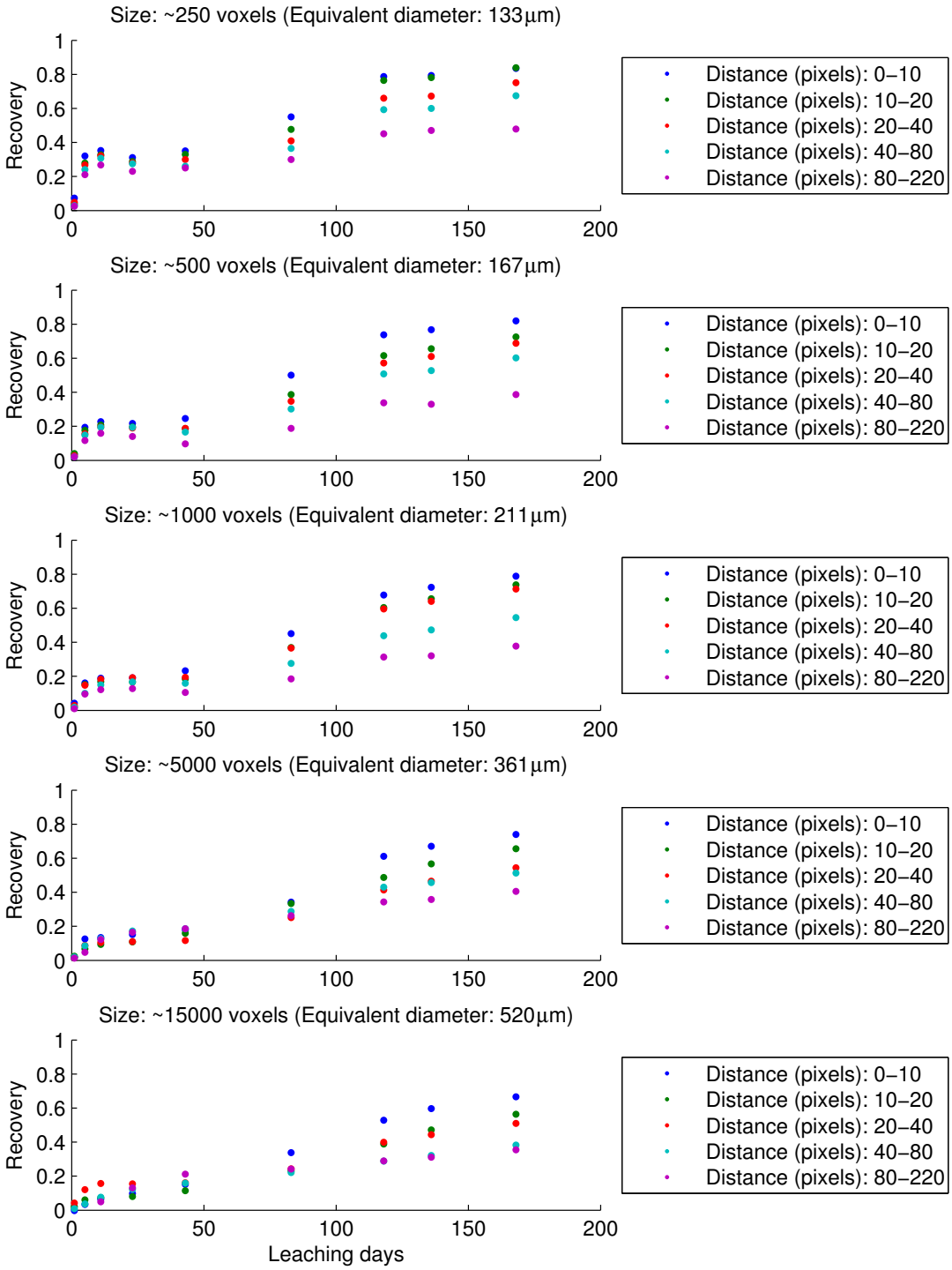


Figure 5.15.: The recovery for categories with different average initial grain size at different distance against leaching time: e.g. ∼250 voxels, ∼500 voxels, ∼1000 voxels, ∼5000 voxels and ∼15000 voxels.

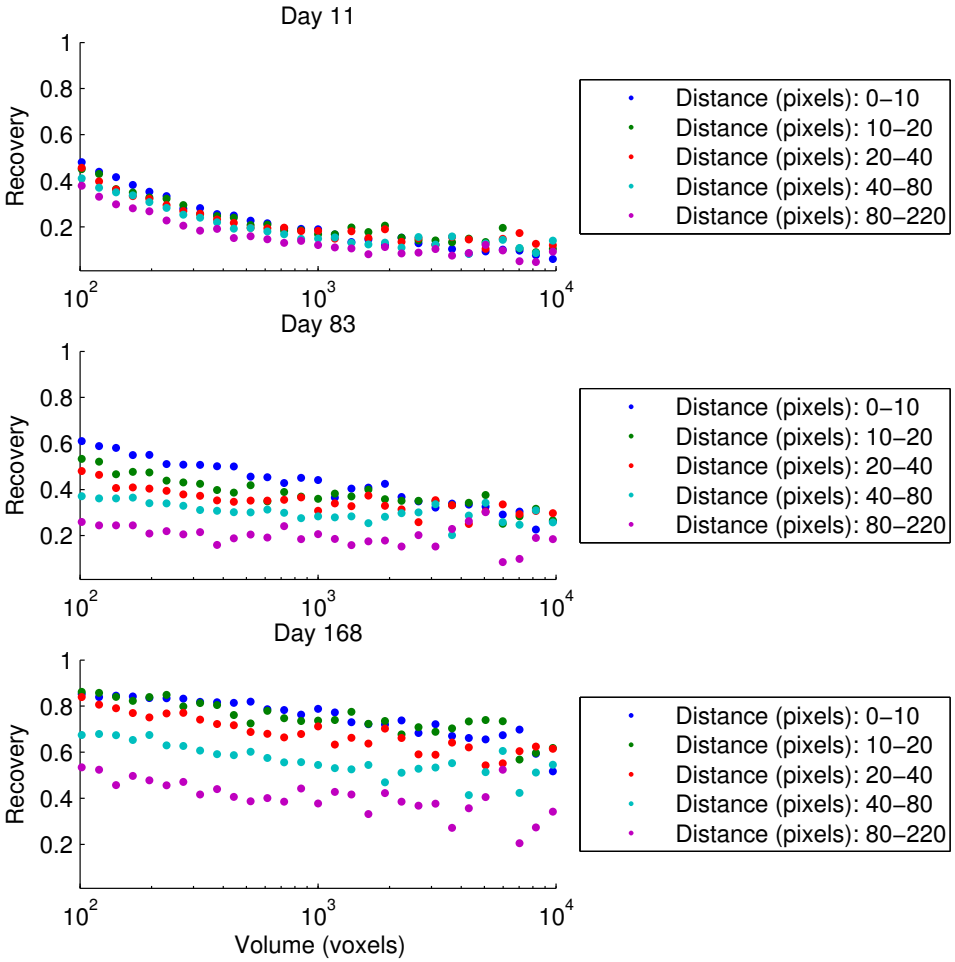


Figure 5.16.: The recovery for different categories at different distance against average initial mineral grain size at different time points: e.g. Day 11, Day 83 and Day 168.

5.4.2. Error Analysis of Leaching at the Grain Scale

The leaching variability obtained from the image quantification (overall measured variability), as shown in Figure 5.14, contains contributions from both the measurement variability and the underlying uncertainty, both of which will vary with the size of the mineral grains. Quantifying the measurement uncertainty in terms of the overall uncertainty and the underlying uncertainty is also crucial when analysing the leach performance statically based on image measurements.

The measurement uncertainty is a function of the size measurement, the leaching time (which can affect the size measurement after volume reduction due to leaching) and the number of mineral grain measurements within each category (Figure 5.12). The measurement uncertainty for individual grain volume measurement is purely size dependent and for individual mineral grain with a size larger than 100 voxels, the measurement error is less than than 10% (see Figure 4.26 in Section 4.5.2). The underlying variability will be due to a large number of different factors, including differences in mineralogy of both the mineral grains themselves and the surrounding gangue material, differences in reagent accessibility not only due to differences in distance to the surface (which can be accounted for), but also differences in the permeability/diffusivity of the material between the grain and the surface and many other effects.

The underlying variability among different size-distance categories is the key aspect we are interested in. In each category at each time point t, the average size can be calculated as:

$$\overline{V_i(t)} = \frac{\sum_{i=1}^{N} V_i(t)}{N} \tag{5.1}$$

where N is the total number of grains in a particular category. The standard deviation, which represents the observed overall uncertainty in the leach behaviour, can be expressed as:

$$\sigma_{\text{overall}}\left(\overline{\Delta V_i(t)}\right) = std\left(V_i(0) - V_i(t)\right) \tag{5.2}$$

$$\sigma_{\text{overall_relative}} = \frac{\sigma_{\text{overall}}}{\overline{V_i(0)}} \tag{5.3}$$

where i means each grain in the category, $\sigma_{\text{overall}}\left(\overline{\Delta V_i(t)}\right)$ is the standard deviation of the volume change after a certain leaching time (t). In these calculations, the standard deviation in the error in the volume is more useful than that of the relative error (Figure 4.26 in Section 4.5.2). Figure 5.17 is calculated based on the data in Figure 4.26.

Using Figure 5.17, the average measurement error can be calculated as:

$$\sigma_{\text{measurement}}\left(\overline{\Delta V_i(t)}\right) = \sqrt{\frac{\sigma(V_i(0) - V_i(t))^2}{N}} \tag{5.4}$$

$$\sigma(V_i(0) - V_i(t))^2 = \sigma(V_i(0))^2 + \sigma(V_i(t))^2 \tag{5.5}$$

$$\sigma\left(V_i(t)\right) = \left(\frac{1}{aV_i(t)^b} + \frac{b}{V_i(t)}\right)^{-1} \tag{5.6}$$

$$\sigma_{\text{measurement_relative}} = \frac{\sigma_{\text{measurement}}}{\overline{V_i(0)}} \tag{5.7}$$

where $\sigma_{\text{measurement}}\left(\overline{\Delta V_i(t)}\right)$ is the average measurement error, a is the prefactor in the power law relationship (2.6296) and b is the power law exponent (0.4). The derivation of Equation (5.6) can be found in Appendix B.1.

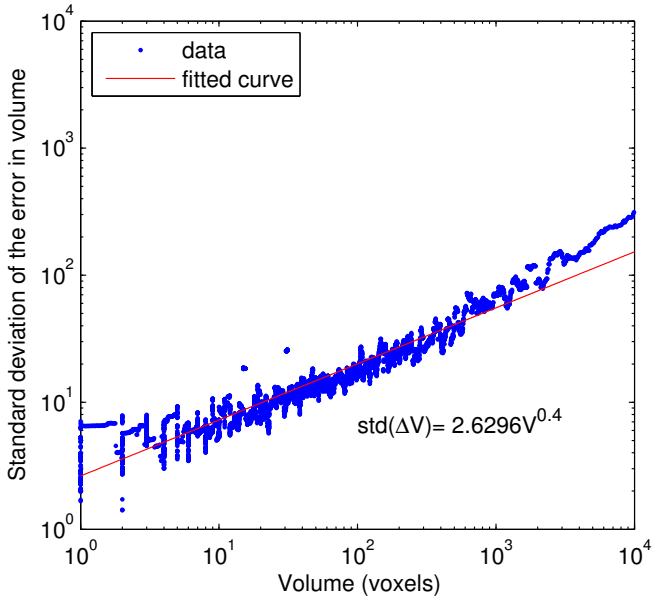


Figure 5.17.: The plot of standard deviation of the error error in volume.

If it is assumed that the underlying variability and the measurement uncertainty are independent of one another, then the overall uncertainty can be written as a function of the measurement and underlying uncertainties.

$$\sigma^2_{\text{overall}} = \sigma^2_{\text{measurement}} + \sigma^2_{\text{underlying}} \tag{5.8}$$

$$\sigma^2_{\text{overall_relative}} = \sigma^2_{\text{measurement_relative}} + \sigma^2_{\text{underlying_relative}} \tag{5.9}$$

where σ is the standard deviation. It should be noted that this can only easily be used for narrow size intervals since the measurement uncertainty is a strong function of the grain size.

Assuming that the measurement uncertainty is approximately the same for each scan and any systematic error has been accounted for, using the equations above (Equation (5.4), Equation (5.5), Equation (5.6) and Equation (5.7)) and the relative error plot in Figure 5.17 will allow us to quantify the measurement uncertainty.

Figure 5.18 shows the measured overall uncertainty expressed as a relative standard deviation after two different times (Day 11 and Day 168) together with the the estimated measurement errors. The measurement error is mainly a function of grain size, but will also depend on the extent of extraction in the categories. During leaching, the volume reduction is also a function of time. At the early stage of the leaching, the measurement errors for different categories are almost only size dependent and are overlapping. This is mainly due to the limited amount leaching that has happened. There is some scattering at Day 11 when the size is small, the main reason is the slight different sample size for these categories. At Day 168, due to the leaching, the measurement errors increase due to the volume reduction of grains which give high measurement error for the individual measurement. Due to the dominant distance dependency at the late stage of the leaching, the measurement errors for different categories also have distance dependency, especially for the categories with smaller grain sizes.

After combining a large number of grains in each categories, from Figure 5.18 the measurement errors are comparable and become not significant for most of the categories when the initial grain size is larger than 100 voxels. However, Equation (5.8) and Equation (5.9) become hard to apply when overall uncertainty and the measured uncertainty are similar to one another as both errors in the estimate of the measurement uncertainty and the overall uncertainty (which is based on a finite sample size) can swamp the effect of the underlying uncertainty. This becomes the case when looking at grains with smaller sizes in Figure 5.18 where the estimated measurement error is larger than overall uncertainty and the overall measured variability.

5.4.3. Effects of leaching parameters at sub particle level

Heap leaching is a complex process and the leach performance can be affected by different parameters, such as flow rate, ore type, temperature, chemistry, Eh, etc.. The main interest in the leaching analysis is to understand how these parameters can affect the leach performance. Some of the information can be obtained by comparing the

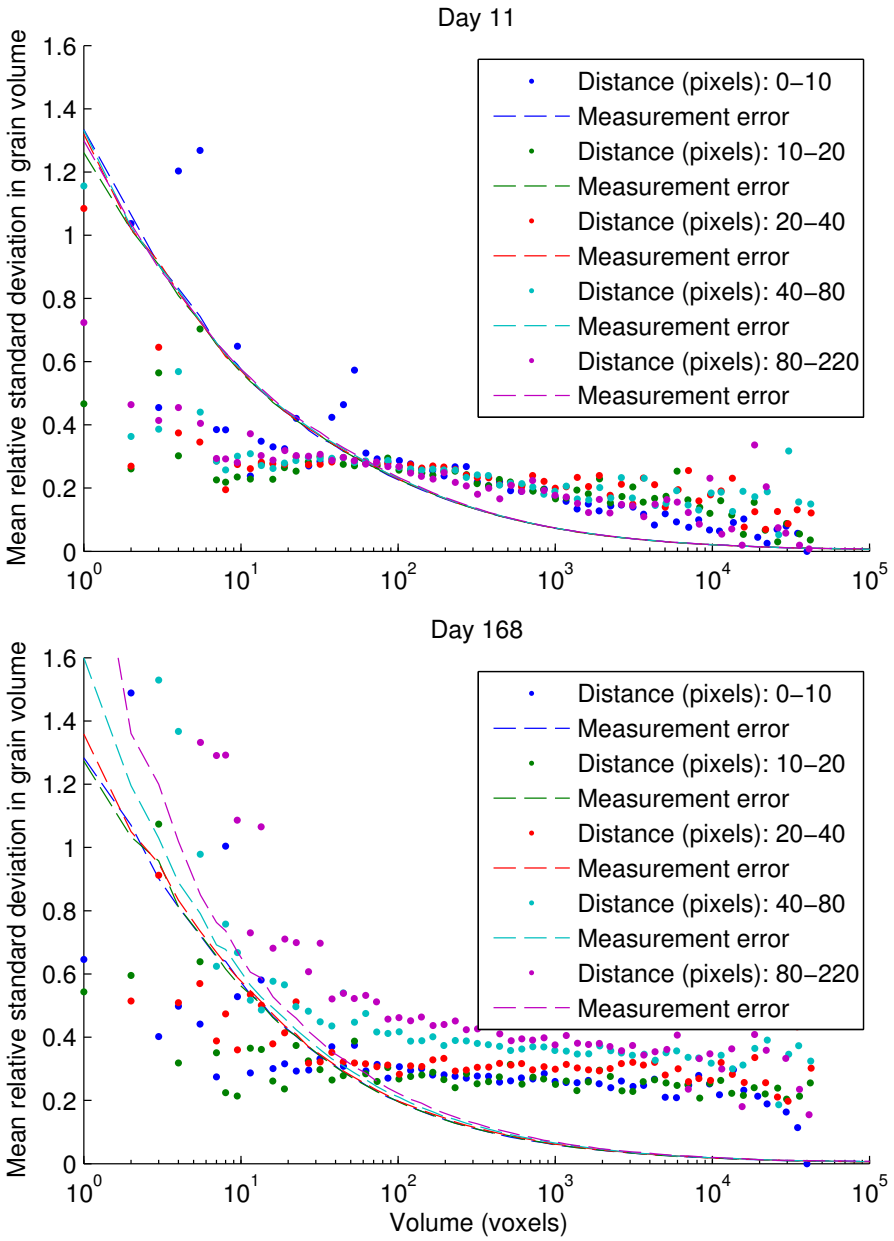


Figure 5.18.: Plot of overall uncertainty (expressed as a relative standard deviation) and measurement uncertainty (underlying uncertainty is the difference) for the example ore particle at Day 11 and Day 168.

ultimate recovery for the entire column at different leaching conditions. The limitation of comparing only the average recovery for the columns is that it needs to assume the change of parameters will have the same effect for all the grains. However, in reality, it has been shown in Section 5.4.1 that the leach performance for mineral grains is not only controlled by their initial sizes, but also the grain distribution which is defined by both their size and the distance to the surface. Therefore, it is important to investigate the

effect of changing leaching parameters in depth because the change of leaching conditions may affect the leaching process at different stages, or it may affect different mineral grains (e.g. different initial sizes and distances to the surfaces) differently. More complex leaching strategies can therefore be developed to improve the leaching efficiency.

As shown in the previous section, the average leaching recovery for different size-distance categories at the grain level can be used to quantify the leach performance and its variability within a single column. In this section, the leach behaviour for the three columns with different flow rates were compared to see how flow rate can affect the leaching process for particles of different sizes and distances to the surface.

The main influences of applying different flow rates is the amount of fresh leaching solution supplied, and the effect on air ingress into the column. It can significantly affect the performance that is limited by the reaction rate. According to Section 5.4.1, it can be concluded that the distance dependency is dominant for the ultimate leach recovery whereas the size dependency, which is more reaction limited, is only dominant at the early stage of the leaching process. It becomes possible to investigate how different flow rates can affect the leaching process by plotting the average leach recovery for categories at each distance value (shown in Figure 5.19). It can be seen that the leach recovery for the column with medium flow rate has the best or close to best recovery at all distance values, which finally leads to the best ultimate recovery (see Figure 5.1). The column with high flow rate has quite high recovery for the grains closer to the surface due to the sufficient reagent supply, but the recovery drops quickly when the distance value increases. This is likely caused by the lack of oxygen due to the high flow rate. In contrast, the leach recovery for the column with low flow rate is quite low for the categories with smaller distance value compared to the columns with high and medium recovery. However, its recovery for the grains with higher distance value is higher than the column with high flow rate and is similar to the column with medium flow rate. This indicates that the mineral grains within the ore particles are more diffusion limited.

5.5. Summary

When analysing the leach performance based on image measurements, it is important to validate the image measurement by comparing the results with the results obtained from conventional chemistry measurement. The main reason is due to the limitation that X-ray cannot distinguish different sulphide phases within the image. The results from the image measurement is actually the total mineral recovery whereas the results from chemistry is the actual copper recovery. After comparing the results from both methods,

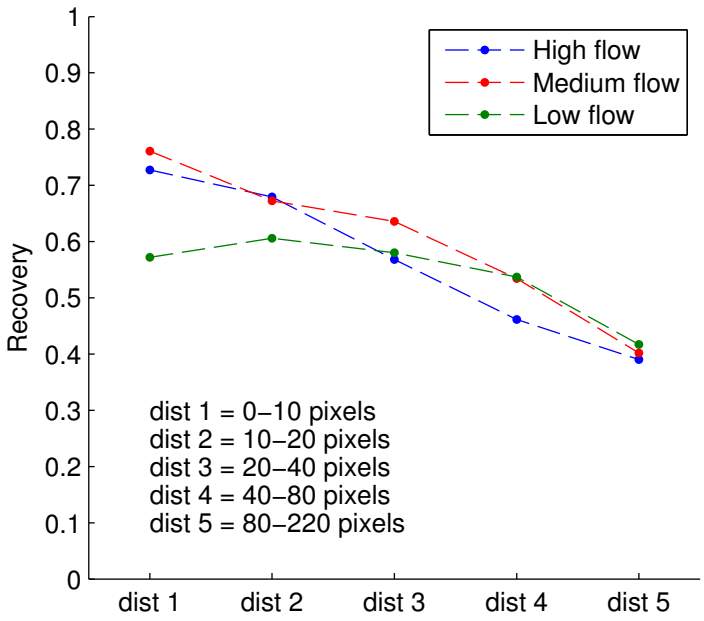


Figure 5.19.: Comparison of the average leach recovery at different distance to surface values among three columns with different flow rates at Day 168.

there was an obvious difference in the leach recovery for the columns with different flow rates based on the chemistry measurements for copper whereas the leach recovery for the columns based on the image measurements were quite similar. This was due to the low content for the copper species within the ore particles. Despite this the copper extraction and total sulphide exaction are quite strongly correlated at shorter leach times.

Based on the developed imaging algorithms, an example leaching column was used to study its leach performance and its leaching variability at different scales. At the column scale, the three scanned volumes within the column (top, middle and bottom) were compared. It was found that the initial ore volumes, the initial gain volume and the initial grain content were quite similar in all the three volumes and the ultimate recoveries (Day 168) were also similar. There was thus little variability at the column scale. After applying the centroid tracking algorithm, the leach behaviour can be analysed at the individual ore particle scale. Large leaching variability for the recovery can be observed between ore particles, ranging from approximately 18% to 96%. The ore sizes, mineral grain content for individual ore particles and location of the ore particles were further investigate. There was a slight ore size dependency where the overall recovery decreases when the ore volume increases.However, though the limited size rage for the particles in the column precluded a detailed analysis of the effect of particle size on leach rate.

After plotting the grain recovery against the location of the grains within ore particles, which is defined as the distance between the grains and the nearest surface, a strong

distance dependency was found.

At grain scale, after tracking all the grains individually, the tracked grains were subdivided into different size-distance categories to analyse the average leach performance and the variability for different categories. The results showed that both grain size and distance have a big impact affecting the leach performance. The size dependency is dominant at the early stage of the leaching while the distance dependency is more dominant for later stage and long term leaching. The variability of leach performance for different categories after considering the measurement errors was quantified. Moreover, the statistical analysis can also be used to investigate how a parameter can affect the leaching process. Examples of analysing the leach recovery for the columns with different flow rates show that, although the high flow rate can enhance leaching closer to the surface, due to the sufficient leach reagent, it can lower the recovery for the grains with higher distance values. This is likely caused by a lack of oxygen.

Chapter 6

Modelling of Apparent Leach Kinetics

6.1. Introduction

The conditions within the fluid surrounding the particles have been studied at both heap and column scale experimentally and via simulation (Mostaghimi et al., 2014; Petersen and Dixon, 2007; van Hille et al., 2010) while the surface reaction rates have typically been studied using finely milled particles in stirred tanks (Córdoba et al., 2008a; Koleini et al., 2011). Where the understanding is most lacking is in the processes occurring within the individual ore particles and, in particular, how the external conditions, internal mass transport processes and surface reaction kinetics interact to produce the apparent leach kinetics that are observed.

Understanding these apparent kinetics and how they depend upon the chemical conditions and the extent of extraction is an important consideration in the modelling and simulation of heap leaching. Current heap leaching simulators typically make use of simplified models to describe this relationship often based on shrinking core models (reviewed in Section 2.4.3) and variants on this model (Bartlett, 1998; Dhawan et al., 2012; Dixon and Petersen, 2003; Ogbonna et al., 2006). These models make a number of implicit and explicit assumptions about the leach behaviour at the particle scale. The assumptions made by some or all of these models include that the particles are spherical and all the same size, the mineral grains are uniformly distributed throughout the particle, there is uniform porosity and that there is a sharp interface between the leached and unleached portions of the particle. In reality none of these assumptions are particularly applicable as there is a considerable variability both within individual particles and between

different particles. This variability includes ore type, shape, mineralogy, porosity, grain distribution, etc.. Moreover, there has been limited work on using XMT images as direct inputs to model the leaching process which can relax many assumptions using simplified models.

In this chapter, a new model is produced to simulate the leach performance. It demonstrates a methodology by which the XMT data is not only used to validate the modelling, but also forms a key part of the modelling input as it can relax some common assumptions such as shape, porosity, grain distribution, etc.. The main purpose of this model is to use the initial XMT scans before leaching and the short term leaching behaviour extracted from leaching analysis to simulate and predict the long term leach performance.

6.2. 3D Image Processing

The example ore sample and its XMT data used in this section come from one of the leaching columns (Column 1 in Table 3.2). Thresholding was applied to differentiate between the rock and the air phase, including internal porosity, and between the gangue and sulphide phases. All the mineral grains within the field of view were tracked individually over the course of the experiment. The methodology for tracking these grains has been described in Section 4.4. The algorithm labelled the features within the image, with the external air being given an integer label of 0, the gangue phase a label of 1, the internal porosity a label of 2 and each of the sulphide grains a unique identifier starting from label 3 (Figure 6.1).

6.3. Mathematical Model

The mathematical model takes the form of a set of partial differential equations that describe the motion of reagents and which are coupled to a model for the mineral grain dissolution. These must then be solved numerically as the system geometry and its evolution is too complex for analytical solutions. This section describes the derivation of the governing equations and the methods used for numerically solving them.

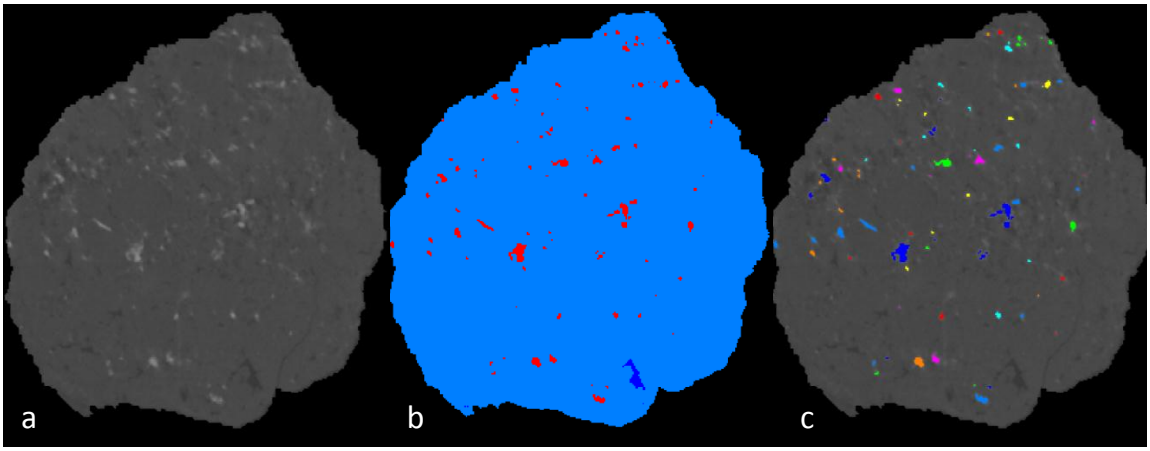


Figure 6.1.: Example slice showing phase segmentation: a) Original image, b) phase segmentation into external air (black), gangue (light blue), internal porosity (dark blue) and mineral grains (red). c) Colouring of the sulphide grains by unique identifiers.

6.3.1. Reagent Motion

Assuming that the reagent motion is predominantly diffusive, its flux, $\widehat{F}$, can be described by:

$$\widehat{F} = -D\nabla C \tag{6.1}$$

where C is the reagent concentration and D is the effective diffusivity. A continuity equation is required to solve for the concentration within the ore particles as a function of time, t:

$$\frac{\partial C}{\partial t} = -\nabla \cdot \left(\widehat{F}\right) \tag{6.2}$$

In this work, this equation is simplified by making the approximation that the behaviour is quasi-steady state. In other words it is assumed that the accumulation of reagent species within the ore particles has an unimportant impact on the flux of the reagent through the particle and that the diffusion timescale is shorter than the reaction timescale:

$$\nabla \cdot \left(\widehat{F}\right) = 0 \tag{6.3}$$

Within the bulk of the ore particles this means that the concentration is governed by the following equation:

$$\nabla \cdot (D\nabla C) = 0 \tag{6.4}$$

The diffusivity will vary with the properties of the gangue through which it is moving, particularly the micro-scale porosity, which will typically be below the resolution at which

the samples in this work are scanned. While the simulation framework that has been developed allows different regions to be assigned different diffusivities based, for instance, on differences in gangue mineralogy, without data on the variability of the diffusivity it is assumed constant here.

Chemical reactions occur at the surface of the metal sulphide. In general these reactions will be dependent on the concentration of both reactant and product species. For the purpose here, it will be assumed that there is a single limiting reagent and that the surface reaction kinetics are first order w.r.t. this reagent:

$$\widehat{F} \cdot \widehat{n} \,|_{\partial \mathrm{MS}} = k_{\mathrm{react}} C \tag{6.5}$$

where $\widehat{n}$ is the outward unit normal for the sulphide grain boundary ∂MS and k_{react} is the first order surface rate constant for the reaction (note that unlike a volumetric first order rate constant, which has units of inverse time, the first order surface rate constant has units of length per unit time). Since the flux due to the reaction must match the diffusive flux into the surface:

$$\nabla C \cdot \widehat{n} \,\Big|_{\partial \mathrm{MS}} = -\frac{k_{\mathrm{react}}}{D} C \tag{6.6}$$

At the surface of ore particle there will be mass transport between the particle and the bulk fluid. The effect of boundary layers in the fluid and other related phenomena can be modelled using an external mass transfer coefficient, k_{ext}.

$$\widehat{F} \cdot \widehat{n} \,|_{\partial \mathrm{Rock}} = k_{\mathrm{ext}} \left(C_{\mathrm{ext}} - C \right) \tag{6.7}$$

Similarly to the reaction flux, the mass transfer into the particle must match the flux within the particle:

$$\nabla C \cdot \widehat{n} \,\Big|_{\partial \mathrm{Rock}} = \frac{k_{\mathrm{ext}}}{D} \left(C_{\mathrm{ext}} - C \right) \tag{6.8}$$

As the rates will all scale with the external concentration, C_{ext}, it is useful to non-dimensionalise the concentrations using this quantity:

$$C^{*} = \frac{C}{C_{\mathrm{ext}}} \tag{6.9}$$

The following set of equations can therefore be used to model the quasi-steady state reagent concentration within the ore particle. The governing equation can be expressed

as:

$$\nabla \cdot (D \nabla C^*) = 0 \tag{6.10}$$

The boundary conditions at surface of mineral grains and the surface of ore particle can be defined as:

$$\nabla C^* \cdot \widehat{n} \Big|_{\partial \mathrm{MS}} = -\frac{k_{\mathrm{react}}}{D} C^* \tag{6.11}$$

$$\nabla C^* \cdot \widehat{n} \Big|_{\partial \mathrm{Rock}} = \frac{k_{\mathrm{ext}}}{D} (1 - C^*) \tag{6.12}$$

The set of equations is solved in 3D using the voxelised grid obtained from the XMT imaging. It is solved using a finite volume scheme for the discretisation, with the fluxes calculated on a staggered grid. As the voxels are cubic, the approximation is very similar to that which would be obtained by simple finite differencing, though the finite volume scheme allows the complex shaped boundaries of both the ore particle and the mineral grains within it to be more naturally accommodated.

The problem is solved by matrix inversion as the assumption of first order kinetics means that the discretised equations are linear. As the XMT images are very large (10^8 to 10^9 voxels) and the numerical solution is obtained at the same resolution, the solver was implemented in parallel to both improve the computational times and to distribute the very large memory requirements over a number of nodes. The code was written in C++ and made use of MPI and the PETSc library (Balay et al., 2014) for the parallel implementation and matrix inversion.

Figure 6.2 shows a cross-section through a 3D volume of the non-dimensionalised reagent concentration. This simulation contained $\sim$ 300 million voxels and took about 48 minutes to solve on 50 cores.

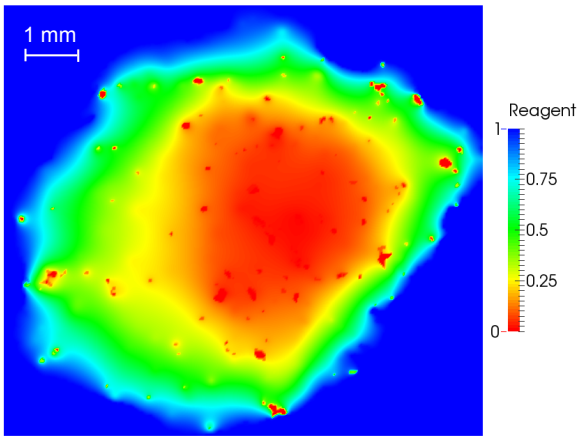


Figure 6.2.: The steady-state reagent concentration within the ore.

6.3.2. Mineral Grain Dissolution

The model can be used to calculate both the reagent concentration and its flux at each point in the system. In order to use this information to predict the dissolution process, the fluxes must be coupled to a model for the evolution of the mineral grains. If it is assumed that ratio of volume of mineral grain leached to reagent consumed is κ, then the rate of change of a grain's volume, V, can be expressed as follows:

$$\frac{dV}{dt} = \kappa \oint_{\partial \mathrm{MS}} \widehat{F} \cdot \widehat{n} \cdot dS \tag{6.13}$$

This equation on its own will only give the change of volume of the grain, but not the change in shape. In order to estimate both the change in shape and the change in volume, the equation must be applied at the voxel rather than the grain level. To avoid the dissolution of mineral within a voxel being binary, an additional scalar field S is introduced, which is the fraction of metal sulphide remaining within a voxel. Initially all the voxels that are identified as being within sulphide grains are assigned a value of $S = 1$, while $S = 0$ in all other voxels. The value of S in voxel i is then evolved using the following equation in which the fluxes over the surface of the voxel are summed:

$$\frac{dS_i}{dt} = \frac{\kappa}{\Delta x} \sum_{\partial voxel_i} \widehat{F} \cdot \widehat{n} \tag{6.14}$$

where Δx is the edge length of the cubic voxels. Equation (6.14) is the voxel level equivalent of Equation (6.13), where the flux over a voxel face is assumed constant. As the fluxes are zero at all boundaries between sulphide voxels, the value of S will only change in voxels at the boundary of the mineral grains. When the value of $S \leq 0$, the index for that voxel is changed from that of the mineral grain to that of the gangue, indicating that sulphide within that voxel is completely leached. To accurately capture the dissolution processes, the time step must be such that the fastest dissolving voxel takes no less than one time step to disappear:

$$\Delta t \ll \frac{\Delta x}{\kappa \cdot \max(\left|\widehat{F}\right|)} \tag{6.15}$$

As the disappearance of mineral voxels will impact the fluxes within the system, the concentration (and thence the fluxes) needs to be recalculated at every time step during which a metal sulphide voxel becomes completely leached. Between such steps, however,

S_i can be updated without needing to recalculate the concentration field.

6.4. Ore Particle Case Study

In addition to non-dimensionalising the concentration using the external reagent concentration, the simulation parameters also form dimensionless groups which allow us to reduce the number of independent parameters that need to be examined. The most important of these dimensionless groups is one which dictates the relative importance of the diffusive mass transport and the surface reaction rate:

$$\delta = \frac{D}{l\, k_{react}} \tag{6.16}$$

where l is a length scale associated with the particle, taken to be the equivalent spherical diameter. While the actual values of the flux will depend upon the specific values of the external concentration, diffusivity and rate constant, the shape of the internal concentration profile depends only on this dimensionless group (assuming that the external mass transport coefficient is very large relative to the surface rate constant, an assumption made in this study). The leaching becomes diffusion limited when $\delta \ll 1$ and reaction limited when $\delta \gg 1$.

The simulations are carried out using a dimensionless time, t^*, which is related to the actual time by the following relationship:

$$t^* = \frac{t k_{\text{react}}}{l} \tag{6.17}$$

6.4.1. Diffusion Limited and Reaction Limited Case

The shrinking core model has been used for many theoretical leaching simulations. Based on the assumptions of which the recovery curve shifts into the ore particles as time progresses, the leached region has 100% recovery whereas the unleached region has 0% recovery.

Figure 6.3 shows the reagent concentration on a slice through the 3D simulation of an ore particle at four different time steps for a simulation with a low value of δ ($\delta = 0.01 \ll 1$). The completely diffusion limited case ($\delta = 0$) cannot be directly simulated as it would require either a zero diffusion coefficient or an infinite reaction rate, but this simulation approaches this limit. In the diffusion limited case there is a distinct profile in the reagent concentration, with high reagent concentrations near the

edges and low concentrations in the middle of the ore particle. This results in faster leaching of the mineral grains which are closer to the edge of the particle and slower leaching of those in the middle.

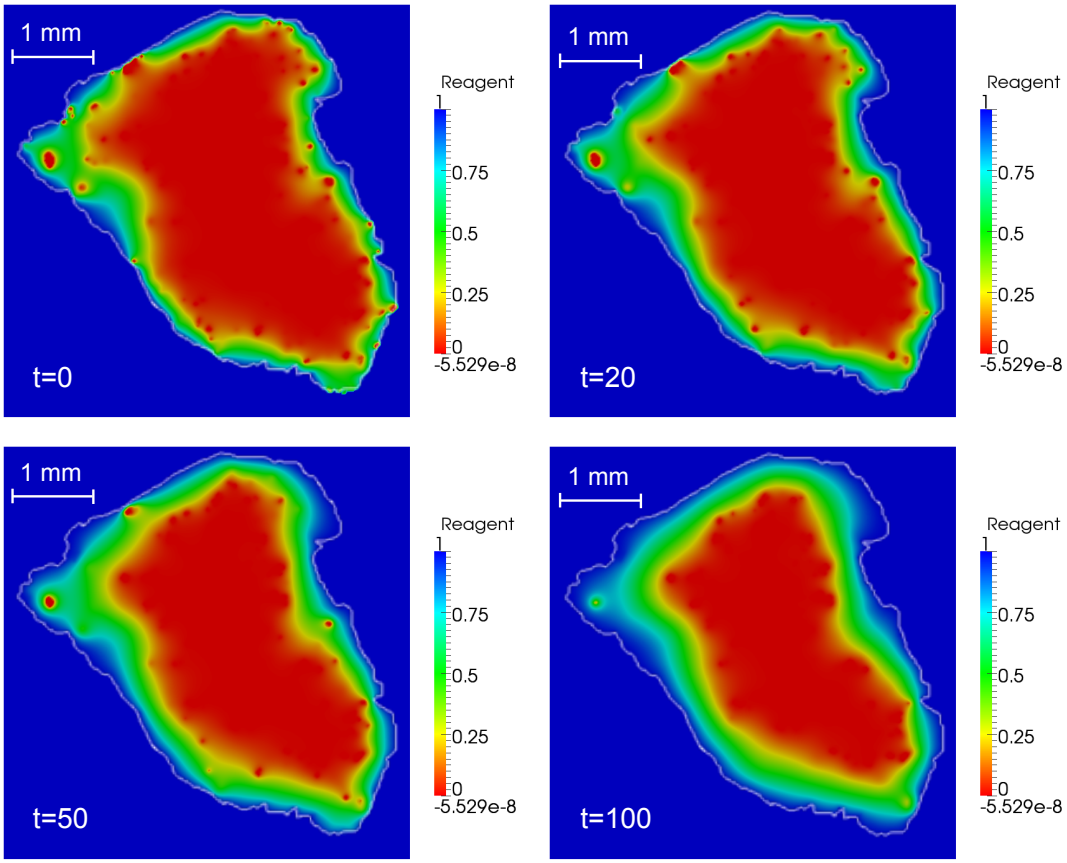


Figure 6.3.: Reagent concentration for an ore particle at four different time steps with $\delta = 0.01$ (diffusion limited). The white contour shows the outline of the ore particle.

Figure 6.4 a-c show the 3D distribution of the mineral grains and their evolution with time. Given the 3D nature of these images, it is hard to see the change in size of the grains and their position relative to the surface. To address this, a plot (Figure 6.6a) is generated showing the average dissolution of grains at a particular distance from the surface as function of both that distance (x axis) and time (colour). It is clear from this plot that the dissolution progresses from the outside inwards. This inward progression of the leaching is similar to that predicted by the shrinking core model, though even when the system is very diffusion limited, as in this case, there is still not a distinct separation between the leached and unleached portions of the particle, with larger mineral grains that are close to the outer edge of the particle lasting longer than some smaller grains

that are further in, with the shape of the ore particle and the distribution of the mineral grains further complicating the dissolution pattern. It is this variability in leach rate that causes the variability in average extraction with distance seen in Figure 6.6a.

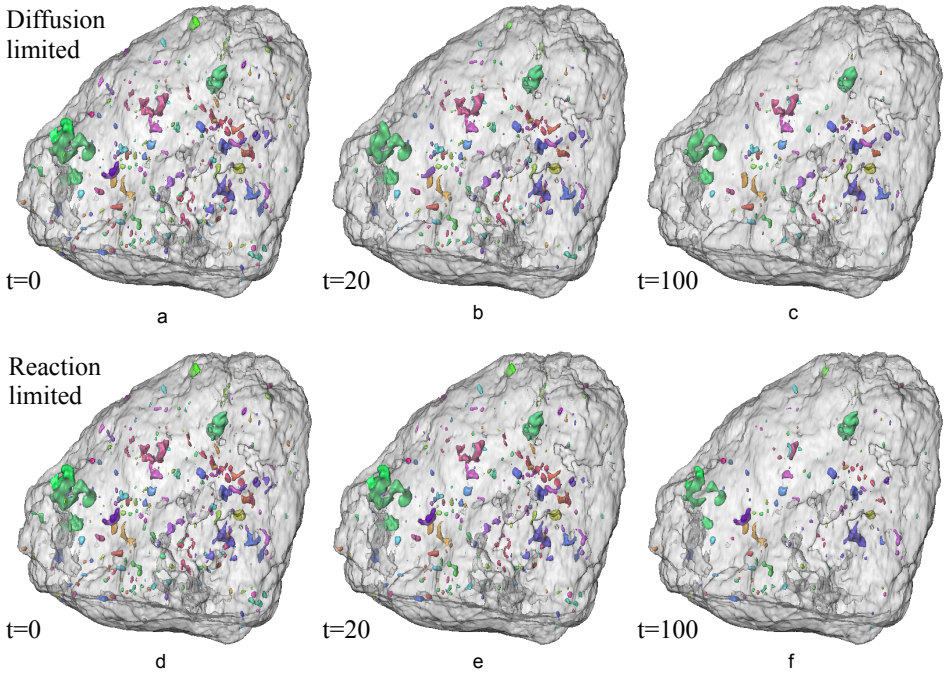


Figure 6.4.: 3D visualisation of the simulation of mineral grains within an ore particle under: a)-c) diffusion limited case and d)-f) reaction limited case.

At much higher values of δ ($\delta = 1000 \gg 1$) the reaction limited case is approached (Figure 6.5), which is characterised by reagent concentrations throughout the particle that are virtually the same as those in surrounding fluid (the zero concentrations in Figure 6.5 are in the interior of mineral grains as all reactions occur at the surface of the grains). The slight decrease in concentration with distance is due to the fact that, while δ is large, it is not infinite. As the concentration of reagent is essentially constant in this case, the rate of dissolution of the individual grains is essentially independent of their position within the ore particle. The extraction rates will depend on the size of the mineral grains, though, as well as any variability in the surface reaction rates (assumed constant in these simulations, though this assumption is relaxed in Section 6.4.2). This can be seen in Figure 6.4 d-f and more clearly in Figure 6.6b.

Figure 6.9 Top shows the experimentally obtained leaching profile based on XMT measurements through time. It is clear from the figure that the leaching profile does follow the shrinking core behaviour as there is a gradual change in the average extent of dissolution with distance from the surface rather than a distinct separation between

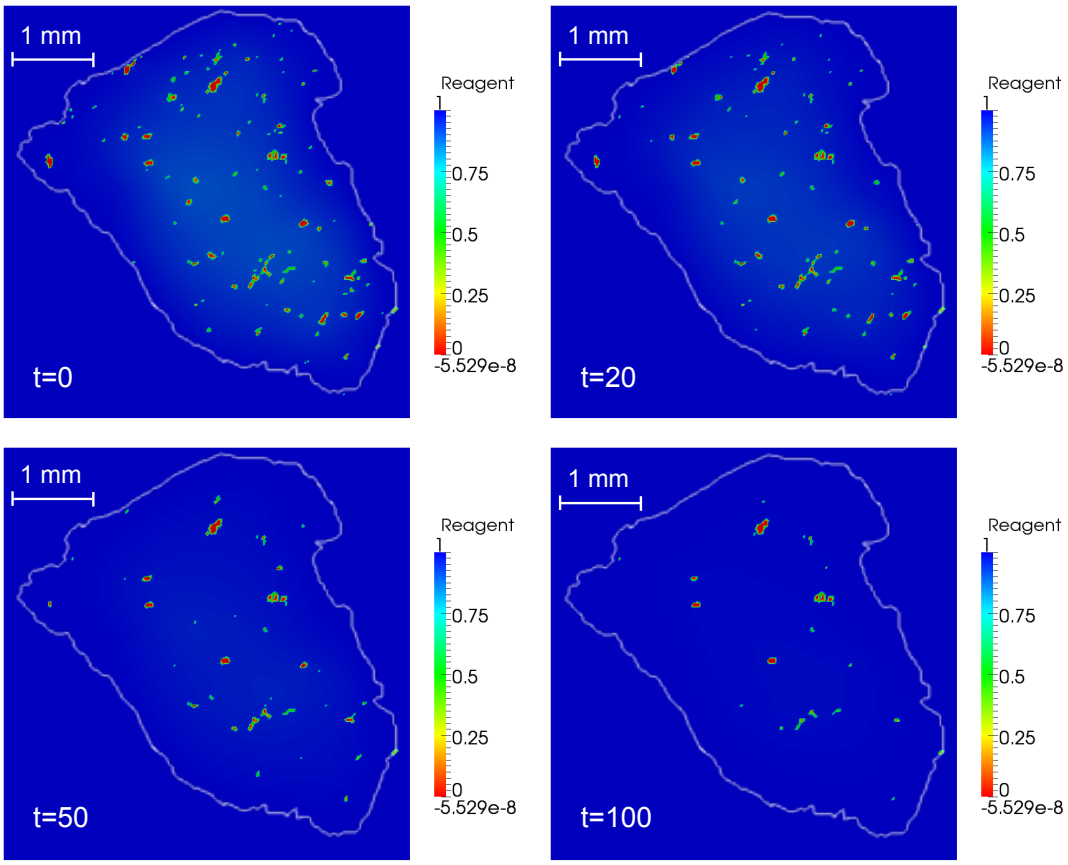


Figure 6.5.: Reagent concentration for an ore particle at four different time steps with $\delta = 1000$ (reaction limited). The white contour shows the outline of the ore particle.

leached and unleached regions. The leach behaviour is closer to the diffusion limited case than the reaction limited one, but the fact that leaching occurs in the centre of the particle (extraction increasing) at all times, albeit much slower than towards the outside of the particle, indicates that in this system both diffusion and surface reaction rates play a role in the apparent kinetics. In a system with an intermediate value for δ, the observed rate will initially be dictated by the surface reaction kinetics as the grains near the surface, which will have minimal diffusion resistance to their leaching, will contribute most to the leaching rate. As these grains are depleted the grains deeper in the particle contribute more to the apparent leach rate and the effect of the diffusion resistance becomes stronger.

While in the idealised simulations above the surface leach kinetics rate constant for all the grains was assumed to be the same, the situation in the real particle is that the surface rate constants will vary from grain to grain due to differences in the mineralogy of the grains and their associations. A method for estimating the distribution of these

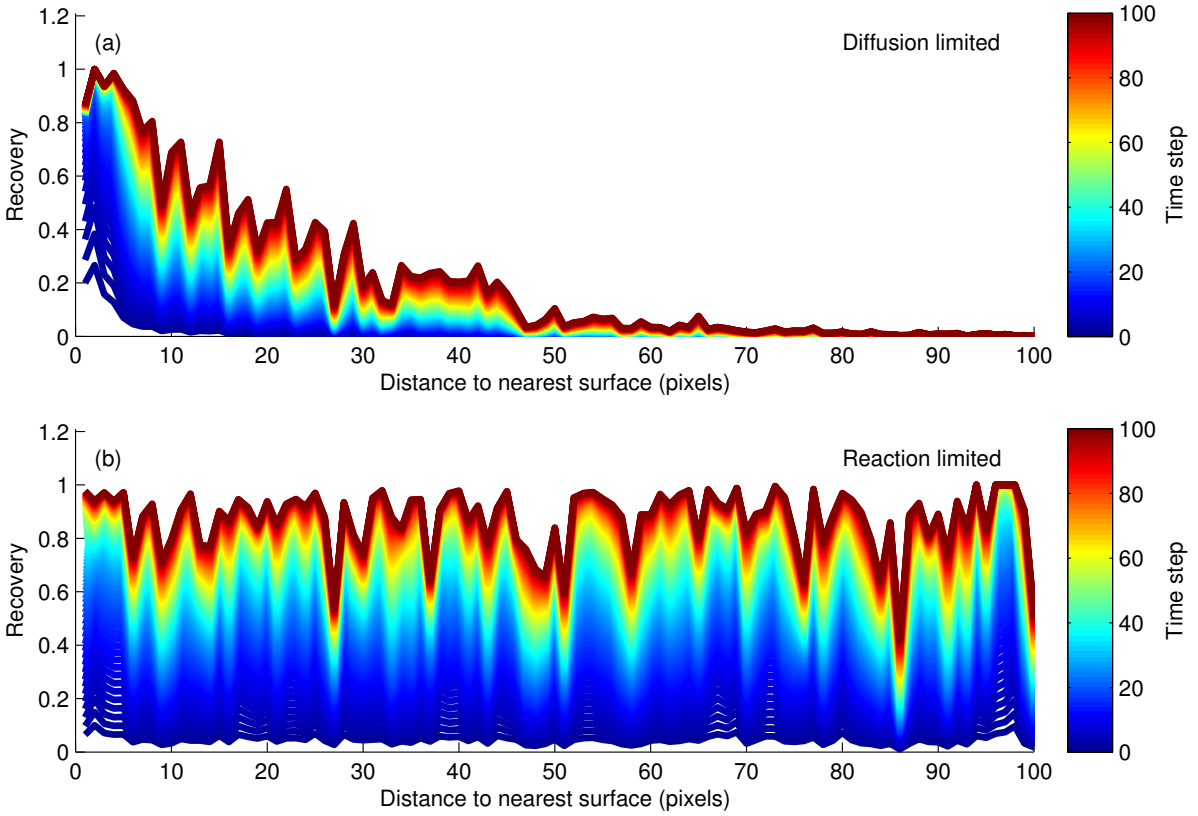


Figure 6.6.: Comparison between: a) reaction limited case; and b) diffusion limited case showing recovery against distance.

rate constants is thus required before accurate simulations of the ore behaviour can be carried out.

6.4.2. Reaction Kinetics Distribution

In the leaching experiments the dissolution of every grain in the column is tracked as a function of time. This provides a lot of data as there are hundreds of thousands of grains in each column. Due to the large amount of available data, it is possible to divide the mineral grains into quite narrow categories based on their initial size and distance from the surface while still having quite a large amount of data in each category. All the tracked grains (136443 grains in total shown in Section 5.4) which are then divided into different size-distance categories (Section 5.4.1) are used as the database. It needs to be noted that the ultimate objective for the model is to simulate the leach behaviour for a larger system (e.g. a leaching column). Extracting the reaction kinetics distribution using the large database from the entire column to model the leach behaviour for a single ore particle is the first stage and has been performed in this and later sections.

If it is assumed that the size classes are narrow enough that the effect of particle size on the recovery within the category is small and that the distance from the surface can be used as a proxy for the chemical conditions experienced by the grain, then the remaining variability in the leach rate is due to variability in the surface kinetics. Note that it is not required that the chemical conditions experienced by a grain within a category be constant with time over the time interval being considered, only that the grains in a category experience a similar set of chemical conditions.

At time t, the leaching rate of grain i of size $V_i(t)$ and in initial size category $V_i(0)$ when exposed to a concentration C can be expressed as follows, again assuming linear surface kinetics:

$$\frac{dV_i(t)}{dt} = -k_i A_i(t) C \tag{6.18}$$

$$\frac{dV_i(t)}{dt} = -k_i a V_i(t)^{2/3} C \tag{6.19}$$

where k_i is the surface rate constant for grain i, A_i is the surface area of grain i at time t, V_i is the volume of grain i remaining at time t, and a is the proportionality in the relationship between volume and surface area. From Equation (6.19), the reaction kinetics can be derived as:

$$\int_{V_i(0)}^{V_i(t)} \frac{1}{-k_i \cdot a V_i(t)^{2/3}} dV_i(t) = \int_0^t C dt \tag{6.20}$$

Integrating this equation gives:

$$k_i = \frac{3}{at\overline{C}} \left(V_i(0)^{1/3} - V_i(t)^{1/3} \right) \tag{6.21}$$

where

$$\overline{C} = \left(\int_0^t C dt \right) / t \tag{6.22}$$

The ratio of the surface rate constant for grain i to the average surface rate constant, k_{mean}, can thus be calculated from the experimental data where N is the total number of grains in the category:

$$\frac{k_i}{k_{mean}} = \frac{V_i(0)^{1/3} - V_i(t)^{1/3}}{\overline{V_i(0)^{1/3} - V_i(t)^{1/3}}} \tag{6.23}$$

where $\overline{V_i(0)^{1/3} - V_i(t)^{1/3}}$ is the value of this function at the average leach rate of the

grains, given by:

$$\overline{V_i(0)^{1/3} - V_i(t)^{1/3}} = \left(\sum_{i=1}^{N} \left(V_i(0)^{1/3} - V_i(t)^{1/3} \right) \right) / N \tag{6.24}$$

Figure 6.7 shows the cumulative distribution function of the rate constants for different size and distance categories. While the average rate constant varies markedly with position in the ore particle and with the size of the mineral grains, the distribution of rate constants relative to the mean is essentially the same in all categories. The slight scatter in the plots at high values of the rate constant is due to the fact that there is a finite range of rate constants that can be measured, since some of the fastest leaching grains disappear over the finite time interval used in the categories with the highest leach rates (small grains near the surface). It can also be observed that there is a small portion of grains with negative values of their relative rate constant (∼5% in volume). This is mainly due to measurement error as there is some uncertainty in the measured volumes and thus a few grains with a rate around zero will appear to have a negative rate.

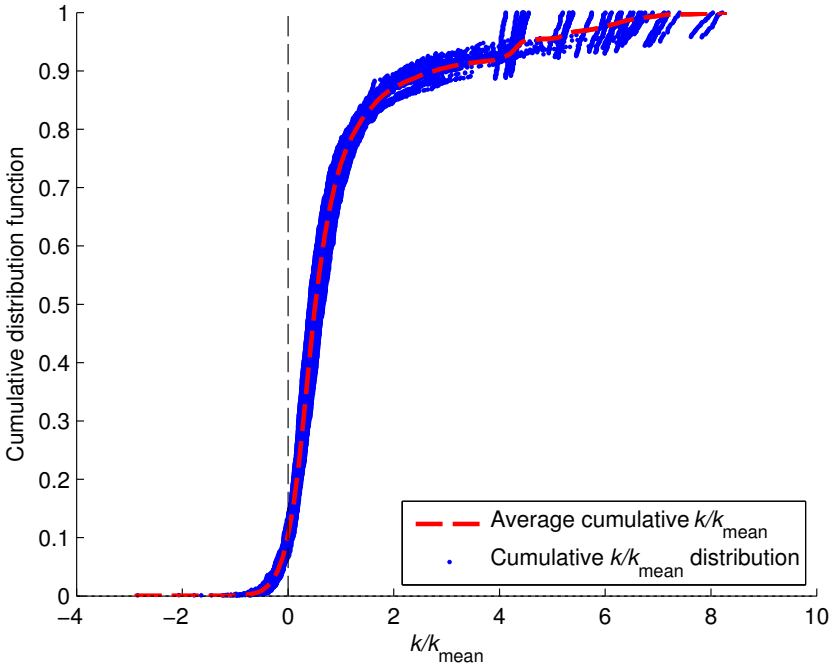


Figure 6.7.: Cumulative distribution function of the rate constants for different size and distance categories, with the average distribution function for all the plotted data.

Therefore, this average distribution can be used as the basis of a Monte-Carlo type simulation in which the surface rate constant for each grain is assigned randomly based on

the distribution, with the simulation repeated to ensure that the results are not strongly dependent on the rate constants assigned to specific grains (while there are a very large number of grains in the system, a lot of the grain volume is contained in a comparatively small number of larger grains). The cumulative distribution function can be converted to a probability density function and needs to be parameterised so that it can be easily input into the simulations. As can be seen from Figure 6.8, a gamma distribution fits the data with positive reaction rates quite well. The blue area shows the portion with negative values (∼5% in volume), which is mainly caused by the measurement error for non-leachable grains. 5% of the grains are thus assigned a rate constant of zero to account for the non-leaching portion. It can also be observed that there is a peak in the plot for the grains with higher reaction kinetic rate. This peak is probably caused by grains composed of faster leaching minerals such as oxides and secondary sulphides.

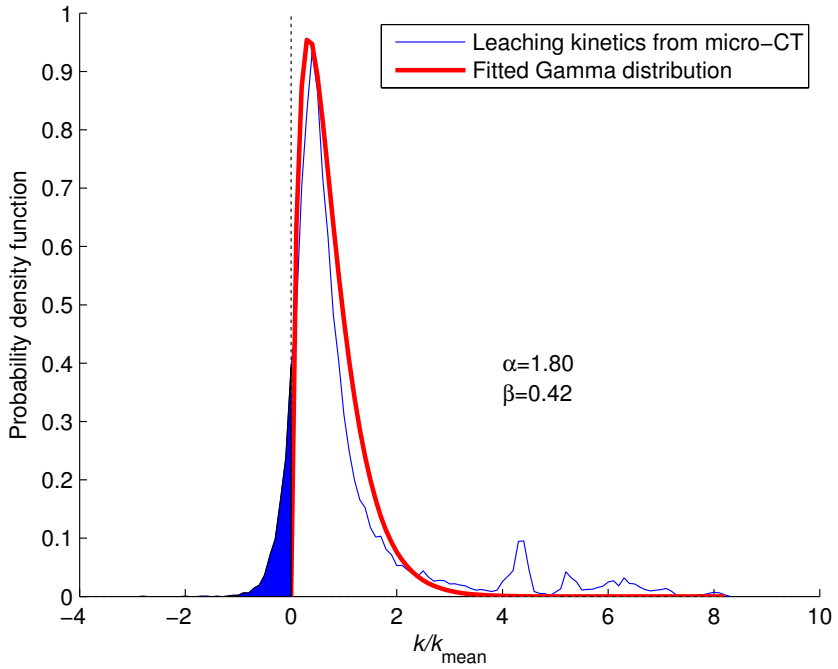


Figure 6.8.: Probability density function of individual reaction kinetics over average reaction kinetics with fitted gamma distribution.

6.4.3. Simulation Results with Gamma Distributed Kinetics

The apparent leach kinetics of the ore particles depend on a number of factors such as particle size, porosity and mineralogy. As Figure 6.9 Top indicates that the actual behaviour is neither completely reaction nor diffusion limited, δ was tested at intermediate values, with a value of about 1 producing the closest fit. Figure 6.9 Bottom shows the

leaching profile using $\delta = 1$ with the plot showing the average extraction as a function of distance at a number of time points. Comparing with Figure 6.9 Top, it can be observed that although the recovery against distance profile is not exactly the same as the profile obtained from the experiment, the general shape and trend of the profile are similar. The small scale variability in both Figure 6.9 Top and Figure 6.9 Bottom are mainly due to the leach kinetics of specific larger grains, which in the simulations are assigned randomly from the experimentally obtained distribution.

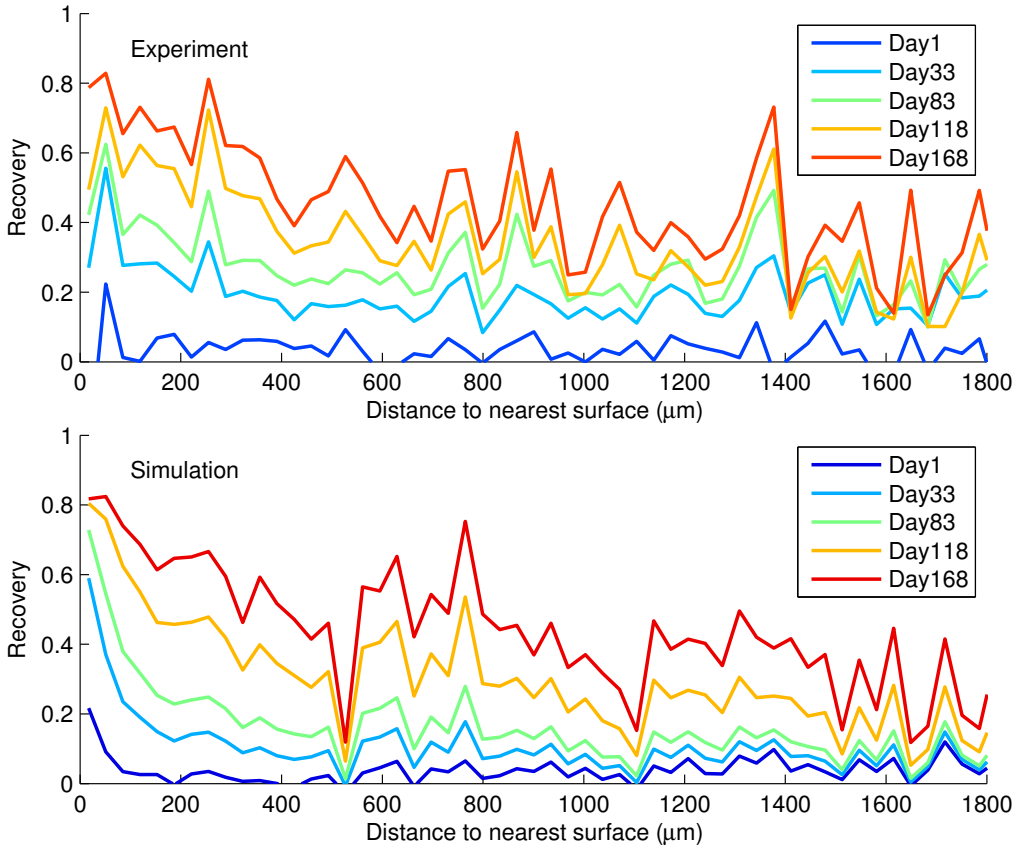


Figure 6.9.: Recovery against distance for an example ore particle based on simulation ($\delta = 1$).

The main objective of this method is to simulate the leach behaviour at longer times based on the initial response. The distribution of rate constants is found experimentally based on the measured extraction over the first 23 days using Equation (6.23). The scaling factor for the time scale is fitted based on the first 53 days of leaching according to Equation (6.17). Figure 6.10 shows that the comparison between experimental measurements and simulated extraction using Gamma distributed kinetics is excellent, especially given the fact that only one independent fitting parameter is adjusted. The single reaction kinetic is the average kinetic (k_{mean} in Figure 6.7 and Figure 6.8) used

to generate Gamma distributed kinetics. It can be observed that when applying a single reaction kinetics, there is an over estimation of the recovery. This is because the fast leaching material disappears and the apparent kinetics become slower, while the average kinetics remain the same when a single value is used.

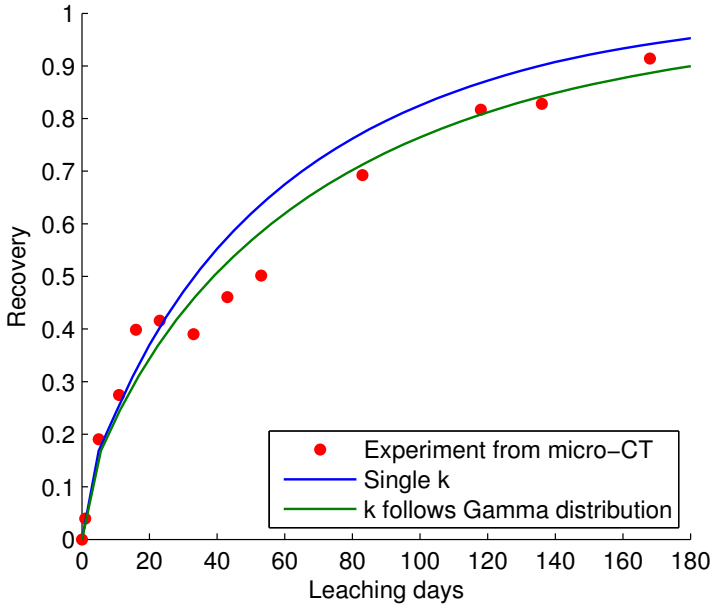


Figure 6.10.: Comparison between experiment from XMT measurement and simulation using both single leach kinetics and Gamma distributed kinetics.

Figure 6.11 shows the parity between the experimental and simulated average recovery at the measurement time points, with each of the sub-figures being for a different grain size and distance category. It shows that not only is the simulator able to predict the average behaviour, it is also able to predict the behaviour of specific categories of mineral grains.

6.5. Summary

In this chapter a simulation methodology for predicting the grain scale behaviour within individual particles was introduced. The balance between mass transfer and surface kinetics was characterised by a dimensionless group δ. The simulation was carried out using a XMT volume of the ore particle as its simulation grid. This required that the implementation be massively parallel given the high resolution and large number of voxels involved. An analysis method was introduced allowing the variability in surface rate kinetics to be distinguished from the mass transfer effects, with this data being used as

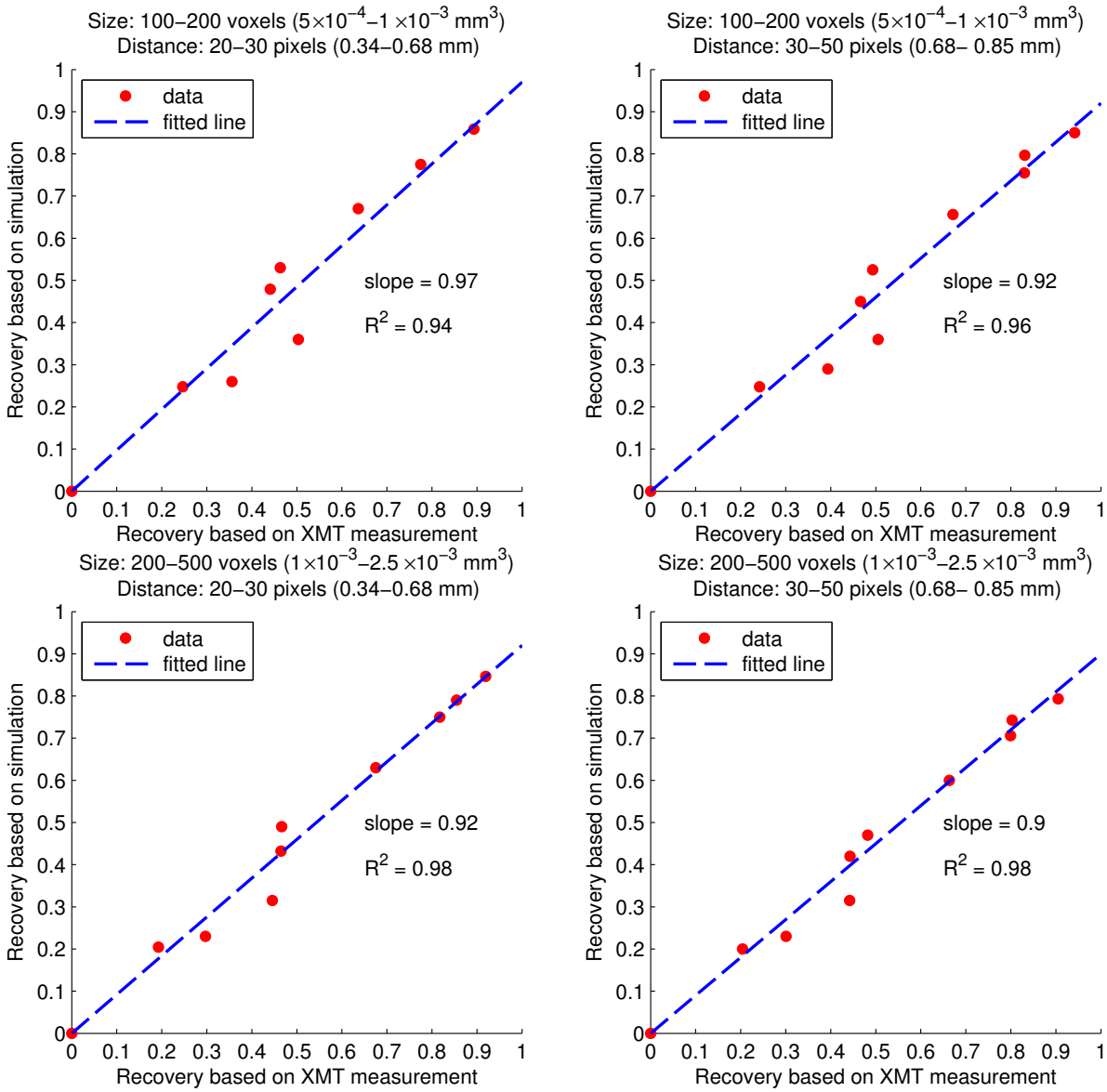


Figure 6.11.: Plot of average recovery based on XMT measurement against simulation results for different size-distance categories with fitted lines. The resolution of the image is ∼17 microns.

an input into the simulation. It was found that approximately 5% of the grains had a zero rate constant, with the remaining grains following approximately a gamma distribution. Using only one independent calibration parameter, the simulation was able to accurately predict not only the average leach behaviour, but also the behaviour of mineral grains within specific size and distance to the surface categories.

Chapter 7

Conclusions and Future Directions

In this thesis, the main objective was to study the leach behaviour in a more quantitative way by applying XMT and image processing techniques. In order to quantify the leach behaviour based on image analysis, more advanced image processing algorithms were developed with related measurement errors understood. Additionally, mode advanced leach performance analysis was carried out at individual ore particle scale and also mineral grain scale based on the ore particle tracking and mineral grain tracking algorithms. Finally, the leach behaviour was also modelled and predicted by using both the initial XMT images and the extracted leaching kinetics as inputs.

The existing literature review about the XMT applications in heap leach shows that the majority of the current studies are more qualitative and this is mainly caused by the limited application of more advanced image processing algorithms. The development of a series of image processing algorithms for column leaching experiments made it possible to process vast amount of XMT data automatically and in a consistent way. The related uncertainties and errors were also quantified. The main advantage of the developed algorithms is that they can track individual ore particles and individual grains over the entire leaching period. This allows more detailed and advanced leach behaviour analysis to be done by looking at leach performance at different scales. Moreover, the developed algorithms can also be easily modified and applied to quantify mineral dissolution for other leaching systems.

One of the most important achievement is the development of the mineral grain tracking algorithm. It is a novel, fast masking based algorithm to track individual grains and their dissolution through time and it can handle grain splitting and disappearance. One of the novelties of this algorithm is that it uses the transformed label image as the mask which does not require resampling of the raw image after the registration process which

significantly reduces the measurement error. While the algorithm described is applied for the identification of the valuable mineral phases within ore particles, the algorithm itself is more generally applicable and relevant to other systems in which volumes are obtained from XMT data.

The development of the mineral grain tracking algorithm also forms the basis of the image error quantification and leach behaviour analysis. Similar to the tracking algorithm itself, the systematic and random errors and uncertainties in the volume measurement can also also quantified, and this can also be applied to many other image analysis cases. The direct output from the error analysis is that to achieve a desired level of uncertainty due to random errors, the results from repeat scans or scans of similar objects need to be combined. The relative error for image measurement follows a power law against the grain size with a power exponent of -2/3. A methodology for eliminating systematic errors based on knowledge of how changes in threshold effect the measured volume and its dependency upon size was also developed. This method introduces a new image calibration method between different scans, which is using sample standards (containing features of interest) rather than only intensity standards.

Before doing image analysis to quantify the leach performance, the comparison between image measurements and conventional chemistry measurements was investigated. This has not been done in previous studies but is a crucial step when using images to analyse leach recovery as XMT cannot easily distinguish between different sulphide mineral phases such as chalcopyrite and pyrite. It is important to validate that the trends in both measurements are similar, which indicates that the results obtained from images can be used to assess leach performance.

By using the ore particle tracking and mineral tracking algorithms, the leach performance was then analysed at different scales. The studies for larger scales including column scale and individual ore particle scale show that there is a huge recovery variation (18% - 96%) among ore particles, but there is not a strong correlation between leach recovery and leaching parameters such as ore particle size, initial grain content, location of the ore particles, etc.. At grain level, a novel leach performance analysis method was developed by dividing all the tracked grains into different size and distance to surface categories and studying the average behaviour in each category. By using this analysing method, the size effect and distance effect were quantified. It shows that in a typical leaching process, the size dependency is stronger at the early stage while the distance dependency dominants the ultimate recovery. This indicates that the leaching process can potentially be enhanced by decreasing distance values by, for instance, producing cracks in the ore preparation stage. This is the primary explanation for enhanced leach-

ing when using HPGR and microwave treatment for ore preparation. Another potential application using this analysing method is to assess the effects of leaching parameters. Examples were shown comparing different flow rates for different leaching columns, but this can be applied to other parameters to assess how each potential improvement (or change) of the parameter affects the leaching process, in particular to investigate if it can affect the recovery of all the grains within the system, or part of the grains within a specific size or distance range.

Finally, a model for predicting the grain scale behaviour within individual particles was introduced. This work is entirely new in the field as it uses the initial XMT images and extracted leach kinetics as inputs whereas the most common existing models are either based on shrinking core model or with semi-empirical adjustments to the model to account for fracturing. The main achievement for this model is that it can accurately predict not only the average leach behaviour, but also the behaviour of mineral grains within specific size-distance categories. More importantly, it can simulate the ultimate (or long term) leach process for an single ore particle based on analysing short term leach behaviour. This has the potential for shortening the current very long experimental time required when assessing leach performance.

7.1. Future Work

The studies in this thesis have formed the basis of quantifying, understanding and simulating the leach behaviour at individual ore particle scale as well as individual mineral grain scale by using the developed automatic image processing algorithms. There are many areas which can be investigated in future work based on the methods and understanding from this thesis.

The quantification methodology can be further applied to other leaching columns with different leaching parameters to carry out a systemic analysis to understand how different parameters (e.g. ore type, flow rate, feed solution, temperature) can affect the leach behaviour. More experiments on different systems can be carried out to investigate what other factors may influence the leaching process. More complex ore preparation and leaching strategies can be developed to optimise the leach efficiency.

One of the main limitations for using XMT in heap leaching research is that it cannot easily distinguish the difference between different sulphide mineral phases. Having thin sections from the residue ore particles can solve part of this issue. Combining XMT with other technique (e.g. XRF) to map the 3D chemical composition with the 3D tomographic images can allow us to achieve individual mineral grain tracking and analysis

for a particular mineral species. The mineral species tracking can also be used to simulate the leach behaviour more efficiently.

In order to simulate and predict the leach behaviour more accurately, the existing model can be potentially improved by applying fully transient simulation, applying non-linear surface kinetics, and developing models for fracture transport. The models can also be used to simulate a larger system.

Bibliography

Acevedo, F., 2002. Present and future of bioleaching in developing countries. EJB Electronic Journal of Biotechnology 5 (2).

Al-Harahsheh, M., Kingman, S., Hankins, N., Somerfield, C., Bradshaw, S., Louw, W., 2005. The influence of microwaves on the leaching kinetics of chalcopyrite. Minerals Engineering 18 (13-14), 1259–1268.

Al-Harahsheh, M., Kingman, S. W., 2004. Microwave-assisted leaching - a review. Hydrometallurgy 73 (34), 189–203.

Antonijević, M. M., Bogdanović, G. D., 2004. Investigation of the leaching of chalcopyritic ore in acidic solutions. Hydrometallurgy 73 (3-4), 245–256.

Aydoan, N. A., Ergün, L., Benzer, H., 2006. High pressure grinding rolls (HPGR) applications in the cement industry. Minerals Engineering 19 (2), 130–139.

Balay, S., Abhyankar, S., Adams, M. F., Brown, J., Brune, P., Buschelman, K., Eijkhout, V., Gropp, W. D., Kaushik, D., Knepley, M. G., McInnes, L. C., Rupp, K., Smith, B. F., Zhang, H., 2014. PETSc Web page. Last accessed: 2015-04-20.
URL http://www.mcs.anl.gov/petsc

Barr, D. W., Jordan, M. A., Norris, P. R., Phillips, C. V., 1992. An investigation into bacterial cell, ferrous iron, pH and Eh interactions during thermophilic leaching of copper concentrates. Minerals Engineering 5 (35), 557–567.

Barriga Mateos, F., Palencia Pérez, I., Carranza Mora, F., 1987. The passivation of chalcopyrite subjected to ferric sulfate leaching and its reactivation with metal sulfides. Hydrometallurgy 19 (2), 159–167.

Bartlett, R. W., 1997. Metal extraction from ores by heap leaching. Metallurgical and Materials Transactions B 28 (4), 529–545.

Bartlett, R. W., 1998. Solution Mining: Leaching and Fluid Recovery of Materials. 2nd Edition. Australia : Gordon and Breach Science Publishers.

Baum, W., Ausburn, K., 2011. HPGR comminution for optimization of copper leaching. Minerals & Metallurgical Processing 28 (2), 77–81.

Berger, M. J., Hubbell, J. H., Seltzer, S. M., Chang, J., Coursey, J. S., Sukumar, R., Zucker, D. S., Olsen, 2010. XCOM: Photon Cross Sections Database. NIST Standard Reference Database 8 (XGAM).

Blair, D., Dufresne, E., 2008. The Matlab Particle Tracking Code Repository. Last accessed: 2015-04-20.
URL http://physics.georgetown.edu/matlab/

Bouffard, S. C., West-Sells, P. G., 2009. Hydrodynamic behavior of heap leach piles: Influence of testing scale and material properties. Hydrometallurgy 98 (1-2), 136–142.

Brandl, H., 2008. Microbial Leaching of Metals. In: Biotechnology Set. Wiley-VCH Verlag GmbH, pp. 191–224.

Burlion, N., Bernard, D., Chen, D., 2006. X-ray microtomography: Application to microstructure analysis of a cementitious material during leaching process. Cement and Concrete Research 36 (2), 346–357.

Cai, L., Ferrier, R. J., Lin, Q., Mostaghimi, P., Gorman, G. J., Neethling, S. J., 2014. Heap leaching simulation: beyond shrinking core models. No. June. 10th International Conference on CFD in Oil & Gas, Metallurgical and Process Industries SINTEF, Trondheim, NORWAY, pp. 1–7.

Cariaga, E., Concha, F., Sepúlveda, M., 2005. Flow through porous media with applications to heap leaching of copper ores. Chemical Engineering Journal 111 (23), 151–165.

Córdoba, E. M., Muñoz, J. A., Blázquez, M. L., González, F., Ballester, A., 2008a. Leaching of chalcopyrite with ferric ion. Part I: General aspects. Hydrometallurgy 93 (3-4), 81–87.

Córdoba, E. M., Muñoz, J. A., Blázquez, M. L., González, F., Ballester, A., 2008b. Leaching of chalcopyrite with ferric ion. Part II: Effect of redox potential. Hydrometallurgy 93 (3-4), 88–96.

Córdoba, E. M., Muñoz, J. A., Blázquez, M. L., González, F., Ballester, A., 2009. Passivation of chalcopyrite during its chemical leaching with ferric ion at 68C. Minerals Engineering 22 (3), 229–235.

Crocker, J. C., Grier, D. G., 1996. Methods of Digital Video Microscopy for Colloidal Studies. Journal of Colloid and Interface Science 179 (1), 298–310.

Curry, T. S., Dowdey, J. E., Murry, R. C., 1990. Christensen's Physics of Diagnostic Radiology. Lea & Febiger.

Davenport, W. G., King, M., Schlesinger, M., Biswas, A. K., 2002. Extractive Metallurgy of Copper (Fourth Edition). Pergamon, Oxford.

Dhawan, N., Safarzadeh, M. S., Miller, J. D., Moats, M. S., Rajamani, R. K., Lin, C.-L., 2012. Recent advances in the application of X-ray computed tomography in the analysis of heap leaching systems. Minerals Engineering 35 (0), 75–86.

Dixon, D. G., Petersen, J., 2003. Comprehensive modelling study of chalcocite column and heap bioleaching. In: Riveros, P. A., Dixon, D. G., Dreisinger, D. B., Menacho, J. (Eds.), Copper 2003 - Hydrometallurgy of Copper (Book 2). Vol. VI. CIM, Montreal, Canada, pp. 493–516.

Donath, T., 2006. Quantitative x-ray microtomography with synchrotron radiation. GKSS-Forschungszentrum Geesthacht, Bibliothek.

Dutrizac, J., 1978. The kinetics of dissolution of chalcopyrite in ferric ion media. Metallurgical and Materials Transactions B 9 (4), 431–439.

Dutrizac, J., MacDonald, R., 1971. The effect of sodium chloride on the dissolution of chalcopyrite under simulated dump leaching conditions. Metallurgical and Materials Transactions B 2 (8), 2310–2312.

Dutrizac, J. E., MacDonald, R. J. C., Lngraham, T. R., 1969. The kinetics of the dissolution of synthetic chalcopyrite in aqueous acidic ferric sulphate solution. Trans. Metall. Soc. AIME 245, 955–959.

Feldkamp, L. A., Goldstein, S. A., Parfitt, M. A., Jesion, G., Kleerekoper, M., 1989. The direct examination of three-dimensional bone architecture in vitro by computed tomography. Journal of Bone and Mineral Research 4 (1), 3–11.

Fiji, 2013. Auto Threshold. Last accessed: 2015-04-20.
URL http://fiji.sc/wiki/index.php/Auto_Threshold#

Ghorbani, Y., Becker, M., Mainza, A., Franzidis, J.-P., Petersen, J., 2011a. Large particle effects in chemical/biochemical heap leach processes A review. Minerals Engineering 24 (11), 1172–1184.

Ghorbani, Y., Becker, M., Petersen, J., Morar, S. H., Mainza, A., Franzidis, J. P., 2011b. Use of X-ray computed tomography to investigate crack distribution and mineral dissemination in sphalerite ore particles. Minerals Engineering 24 (12), 1249–1257.

Ghorbani, Y., Oliazadeh, M., Shahverdian, A., 2008. Aluminum solubilization from red mud by someindigenous fungi in Iran. Journal of Applied Biosciences 7, 207–213.

Ghorbani, Y., Petersen, J., Becker, M., Mainza, A. N., Franzidis, J.-P., 2013. Investigation and modelling of the progression of zinc leaching from large sphalerite ore particles. Hydrometallurgy 131132 (0), 8–23.

Goldman, L. W., 2007. Principles of CT and CT technology. Journal of nuclear medicine technology 35, 115–128; quiz 129–130.

Gonzalez, R. C., Woods, R. E., Eddins, S. L., 2003. Digital Image Processing Using MATLAB. Prentice-Hall, Inc.

Habashi, F., 1999. A Textbook of Hydrometallurgy, 2nd edition. Metallurgie Extractive Quebec.

Hackl, R. P., Dreisinger, D. B., Peters, E., King, J. A., 1995. Passivation of chalcopyrite during oxidative leaching in sulfate media. Hydrometallurgy 39 (1-3), 25–48.

Hammersberg, P., Mångård, M., 1998. Correction for beam hardening artefacts in computerised tomography. Journal of X-Ray Science and Technology 8 (1), 75–93.

Hirato, T., Majima, H., Awakura, Y., 1987a. The leaching of chalcopyrite with cupric chloride. Metallurgical and Materials Transactions B 18 (1), 31–39.

Hirato, T., Majima, H., Awakura, Y., 1987b. The leaching of chalcopyrite with ferric sulfate. Metallurgical and Materials Transactions B 18 (3), 489–496.

Hiroyoshi, N., Kitagawa, H., Tsunekawa, M., 2008. Effect of solution composition on the optimum redox potential for chalcopyrite leaching in sulfuric acid solutions. Hydrometallurgy 91 (14), 144–149.

Hiroyoshi, N., Miki, H., Hirajima, T., Tsunekawa, M., 2000. A model for ferrous-promoted chalcopyrite leaching. Hydrometallurgy 57 (1), 31–38.

Hiroyoshi, N., Miki, H., Hirajima, T., Tsunekawa, M., 2001. Enhancement of chalcopyrite leaching by ferrous ions in acidic ferric sulfate solutions. Hydrometallurgy 60 (3), 185–197.

House, C. I., 1987. Potential pH diagrams and their application to hydrometallurgical systems. In: Davies, G. A. (Ed.), Separation processes in hydrometallurgy. Chichester: Ellis Horwood, pp. 3–19.

Hsih, C. S., Wen, S. B., Kuan, C. C., 1995. An exposure model for valuable components in comminuted particles. International Journal of Mineral Processing 43 (34), 145–165.

Hubbell, J. H., 1996. Tables of X-ray mass attenuation coefficients and mass energy-absorption coefficients 1 keV to 20 MeV for elements Z=1 to 92 and 48 additional substances of dosimetric interest [electronic resource] / J.H. Hubbell and S.M. Seltzer. No. Accessed from http://nla.gov.au/nla.cat-vn3823794. U.S. Department of Commerce, Technology Administration, National Institute of Standards and Technology, Gaithersburg, MD :.

Ilankoon, I., Neethling, S., 2012. Hydrodynamics of Unsaturated Particle Beds Pertaining to Heap Leaching. Imperial College London, last accessed: 2015-04-20.
URL http://books.google.co.uk/books?id=Cj5pmwEACAAJ

Ilankoon, I., Neethling, S., 2013. The effect of particle porosity on liquid holdup in heap leaching. Minerals Engineering 45 (0), 73–80.

Kappes, D. W., 2005. Heap leaching of gold and silver ores. In: Mike, D. A., Wills, B. A. (Eds.), Developments in Mineral Processing. Vol. Volume 15. Elsevier, pp. 456–478.

Kapur, J. N., Sahoo, P. K., Wong, A. K. C., 1985. A new method for gray-level picture thresholding using the entropy of the histogram. Computer Vision, Graphics, and Image Processing 29 (3), 273–285.

Ketcham, R. A., 2006. Accurate Three-dimensional Measurements of Features in Geological Materials from X-ray Computed Tomography Data. In: Advances in X-ray Tomography for Geomaterials. ISTE, pp. 143–148.

Ketcham, R. A., 2011. X-ray Computed Tomography (CT). Last accessed: 2015-04-20.
URL http://serc.carleton.edu/research_education/geochemsheets/techniques/CT.html

Ketcham, R. A., Carlson, W. D., 2001. Acquisition, optimization and interpretation of x-ray computed tomographic imagery: Applications to the geosciences. Computers and Geosciences 27, 381–400.

Ketcham, R. A., Hildebrandt, J., 2014. Characterizing, measuring, and utilizing the resolution of CT imagery for improved quantification of fine-scale features. Nuclear Instruments and Methods in Physics Research, Section B: Beam Interactions with Materials and Atoms 324, 80–87.

Kinney, J. H., Haupt, D. L., Nichols, M. C., Breunig, T. M., Marshall Jr, G. W., Marshall, S. J., 1994. The X-ray tomographic microscope: Three-dimensional perspectives of evolving microstructures. Nuclear Instruments and Methods in Physics Research Section A: Accelerators, Spectrometers, Detectors and Associated Equipment 347 (13), 480–486.

Klauber, C., 2008. A critical review of the surface chemistry of acidic ferric sulphate dissolution of chalcopyrite with regards to hindered dissolution. International Journal of Mineral Processing 86 (1-4), 1–17.

Kodali, P., Dhawan, N., Depci, T., Lin, C. L., Miller, J. D., 2011. Particle damage and exposure analysis in HPGR crushing of selected copper ores for column leaching. Minerals Engineering 24 (13), 1478–1487.

Koleini, S. M. J., Aghazadeh, V., Sandström, A. k., 2011. Acidic sulphate leaching of chalcopyrite concentrates in presence of pyrite. Minerals Engineering 24 (5), 381–386.

Landis, E. N., Keane, D. T., 2010. X-ray microtomography. Materials Characterization 61 (12), 1305–1316.

Levenspiel, O., 1999. Chemical reaction engineering. Wiley, last accessed: 2015-04-20. URL http://books.google.co.uk/books?id=X4svAQAAIAAJ

Liddell, K. C., 2005. Shrinking core models in hydrometallurgy: What students are not being told about the pseudo-steady approximation. Hydrometallurgy 79 (1-2), 62–68.

Lifshin, E., 1999. X-ray Characterization of Materials. Wiley-VCH.

Lin, C. L., Miller, J. D., 2005. 3D characterization and analysis of particle shape using X-ray microtomography (XMT). Powder Technology 154 (1), 61–69.

Lin, M. D., 2008. High Resolution X-ray Microscopy Using Digital Subtraction Angiography for Small Animal Functional Imaging. Ph.D. thesis.

Lin, Q., Neethling, S. J., Dobson, K. J., Courtois, L., Lee, P. D., 2014. 4D automatic quantification of ore particles in heap leaching from X-ray micro computed tomography. In: Valenzuela, F. (Ed.), Hydroprocess 2014, 6th International Seminar on Process Hydrometallurgy. Gecamin, Viña del Mar, Chile, pp. 47–56.

Lin, Q., Neethling, S. J., Dobson, K. J., Courtois, L., Lee, P. D., 2015. Quantifying and minimising systematic and random errors in X-ray micro-tomography based volume measurements. Computers & Geosciences 77 (0), 1–7.

Lu, Z. Y., Jeffrey, M. I., Lawson, F., 2000. An electrochemical study of the effect of chloride ions on the dissolution of chalcopyrite in acidic solutions. Hydrometallurgy 56 (2), 145–155.

Lufkin, J. L., 2010. Origin of ore textures: porphyry copper deposits. eological Society of America Abstracts with Programs 42 (3), 1.

Majima, H., Awakura, Y., Hirato, T., Tanaka, T., 1985. The Leaching of Chalcopyrite in Ferric Chloride and Ferric Sulfate Solutions. Canadian Metallurgical Quarterly 24 (4), 283–291.

MathWorks, 2013. Image Processing Toolbox Users Guide. Last accessed: 2015-04-20. URL http://www.mathworks.co.uk/help/pdf_doc/images/images_tb.pdf

McKinney L., M., Schoch Robert, M., Yonavjak, L., 2007. Environmental Science: Systems and Solutions. Jones and Bartlett Publishers.

Miller, G. M., 2003. Ore geotechnical effects on copper heap leach kinetics.

Miller, J. D., Lin, C. L., Garcia, C., Arias, H., 2003. Ultimate recovery in heap leaching operations as established from mineral exposure analysis by X-ray microtomography. International Journal of Mineral Processing 72 (14), 331–340.

Mostaghimi, P., Tollit, B., Neethling, S., Gorman, G., Pain, C., 2014. A control volume finite element method for adaptive mesh simulation of flow in heap leaching. Journal of Engineering Mathematics 87 (1), 111–121.

Muñoz, J. A., González, F., Blázquez, M. L., Ballester, A., 1995. A study of the bioleaching of a Spanish uranium ore. Part I: A review of the bacterial leaching in the treatment of uranium ores. Hydrometallurgy 38 (1), 39–57.

Mular, A. L., Halbe, D. N., Barratt, D. J., 2002. Mineral Processing Plant Design, Practice, and Control Proceedings, Volumes 1-2.

Munoz, P., Miller, J., Wadsworth, M., 1979. Reaction mechanism for the acid ferric sulfate leaching of chalcopyrite. Metallurgical and Materials Transactions B 10 (2), 149–158.

Ogbonna, N., Petersen, J., Laurie, H., 2006. An agglomerate scale model for the heap bioleaching of chalcocite. The Journal of The South African Institute of Mining and Metallurgy 106, 433–442.

Otsu, N., 1979. A threshold selection method from gray-level histograms. IEEE Transactions on Systems, Man and Cybernetics 9 (1), 62–66.

Padilla, G. A., Cisternas, L. A., Cueto, J. Y., 2008. On the optimization of heap leaching. Minerals Engineering 21 (9), 673–678.

Petersen, J., Dixon, D. G., 2002. Thermophilic heap leaching of a chalcopyrite concentrate. Minerals Engineering 15 (11), 777–785.

Petersen, J., Dixon, D. G., 2007. Modelling zinc heap bioleaching. Hydrometallurgy 85, 127–143.

Pradhan, N., Nathsarma, K. C., Srinivasa Rao, K., Sukla, L. B., Mishra, B. K., 2008. Heap bioleaching of chalcopyrite: A review. Minerals Engineering 21 (5), 355–365.

Puncreobutr, C., Lee, P. D., Hamilton, R. W., Phillion, A. B., 2012. Quantitative 3D Characterization of Solidification Structure and Defect Evolution in Al Alloys. JOM 64 (1), 89–95.

Rio Tinto, 2009. Kennecott Utah coppers Bingham Canyon mine: Teacher guide. Last accessed: 2015-04-20.
URL http://www.kennecott.com/library/media/TeacherGuide.pdf

Ritchie, A., 1997. Optimization of biooxidation heaps. In: Rawling, D. E. (Ed.), Biomining: Theory, Microbes and Industrial Processes. Springer, Berlin, Heidelberg, New York, pp. 211–226.

Rossi, G., 1990. Biohydrometallurgy. McGraw-Hill.

Safari, V., Arzpeyma, G., Rashchi, F., Mostoufi, N., 2009. A shrinking particleshrinking core model for leaching of a zinc ore containing silica. International Journal of Mineral Processing 93 (1), 79–83.

Schlesinger, M. E., King, M. J., Sole, K. C., Davenport, W. G., 2011. Extractive Metallurgy of Copper (Fifth Edition). Elsevier, Oxford.

Stauber, M., Müller, R., 2008. Micro-Computed Tomography: A Method for the Non-Destructive Evaluation of the Three-Dimensional Structure of Biological Specimens Osteoporosis. Vol. 455. Humana Press, pp. 273–292.

Stock, S. R., 1999. X-ray microtomography of materials. International Materials Reviews 44 (4), 141–164.

Stock, S. R., 2008. Recent advances in X-ray microtomography applied to materials. International Materials Reviews 53 (3), 129–181.

Strömberg, B., Banwart, S. A., 1999. Experimental study of acidity-consuming processes in mining waste rock: some influences of mineralogy and particle size. Applied Geochemistry 14 (1), 1–16.

Studholme, C., Hill, D. L. G., Hawkes, D. J., 1999. An overlap invariant entropy measure of 3D medical image alignment. Pattern Recognition 32 (1), 71–86.

Thompson, M., Thompson, M., Walsh, J. N., 1983. A handbook of inductively coupled plasma spectrometry. Blackie.

Thompson, M., Wood, S. J., 1982. Atomic Absorption Spectrometry. Vol. 5 of Techniques and Instrumentation in Analytical Chemistry. Elsevier.

Tsai, W.-H., 1985. Moment-preserving thresolding: A new approach. Computer Vision, Graphics, and Image Processing 29 (3), 377–393.

U.S. Geological Survey, 2001. U. S. Geological Survey: A Laboratory Manual for X-Ray Powder Diffraction. Last accessed: 2015-04-20.
URL http://pubs.usgs.gov/of/2001/of01-041/htmldocs/xrpd.htm

U.S. Geological Survey, 2014. Historical statistics for mineral and material commodities in the United States: U.S. Geological Survey Data Series 140. Last accessed: 2015-04-20.
URL http://minerals.usgs.gov/minerals/pubs/historical-statistics/

van Hille, R. P., van Zyl, A. W., Spurr, N. R. L., Harrison, S. T. L., 2010. Investigating heap bioleaching: Effect of feed iron concentration on bioleaching performance. Minerals Engineering 23 (6), 518–525.

Visualization Sciences Group, 2011. Avizo 7 Avizo User's Guide. Last accessed: 2015-04-20.
URL http://www.vsg3d.com/sites/default/files/AvizoUsersGuide.pdf

Watling, H. R., 2006. The bioleaching of sulphide minerals with emphasis on copper sulphides A review. Hydrometallurgy 84 (1-2), 81–108.

Wills, B., Napier-Munn, T., 2006. Mineral Processing Technology. Seventh Edition. Elsevier Science & Technology Books.

Wulfsberg, G., 1992. Principles of descriptive inorganic chemistry. Univ Science Books.

Yang, B.-h., Wu, A.-x., Jiang, H.-c., Chen, X.-s., 2008. Evolvement of permeability of ore granular media during heap leaching based on image analysis. Transactions of Nonferrous Metals Society of China 18 (2), 426–431.

Yen, J.-C., Chang, F.-J., Chang, S., 1995. A new criterion for automatic multilevel thresholding. Image Processing, IEEE Transactions on 4 (3), 370–378.

Yue, S., Lee, P. D., Poologasundarampillai, G., Jones, J. R., 2011. Evaluation of 3-D bioactive glass scaffolds dissolution in a perfusion flow system with X-ray microtomography. Acta biomaterialia 7 (6), 2637–43.

Appendices

Appendix A

Expectational procedure and related information

A.1. Procedure for sample decomposition

According to Thompson and Wood (1982) and Thompson et al. (1983), the main steps for preparing samples for sample decomposition for ICP-OES analysis are:

1. Place 0.0250±0.001 g samples into sample tubes.
2. Add 4.0 ml Nitric Acid (A.R. 70% w/w) into each tube from an Oxford dispenser.
3. Add 1.0 ml Perchloric Acid (A.R. 60% w/w) from an Oxford dispenser.
4. Place tubes in the aluminium heating block till dry.
5. When tubes are cool, add 2.0 ml of 2M Nitric acid to each tube from an Oxford dispenser.
6. Place tubes in a shallow heating block and leave to leach for one hour at 60°C.
7. After the tube becomes cool, add 8.0 ml de-ionised water from an Oxford dispenser and mix each tube, using a vortex mixer.
8. Decant the solution into polystyrene tubes and cap, centrifuge at 2000 rpm for 2 minutes.

A.2. Procedure for acid titration

The general procedure for acid titration using methyl orange as indicator is:

1. Transfer 1 ml of sample (sulphuric acid solution for titration) to an Erlenmeyer flask by pipette.
2. Dilute the 1 ml sample to around 50 ml with de-ionised water.
3. Add several drops of methyl orange.
4. Titrate with NaOH till the colour changes to orange.
5. Calculate the acid concentration.

A.3. Procedure for validating iron content from raw chemicals

The general procedure for testing the actual iron concentration is:

1. Make 2M nitric acid by diluting 70% nitric acid.
2. Take 0.07 g $Fe_2(SO_4)_3 \cdot nH_2O$ (using digital balance with 4 decimal places) and dissolve in 2 L nitric acid (2M).
3. Take 0.14 g $Fe_2(SO_4)_3 \cdot nH_2O$ (using digital balance with 4 decimal places)and dissolve in 2 L nitric acid (2M).
4. Take 0.075 g $FeSO_4 \cdot 7\,H_2O$ (using digital balance with 4 decimal places) and dissolve in 2 L nitric acid (2M). (It needs to be noted that ferrous ions are oxidised to ferric by nitric acid, the total amount of iron can still be measured by ICP-OES)
5. Take 0.15 g $FeSO_4 \cdot 7\,H_2O$ (using digital balance with 4 decimal places) and dissolve in 2 L nitric acid (2M).
6. Mix the solution well and do ICP-OES (The calibration standards are 0 ppm, 1 ppm, 5 ppm and 20 ppm).

A.4. Standard potentials (mV) of some reference electrodes

Data source: Galster H., pH-Messung, Weinheim, VCH, 1990.

Table A.1.: Volts (mV) related to standard hydrogen electrode.

	Silver chloride, Argenthal, Silamid Ag/AgCl, KCl				Calomel Hg/Hg_2Cl_2, KCl			Thalamid Tl,Hg/ TlCl,KCl	Mercury sulphate Hg/Hg_2SO_4, K_2SO_4
Temp	1 mol/l	3 mol/l	3.5 mol/l	saturated	0.1 mol/l	1 mol/l	saturated	3.5 mol/l	saturated
0 °C	249	224	222.1	220.5	333.8	285	260.2	558.5	671.8
5 °C	247	221	218.7	216.1	334.1	285	257.2	561.0	667.6
10 °C	244	217	215.2	211.5	334.3	284	254.1	563.5	663.5
15 °C	242	214	211.5	206.8	334.2	283	250.9	566.0	659.4
20 °C	240	211	207.6	201.9	334	282	247.7	568.6	655.3
25 °C	236	207	203.7	197	333.7	280	244.4	571.3	651.3
30 °C	233	203	199.6	191.9	333.2	279	241.1	574.0	647.3
35 °C	230	200	195.4	186.7	332.4	277	237.7	576.7	643.3
40 °C	227	196	191.2	181.4	331.6	275	234.3	579.6	639.2
45 °C	224	192	186.8	176.1	330.6	274	230.8	582.5	635.1
50 °C	221	188	182.4	170.7	329.6	272	227.2	585.4	630.9
55 °C	217	184	178	165.3		270	223.6	588.5	626.6
60 °C	214	180	173.5	159.8		267	219.9	591.6	622.6
65 °C	210	176	169	154.3		265	216.2	594.8	617.7
70 °C	207	172	164.5	148.8		262	212.4	598.0	613.3
75 °C	203	168	160	143.3				601.4	608.4
80 °C	200	163	155.6	137.8				604.8	603.4
85 °C	196	158	151.1	132.3				608.3	598.4
90 °C	193	153	146.8	126.9				611.9	593.1
95 °C	189	148	142.5	121.5				615.6	578.6

A.5. Interference table for Cu and Fe measurement using ICP-OES

Interferences for Cu (224.700)			Interferences for Fe (238.204)		
Element	Wavelength (nm)	Intensity	Element	Wavelength (nm)	Intensity
Sn (I)	224.605	50000	W (II)	238.110	1800
Sn (II)	224.607	643	Ta (II)	238.113	50000
Rh (II)	224.638	4000	Mo (II)	238.114	1000
Os	224.640	1000	Re (I)	238.114	1500
Ag (II)	224.641	20000	As (I)	238.118	2500
Re	224.650	1000	W (II)	238.133	0
Nb (II)	224.650	2000	Mo (II)	238.147	2000
W (II)	224.663	12000	Cr (II)	238.148	3000
Pb (I)	224.688	15000	Ta (II)	238.152	15000
Pb (I)	224.689	30	Li (II)	238.154	0
Ir (II)	224.690	7000	Ir (i)	238.162	30000
Nb (II)	224.697	1200	Co (II)	238.175	20000
Cu (II)	**224.700**	**1000000**	Fe (I)	238.184	30000
Nb (II)	224.719	0	Dy	238.195	120000
Ni (II)	224.723	6000	Ru (II)	238.199	25000
Re (II)	224.733	1000	**Fe (II)**	**238.204**	**1800000**
Re (II)	224.751	0	U	238.230	1000
Hg (II)	224.755	120	W (II)	238.234	1800
W (II)	224.767	2000	Co	238.234	1800
Os	224.768	2000	Zr	238.236	1200
			Fe (II)	238.236	1200
			Os (I)	238.246	1000
			V (III)	238.247	1000
			In (II)	238.263	1222
			W (II)	238.267	1200
			Rh (I)	238.289	12000
			Fe (II)	238.290	4000
			W (I)	238.299	2500

Appendix B

Derivations

B.1. Derivation of measurement error within each categories

Within each size-distance categories, if the interval of the size range is narrow, the observed measurement error in volume for a grain at any time step, $\sigma(\widetilde{V}_i)$ (equation shown in Figure 5.17), can be expressed as a function of its actual size:

$$\sigma\left(\widetilde{V}_i\right) = \sigma\left(V_i + f_\varepsilon(V_i)\right) \tag{B.1}$$

$$\sigma\left(\widetilde{V}_i\right) = \sigma\left(V_i\right) + \sigma'\left(V_i\right) f_\varepsilon(V_i) \tag{B.2}$$

where V_i is the actual size of the grain, $f_\varepsilon(V_i)$ is the uncertainty of the actual size, which is also a function function of V_i, $\sigma\left(V_i\right)$ is the overall measurement error. Therefore, the overall measurement error can be expressed as:

$$\sigma\left(\widetilde{V}_i\right) \approx \sigma\left(V_i\right)\left(1 + \sigma'\left(V_i\right)\right) \tag{B.3}$$

$$\sigma\left(V_i\right) = \frac{\sigma\left(\widetilde{V}_i\right)}{1 + \sigma'\left(V_i\right)} \tag{B.4}$$

$$\sigma\left(\widetilde{V}_i\right) = a{V_i}^b \tag{B.5}$$

$$\sigma\left(V_i\right) = \frac{a{V_i}^b}{1 + ab{V_i}^{(b-1)}} = \left(\frac{1}{a{V_i}^b} + \frac{b}{V_i}\right)^{-1} \tag{B.6}$$

where a is the prefactor in the power law relationship and b is the power law exponent.

Appendix C

Codes and Scripts

Part of the source codes developed in this thesis for 3D image processing are not available within this thesis due to the legal and licensing agreement with Rio Tinto. However, pseudocode and some of the source codes are included in an attached DVD and the core functions are listed with brief summaries, shown in Table C.1. If there is any enquiry for a copy of any source code or script, please either contact my supervisor or myself:

Mr Qingyang Lin
Department of Earth Science and Engineering, Imperial College London.
Email: q.lin11@imperial.ac.uk

Dr. Stephen Neethling
RSM 2.35, Department of Earth Science and Engineering, Imperial College London.
Tel: +44 (0)20 7594 9341
Email: s.neethling@imperial.ac.uk

Table C.1.: Codes for 3D image processing, quantification and modelling.

Name	Purpose
data_conversion.m	Image Conversion and Calibration
median_filter.tcl	Applying Median Filter
rock_thresholds.m	Calculating the threshold value for rock phase
column_preseg.m	Preparation for Ore Particle Separation
separation.tcl	Ore Particle Separation
ore_tracking_relabel.m	Ore Particle Tracking and Relabelling
rock_extraction.m	Individual Rock Extraction
registration.tcl	Ore Particle Registration
phase_threshold.m	Rock and Mineral Grain Phase Threshold
d0_tracking.m	Mineral Grain Tracking and Quantification
tracking_quan.m	
modelling.cpp	Modelling of Apparent Leach Kinetics

Appendix D

Publications

Lin, Q., Neethling, S. J., Dobson, K. J., Courtois, L., Lee, P. D., 2014. 4D automatic quantification of ore particles in heap leaching from X-ray micro computed tomography. In: Valenzuela, F. (Ed.), Hydroprocess 2014, 6th International Seminar on Process Hydrometallurgy. Gecamin, Viña del Mar, Chile, pp. 47–56

Lin, Q., Neethling, S. J., Dobson, K. J., Courtois, L., Lee, P. D., 2015. Quantifying and minimising systematic and random errors in X-ray micro-tomography based volume measurements. Computers & Geosciences 77 (0), 1–7

Cai, L., Ferrier, R. J., Lin, Q., Mostaghimi, P., Gorman, G. J., Neethling, S. J., 2014. Heap leaching simulation: beyond shrinking core models. No. June. 10th International Conference on CFD in Oil & Gas, Metallurgical and Process Industries SINTEF, Trondheim, NORWAY, pp. 1–7